

**A 3D Continuum Finite Element Muscle Model for the Investigation of Cervical
Spine Load-Sharing Mechanisms and Injury Assessment during Impact Loading**

Scenarios

by

Fatemeh Moghaddam

A thesis submitted in partial fulfillment of the requirements for the degree of

Doctor of Philosophy

in

Structural Engineering

Department of Civil and Environmental Engineering

University of Alberta

© Fatemeh Moghaddam, 2018

Abstract

The mechanical behavior of the individual cervical tissues as well as the head-neck complex kinematics plays a very important role in proper functioning of the cervical spine and is a key factor in more appropriate understanding of injury mechanism, prevention, detection, control and treatment. This aids clinicians, engineers and other involved researchers to develop better detective, preventive and treatment techniques for cervical disorders. Although great efforts have been made to understand the biomechanics of the cervical spine tissues, and the cervical musculature in particular, many aspects are still challenge. The cervical musculature is the major stabilizer of the neck and head, and is composed of active and passive components. The majority of FE models have used discrete spring elements to simulate the muscles. These elements fail to represent mass inertia, and the real geometry of the muscles. Hence, computational 3D FE models have been proposed to overcome these limitations. Moreover, such 3D computational FE models can be a useful tool considering difficulties associated with *in-vivo* and *in-vitro* impact tests on human subjects.

The main objective of this study was to develop a 3D FE model of the cervical spine including a 3D continuum cervical musculature governed by a new material model. This material simulates both active and passive parts of the muscle. The muscle behavior was numerically formulated and a user defined FORTRAN subroutine, UMAT, was developed to implement the model into the software ABAQUS. In addition, 3D continuum cervical muscles constructed from Magnetic Resonance Images (MRI) were added to a detailed FE model of a Ligamentous Spine (LS). This is the first FE model of the cervical spine that has 3D musculature including both active and passive properties of the muscle governed by only one constitutive equation. This new

thorough cervical spine model was used to investigate the overall kinematics of the head and neck as well as the mechanical responses of the individual cervical tissues. Moreover, the responses of the LS model and a spine with only Passive Musculature (PMS) were compared to the response of a spine with both active and passive musculature (FMS) to investigate the effect of the muscle activation on the behavior of the cervical spine during dynamic loading conditions. And finally, the concept of Strain Energy (S.E.) was used to investigate how spinal components interact together during a specific loading condition.

The obtained results indicated the important role of the cervical musculature and its active part in particular, in the cervical spine behavior under impact loading scenarios. Adding the passive musculature to the LS model not only restricted the movement of the head and neck, but also altered the stress and stress distribution in the cervical tissues. More importantly, adding the muscle activation to the spine model significantly reduced the head and neck range of motion, and, in consequence, improved the stability of the spine.

Additionally, the results of spinal load sharing analyses pointed out that the amount of S.E. in the spine during frontal impact scenarios was significantly greater than that during rear-end impact scenarios. In addition, the spinal load sharing results showed, regardless of the impact direction and severity, adding the muscle activation to the spine decreased the amount of S.E. absorbed by the spine.

Finally, the new continuum muscle model was able to predict strain, force, and energy distribution in the muscles and indicated which muscle bears the major role during a specific impact loading scenario. The results agreed with the experimental data (EMG) and previous numerical studies.

Preface

This dissertation is an original work done by Fatemeh Moghaddam. The concluding analyses in Chapters Six-Eight are my original work.

Some parts of Chapter Eight have been:

- accepted to The “8th World Congress of Biomechanics” (<http://wcb2018.com/>) as Fatemeh Moghaddam, Marwan El-Rich, and Samer Adeeb, “Cervical Spine Response to Impact with and without Muscle Activation: A Numerical Model”.
- presented in the “ASME International Mechanical Engineering Congress & Exposition” (<http://www.asmeconferences.org/congress2014/>) as Fatemeh Moghaddam and Marwan El-Rich, “Cervical Musculature Injury Prediction using a New Approach of 3D Muscle Modeling”. Paper No: IMECE 2014-40119

To my father in heaven

Acknowledgements

I would like to express my special thanks to my beloved mother and siblings for their unconditional support throughout my life. I am forever grateful to you.

I would like to especially thank my supervisor Dr. Marwan El-Rich for his guidance, support, and time throughout my PhD journey.

I would like to thank Dr. Samer Adeeb for all his support and continuous helps.

I am very thankful to my respected colleagues: Behzad Vafaeian, Sadegh Naserkhaki, Faisal Agah, and Tanvir Mustafy for their valuable opinions and collaborations, and friendship.

I would also like to thank the WestGrid Support Team for their prompt and instructive helps.

Table of Contents

CHAPTER ONE: INTRODUCTION.....	1
1.1 Motivation.....	2
1.2 Research Objectives.....	4
1.3 Dissertation Outline.....	8
CHAPTER TWO: BACKGROUND AND LITERATURE REVIEW.....	12
2.1 Mechanical Structure of the Cervical Spine.....	12
2.2 Review of Anatomy, Function, and Modelling of Ligamentous Cervical Spine Components.....	12
2.2.1 Vertebrae.....	13
2.2.2 Ligaments.....	13
2.2.3 Intervertebral Disc (IVD).....	17
2.2.4 Facet Joint (FJ).....	17
2.3 Review of Anatomy, Function, and Modelling Approaches of the Cervical Spine Musculature.....	18
2.3.1 Skeletal Muscle Anatomy.....	18
2.3.1.1 Muscle Architecture.....	20
2.3.1.2 Force-Activation Relation.....	22
2.3.1.3 Force-Length Relation.....	23
2.3.1.4 Force-Velocity Relation.....	24
2.3.2 Skeletal Muscle Models.....	24
2.3.3 Cervical Musculature.....	28
2.3.3.1 Cervical Musculature Models.....	30
2.3.4 Tendon.....	31
CHAPTER THREE: CONTINUUM CONSTITUTIVE MODELLING OF THE SKELETAL MUSCLE.....	32
3.1 Constitutive Model.....	33
3.1.1 Principal Structure of the Constitutive Model.....	33
3.1.2 Fiber Stress Calculation.....	36
3.1.3 Connective Tissue Stress Calculation.....	37
3.1.4 Generalizing the Constitutive Equations to the Pennate Structures.....	38
3.2 Numerical Formulation and Discretization of the Constitutive Model.....	38
3.2.1 Deformable Body General Equilibrium Equation.....	38
3.2.2 Finite Element Implementation.....	40
3.2.3 Calculation of the Jacobian.....	42

3.2.4 The Linearization Moduli	45
3.3 Summary of My Contribution	49
CHAPTER FOUR: NUMERICAL IMPLEMENTATION, VERIFICATION AND VALIDATION OF THE MATERIAL MODEL	51
4.1. UMAT Implementation	51
4.2. UMAT Verification.....	57
4.2.1. Convergence Test.....	57
4.2.2. Extension of a Squid Tentacle: Validation Test.....	62
4.3. Summary of my Contribution	65
CHAPTER FIVE: GEOMETRY RECONSTRUCTION, MESH GENERATION, AND MATERIAL PROPERTIES	66
5.1. Geometry Reconstruction.....	66
5.2. Mesh Generation	67
5.2.1. Bony Structures.....	67
5.2.2. Ligaments.....	68
5.2.3. IVD.....	69
5.2.4. Muscles and Tendons.....	71
5.3. Material Properties.....	74
5.3.1. Vertebra	74
5.3.2. IVD.....	76
5.3.3. Ligaments.....	76
5.4. Muscle and Tendon.....	78
CHAPTER SIX: LIGAMENOUS CERVICAL SPINE RESPONSE (LOAD SHARING) UNDER FRONTAL AND REAR-END IMPACT LOADING SCENARIOS: A 3D FINITE ELEMENT STUDY	79
6.1 Problem Description	79
6.2 Solution Techniques, Loading and Boundary Conditions	79
6.2.1 Model Validation Tests	81
6.2.1.1 FSU Validation.....	81
6.2.1.2 Cervical Spine Kinematics Validation	82
6.3 Results.....	84
6.3.1 FSU Validation Results	84
6.3.2 Cervical Spine Validation in Frontal and Rear-End Impacts Results	84
6.3.3 Ligaments Injury Prediction using Stress Failure Criteria	84

6.3.4 Strain Distribution in Cervical Ligaments during 15G Frontal and Rear-End Impacts	90
6.3.5 Contact Force and Pressure in Facet Joints	96
6.3.6 Cervical Spinal Load Sharing	98
6.4 Discussion and Conclusion	108
CHAPTER SEVEN: INVESTIGATING THE EFFECT OF 3D PASSIVE MUSCULATURE ON THE BEHAVIOR OF THE CERVICAL SPINE UNDER IMPACT LOADING SCENARIOS.....	110
7.1 Problem Description	110
7.2 Geometry and Material Properties of Cervical Musculature, Loading and Boundary Conditions, and Solution	110
7.3 Results.....	111
7.3.1 Ligaments Injury Prediction using Stress Failure Criteria	111
7.3.2 Effect of the Musculature on Strain Distribution in the Cervical Spine Soft Tissues	115
.....	119
7.3.3 Contact Force and Pressure in Facet Joints	120
7.3.4 Cervical Spine Load Sharing	123
7.3.4.1 Frontal Impact Load Sharing Results.....	123
7.3.4.2 Rear-End Impact Load Sharing Results	124
7.3.5 Energy Distribution in the Cervical Muscles	140
7.4 Discussion and Conclusion	141
CHAPTER EIGHT: INVESTIGATING THE EFFECT OF THE CERVICAL MUSCULATURE ON THE BEHAVIOR OF THE CERVICAL SPINE USING A NEW 3D CONTINUUM CONSTITUTIVE MODEL CONSIDERING BOTH ACTIVE AND PASSIVE MECHANICAL PROPERTIES OF THE CERVICAL MUSCULATURE	144
8.1 Problem Description	144
8.2 Material Properties, Loading and Boundary Conditions.....	145
8.2.1 Cervical Muscle Material Properties.....	145
8.2.2 Cervical Spine Kinematics Validation during Rear-End Impact.....	147
8.3 Results.....	147
8.3.1 Cervical Spine Validation during Rear-End Impact Results.....	147
8.3.2 Effect of Muscles Contraction-only on the Spinal Tissues Behaviour.....	148
8.3.3 Load Distribution in the Cervical Muscles.....	150
8.3.4 Strain and Stress Distributions in the Cervical Ligaments.....	151
8.3.5 Effect of Muscle Activation on the Pressure Distribution in the Intervertebral Discs.....	155
8.3.6 Contact Force and Pressure in Facet Joints	157

8.3.7 Cervical Spinal Load Sharing	159
8.3.7.1 Frontal Impact Load Sharing Results.....	159
8.3.7.2 Rear-End Impact Load Sharing Results	160
8.4 Discussion and Conclusion	176
CHAPTER NINE: SUMMARY, CONCLUSIONS, LIMITATIONS, AND FUTURE DIRECTIONS	180
9.1 Summary	180
9.2. Conclusions	181
9.2.1 Significance of the Severity and Direction of Impact – <i>Chapter Six</i>	181
9.2.2 Importance of the Passive Musculature - <i>Chapter Seven</i>	182
9.2.3 Significance of the Muscle Activation – <i>Chapter Eight</i>	183
9.3 Modeling Considerations, Limitations, and Future Directions	184
Bibliography	189
Appendix A.....	196
Appendix B	204
Appendix C	220
Appendix D.....	249

List of Tables

Table 2.1 Cross Sectional Area and Length of Cervical Ligaments (Mean (SD) (Yoganandan et al., 2000).	16
Table 2.2 Different types of muscle categories based on function and location.	29
Table 2.3 Cervical muscles with their origin, insertion, mass (gram), and PCSA (mm²) (Adopted from Hedenstierna (2008)).	29
Table 4.1 Constant muscle parameters used in this study, their units and values.	57
Table 4.2 Parameters vary linearly from the base to the end of the stalk.	57
Table 4.3 Parameters vary linearly from the base to the end of the stalk (values used in this dissertation).	65
Table 5.1 Number of elements in bony components	68
Table 5.2a Number of elements in UCS ligaments	69
Table 5.2b Number of elements in LCS ligaments at each cervical level.....	69
Table 5.3 Percentage of annulus and nucleus volume out of disc volume (%)	70
Table 5.4 Number of elements in disc components at different cervical spinal level.....	71
Table 5.5 Number of elements in the cervical muscles and tendons.....	74
Table 5.6 Material Properties of cervical spine bony components	75
Table 5.7 Mechanical properties of disc components.....	76
Table 5.8a Material properties of UCS ligaments	77
Table 5.8b Material properties of LCS ligaments.....	77
Table 5.9 Material properties of passive musculature and tendons	78
Table 7.1 %Energy in each muscle/All muscles	141
Table C 4.1 Constant muscle parameters used in this study, their units and values.	245
Table C 4.2 Parameters vary linearly from the base to the end of the stalk.	245

List of Figures

Figure 2.1 The Upper Cervical Spine (UCS) and the Lower Cervical Spine (LCS) geometry. 12

Figure 2.2 Cortical and cancellous bones (<http://drmchiro.blogspot.ca/2013/02/the-shock-absorbers-of-spine.html>). 13

Figure 2.3 Finite element representation of the cervical spine components: (a) The UCS ligaments including the AAOM, Alar, Apical, Nuchal, and C12 part of PLL, PAAM, and PAOM. (b) The LCS ligaments including the ALL, CL, ISL, ITL, PLL, LF, and SSL; the IVD component (Annulus, Nucleus, and CF); the cortical and cancellous bones, the endplates, and the facets. 14

Figure 2.4 FSU structure used to derive force-displacement in the cervical ligaments (ALL in this case). Lower vertebra is fixed and tensile load is applied to the upper vertebra..... 15

Figure 2.5 A typical view of skeletal muscle hierarchical structure: several types of protein-based tissues i.e. Epimysium, Endomysium, and Perimysium are located around fiber bundles. A tendon attaches a muscle to the nearby bone. (http://www.medicalook.com/human_anatomy/organs/Skeletal_muscle_fiber.html). 20

Figure 2.6 Skeletal muscle microstructure, and contractions types: concentric, isometric, and eccentric. 20

Figure 2.7 Different types of muscle architecture: a) parallel, b) uni-pennate, c) bi-pennate. PCSA is perpendicular to the fibers' direction (Spyrou 2009). 21

Figure 2.8 Active muscle force vs. length of muscle which is a function of the amount of actin and myosin filaments overlap (http://droualb.faculty.mjc.edu/Course%20Materials/Physiology%20101/Chapter%20Notes/Fall%202007/chapter_12%20Fall%202007%20Phy%20101.htm). 23

Figure 2.9 Total, active, and passive forces in a skeletal muscle vs. length of the muscle (<https://www.strongerbyscience.com/how-to-prevent-muscle-strains/>). 23

Figure 2.10 Force vs. velocity of contraction curve during isometric, eccentric and concentric contractions (<https://www.strongerbyscience.com/how-to-prevent-muscle-strains/>). 24

Figure 2.11 Hill model including a contractile element, a parallel and a series element. (a) Parallel muscle, (b) pennate muscle (http://gribblelab.org/compneuro/6_Computational_Motor_Control_Muscle_Models.html and <http://youngmok.com/hill-type-muscle-model-with-matlab-code/>). 26

Figure 3.1 Schematic view of a deformed muscle, fibers direction within the tissue, and an infinitesimal segment of the fiber ds . The orientation of the fibers within a continuum finite element is also depicted. σ_m represents the Cauchy stress in the fiber direction (adopted from Spyrou and Aravas (2011)). 33

Figure 3.2 Configuration of a continuum body in a Cartesian coordinate system and its motion. 39

Figure 4.1 Activation function vs. time for the tentacle muscle.....	54
Figure 4.2 Length function vs. strain for the tentacle muscle.	55
Figure 4.3 Velocity function vs. strain rate for the tentacle muscle.....	56
Figure 4.4 Normalized Passive Stress function vs. strain for the tentacle muscle.	56
Figure 4.5 Squid fish tentacle test set-up. Tentacle base is fixed, while its end is free to extend. Club is considered as undeformable body, whereas stalk is deformable. Number of elements along the stalk length is changed to check the convergence of the developed material.	58
Figure 4.6 (a) Diagram of a squid. (b) Diagram of the morphology of the tentacular stalk in squid with its muscle groups (Van Leeuwen and Kier, 1997).....	59
Figure 4.7 Defined path from tentacle base to the end.	60
Figure 4.8 Position of the nodes along the defined path at t=55 msec.....	60
Figure 4.9 Tentacle tip longitudinal strain at t=55 msec along the defined path.....	61
Figure 4.10 Reaction force in the tentacle base vs. time at different activation levels.	62
Figure 4.11 Tentacle tip displacement vs. time at different activation levels.	62
Figure 4.12 Tentacle length vs. time. Current work predictions fell within 5% of the experimental work done by van Leeuwen and Kier (1997).	64
Figure 4.13 Tentacle tip velocity of contraction vs. time. Current work results are compared with the experimental data reported by van Leeuwen and Kier (1997).....	64
Figure 5.1 (a) Cervical vertebra bony components including cortical, cancellous, endplate, and facets. (b) The IVD components: annulus, nucleus, and 7 layers of collagen fibers.....	68
Figure 5.2 (a) The UCS ligaments: AAOM, Alar, Apical, Nuchal, PAAM, PAOM. (b) The LCS ligaments: ALL, CL, ISL, ITL, LF, PLL, SSL.....	70
Figure 5.3 (a) An overall view of the cervical muscles. (b) Sternocleidomastoid (SCM) is located on the lateral sides of the cervical spine. (c). A schematic view of the cross sectional area of the muscles, Trapezius (TZ), Splenius (SC), and Semispinalis (SSC) located at the posterior side of the cervical spine.....	73
Figure 6.1 A general view of the cervical spine (left), a detailed view of the Upper Cervical Spine (UCS) and the Lower Cervical Spine (LCS) (right up and down, respectively).	80
Figure 6.2 Loading test setup for the ligament validation test (ALL). Same setup is used of the other ligaments: CL, ISL, LF, and PLL.....	81
Figure 6.3 Failure force vs. elongation for the LF, ALL, ISL, CL, and PLL ligaments at medium (20s – 1), and high (150s – 1) strain rates. Average, Upper and Lower Bonds are from Mattucci experimental work (Mattucci et al. 2012). C23-C67 indicates the cervical spinal levels.....	83

Figure 6.4 (a,b) Head relative T1 displacement (translation and rotation) results obtained from the current model validated against experimental data of the volunteer corridors (Ewing et al. 1976), and also is compared with the results reported in the previous numerical simulations during 15G frontal impact (Hedenstierna et al., 2009). (c,d) Head relative T1 displacement (translation and rotation) results obtained from the current model was validated against experimental data of Post Mortem Human Subject (PMHS) corridors (average response \pm 1 Standard Deviation (SD)) (Stemper et al., 2004), and also compared with previous numerical simulation results during a 2.6 m/s rear-end impact (Östh et al. 2017). 86

Figure 6.6 Sequences of failure in the CL ligaments at different cervical spinal levels during 15G impact. 88

Figure 6.5 Sequences of failure in the ALL ligaments at different cervical spinal levels during 15G impact. 88

Figure 6.7 Sequences of failure in the ISL ligaments at different cervical spinal levels during 15G impact. 89

Figure 6.8 Sequences of failure in the LF ligaments at different cervical spinal levels during 15G impact. 89

Figure 6.9 Sequences of failure in the PLL ligaments at different cervical spinal levels during 15G impact. 89

Figure 6.10 (a) The SSL ligaments peak stress at different cervical spinal levels during 15G impact..... 90

Figure 6.10 (b) The ITL ligaments peak stress at different cervical spinal levels during 15G impact. 90

Figure 6.11 Peak strain in the cervical ligaments: the current work results are compared with Panzer et al. (2011) numerical study during 15G frontal impact loading scenario. 91

Figure 6.12 A schematic view of strain distribution in the ALL ligaments during 15G frontal and rear-end impacts captured at the time=0.1 s (Left side). Strain (%) vs. time in the ALL ligaments at different cervical levels during 15G frontal and rear-end impacts (Right side)..... 92

Figure 6.13 A schematic view of strain distribution in the CL ligaments during 15G frontal and rear-end impacts captured at the time=0.1s (Left side). Strain (%) vs. time in the ALL ligament at different cervical levels during 15G frontal and rear-end impacts (Right side)..... 93

Figure 6.14 A schematic view of strain distribution in the ISL ligaments during 15G frontal and rear-end impacts captured at the time=0.1s (Left side). Strain (%) vs. time in the ALL ligaments at different cervical levels during 15G frontal and rear-end impacts (Right side)..... 94

Figure 6.15 A schematic view of strain distribution in the LF ligaments during 15G frontal and rear-end impacts captured at the time=0.1s (Left side). Strain (%) vs. time in the ALL ligaments at different cervical levels during 15G frontal and rear-end impacts (Right side)..... 95

Figure 6.16 Average and maximum nodal contact pressures, as well as contact force in the cervical facet joints at different cervical spinal levels during 15 frontal and rear impacts. 97

Figure 6.17 Cervical spinal load sharing based on Strain Energy (S.E.): The magnitude and percentage of contribution of S.E. of each spinal level, in comparison to all other levels; the magnitude and percentage of S.E. in each spinal tissue, in comparison to all other tissues, the S.E. of each ligament group and its percentage compared to the other ligaments, respectively, resulting from 15G frontal and rear-end impact scenarios.	101
Figure 6.18 S.E. distribution in the spinal level C12 resulting from 15G frontal and rear-end impacts. ...	102
Figure 6.19 S.E. distribution in the spinal level C23 resulting from 15G frontal and rear-end impact conditions.....	103
Figure 6.20 S.E. distribution in the spinal level C34 resulting from 15G frontal and rear-end impact conditions.....	104
Figure 6.21 S.E. distribution in the spinal level C45 resulting from 15G frontal and rear-end impact conditions.....	105
Figure 6.22 S.E. distribution in the spinal level C56 resulting from 15G frontal and rear-end impact conditions.....	106
Figure 6.23 S.E. distribution in the spinal level C67 resulting from 15G frontal and rear-end impact conditions.....	107
Figure 7.1 (a) An overall view of the cervical muscles. (b) Sternocleidomastoid (SCM) is located on the lateral sides of the cervical spine. (c) A schematic view of the cross sectional area of the muscles, Trapezius (TZ), Splenius (SC), and Semispinalis (SSC) located at the posterior side of the cervical spine.....	111
Figure 7.2 Sequences of failure in the ALL ligaments at different cervical spinal levels in the LS and PMS models during 5G frontal and rear-end impact scenarios.....	113
Figure 7.3 Sequences of failure in the CL ligaments at different cervical spinal levels in the LS and PMS models during 5G frontal and rear-end impact scenarios.....	113
Figure 7.4 Sequences of failure in the ISL ligaments at different cervical spinal levels in the LS and PMS models during 5G frontal and rear-end impact scenarios.....	114
Figure 7.5 Sequences of failure in the LF ligaments at different cervical spinal levels in the LS and PMS models during 5G frontal and rear-end impact scenarios.....	114
Figure 7.6 Sequences of failure in the LF ligaments at different cervical spinal levels in the LS and PMS models during 5G frontal and rear-end impact scenarios.....	114
Figure 7.7 Strain distributions in the cervical ligaments during 8G frontal impact. The LS and PMS models predictions were compared with the numerical and experimental studies results.....	115
Figure 7.8 Strain distributions in the anterior and posterior parts of IVDs during 8G frontal impact. The LS and PMS models predictions were compared with the numerical and experimental studies results.	117

Figure 7.9 History of strain (%) in the ALL ligaments over time in the LS and PMS models during 5G frontal and rear-end impact scenarios.	118
Figure 7.10 History of strain (%) in the CL ligaments over time in the LS and PMS models during 5G frontal and rear-end impact scenarios.	118
Figure 7.11 History of strain (%) in the ISL ligaments over time in the LS and PMS models during 5G frontal and rear-end impact scenarios.	118
Figure 7.12 History of strain (%) in the LF ligaments over time in the LS and PMS models during 5G frontal and rear-end impact scenarios.	119
Figure 7.13 History of strain (%) in the PLL ligaments over time in the LS and PMS models during 5G frontal and rear-end impact scenarios.	119
Figure 7.14 History of strain (%) in the UCS ligaments over time in the LS and PMS models during 5G frontal and rear-end impact scenarios.	119
Figure 7.15 Average and maximum contact pressures and contact force in the FJs at different spinal levels during 8G frontal and rear impact scenarios.	121
Figure 7.16 Average and maximum contact pressures and contact force in the FJs at different spinal levels during 5G frontal and rear impacts.	122
Figure 7.17 Cervical spinal load sharing based on Strain Energy (S.E.): The magnitude and percentage of contribution of S.E. of each spinal level in comparison to all other levels; the magnitude and percentage of S.E. in each spinal tissue and in comparison to all other tissues, the S.E. of each ligament group and its percentage compared to the other ligaments, respectively, predicted by the LS and PMS models resulting from 5G frontal impact.	126
Figure 7.18 S.E. distribution in the spinal level C12 predicted by the LS and PMS models during 5G frontal impact.	127
Figure 7.19 S.E. distribution in the spinal level C23 predicted by the LS and PMS models during 5G frontal impact.	128
Figure 7.20 S.E. distribution in the spinal level C34 predicted by the LS and PMS models during 5G frontal impact.	129
Figure 7.21 S.E. distribution in the spinal level C45 predicted by the LS and PMS models during 5G frontal impact.	130
Figure 7.22 S.E. distribution in the spinal level C56 predicted by the LS and PMS models during 5G frontal impact.	131
Figure 7.23 S.E. distribution in the spinal level C67 predicted by the LS and PMS models during 5G frontal impact.	132
Figure 7.24 Cervical spinal load sharing based on Strain Energy (S.E.): The magnitude and percentage of contribution of S.E. of each spinal level in comparison to all other levels; the magnitude and percentage of S.E. in each spinal tissue and in comparison to all other tissues, the S.E. of each	

ligament group and its percentage compared to the other ligaments, respectively, predicted by the LS and PMS models resulting from 5G rear-end impact.....	133
Figure 7.25 S.E. distribution in the spinal level C12 predicted by the LS and PMS models during 5G rear-end impact.	134
Figure 7.26 S.E. distribution in the spinal level C23 predicted by the LS and PMS models during 5G rear-end impact.	135
Figure 7.27 S.E. distribution in the spinal level C34 predicted by the LS and PMS models during 5G rear-end impact	136
Figure 7.28 S.E. distribution in the spinal level C45 predicted by the LS and PMS models during 5G rear-end impact.	137
Figure 7.29 S.E. distribution in the spinal level C56 predicted by the LS and PMS models during 5G rear-end impact.	138
Figure 7.30 S.E. distribution in the spinal level C67 predicted by the LS and PMS models during 5G rear-end impact.	139
Figure 7.31 Peak muscle energy vs. peak acceleration during frontal impact scenarios. The current model results for Trapezius (TZ), Sternocleidomastoid (SCM), Splenius (SC), and Semispinalis (SSC) were compared with the results reported by Hedenstierna et al. (2009).....	140
Figure 8.1 (a,b) Posterior displacement of the head relative to the T1 and rotation of the head around the x-axis relative to the extension of T1 predicted by the FMS and PMS models are validated against volunteer corridors, and compared to results reported by a numerical study.....	148
Figure 8.2 Peak pressure in the IVDs at different cervical spinal levels.	149
Figure 8.3 Maximum Strain (%) in the ligament groups at different cervical spinal levels.	149
Figure 8.4 Maximum Stress (MPa) in the ligament groups at different cervical spinal levels.....	150
Figure 8.5 Peak force in the cervical muscles predicted by the FMS model and the results reported by Hedenstierna and colleagues during 1G frontal and rear-end impact loading scenarios (Hedenstierna et al., 2009).	151
Figure 8.6 Peak stress and strain in the ALL ligaments at different cervical levels predicted by the PMS and FMS models during 2G frontal and rear impacts.....	153
Figure 8.7 Peak stress and strain in the CL ligaments at different cervical levels predicted by the PMS and FMS models during 2G frontal and rear impacts. The thick blue horizontal line indicates the failure stress level obtained from in vitro experimental tests (Mattucci et al., 2012).	153
Figure 8.8 Peak stress and strain in the ISL ligaments at different cervical levels predicted by the PMS and FMS models during 2G frontal and rear impacts. The thick blue horizontal line indicates the failure stress level obtained from in vitro experimental tests (Mattucci et al., 2012).	154

Figure 8.9 Peak stress and strain in the LF ligaments at different cervical levels predicted by the PMS and FMS models during 2G frontal and rear impacts. The thick blue horizontal line indicates the failure stress level obtained from in vitro experimental tests (Mattucci et al., 2012).	154
Figure 8.10 Peak stress and strain in the PLL ligaments at different cervical levels predicted by the PMS and FMS models during 2G frontal and rear impacts.....	154
Figure 8.11 Peak stress and strain in the SSL ligaments at different cervical levels predicted by the PMS and FMS models during 2G frontal and rear impacts.....	155
Figure 8.12 Peak stress and strain in the ITL ligaments at different cervical levels predicted by the PMS and FMS models during 2G frontal and rear impacts.....	155
Figure 8.13 Peak pressure in the IVDs at different cervical levels predicted by the FMS and PMS models during 2G and 4G frontal and rear impact loading scenarios.....	156
Figure 8.14 A schematic view of the location of the maximum pressure in the IVDs under 4G impact scenarios predicted by the PMS and FMS models.....	156
Figure 8.15 Contact average and maximum pressures and contact force at the FJs at different spinal levels during 4G frontal and rear impact loading scenarios. The results predicted by the PMS and FMS models are compared.	158
Figure 8.16 Cervical spinal load sharing based on Strain Energy (S.E.). Magnitude of S.E. in each spinal level, Magnitude of S.E. in each spinal tissue, magnitude of cervical ligaments S.E., and magnitude of S.E. in discs at different levels, respectively, predicted by the FMS and PMS models during 2G frontal impact.	162
Figure 8.17 S.E. distribution in the spinal level C12 during 2G frontal impact.	163
Figure 8.18 S.E. distribution in the spinal level C23 during 2G frontal impact.	164
Figure 8.19 S.E. distribution in the spinal level C34 during 2G frontal impact.	165
Figure 8.20 S.E. distribution in the spinal level C45 during 2G frontal impact.	166
Figure 8.21 S.E. distribution in the spinal level C56 during 2G frontal impact.	167
Figure 8.22 S.E. distribution in the spinal level C67 during 2G frontal impact.	168
Figure 8.23 Cervical spinal load sharing based on Strain Energy (S.E.). Magnitude of S.E. in each spinal level, Magnitude of S.E. in each spinal tissue, magnitude of cervical ligaments S.E., and magnitude of S.E. in discs at different levels, respectively, predicted by the FMS and PMS models during 2G rear impact.....	169
Figure 8.24 S.E. distribution in the spinal level C12 during 2G rear impact.	170
Figure 8.25 S.E. distribution in the spinal level C23 during 2G rear impact.	171
Figure 8.26 S.E. distribution in the spinal level C34 during 2G rear impact.	172
Figure 8.27 S.E. distribution in the spinal level C45 during 2G rear impact.	173

Figure 8.28 S.E. distribution in the spinal level C56 during 2G rear impact.	174
Figure 8.29 S.E. distribution in the spinal level C67 during 2G rear impact.	175
Figure A.1 Stress distribution vs. time in the ALL elements at different cervical spinal levels in 15G frontal (left) and rear-end (right) impacts. The thick horizontal line indicates the catastrophic stress failure level (Mattucci et al., 2012).	196
Figure A.2 Stress distribution vs. time in the CL elements at different cervical spinal levels in 15G frontal (left) and rear-end (right) impacts. The thick horizontal line indicates the catastrophic stress failure level (Mattucci et al., 2012).	197
Figure A.3 Stress distribution vs. time in the ISL elements at different cervical spinal levels in 15G frontal (left) and rear-end (right) impacts. The thick horizontal line indicates the catastrophic stress failure level (Mattucci et al., 2012).	198
Figure A.4 Stress distribution vs. time in the LF elements at different cervical spinal levels in 15G frontal (left) and rear-end (right) impacts. The thick horizontal line indicates the catastrophic stress failure level (Mattucci et al., 2012).	199
Figure A.5 Stress distribution vs. time in the PLL elements at different cervical spinal levels in 15G frontal (left) and rear-end (right) impacts. The thick horizontal line indicates the catastrophic stress failure level (Mattucci et al., 2012).	200
Figure A.6 A schematic view of strain distribution in the ITL ligaments in 15G frontal and rear-end impact captured at the time=0.1s (Left side). Strain (%) vs. time in ALLs at different cervical levels in 15G frontal and rear-end impacts (Right side).	201
Figure A.7 A schematic view of strain distribution in the PLL ligaments in 15G frontal and rear-end impact captured at the time=0.1s (Left side). Strain (%) vs. time in ALLs at different cervical levels in 15G frontal and rear-end impacts (Right side).	202
Figure A.8 A schematic view of strain distribution in SSLs in 15G frontal and rear-end impact captured at the time=0.1s (Left side). Strain (%) vs. time in the SSL ligaments at different cervical levels in 15G frontal and rear-end impacts (Right side).	203
Figure C 3.1 Schematic view of a deformed muscle, fibers direction within the tissue, and an infinitesimal segment of the fiber ds . The orientation of the fibers within a continuum finite element is also depicted. σ_m represents the Cauchy stress in the fiber direction.	221
Figure C 3.2 Configuration of a continuum body in a Cartesian coordinate system and its motion.	226
Figure C 4.1 Activation function vs. time for the tentacle muscle.	241
Figure C 4.2 Length function vs. strain for the tentacle muscle.	243
Figure C 4.3 Velocity function vs. strain rate for the tentacle muscle.	244
Figure C 4.4 Normalized Passive Stress function vs. strain for the tentacle muscle.	244

Figure C 4.5 Stress distribution (z-component) in a cube element subjected to activation signal to verify the UMAT behavior..... 246

Figure C 4.6 Stress distribution in the muscle as function of strain in the fiber direction (z-axis). 246

Figure C 4.7 (a) Diagram of a squid. (b) Diagram of the morphology of the tentacular stalk in squid with its muscle groups (Van Leeuwen and Kier, 1997). 246

Figure C 4.8 Top figure shows the FE model of a squid fish tentacle. Bottom figures compare the prediction of the current model with the results reported by Liang et al., (2006). 246

CHAPTER ONE: INTRODUCTION

Head and neck injuries due to impact loading scenarios caused by car collision, falling, and sport activities are very common. The cervical spine is the major location for serious injuries occur during Motor Vehicle Crashes (MVCs) with high risk of fatality or paraplegia. A statistical study showed that around 40–65% of all spine-related injuries are associated with MVCs, where cervical spine is being the most frequently affected injury site accounting for 50.7% of all spine injuries (Yoganandan *et al.*, 1989; Robertson *et al.*, 2002). The cervical spine injuries occurrence in frontal, rear and lateral impact conditions can eventually leave a victim with long-term disabilities. These injuries can be costly to the person and society (Priebe *et al.*, 2007). It is estimated that there are 200,000 people living with spinal cord injury in the United States (Sekhon and Fehlings, 2001), with total annual medical costs estimated between \$3 and \$6 billion (Bernhard *et al.*, 2005; French *et al.*, 2007).

Depending on the severity of the injury, different tissues of the head and neck can be involved. Although the specific mechanisms of injury are still under investigation, several theories link the facet joints, spinal ligaments, inter-vertebral discs (IVDs), vertebral arteries, dorsal root ganglia, and neck muscles to possible sites of injury under high-velocity impact conditions (Siegmond *et al.*, 2009). The cervical musculature is one potential site of less serious injuries such as whiplash associated disorders (WAD) and also a potential site for acute muscle strain that can eventually cause neck pain (Brault *et al.*, 2000). Consequently, understanding the anatomical functioning and mechanical behavior of the neck musculature is a big step toward deeper understanding of the injuries.

1.1 Motivation

The mechanical behavior of the individual cervical spinal tissues as well as the whole head- neck complex kinematics plays a very important role in proper functioning of the cervical spine and is a key factor in more appropriate understanding of injury prevention, detection, control and treatment. Although great efforts have been made to understand the biomechanics of the cervical spine tissues, many aspects are still challenging and not completely clear. A thorough and comprehensive understanding of the neck biomechanics is still needed to aid clinicians, engineers and other involved researchers to develop better detective, preventive and treatment techniques for WAD and other related cervical disorders.

The cervical musculature is the major stabilizer of the neck and head (Brolin *et al.*, 2008). Unlike other tissues consisting of passive structure such as discs and ligaments, the skeletal muscle is composed of active and passive components. Muscle activation has been reported as an essential factor in the head and neck mechanical functioning (Dibb *et al.*, 2013). In response to an external stimulus, activation signal is sent down from the Central Nervous System (CNS) to the muscle within a very short time called delay time. Activated muscle can stabilize the head movement specially under impact loading conditions when the delay time is not too long (Chancey *et al.*, 2003; Ejima *et al.*, 2005; Brolin *et al.*, 2008). The Finite Element (FE) method is a very effective tool that helps understanding the mechanics of the spine. Compared to experimental studies, advantages of the FE modeling include but not limited to the easy control of boundary conditions and loading scenarios, convenient parametric studies and sensitivity analyses as well as efficiency in time and cost. Certain important mechanical parameters such as stress and strain distribution in individual muscles as well as interaction and contact between

them can be investigated by modeling, while they are very challenging or even impossible to measure experimentally.

Human volunteers, mechanical dummies and Post Mortem Human Subjects (PMHS) have been used in impact experimental studies. However, each one of these methods has limitations. For instance, high velocity impacts cannot be applied to human volunteers due to the high risk of injury that it could cause. Furthermore, dummies are not biofidelic, thus do not mimic the human body accurately. Although PMHS can be subjected to the high velocity impact loading scenarios, the muscle activation is missing; therefore, the results are not accurately reliable.

In order to overcome those limitations, numerical approaches such as the FE models have been widely used in biomechanical studies. The majority of today's FE models of the cervical spine includes discrete spring elements to simulate muscles (Deng and Goldsmith, 1987; van der Horst *et al.*, 1997; de Jager, 1996; Wittek, 2000; Chancey *et al.*, 2003; Brodin *et al.*, 2006). These 1 and 2D spring elements fail to represent mass inertia, friction and interaction between individual muscles and other cervical components, and last but not least the real geometry of muscles. Hence, computational 3D FE models have been proposed to overcome these limitations (Hedenstierna *et al.*, 2008). However, in most of those studies, 1D springs were used to simulate the active part of muscle and either 1, 2 or 3D elements represented the passive part. This approach has also limitations. For instance, it causes numerical instability during wide ranges of motions when too many solid and discrete spring elements in series are following the spine curvature (Hedenstierna *et al.*, 2009).

Therefore, creation of a continuum model that combines both the active and passive components of the muscle in just one solid media is necessary. Such a model is able to consider

changes in the muscle activation level which plays an extremely important role in the cervical spine response to the various loading scenarios (Vasavada *et al.*, 2007; Siegmund *et al.*, 2007; Hedenstierna, 2008; Brault *et al.*, 2000). It also considers changes in the mechanical properties of the passive part of the muscle (Blackburn *et al.*, 2004; McHugh and Hogan, 2004). Moreover, such 3D computational models can be a useful tool considering difficulties associated with *in-vivo* and *in-vitro* impact tests on human subjects. And consequently such thorough and detailed computational FE models are capable of predicting more accurate response of the cervical spine to all dynamic loading scenarios in general and impact loading scenario in particular, and is a step toward developing more realistic representations of the head-neck complex.

In this dissertation, 3D continuum cervical muscles constructed from Magnetic Resonance Images (MRI) are added to a validated and detailed three-dimensional FE model of a ligamentous spine. This is the first FE model of the cervical spine that has 3D cervical musculature including both active and passive properties of the muscle governed by one constitutive equation simultaneously. The response of the cervical spine to various loading conditions is investigated.

1.2 Research Objectives

The main goal of this study is to develop a 3D FE model of the cervical spine including a 3D continuum cervical musculature governed by a new material model. This material simulates both active and passive parts of the muscle. The active and passive behaviors of the muscle are simulated based on some modifications done by the author in a previous work done by Spyrou and Aravas (2011). Next, the muscle stress-strain constitutive behavior is numerically formulated based on previous numerical formulations developed by Liang *et al.* (2006) and

Spyrou and Aravas (2011). A user defined FORTRAN subroutine, UMAT, is written to implement the material model into the FE software ABAQUS (Simulia Inc.). This new thorough cervical spine model is used to investigate the overall kinematics of the head and neck as well as the mechanical responses of the cervical individual tissues i.e. muscles, ligaments, discs, and bony structures to various loading conditions. In addition, the responses of the Ligamentous Spine (LS) and a spine with only Passive Musculature (PMS) are compared to the response of a spine with both active and passive musculature (FMS) to investigate the effect of the 3D cervical musculature in the modeling of cervical spine at first, and more importantly, to investigate the importance of the muscle activation on the overall behavior of the cervical spine and its individual tissues.

In summary, the objectives of this research are to:

- **Develop a continuous material model to simulate both passive and active components of the skeletal muscle, model validation**

To achieve this purpose, it is assumed that the amount of force produced by each muscle is sum of its active and passive forces. The numerical formulation is derived from physiological microstructural features of muscle fibers and connective tissues, as well as the existing experimental data and numerical approaches. A user defined FORTRAN code is developed and implemented into the FE software ABAQUS via UMAT subroutine. The original model was developed by other research groups (Van Leeuwen and Kier, (1997); Liang et al., (2006); Spyrou and Aravas (2011). In this dissertation, further improvements are made in the basic assumptions about the

stress and strain distributions in the different parts of the muscle, as well as corrections that are made in their numerical approach. The subroutine convergence is verified first and then, for more general validation purpose, applied to a model of a squid fish tentacle. The squid tentacle and the human skeletal muscle are assumed to show similar behaviour during contraction (See Chapters Three and Four for the developed material in this dissertation and validation procedure. Also, the developed UMAT in this work, the previous one developed by Spyrou (2009) and the original versions of Chapters Three and Four are presented in Appendices B-D).

- **Improve an existing nonlinear FE model of a ligamentous cervical spine, model verification**

Computerized Topography Scan (CTS) and Magnetic Resonance Images (MRI) of a 39-year old male subject are used to construct the 3D geometry of ligamentous spine (Agah, 2016). The intervertebral disc's collagen fibers are reconstructed. The facet joints are defined by assigning appropriate contact properties to the gap between the adjacent facets. Material properties of the cervical tissues are updated based on the existing literature. Functional Spinal Unit (FSU) is created for each cervical level and all 2D membrane ligaments are validated under medium and high rate velocity. The ligamentous spine kinematical behavior is verified by comparing the head and neck Range of Motion (ROM) to existing experimental data and numerical studies results obtained from frontal and rear-end impact loading tests.

- **Construct 3D cervical musculature and add it to the validated ligamentous spine**

MRI of the same subject is used to construct 3D cervical muscles. The Mimics software is used for individual muscles segmentation. Then they are imported to the Geomagic software to clean their constructed geometry from spikes and holes. Next, to generate the mesh, they are imported to the Hyperworks software. Finally, 3D meshed muscles are imported to the ABAQUS software and added to the ligamentous spine for FE simulations. Simulations are performed using Compute Canada facility (WestGrid, Jasper platform).

- **Investigate the effect of passive musculature on the response of the cervical spine to various dynamic and impact loading scenarios by comparing the results predicted by the LS model with the PMS model.**

The cervical spine overall kinematic response to various loading conditions is investigated. The mechanical response of each tissue such as stress and strain distribution in intervertebral discs (IVDs), vertebrae, 2D ligaments, and contact force and pressure in Facet Joints (FJs) in a validated ligamentous spine model is compared with the outcomes of the model that includes passive cervical musculature. The loading scenarios are selected in accordance with the relevant numerical and experimental studies mostly to simulate frontal and rear-end car crash impact scenarios. In addition, the mechanical behaviors of the individual cervical muscles i.e. the amount of force that each one can produce, as well as stress and strain distribution within them are investigated.

The achieved results are either fully or partially validated and verified using existing numerical and experimental data in the relevant literature.

- **Study the effect of muscle activation on the overall behaviour of the cervical spine as well as its individual tissues.**

The developed UMAT is assigned to the constructed cervical muscles and various dynamic loads are applied to our main and final model that contains both active and passive properties of the muscle (FMS). The results predicted by the FMS model are compared to those of the LS and PMS models to investigate the effect of muscle activation on the overall behavior of the spine and its individual tissues.

The novel contributions of this study are listed as:

- 3D continuum modeling of the skeletal muscle that combines both active and passive behaviours;
- Using only one type of element to simulate the spinal muscles;
- Construction of 3D geometry of cervical muscles from MR images;
- Creation of a FE model of the head and the neck including passive and active structures;
- Study the effects of the musculature on the response of the cervical spine to different mechanical loading scenarios.

1.3 Dissertation Outline

This dissertation comprises nine chapters, including this introduction:

Chapter Two

This chapter begins with background on the human cervical spine anatomy. The material and mechanical characteristics of cervical spine tissues i.e. cortical and cancellous bones, ligaments, discs, articular cartilage and tendon in general, and muscle in particular, are outlined in this chapter. The constitutive equations and models for the cervical tissues used in the FE model of the ligamentous spine are described too. The previous studies on the constitutive modeling of the skeletal muscle tissue are then reviewed. Next, the evolution of muscle models from the Hill-type model to the constitutive models is presented. Computational models of the cervical spine that include the musculature are reviewed thereafter.

Chapter Three

The numerical formulation for the continuum model of the skeletal muscle is presented in this chapter. Constitutive equations that relate stress to strain in different directions are written. Consequently, tensors of stress, strain, and Jacobian are derived and updated at each time increment. Additionally, linearization of equations used in the calculation of Jacobian matrix is explained. These constitutive equations are then implemented into the FE solver.

Chapter Four

The implementation of the numerical constitutive formulation for the muscle tissue is described in this chapter. A brief introduction about the UMAT environment and the coding procedure is presented. Next, a setup used for validation of the UMAT based on experimental and numerical procedures is explained.

Chapter Five

Geometry construction of an existing ligamentous cervical spine and its components is presented in this chapter. Mesh generation procedure is explained step-by-step from Mimics to ABAQUS. The 3D musculature of the same subject is constructed and added to the ligamentous spine. Type and number of elements in each spinal tissue are also described. And finally, the material laws governing the cervical spinal tissues are presented here.

Chapter Six

Validation of the ligamentous spine response to the frontal and rear-end impact loading scenarios against existing experimental data and numerical studies are presented in this study. The dynamic implicit code is used to run all models. In addition to the verification of the overall cervical kinematical behavior, the failure stress level in each ligament at different spinal levels is calculated and compared with the experimental data. Moreover, the Strain Energy (S.E.) is used to develop the concept of load-sharing during dynamic loading conditions.

Chapter Seven

To investigate the influence of the passive musculature on the response of the whole cervical spine and its individual tissues, the constructed 3D muscles governed by a hyperelastic passive material model are added to the validated ligamentous spine and similar analyses are performed.

Chapter Eight

The validated UMAT is applied to the 3D muscles in the final model. The FMS predictions are compared with the predictions of the PMS and LS models to investigate the importance of the

muscle activation on the overall behavior of the cervical spine and its individual components. The amount of force in each muscle is also presented.

Chapter Nine

The summary and conclusions of this work are presented in this chapter. Challenges in validation are explained and consequently, some suggestions for further verification of the computational model are derived. Eventually, main limitations and assumptions as well as future works are addressed.

CHAPTER TWO: BACKGROUND AND LITERATURE REVIEW

2.1 Mechanical Structure of the Cervical Spine

The cervical spine is the most mobile part of the spine that bears the weight of the head. It consists of seven bony structures called vertebrae and 6 intervertebral discs (IVD) stacked on each other. The cervical spine is divided into Upper Cervical Spine (UCS) and Lower Cervical Spine (LCS). The UCS includes the vertebrae C1 (Atlas) and C2 (Axis), and the occipital bone of the skull called C0. The LCS includes the vertebrae C3 to C7 (Fig. 2.1). There is no IVD between Atlas and Axis. The Atlas and Axis together form a ring structure providing a wide range of motion to the skull. From the functioning point of view, previous studies showed that around 50% of total rotation occurs in the UCS, while flexion and extension mostly occur in the LCS (White and Panjabi 1990).

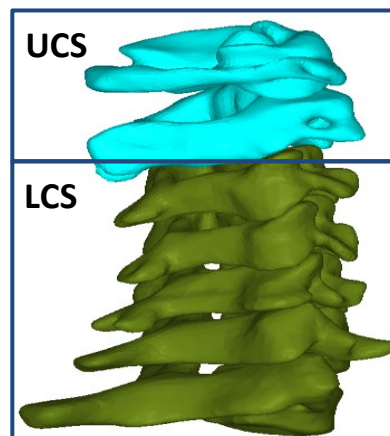


Figure 2.1 The Upper Cervical Spine (UCS) and the Lower Cervical Spine (LCS) geometry.

2.2 Review of Anatomy, Function, and Modelling of Ligamentous Cervical Spine Components

2.2.1 Vertebrae

Each vertebra is composed of two types of bony components: Cortical and cancellous bones. The cancellous bone has a spongy structure and forms a large volume of each vertebra. It is surrounded by a thin layer of a denser bone called the cortical bone (Fig. 2.2). Some studies assumed all bony components behave elastically (Naserkhaki *et al.*, 2016; Park *et al.*, 2013; Schmidt *et al.*, 2007), while others used an isotropic rate-dependent elasto-plastic Johnson-Cook formulation, allowing for computing von Mises hardening with ductile damage until potential rupture (El-Rich *et al.*, 2009; Wagnac *et al.*, 2012; Garo *et al.*, 2011). In the majority of the FE models, solid and shell elements were used to simulate the cancellous and cortical bones, respectively (Naserkhaki *et al.*, 2016; Mustafy *et al.*, 2016; El-Rich *et al.*, 2009).

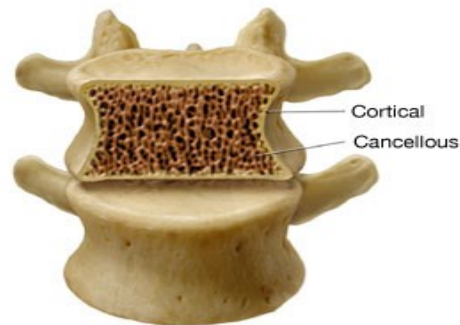


Figure 2.2 Cortical and cancellous bones (<http://drmchiro.blogspot.ca/2013/02/the-shock-absorbers-of-spine.html>).

2.2.2 Ligaments

Ligaments are soft tissues consisting collagen fibers aligned in a surrounding matrix. The UCS has a series of complex ligaments such as: Anterior Atlanto-Axial Membrane (AAAM), Anterior Atlanto-Occipital Membrane (AAOM), Alar, Ligamentum Nuchae (Nuchal), Posterior Atlanto-

Axial Membrane (PAAM), Posterior Atlanto-Occipital Membrane (PAOM), and Apical ligament (Fig. 2.3a). The major LCS ligaments are: Anterior Longitudinal Ligament (ALL), Posterior Longitudinal Ligament (PLL), Flavum Ligament (FL), Capsular Ligament (CL), Intertransverse Ligament (ITL), Supraspinous Ligament (SSL) and Interspinous Ligament (ISL) (Fig. 2.3b). These uniaxial structures resist only tensile forces. Therefore, they are most effective when distracted along their fibers direction (White *et al.*, 1990; Myklebust *et al.*, 1988).

Depending on the location of each ligament, and its distance to the center of rotation of the adjacent vertebra, as well as the direction of the applied load, the response of the ligaments varies. For example, the ALL is more effective during extension, while the ISL is more effective during flexion (Myklebust *et al.*, 1988).

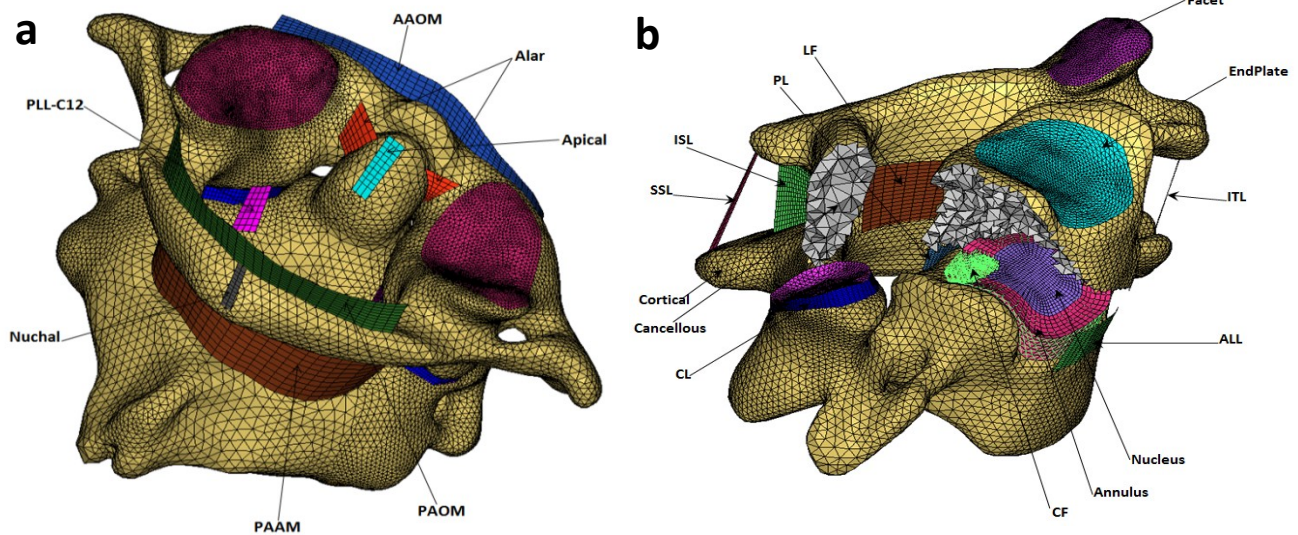


Figure 2.3 Finite element representation of the cervical spine components: (a) The UCS ligaments including the AAOM, Alar, Apical, Nuchal, and C12 part of PLL, PAAM, and PAOM. (b) The LCS ligaments including the ALL, CL, ISL, ITL, PLL, LF, and SSL; the IVD component (Annulus, Nucleus, and CF); the cortical and cancellous bones, the endplates, and the facets.

The geometrical characteristics of the cervical ligaments such as the origin and insertion, length, and cross-sectional area, as well as material properties identify the role of each ligament in the structural behavior of the spine. Table 2.1 provides length and cross sectional area of major cervical ligaments (Panjabi *et al.*, 1991). The material properties are obtained by applying tensile load to an isolated Functional Spinal Unit (FSU) including bone-ligament-bone structure. The FSU was segmented from human cadaver cervical spine *in situ* (Yoganandan *et al.*, 1989; Yoganandan *et al.*, 2000; Chazal *et al.*, 1985). The lower vertebra was fixed while, the upper vertebra was subjected to axial tensile loading and the load-deformation response is derived (Fig. 2.4).

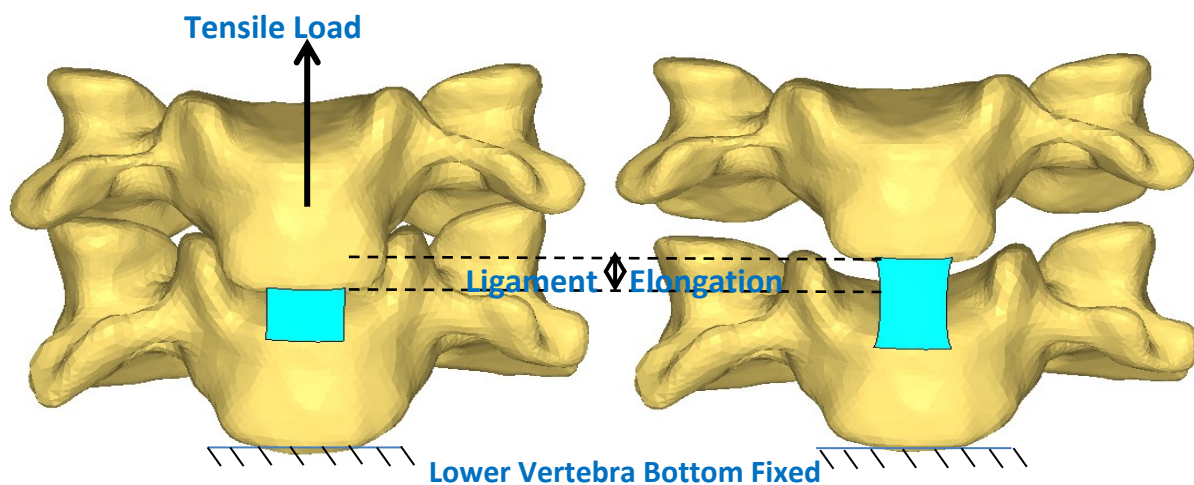


Figure 2.4 FSU structure used to derive force-displacement in the cervical ligaments (ALL in this case). Lower vertebra is fixed and tensile load is applied to the upper vertebra.

The human body reacts and resists external loads in a dynamic environment (e.g., MVCs, athletic activities) (Maiman *et al.*, 1983). Relevant studies reported the rate-dependent or viscoelastic behavior of the ligaments, particularly, their failure (tear) has been observed during high rates of loading (Yoganandan *et al.*, 1989). However, once a stretch level is attained, regardless of the loading rate, failure is imminent (Yoganandan *et al.*, 2001).

The FE modelling has been used to define the characteristic properties of the cervical ligaments (Kumaresan, 1997; Maurel *et al.*, 1997; Clausen *et al.*, 1997). Various assumptions and simplifications have been considered to simulate them. Linear and non-linear tension only spring elements (Nightingale *et al.*, 1997; Brodin and Halldin, 2004; Hedenstierna, 2008), cable elements (Maurel *et al.* 1997; Kumaresan *et al.*, 1997-2000), truss elements (Kumaresan *et al.*, 2000), as well as 2D membrane elements (Yang *et al.*, 1998; Mustafy *et al.*, 2014-2016) have been used. In recent FE models, the ligaments have been governed by visco-elastic (time- and rate- dependent Prony Series) material laws (Yoganandan *et al.*, 1996; Kumaresan *et al.*, 1999; Wagnac, 2011; Mustafy *et al.*, 2014-2016).

Table 2.1 Cross Sectional Area and Length of Cervical Ligaments (Mean (SD) (Yoganandan *et al.*, 2000).

Ligament	Area (mm^2)	Length (mm)
	C2-C5	
ALL	11.1 (1.9)	18.8 (1.0)
PLL	11.3 (2.0)	19.0 (1.0)
LF	46.0 (5.8)	8.5 (0.9)
ISL	13.0 (3.3)	10.4 (0.8)
	C5-T1	
ALL	12.1 (2.7)	18.3 (0.5)
PLL	14.7 (6.8)	17.9 (0.5)
LF	48.9 (7.9)	10.6 (0.6)
ISL	13.4 (1.0)	9.9 (0.7)

2.2.3 Intervertebral Disc (IVD)

The IVD comprises of annulus fibrosis, nucleus pulposus and two cartilaginous end plates. The annulus is reinforced with several layers of collagen fibers (CF) (Fig. 2.3). Unlike ligaments that only resist uniaxial tension, the IVD responds to multi-direction loads (White and Panjabi, 1990) but its main role is to resist compression. With the exception of tension, under any external load i.e. lateral bending, flexion and extension, the IVD carries compressive forces in association with other spinal components (Wolfa 1998).

Several FE models have simulated the nucleus using incompressible fluid cavity and the annulus using solid media (Mustafy *et al.*, 2014; Park *et al.*, 2013). Others have assigned elastic or hyper-elastic material properties to the solid elements that represent annulus (El-Rich *et al.*, 2009; Schmidt *et al.*, 2007; Chen *et al.*, 2001; Naserkhaki 2016).

2.2.4 Facet Joint (FJ)

A Thin layer of articular cartilage covers the facet surface of the articular process of each vertebra. Two adjacent articular facets are connected by the CL ligament to form a confined space called FJ filled by synovial fluid. From the FE modeling point of view, the facet surfaces are usually modeled by either solid or membrane (shell) elements (El-Rich *et al.*, 2009; Mustafy *et al.*, 2014, 2016; Naserkhaki *et al.*, 2016). Contact in the FJ is usually simulated by using frictionless surface-to-surface contact with a predefined gap between the two facets (Dreischarf *et al.* 2014).

Like the IVD, the FJ responds to multi-direction loads. Together with the IVDs, the FJs resist compressive forces in the cervical spine. The share of the compressive load resisted by the FJs

and the IVD in each vertebral level depends on the orientation of each joint as well as the direction of the applied external load (Kumaresan *et al.*, 1998). The FJs provide a complementary role to the IVDs (Milne 1991) and also limit the torsion of the IVDs (Yoganandan *et al.*, 2001).

2.3 Review of Anatomy, Function, and Modelling Approaches of the Cervical Spine Musculature

2.3.1 Skeletal Muscle Anatomy

There are three major types of muscles in the human body: cardiac, smooth and skeletal muscles. About 40% of body weight is composed of the skeletal muscles (Guyton and Hall, 2006). The main functions of the skeletal muscles are moving and providing stability for the body under its own weight and any external perturbation. The skeletal muscle connects two (sometimes more) bones together.

Fig. 2.5 shows the hierarchical structure of a typical skeletal muscle. The skeletal muscle is a live composite material including several parallel bundles of fibers surrounded by a matrix that is called connective tissue. The connective tissue includes three types of fatty materials: Epimysium, Endomysium, and Perimysium. Each muscle fiber consists of a series of sarcomeres. Each sarcomere includes two main components: actin and myosin filaments. The actin and myosin are large polymerized protein molecules that are responsible for the actual muscle contraction (Guyton and Hall, 2006). As a result of an electrochemical process, a force is generated in the cross-bridges between actin and myosin causing the sliding of the actins along the myosin. The generated force is called active force and consequently, the sliding procedure causes the muscle contraction. The theory behind muscle contraction is known as Sliding

Filament Theory or Cross-Bridge Theory (Huxley 1957). When the muscle fiber is fully contracted, the actin filament completely overlaps the myosin filament and vice versa. There are two types of muscle contraction: isometric and isotonic contractions. If the muscle length does not change during the contraction, the contraction is called isometric contraction. In contrast, if the length of the muscle changes during the contraction, this later is called isotonic contraction. In the last case, the muscle length either decreases (concentric contraction) or increases (eccentric contraction) as shown in Fig. 2.6. When a fully contracted muscle is bearing a load that is less than its maximum capacity, its length decreases and the contraction is called the concentric contraction. By increasing the external load, the muscle reaches to a point where the applied load is greater than its internal load generation capacity, so at this point, the muscle length starts increasing. This type of contraction is known as eccentric contraction.

The active force generated in the muscle during the contraction depends on several material and geometrical characteristics of the muscle such as the activation level and pattern, the variation of the muscle length, the velocity of the contraction, the Physiological Cross Sectional Area (PCSA), the orientation of the fibers inside the muscle (Pennation angle), and the fiber types. Besides the active force, and in the absence of electrical stimulation, each muscle produces passive force. The passive force is produced by both fibers and the connective tissues.

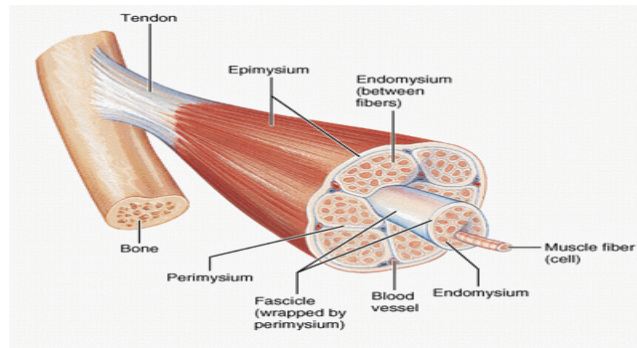


Figure 2.5 A typical view of skeletal muscle hierarchical structure: several types of protein-based tissues i.e. Epimysium, Endomysium, and Perimysium are located around fiber bundles. A tendon attaches a muscle to the nearby bone.

(http://www.medicallook.com/human_anatomy/organs/Skeletal_muscle_fiber.html).

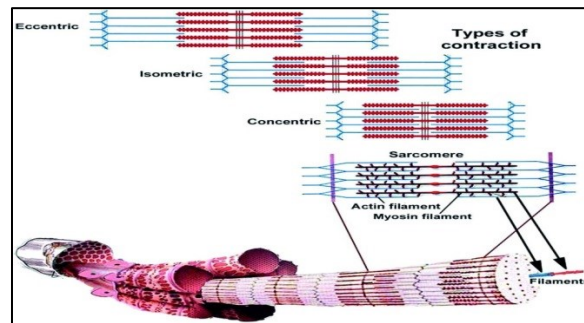


Figure 2.6 Skeletal muscle microstructure, and contractions types: concentric, isometric, and eccentric.

2.3.1.1 Muscle Architecture

- *Pennation Angle*

The physical function and the amount of force that a muscle can produce are directly affected by the arrangement of fibers inside the muscle. The major types of muscle architecture are: parallel and pennate. When all the fibers are parallel to the force-generating axis (muscle's line of action), the muscle has a parallel architecture. Therefore, all fibers generate force in only one

direction. On the other hand, when the fibers form an angle (0 to 30 degree) with the line of action, the muscle has pennate architecture. If all the muscle fibers are oriented at one angle to the line of action, the muscle is called uni-pennate or fusiform muscle. However, if the fibers are oriented in two or more directions with respect to the line of action, the muscle is called bi-pennate or multi-pennate muscle, respectively (Lieber and Fridé, 2000). Fig 2.7 shows different types of the muscle architecture.

- PCSA

The PCSA (Physiological Cross Sectional Area) is another important architectural characteristic parameter of the skeletal muscle. It is the area of the cross section taken perpendicular to the fibers direction and is calculated by dividing the volume of the muscle by the length of the fibers (Eq. 2.1).

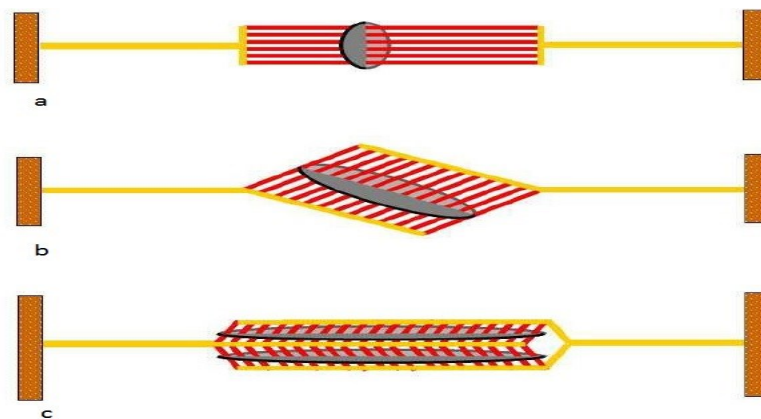


Figure 2.7 Different types of muscle architecture: a) parallel, b) uni-pennate, c) bi-pennate. PCSA is perpendicular to the fibers' direction (Spyrou 2009).

$$PCSA = \frac{\text{muscle volume}}{\text{fiber length}} \quad (2.1)$$

The PCSA in the pennate muscles is greater than that in the parallel muscles as shown in Fig. 2.7. The maximum amount of the force that a muscle can produce, F_{max} , is linearly related to its PCSA:

$$F_{max} = PCSA \times \sigma_{max} \quad (2.2)$$

where the peak isometric muscle strength, σ_{max} , is obtained experimentally. Previous studies reported a wide range of data for σ_{max} , but most of the numerical works used the average value of 500 kPa (Winters and Stark, 1988; Davis *et al.*, 2003).

- *Optimal and relative muscle lengths*

The maximum active force that a muscle can generate happens at its optimal length (l_{opt}) which is usually longer than the muscle current length, l . (Best 1993; van der Horst, 2002; Langenderfer *et al.*, 2004). The relative length (l_{rel}) is another important length of the muscle and is calculated using the following relation:

$$l_{rel} = \frac{l}{l_{opt}} \quad (2.3)$$

2.3.1.2 Force-Activation Relation

It takes some time for the Central Nervous System (CNS) to send the activation signal down to the muscle. This time is known as delay time that varies depending on several parameters, for instance, the distance of the muscle from the CNS. Immediately after that, the muscle starts producing the active force until it is fully activated (fully activation time). After the muscle is fully activated, the amount of active force remains constant.

2.3.1.3 Force-Length Relation

In 1960's, Gordon and his colleague conducted experiments on frog's skeletal muscle fibers. The maximum generated force in the fully activated fiber was measured during isometric contraction condition. This experiment was repeated at different fiber lengths. Fig. 2.8 shows the obtained isometric forces at various lengths. When the muscle length becomes greater than its optimal length, the passive force plays more significant role in the overall force-length relationship of a muscle (Guyton and Hall, 2006). Fig. 2.9 shows the active, passive and total forces in the muscle as function of the muscle length.

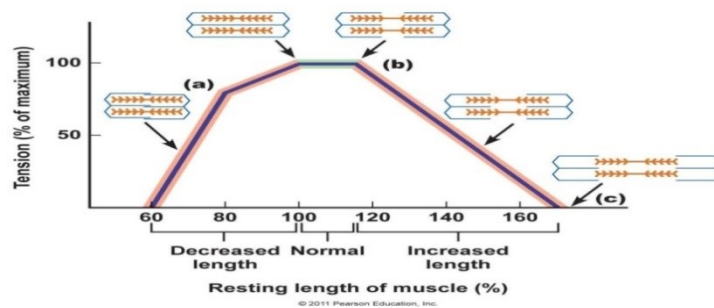


Figure 2.8 Active muscle force vs. length of muscle which is a function of the amount of actin and myosin filaments overlap

(http://droualb.faculty.mjc.edu/Course%20Materials/Physiology%20101/Chapter%20Notes/Fall%202007/chapter_12%20Fall%202007%20Phy%20101.htm).

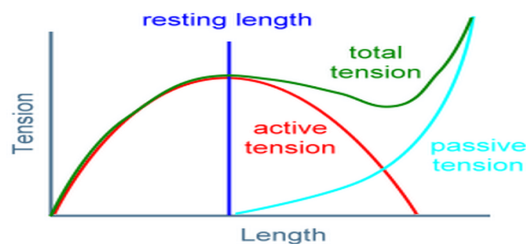


Figure 2.9 Total, active, and passive forces in a skeletal muscle vs. length of the muscle

(<https://www.strongerbyscience.com/how-to-prevent-muscle-strains/>).

2.3.1.4 Force-Velocity Relation

In 1938, Hill and colleagues investigated the relationship between the maximum force that a muscle can generate and the rate of change of its length or the velocity of contraction using an experiment conducted on an isolated muscle. Likewise the force-length curve, the force-velocity curve shows the maximum forces generated at different velocity plotted against the velocities. Fig. 2.10 shows the typical force-velocity relationship for the muscle under both concentric and eccentric contractions. The force-velocity relationship reveals the viscoelastic nature of the muscle behavior.

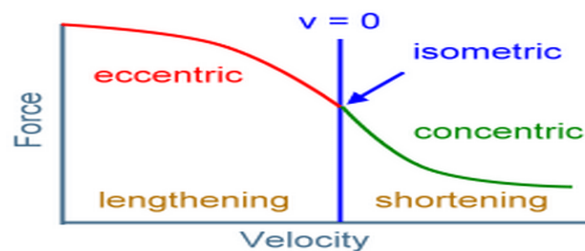


Figure 2.10 Force vs. velocity of contraction curve during isometric, eccentric and concentric contractions (<https://www.strongerbyscience.com/how-to-prevent-muscle-strains/>).

2.3.2 Skeletal Muscle Models

The most fundamental models describing the muscle behavior used in literature are:

- ***Huxley Model***

In 1957, Huxley presented his model which is based on the cross-bridges theory mentioned in Section 2.3.1. In brief, this theory claims that the muscle contraction is a consequence of sliding the thin actin filaments along thick myosin filaments. This hypothesis has been experimentally

proved later (Gordon *et al.*, 1966). The places where the actin and myosin attachment generates force are called bridges.

Although Huxley model is a great tool to measure force and energy generation mechanisms in the muscle, it is unable to take into consideration the overall geometrical characteristics of the muscle, such as, the variation in the shape and the PCSA along the length of the muscle. Huxley approach represents the muscle as a linear elastic material which disagrees with experimental findings. In addition, Huxley model cannot describe the dynamic nature of the musculature behaviors i.e., time-dependent force production phenomenon.

- **Hill Model**

In 1938, Hill proposed a discrete model to describe the mechanical behavior of the muscle. This model which is still utilized in the most numerical models of the skeletal muscle has two main components: one active contractile component and series and parallel elastic elements that simulate the passive properties of the fibers and the connective tissues, respectively (Fig. 2.11). This discrete model has been developed over the years (Hill, 1938; Hill, 1970). Hill model is the first model that added the active part of the muscle to the previous approaches that only simulated the passive components of the muscle. Equation (2.4) known as Hill equation describes the relation between the active force, F_{act} , the velocity of contraction, v , and the maximum isometric force, F_{max} .

$$(F_{act} + a)(v + b) = b(F_{max} + a) \quad (2.4)$$

where a and b are constants.

The total generated force in the muscle is the summation of the active and passive forces:

$$F = F_{act} + F_{pas} \quad (2.5)$$

The active force is assumed to be a function of the muscle activity pattern, f_a , the muscle length, f_l , and the velocity of contraction, f_v , as well as the maximum isometric force:

$$F_{act} = F_{max} \cdot f_a f_l f_v \quad (2.6)$$

where f_a, f_l, f_v , are dimensionless functions that will be described with more details in the next chapters.

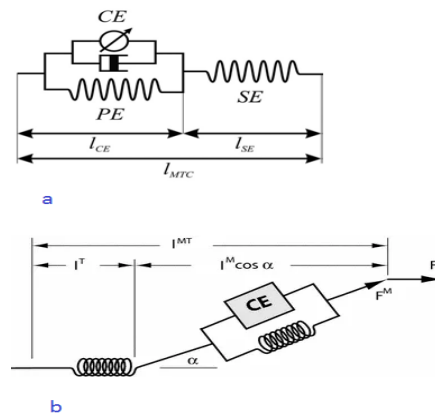


Figure 2.11 Hill model including a contractile element, a parallel and a series element. **(a)** Parallel muscle, **(b)** pennate muscle

(http://gribblelab.org/compneuro/6_Computational_Motor_Control_Muscle_Models.html and <http://youngmok.com/hill-type-muscle-model-with-matlab-code/>).

The main advantages of the Hill model are its simplicity and good agreement with experimental data, as well as its ability to simulate the overall behavior of the musculature in just one dimension. Nevertheless, it has several limitations that are briefly mentioned below:

- As a 1D model the Hill model is unable to simulate the effect of inertia (mass).
- Unable to simulate the changes in the shape of the muscle and the variation of the PCSA along the length of the muscle.
- Unable to model the intra-muscular pressure as well as the friction between individual muscles due to its 1D nature.

- One dimensional springs and dashpots used in the Hill model causes unrealistically high stress concentration in the area of muscles attachment to the surrounding tissues.
- Discrete elements provide neither strain distribution inside the element, nor the shear and compression responses.

- ***Continuum Models***

To overcome Huxley and Hill models' limitations and to provide more realistic method for the simulation of skeletal muscles, recently, several studies have developed 3D continuum constitutive models (Blemker *et al.*, 2005; Cheung *et al.*, 2005; Liang *et al.*, 2006). These models tried to include the tissue inertia as well as the compressive and shear stiffnesses into the muscle models. They are also able to show strain distribution in the 3D elements. Unlike the Hill model, the continuum models simulate both the active and passive parts of a muscle in just one type of element. The early attempts mainly focused on the principle of volume preservation and incompressibility of the biological tissues. In 1984, Spencer used the concept of strain energy to develop a constitutive hyperelastic model for the composite materials that was based on the initial orientation of the fibers in the tissue. It was later used by other researchers (Otten, 1987,1995; Zajac, 1989; Weiss 1996) to model human body soft tissues. Lemos and colleagues (2004) also provided a framework for structural modeling of the skeletal muscle. In their work, muscle fibers were oriented in only one direction within each element. The connective tissue was also missed in their approach. They used the experimental data obtained from the cat medial gastrocnemius to validate their model. The latest approach was based on the coordinate system of each nodes of an element in the muscle FE model. Moreover, the stress-strain constitutive equations were derived based on the concept of virtual work and

strain energy. Therefore, the approach is more convenient for developing a geometrical (element-based) model rather than developing a material model (material-based). Van Leeuwen and Kier (1997) derived dynamic multi-level governing equations to model the extension of a squid tentacle that is similar to the contraction of a human skeletal muscle. Using a thorough parametric optimization approach, the results of the derived equations were in a good agreement with the experimental data reported by Kier and Van Leeuwen (1997). Their approach has been modified later by Johansson *et al.* (2000) and Yekutieli *et al.* (2005). In 2006, Liang and colleagues proposed a model for muscular hydrostats. In their approach, the muscle was considered as a composite material consisting of fibers and surrounding connective tissue. Later on, Spyrou and colleague used Liang's approach to model the muscle and tendon tissue (Spyrou and Aravas 2011). This approach will be described with more detail in next chapters of this dissertation.

2.3.3 Cervical Musculature

The neck muscles support the head and provide stability and movements around the cervical vertebrae. The insertions and origins of these muscles are mostly located around shoulder girdle, cervical vertebrae and skull. They are categorized based on their function, location, and shape (Table 2.2). The major cervical muscles, their origin and insertion, mass and PCSA are summarized in Table 2.3. The Trapezius (TZ), Sternocleidomastoid (SCM), Splenius Capitis and Cervicis and Semispinalis Capitis and Cervicis have the greatest PCSA and mass amongst other neck muscles (around 70% of the neck musculature mass). They also have the longest length and likewise cover the neck area entirely. These groups of muscles are the major flexors and extensors of the neck and head under the impact loading scenarios (Chancey *et al.*, 2003). It has

been revealed that the small deep muscles are responsible for stabilizing the head and neck during normal movements such as keeping the head upright in neutral position and chewing food, and they do not play an important role in wider ranges of motion (Chancey *et al.*, 2003).

Table 2.2 Different types of muscle categories based on function and location.

Type of Muscles (based on function)	Main Location	Example
Extensors	Posterior	Trapezius
Forward Flexors	Anterior	Rectus Capitis Anterior
Lateral Flexors & Rotators	Lateral	Sternocleidomastoid

Table 2.3 Cervical muscles with their origin, insertion, mass (gram), and PCSA (mm^2) (Adopted from Hedenstierna (2008)).

Muscle	Origin	Insertion	Mass	PCSA
Upper Trapezius	Lig. nuch. & spinous proc. of C7	Lat. third of clavicle & scapula	180	13.7
Sternocleidomastoid	Ant. sternum & medial 3rd clavicle	Mastoid proc. & super. nuchal line	39.5	4.9
Semispinalis Cervicis	Trans. Proc. T1-T6	Spin. proc. C2-C5	21.8	8.6
Semispinalis Capitis	Trans. proc. C7 -T6 & articular proc C4-C6	Between occipital superior -inferior nuch. line	36.6	
Splenius Cervicis	Spin. proc. T3-T6	Trans. Proc. C1-C3.	14.6	4.5
Splenius Capitis	Lower Lig. nuch. & Spin proc C7-T2.	Mastoid proc. & occipital bone	17.6	
Longissimus Capitis	Trans. Proc. T1-T5 & art. Proc. C4-C7	Posterior mastoid proc.	32.3	2.5
Longissimus Cervicis	Trans. Proc. T1-T5	Trans. proc. C2-C6	32.5	
Illiocostalis Cervicis	Angle of rib 3-6	Trans. proc. C4-C6		
Levator Scapola	Trans. Proc. C1-C4	Border of scapula	29.2	3.1
Longus Coli	Trans. proc C3-C5	Ant. arch of atlas	6.9	1.4
Longus Capitis	Trans. proc. C3-C6	Basilar part of occipital	4.9	1.7
Scalenus anterior	Ant. Trans. proc. C3-C6	Inner border first rib	7.8	4.3
Scalenus medius	Post. Trans. proc. C2-C7	Upper surf first rib	5	
Scalenus posterior	Post. Trans. proc. C5-C7	Trans. proc. C4-C6	8.5	
Rectus Capitis post. minor	Post. arch of atlas	Med. inf. nuch. line & surface to foramen magna	4	1
Oblique Capitis superior	Front. T1-T3	Trans. proc. C5-C6	2.6	
Oblique Capitis inferior	Front. T1-T3, C5-C7	Front. C2-C4	4.6	
Rectus Capitis post. major	Spinous proc. C2	Lat. Inf. nuch. line & below surface	3.6	1

2.3.3.1 Cervical Musculature Models

There are significant numbers of cervical spine FE models that include the musculature. Majority of these works used discrete elements to simulate the active and passive parts of the muscle, separately. The Hill-type active spring elements have been used in combination with 1D passive spring elements (Wittek, 2000; van der Horst, 2002; Chancey *et al.*, 2003; Brodin *et al.*, 2003; Teo *et al.*, 2007).

Wittek (2000) has used 86 spring elements to model 16 pairs of neck muscles. He used the dynamic explicit feature of PAM-SAFE FE software. Van der Horst (2002) has developed a model consists of 68 Hill-type spring elements to represent 16 pairs of the cervical muscles in MADYMO software. Chancey *et al.*, (2003) have used contractile spring elements to represent the active part of the muscle and nonlinear elastic springs to simulate the passive part. In total, they have modeled 23 groups of the cervical muscles. Brodin *et al.* (2003) have used 337 elements including the Hill type springs in parallel with dampers and passive spring elements to model 14 muscle groups in LS-DYNA.

However, there are few works that have used 2D shell elements (Jost and Nurick 2000) or 3D solid elements (Ejima *et al.*, 2005; Frechede *et al.*, 2005) to represent the passive muscles. In these models, the active part was ignored. In Ejima *et al.* (2005) work, 3D geometry of the cervical muscles was constructed from MRI, and all FE analyses were conducted in the LS-DYNA environment. Nonlinear elastic material properties were assigned to the muscles (Ejima *et al.*, 2005). Frechede *et al.* (2005) used orthotropic linear elastic material properties to model 3D cervical muscles covered by skin using RADIOSS FE software.

In 2008, Hedenstierna and Halldin have proposed a continuum model that includes 3D elements constructed from MRI to model the passive musculature in combination with 1D beam elements to model the active part of the musculature. Hedenstierna et al. (2008) also proposed a new continuum 3D model for the cervical musculature using 3D passive elements and 1D active springs. The springs were attached to the nodes of solid elements and the concept of superposition was used to calculate the resultant force predicted by these two different elements at the attachment points. Linear viscoelastic material properties were assigned to the passive part, while the active spring elements were governed by the Hill material model (Hedenstierna et al., 2008). Using the software LS-DYANA, they modeled 25 groups of muscles.

2.3.4 Tendon

The tendon is a dense connective tissue connecting muscle to bone. The tendon size and shape changes depend on the physiological and mechanical characteristics of the adjacent muscle and bone (Fig. 2.5).

Similar to the ligament, the tendon consists of collagen fibers and its main function is to transfer the force produced by a muscle to the nearby bone. Therefore, it is stronger under tension. The tendons present elastic behavior unless they are overstretched. In that case, they show viscoelastic behavior. However, about 89 to 94% of the energy associated with longitudinal deformation or stretch of a tendon is recovered when the load on the tendon is removed. Therefore, it shows elastic behavior in range of ranges of physiological deformations (Maganaris and Paul, 1999; Spyrou and Aravas, 2011; Maganaris *et al.*, 2017).

CHAPTER THREE: CONTINUUM CONSTITUTIVE MODELLING OF THE SKELETAL MUSCLE

In this chapter, a nonlinear, fiber-reinforced continuum constitutive model is employed to simulate biomechanical behavior of the muscle. The model was first developed by Liang and colleagues (Liang et al., 2006) to simulate muscle hydrostats based on van Leeuwen and Keir experimental and numerical works (Van Leeuwen and Kier, 1997). A muscular hydrostat is a biological tissue found in animals to manipulate things such as food and provide movement. It mainly consists of muscles with no skeletal supports e.g. octopus or human tongue. Later, Spyrou and Aravas (Spyrou and Aravas, 2011; Spyrou, 2009) further developed Liang approach to model the muscle and tendon tissues. In this dissertation, we developed the numerical approach used by Spyrou and other previous researchers, and modified some numerical errors in the above mentioned works. Different assumptions about stress and strain constitutive equations were employed to model the skeletal muscle. First, the constitutive equations are derived in Section 3.1, and then, the numerical formulation and the approach of discretizing the derived equations are presented in Section 3.2. Finally, my contribution is summarized in Section 3.3. The modified material model and the FORTRAN code for it, original Chapters Three and Four (prior to the modifications), and Spyrou's material model are presented in Appendices B-D, respectively.

The notation used in this chapter and the following ones are described briefly (Spyrou and Aravas, 2009). Boldface symbols represent vectors and tensors. The Cartesian coordinate system with base vectors e_i ($i = 1, 2, 3$) is used. The superscript T indicates the transpose, a superposed dot specifies material time derivate, the preface "det" implies the determinant, and

the symbol ∇ is the Jaumann rate index. The following products will be used in this work (assume that \mathbf{a} , \mathbf{b} , \mathbf{c} , and \mathbf{d} are vectors, \mathbf{A} and \mathbf{B} are second-order tensors, and \mathbf{C} and \mathbf{D} are fourth-order tensors):

$$(\mathbf{ab})_{ij} = a_i b_j, (\mathbf{abcd})_{ijkl} = a_i b_j c_k d_l, (\mathbf{a} \cdot \mathbf{A})_i = a_j A_{ji}, (\mathbf{A} \cdot \mathbf{a})_i = A_{ji} a_j, \mathbf{A} : \mathbf{B} = A_{ij} B_{ij}, (\mathbf{A} : \mathbf{C})_{ij} = A_{kl} C_{kl ij}, (\mathbf{C} : \mathbf{A})_{ij} = C_{kl ij} A_{kl}, \text{ and } (\mathbf{C} : \mathbf{D})_{ijkl} = C_{ijpq} D_{pqkl}.$$

3.1 Constitutive Model

3.1.1 Principal Structure of the Constitutive Model

The skeletal muscle is a composite material composed of fibers aligned in a matrix that is called connective tissue. The passive and active forces are generated by the fibers along the fibers' direction. A schematic view of the fiber orientation in the muscle in general, and in a finite element in particular, is shown in Fig. 3.1.

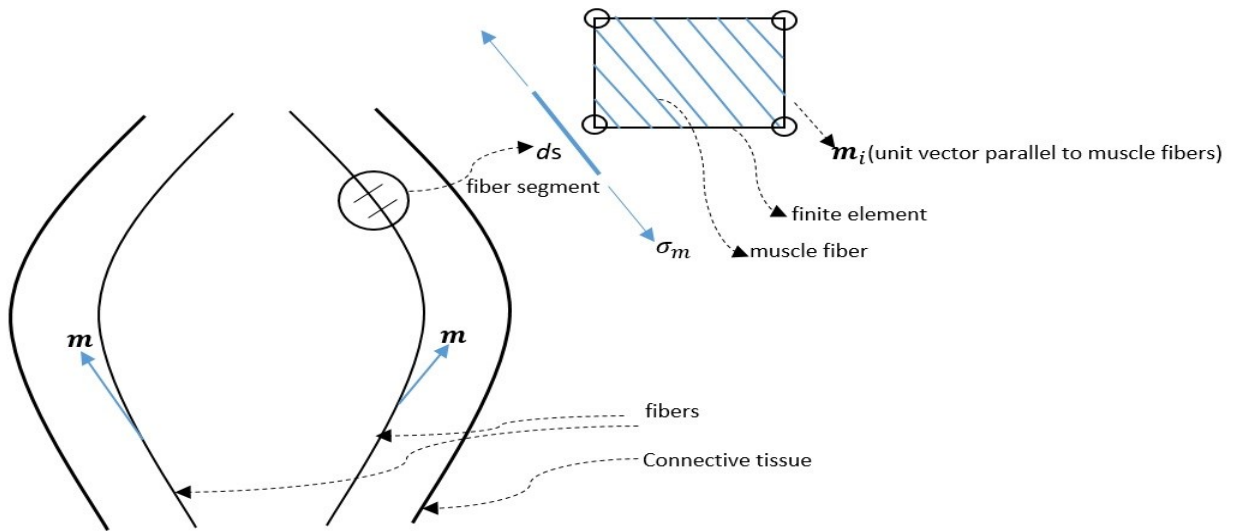


Figure 3.1 Schematic view of a deformed muscle, fibers direction within the tissue, and an infinitesimal segment of the fiber ds . The orientation of the fibers within a continuum finite element is also depicted. σ_m represents the Cauchy stress in the fiber direction (adopted from Spyrou and Aravas (2011)).

While the connective tissue (CT) is a passive tissue produces only passive force, the muscle fibers generate active force when stimulated from the CNS, as well as passive force. Similar to Liang and colleagues (2006) study, it is assumed in this dissertation that the total stress in the muscle is equal to the summation of the stresses in the fiber and connective tissue

$$\boldsymbol{\sigma} = \boldsymbol{\sigma}^f + \boldsymbol{\sigma}^{ct} \quad (3.1.1)$$

Using Spyrou approach (Spyrou, 2009), let the direction of undeformed fibers at every material point to be defined by a unit vector, \mathbf{m}_0 . Then the deformed configuration of that material point at each time increment is defined as:

$$\mathbf{m} = \frac{1}{|\mathbf{F} \cdot \mathbf{m}_0|} \mathbf{F} \cdot \mathbf{m}_0 \quad (3.1.2)$$

where \mathbf{F} is the deformation gradient tensor.

The stretch ratio, λ_m , determines changes in the length of each infinitesimal segment of the fiber in the \mathbf{m} direction (Spyrou and Aravas, 2011).

$$\lambda_m = \frac{ds}{ds_0} = \sqrt{\mathbf{m}_0 \cdot \mathbf{F}^T \cdot \mathbf{F} \cdot \mathbf{m}_0} \quad (3.1.3)$$

where ds_0 is the fiber segment original length, and ds is its current length.

The axial logarithmic strain in the fiber direction is:

$$\varepsilon_m = \ln \lambda_m \quad (3.1.4)$$

And the rate of change of ε_m is written as:

$$\dot{\boldsymbol{\varepsilon}}_{\mathbf{m}} = \frac{\dot{\lambda}_{\mathbf{m}}}{\lambda_{\mathbf{m}}} = \mathbf{m} \cdot \mathbf{D} \cdot \mathbf{m} = \mathbf{m} \mathbf{m} : \mathbf{D} \quad (3.1.5)$$

where \mathbf{D} is the deformation rate tensor which is the symmetric part of spatial velocity gradient tensor, \mathbf{L} .

The skeletal muscle like other soft tissues in the human body acts as an incompressible material. Compressibility is a measure of the relative volume change of a solid or fluid as a response to pressure change. Therefore, an incompressible material is a material with no change in its volume (volume-preserved). The logarithmic strain tensor of the fiber based on the concept of volume conservation of material can be derived as (see Spyrou, 2009: Page 51 for details):

$$\boldsymbol{\varepsilon}^{\mathbf{f}} = \frac{3}{2} \varepsilon_{\mathbf{m}} \left(\mathbf{m} \mathbf{m} - \frac{1}{3} \boldsymbol{\delta} \right) \quad (3.1.6)$$

where $\boldsymbol{\delta}$ is the second order identity tensor.

The total strain in the muscle was assumed to be equal to the summation of the strains in the fibers and connective tissue ($\boldsymbol{\varepsilon} = \boldsymbol{\varepsilon}^{\mathbf{f}} + \boldsymbol{\varepsilon}^{\text{ct}}$) in the previous work (Spyrou and Aravas, 2011). However, the above mentioned assumption is not accurate from the numerical and mechanical point of view. As it was shown in Fig. 2.5, the fiber bundles and connective tissues are arranged as parallel springs in the muscle structure. Therefore, their magnitudes of strains in the fibers and connective tissue are equal:

$$\boldsymbol{\varepsilon}^{\text{ct}} = \boldsymbol{\varepsilon} = \boldsymbol{\varepsilon}^{\mathbf{f}} \quad (3.1.7)$$

Continuing with Liang and colleagues (Liang et al, 2006), and Spyrou and Aravas (2011) approaches, the nominal strain in the fiber is determined as:

$$\varepsilon_0^m = \frac{ds - ds_0}{ds_0} = \lambda_m - 1 = \exp(\varepsilon_m) - 1 \text{ or } \varepsilon_m = \ln(1 + \varepsilon_0^m) \quad (3.1.8)$$

Likewise, nominal stress in the fiber is related to its true stress as:

$$\sigma_0^m = \sigma^m \frac{A}{A_0} = \sigma^m \frac{ds_0}{ds} = \frac{\sigma^m}{\lambda_m} = \frac{\sigma^m}{1 + \varepsilon_0^m} \quad (3.1.9)$$

where A_0 and A are the fiber initial and current cross sectional area.

Consequently, σ^f can be defined as:

$$\sigma^f = \sigma^m \mathbf{mm} \quad (3.1.10)$$

3.1.2 Fiber Stress Calculation

The muscle fibers generate two types of forces: active and passive. While the active force is function of the activation level, fiber length, and velocity of contraction, the passive force is only function of the fiber length. In general, the nominal longitudinal stress in a muscle fiber is written as sum of the active nominal longitudinal stress, $\sigma_0^{m(\text{act})}$, and the passive one, $\sigma_0^{m(\text{pas})}$ (Spyrou and Aravas, 2011):

$$\sigma_0^m = \sigma_0^{m(\text{act})} + \sigma_0^{m(\text{pas})} \quad (3.1.11)$$

Following Liang's approach, $\sigma_0^{m(\text{act})}$ and $\sigma_0^{m(\text{pas})}$ are defined as:

$$\sigma_0^{m(\text{act})} = \sigma_{\text{max}} f_a(t) \cdot f_l(\varepsilon_0^m) \cdot f_v(\dot{\varepsilon}_0^m) \quad \text{and} \quad \sigma_0^{m(\text{pas})} = \sigma_0^{m(\text{pas})}(\varepsilon_0^m) \quad (3.1.12)$$

where σ_{max} is the maximum isometric stress at the optimal fiber length, f_a is the activation function that relates the pattern of the activation to time, f_l is the length function that shows the relation between the active stress and the fiber nominal longitudinal strain, ε_0^m , and finally, f_v is the velocity function that shows the effect of velocity of contraction or nominal longitudinal strain rate on the overall nominal longitudinal stress of the fiber. Therefore, the total nominal stress in the fiber is written as:

$$\sigma_0^m = \sigma_{\text{max}} f_a(t) \cdot f_l(\varepsilon_0^m) \cdot f_v(\dot{\varepsilon}_0^m) + \sigma_0^{m(\text{pas})}(\varepsilon_0^m) \quad (3.1.13)$$

3.1.3 Connective Tissue Stress Calculation

The connective tissue is assumed to behave as a linear isotropic hyperelastic material. St. Venant-Kirchhof law is used to simulate the connective tissue in this dissertation (Bonnet and Wood, 2008). This section formulation and all calculations are totally different than the previous work done by Spyrou and colleagues (Spyrou and Aravas, 2011; Spyrou, 2009).

$$\mathbf{S}^{\text{ct}} = \lambda \text{tr}(\mathbf{E})\boldsymbol{\delta} + 2\mu\mathbf{E} \quad (3.1.14)$$

where \mathbf{E} is the Green-Lagrange strain ($\mathbf{E} = \frac{1}{2}(\mathbf{F}^T \cdot \mathbf{F} - \boldsymbol{\delta})$), \mathbf{S} is the Second Piola-Kirchhoff stress, λ and μ are Lamé parameters, and $\boldsymbol{\delta}$ is the second-order identity tensor.

The Kirchhof ($\boldsymbol{\tau}$) and Cauchy ($\boldsymbol{\sigma}$) stresses in the connective tissue are calculated respectively as:

$$\boldsymbol{\tau}^{\text{ct}} = \mathbf{F} \cdot \mathbf{S} \cdot \mathbf{F}^T \quad (3.1.15)$$

$$\boldsymbol{\sigma}^{\text{ct}} = \mathbf{J}^{-1} \mathbf{F} \cdot \mathbf{S} \cdot \mathbf{F}^T \quad (3.1.16)$$

In the above equation, $\mathbf{J} = \det(\mathbf{F})$.

3.1.4 Generalizing the Constitutive Equations to the Pennate Structures

In case of pennate structure, there are more fiber bundles in different directions. The method of superposition is used to sum up all stresses in different directions (Spyrou and Aravas, 2011).

Therefore, the constitutive equations of fibers can be rewritten as:

$$\boldsymbol{\varepsilon}^f = \frac{3}{2} \sum_{i=1}^n \varepsilon_m^{(i)} \left(\mathbf{m}^{(i)} \mathbf{m}^{(i)} - \frac{1}{3} \boldsymbol{\delta} \right), \quad \mathbf{m}^{(i)} = \frac{1}{|\mathbf{F} \cdot \mathbf{m}_0^{(i)}|} \mathbf{F} \cdot \mathbf{m}_0^{(i)} \quad (3.1.17)$$

$$\lambda_m^{(i)} = \sqrt{\mathbf{m}_0^{(i)} \cdot \mathbf{F}^T \cdot \mathbf{F} \cdot \mathbf{m}_0^{(i)}}, \quad \varepsilon_0^{m(i)} = \lambda_m^{(i)} - 1, \quad \varepsilon_m^{(i)} = \ln \lambda_m^{(i)} \quad (3.1.18)$$

$$\boldsymbol{\sigma}^f = \sum_{i=1}^n \sigma^{m(i)} \mathbf{m}^{(i)} \mathbf{m}^{(i)}, \quad \sigma^{m(i)} = (1 + \varepsilon_0^{m(i)}) \sigma_0^{m(i)} \quad (3.1.19)$$

$$\sigma_0^{m(i)} = \sigma_{\max}^{(i)} \left(f_a^{(i)}(t) f_l^{(i)}(\varepsilon_0^{m(i)}) f_v^{(i)}(\dot{\varepsilon}_0^{m(i)}) \right) + \sigma_{\text{pas}}^{m(i)} \quad (3.1.20)$$

3.2 Numerical Formulation and Discretization of the Constitutive Model

3.2.1 Deformable Body General Equilibrium Equation

To implement the constitutive equations derived in Section 3.1 into the FE solver, the Cauchy stress and material Jacobian tensors should be discretized. Therefore, the equilibrium equation of a general deformable body (Fig. 3.2) is described as (Liang et al., 2006; Spyrou, 2011):

$$\frac{\partial \sigma_{ij}}{\partial x_i} + \rho b_j = 0 \quad (3.2.1)$$

Where σ_{ij} is a typical component of the Cauchy stress tensor, \mathbf{b} is body force per unit of mass, and ρ is the mass density.

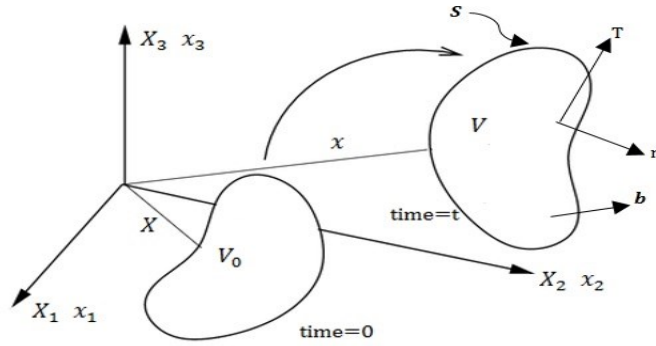


Figure 3.2 Configuration of a continuum body in a Cartesian coordinate system and its motion.

As shown in Fig. 3.2, the body volume changes from V_0 at time=0 to V at time=t. The volume is confined to a boundary surface, S , which is divided to two parts: S_u and S_σ . The displacement vector \mathbf{u} is known on S_u , and the traction forces per unit of area, \mathbf{T} , are known on S_σ (Spyrou, 2009):

$$\mathbf{u} = \hat{\mathbf{u}} \equiv \text{known on } S_u \text{ and } \mathbf{n} \cdot \boldsymbol{\sigma} = \mathbf{T} \equiv \text{known on } S_\sigma \quad (3.2.2)$$

To have a displacement field, $u(x)$, that satisfies the first part of Eq. 3.2.2, Eq. 3.2.1 can be written as:

$$\int_V \left[\frac{\partial \sigma_{ij}(\mathbf{u})}{\partial x_j} + \rho b_i \right] v_i^* dV + \int_{S_\sigma} [T_i - n_j \sigma_{ij}(\mathbf{u})] v_i^* dS = 0 \quad (3.2.3)$$

Where v_i^* represents virtual velocity field that fulfills the condition $v_i^* = 0$ on S_u .

Eq. 3.2.3 can be replaced by the Eq. 3.2.4 using the Green theorem to find a displacement field that satisfies $\mathbf{u} = \hat{\mathbf{u}}$ on S_u . This is the first step in the FE formulation of the problem.

$$\mathbf{G}(\mathbf{u}(\mathbf{x})) \equiv \int_V \boldsymbol{\sigma}(\mathbf{u}(\mathbf{x})) : \mathbf{D}^* dV - \int_V \rho \mathbf{b} \cdot \mathbf{v}^* dV - \int_S \mathbf{T} \cdot \mathbf{v}^* dS = 0 \quad (3.2.4)$$

Where \mathbf{D}^* is given by

$$D_{ij}^* = \frac{1}{2} \left(\frac{\partial v_i^*}{\partial x_j} + \frac{\partial v_j^*}{\partial x_i} \right) \quad (3.2.5)$$

By considering $\boldsymbol{\sigma}$ as a symmetric tensor, Eq. 3.2.4 is written as:

$$\mathbf{G}(\mathbf{u}(\mathbf{x})) \equiv \int_V \boldsymbol{\sigma}(\mathbf{u}(\mathbf{x})) : \mathbf{L}^* dV - \int_V \rho \mathbf{b} \cdot \mathbf{v}^* dV - \int_S \mathbf{T} \cdot \mathbf{v}^* dS = 0 \quad (3.2.6)$$

where

$$L_{ij}^* = \frac{\partial v_i^*}{\partial x_j} \quad (3.2.7)$$

3.2.2 Finite Element Implementation

This section calculations and formulation were taken from Spyrou (2009) to explain how FE method works. To transform the previously mentioned equations to the finite element setting, the amount of displacement increment, $\Delta \mathbf{u}(\mathbf{x})$, at the end of each time increment is calculated:

$$u_{n+1}(x) = u_n(x) + \Delta u(x) \quad (3.2.8)$$

By using finite element interpolation matrix, $N(x)$, the displacement increment vector is related to the nodal displacement at each element, Δu_e^N :

$$\{\Delta u(x)\} = [N(x)]\{\Delta u_e^N\} \quad (3.2.9)$$

Similarly, virtual velocity vector \mathbf{v}^* and velocity gradient $\mathbf{L}^* = \partial \mathbf{v}^* / \partial \mathbf{x}_{n+1}$ are written as:

$$\{\mathbf{v}^*(x)\} = [N(x)]\{\mathbf{v}_e^{*N}\} \quad (3.2.10)$$

$$\{\mathbf{L}^*(x)\} = [B_L(x)]\{\mathbf{v}_e^{*N}\} \quad (3.2.11)$$

Then, by substituting the above equations in Eq. 3.2.6, it is rewritten as:

$$G = [\mathbf{v}^{*N}] \Lambda \left(\int_{V_{n+1}^e} [B_L]_{n+1}^T \{\sigma\}_{n+1} dV - \int_{V_{n+1}^e} [N]_{n+1}^T \rho \{b\}_{n+1} dV \right. \\ \left. - \int_{S_{\sigma}^e|_{n+1}} [N]_{n+1}^T \{T\}_{n+1} dS \right) \quad (3.2.12)$$

where Λ is the “assembly operator”, and $[\mathbf{v}^{*N}]$ is row of virtual nodal velocities.

Also, the applied load vector $\{F\}_{n+1}$ is described as:

$$\{F\}_{n+1} = \Lambda \left(\int_{V_{n+1}^e} [B_L]_{n+1}^T \{\sigma\}_{n+1} dV \right) \quad (3.2.13)$$

which is equal to:

$$\{F\}_{n+1} = \Lambda \left(\int_{V_{n+1}^e} [N]_{n+1}^T \rho \{b\}_{n+1} dV + \int_{S_{\sigma}^e|_{n+1}} [N]_{n+1}^T \{T\}_{n+1} dS \right) \quad (3.2.14)$$

Thus, the residual force vector $R(\Delta u^N)$ can be defined as:

$$\{R(\Delta u^N)\}_{n+1} \equiv \Lambda \left(\int_{V_{n+1}^e} [B_L]_{n+1}^T \{\sigma\}_{n+1} dV \right) - \{F\}_{n+1} = 0 \quad (3.2.15)$$

Hence, the corresponding Jacobian or stiffness matrix $[K]$ is derived from the following equations:

$$G = [v^{*N}] \{R\}_{n+1} = 0 \quad (3.2.16)$$

$$dG = [v^{*N}] \left[\frac{\partial \{R(\Delta u^N)\}_{n+1}}{\partial \{\Delta u^N\}} \right] d\{\Delta u^N\} = [v^{*N}] [K] d\{\Delta u^N\} \quad (3.2.17)$$

3.2.3 Calculation of the Jacobian

By applying the finite element discretization method to the continuum form of G and comparing results to Eq. 3.2.17, the Jacobian matrix $[K]$ can be calculated. The following equations explain the procedure based on the previous reference studies (Spyrou, 2009; Spyrou and Aravas, 2011; Liang et al., 2006; van Leeuwen and Kier, 1997):

$$G(\Delta \mathbf{u}) = \int_V \text{tr} \left(\boldsymbol{\sigma} \cdot \frac{\partial \mathbf{v}^*}{\partial \mathbf{x}} \right) dV - \int_{V_0} \rho_0 \mathbf{b} \cdot \mathbf{v}^* dV_0 - \int_{S_{\sigma}^0} \mathbf{T}^0 \cdot \mathbf{v}^* dS_0 \quad (3.2.18)$$

Where ρ_0 and \mathbf{T}^0 are the initial density and the nominal traction vector, respectively. It should be mentioned that all parameters used from now on are measured at the end of the increment.

$$d\mathbf{x} = d\mathbf{x}_{n+1} = d(\mathbf{x}_n + \Delta\mathbf{u}) = d(\Delta\mathbf{u}) \quad (3.2.19)$$

The first part on the right side of Eq. 3.2.18 can be written as:

$$\int_V \text{tr} \left(\boldsymbol{\sigma} \cdot \frac{\partial \mathbf{v}^*}{\partial \mathbf{x}} \right) dV = \int_{V_0} \text{tr} \left(\boldsymbol{\sigma} \cdot \frac{\partial \mathbf{v}^*}{\partial \mathbf{X}} \cdot \frac{\partial \mathbf{X}}{\partial \mathbf{x}} \right) J dV_0 = \int_{V_0} \text{tr} \left(\boldsymbol{\sigma} \cdot \frac{\partial \mathbf{v}^*}{\partial \mathbf{X}} \cdot \mathbf{F}^{-1} \right) J dV_0 \quad (3.2.20)$$

Then Eq. 3.2.18 is rewritten as:

$$G(\Delta\mathbf{u}) = \int_{V_0} \text{tr} \left(\boldsymbol{\sigma} \cdot \frac{\partial \mathbf{v}^*}{\partial \mathbf{X}} \cdot \mathbf{F}^{-1} \right) J dV_0 - \int_{V_0} \rho_0 \mathbf{b} \cdot \mathbf{v}^* dV_0 - \int_{S_0^g} \mathbf{T}^0 \cdot \mathbf{v}^* dS_0 \quad (3.2.21)$$

Moreover, by assuming that the applied loads are independent of the body motion, follower loads ($\int_{V_0} \rho_0 \mathbf{b} \cdot \mathbf{v}^* dV_0$) are excluded from the previous equations, and hence, differential form of G becomes

$$dG = \int_{V_0} \text{tr} \left\{ \frac{\partial \mathbf{v}^*}{\partial \mathbf{X}} \cdot \left[d(\mathbf{F}^{-1}) \cdot \boldsymbol{\sigma} + \mathbf{F}^{-1} \cdot d\boldsymbol{\sigma} + \mathbf{F}^{-1} \cdot \boldsymbol{\sigma} \frac{dJ}{J} \right] \right\} J dV_0 \quad (3.2.22)$$

where

$$\frac{\partial \mathbf{v}^*}{\partial \mathbf{X}} = \frac{\partial \mathbf{v}^*}{\partial \mathbf{x}} \cdot \frac{\partial \mathbf{x}}{\partial \mathbf{X}} = \mathbf{L}^* \cdot \mathbf{F} \quad (3.2.23)$$

By substituting Eq. 3.2.23 into Eq. 3.2.22, it becomes

$$dG = \int_V \text{tr} \left\{ \mathbf{L}^* \cdot \left[\mathbf{F} \cdot d(\mathbf{F}^{-1}) \cdot \boldsymbol{\sigma} + d\boldsymbol{\sigma} + \frac{dJ}{J} \boldsymbol{\sigma} \right] \right\} dV \quad (3.2.24)$$

Next, each term inside the brackets is introduced:

$$\mathbf{F} = \frac{\partial \mathbf{x}}{\partial \mathbf{X}} \Rightarrow d\mathbf{F} = \frac{\partial(d\mathbf{x})}{\partial \mathbf{X}} \text{ or } d\mathbf{F} = \frac{\partial(d(\Delta \mathbf{u}))}{\partial \mathbf{X}} \quad (3.2.25)$$

also,

$$\mathbf{F} \cdot \mathbf{F}^{-1} = \boldsymbol{\delta} \Rightarrow d\mathbf{F} \cdot \mathbf{F}^{-1} + \mathbf{F} \cdot d\mathbf{F}^{-1} = 0 \Rightarrow \mathbf{F} \cdot d\mathbf{F}^{-1} = -d\mathbf{F} \cdot \mathbf{F}^{-1} \quad (3.2.26)$$

Combining Eqs. 3.2.25 and 3.2.26 results in

$$\mathbf{F} \cdot d\mathbf{F}^{-1} = -\frac{\partial[d(\Delta \mathbf{u})]}{\partial \mathbf{X}} \cdot \frac{\partial \mathbf{X}}{\partial \mathbf{x}} = -\frac{\partial[d(\Delta \mathbf{u})]}{\partial \mathbf{x}} \Rightarrow \mathbf{F} \cdot d\mathbf{F}^{-1} = -d\mathbf{L} \quad (3.2.27)$$

where

$$d\mathbf{L} \equiv \frac{\partial[d(\Delta \mathbf{u})]}{\partial \mathbf{x}} \quad (3.2.28)$$

On the other hand, using the derivative $\frac{\partial J}{\partial F_{ki}}$ leads to

$$\begin{aligned} dJ &= J(F^{-1})_{ik} dF_{ki} = J(F^{-1} \cdot dF)_{ii} = J \operatorname{tr}(F^{-1} \cdot dF) = J \operatorname{tr}\left(\frac{\partial \mathbf{X}}{\partial \mathbf{x}} \cdot \frac{\partial(d\Delta \mathbf{u})}{\partial \mathbf{X}}\right) \\ &= J \operatorname{tr}\left(\frac{\partial(d\Delta \mathbf{u})}{\partial \mathbf{x}}\right) = J \operatorname{tr}(d\mathbf{L}) \end{aligned} \quad (3.2.29)$$

or

$$\frac{dJ}{J} = dL_{kk} \quad (3.2.30)$$

Finally, to simplify the calculation of variation of the stress tensor $\boldsymbol{\sigma}$ with respect to the displacement increment, $\Delta \mathbf{u}$, following approach is applied:

$$\overset{\nabla}{\boldsymbol{\tau}} = \mathbf{CE} : \mathbf{D} \quad (3.2.31)$$

where $\boldsymbol{\tau}$ is the Kirchhoff stress ($\boldsymbol{\tau} = \mathbf{J}\boldsymbol{\sigma}$), $\overset{\nabla}{\boldsymbol{\tau}}$ and \mathbf{CE} Jaumann derivative of $\boldsymbol{\tau}$, and the Jaumann spatial elasticity tensors, respectively. Also, $\mathbf{L} = \partial\mathbf{v}/\partial\mathbf{x}$, and $\mathbf{D} = (1/2)(\mathbf{L} + \mathbf{L}^T)$.

3.2.4 The Linearization Moduli

The ultimate purpose of numerical implementation of the constitutive equations is to relate stress function and its derivatives to the strain and its derivatives:

$$\overset{\nabla}{\boldsymbol{\tau}} = \mathbf{CE} : \mathbf{D} \quad (3.2.32)$$

The Jaumann derivative of the Cauchy stress tensor was used in the Spyrou and Aravas (2011) work, while we used the Jaumann derivative of the Kirchhoff stress in this dissertation (Eq. 3.2.32).

To calculate the Jacobian tensor which is the basis of equilibrium equations in the FE solvers, the so-called “linearization moduli” of the algorithm that handles the constitutive equations are required (Spyrou, 2009). These moduli are defined in terms of the fourth-order tensor, \mathbf{CE} .

In this section the approximate method of calculating \mathbf{CE} is introduced. Back to the total stress of the muscle, $\boldsymbol{\sigma} = \boldsymbol{\sigma}^f + \boldsymbol{\sigma}^{ct}$, its Jaumann derivative can be implied as:

$$\overset{\nabla}{\boldsymbol{\sigma}} = \overset{\nabla}{\boldsymbol{\sigma}^f} + \overset{\nabla}{\boldsymbol{\sigma}^{ct}} \quad (3.2.33)$$

Recalling the fiber part of the stress tensor, $\boldsymbol{\sigma}^f = \sigma^m \mathbf{mm}$, its derivative is defined as:

$$\overset{\nabla}{\boldsymbol{\sigma}}^f = \dot{\sigma}^m \mathbf{m} \mathbf{m} + \sigma^m (\overset{\nabla}{\mathbf{m}} \mathbf{m} + \mathbf{m} \overset{\nabla}{\mathbf{m}}) \quad (3.2.34)$$

where

$$\sigma^m = (1 + \varepsilon_0^m) \sigma_0^m = \exp(\varepsilon_m) \sigma_0^m \quad (3.2.35)$$

To obtain the derivative of the Cauchy stress, $\dot{\sigma}^m$, $\dot{\varepsilon}^m$ and $\dot{\varepsilon}_0^m$ must be derived first:

$$\dot{\varepsilon}^m = \mathbf{m} \cdot \mathbf{D} \cdot \mathbf{m} = (\mathbf{m} \mathbf{m}) : \mathbf{D} \quad (3.2.36)$$

and

$$\varepsilon_0^m = \exp(\varepsilon_m) - 1 \Rightarrow \dot{\varepsilon}_0^m = \exp(\varepsilon_m) \dot{\varepsilon}_m \quad (3.2.37)$$

by substituting Eq.3.2.36 into Eq. 3.2.37

$$\dot{\varepsilon}_0^m = (1 + \varepsilon_0^m) (\mathbf{m} \mathbf{m}) : \mathbf{D} \quad (3.2.38)$$

The nominal stress in the fiber has the form of:

$$\sigma_{0|n+1}^m = f(\varepsilon_{0|n+1}^m, \frac{\varepsilon_{0|n+1}^m - \varepsilon_{0|n}^m}{\Delta t}, t_{n+1}) \quad (3.2.39)$$

Hence, $\dot{\sigma}^m$ becomes

$$\dot{\sigma}_0^m = \frac{\partial f}{\partial \varepsilon_0^m} \dot{\varepsilon}_0^m + \frac{1}{\Delta t} \frac{\partial f}{\partial \dot{\varepsilon}_0^m} \dot{\varepsilon}_0^m = \left(\frac{\partial f}{\partial \varepsilon_0^m} + \frac{1}{\Delta t} \frac{\partial f}{\partial \dot{\varepsilon}_0^m} \right) \dot{\varepsilon}_0^m \xrightarrow{(3.2.37)} \dot{\sigma}_0^m = \mathbf{G}(\mathbf{m} \mathbf{m}) : \mathbf{D} \quad (3.2.40)$$

where

$$\mathbf{G} = (1 + \varepsilon_0^m) \left(\frac{\partial f}{\partial \varepsilon_0^m} + \frac{1}{\Delta t} \frac{\partial f}{\partial \dot{\varepsilon}_0^m} \right) \quad (3.2.41)$$

therefore,

$$\begin{aligned}
\dot{\sigma}^m &= \exp(\varepsilon_m) (\dot{\varepsilon}^m \sigma_0^m + \dot{\sigma}_0^m) \xrightarrow{(3.2.36),(3.2.39)} \dot{\sigma}^m \\
&= \exp(\varepsilon_m) [\sigma_0^m(\mathbf{mm}) : \mathbf{D} + G(\mathbf{mm}) : \mathbf{D}] \\
&= (1 + \varepsilon_0^m)(\sigma_0^m + G)(\mathbf{mm}) : \mathbf{D}
\end{aligned} \tag{3.2.42}$$

The second part of Eq. 3.2.34, $(\overset{\nabla}{\mathbf{m}}\mathbf{m} + \mathbf{m}\overset{\nabla}{\mathbf{m}})$ is calculated using the following relations

$$\dot{\mathbf{m}} = (\mathbf{W} + \mathbf{D} \cdot \mathbf{m}\mathbf{m} - \mathbf{m}\mathbf{m} \cdot \mathbf{D}) \cdot \mathbf{m} \Rightarrow \overset{\nabla}{\mathbf{m}} = (\mathbf{D} \cdot \mathbf{m}\mathbf{m} - \mathbf{m}\mathbf{m} \cdot \mathbf{D}) \cdot \mathbf{m} \tag{3.2.43}$$

or

$$\overset{\nabla}{\mathbf{m}} = \mathbf{D} \cdot \mathbf{m} - \mathbf{m}(\mathbf{m}\mathbf{m}) : \mathbf{D} \tag{3.2.44}$$

so

$$\begin{aligned}
\overset{\nabla}{\mathbf{m}}\mathbf{m} + \mathbf{m}\overset{\nabla}{\mathbf{m}} &= [\mathbf{D} \cdot \mathbf{m} - \mathbf{m}(\mathbf{m}\mathbf{m}) : \mathbf{D}]\mathbf{m} + \mathbf{m}[\mathbf{D} \cdot \mathbf{m} - \mathbf{m}(\mathbf{m}\mathbf{m}) : \mathbf{D}] \\
&= \mathbf{D} \cdot \mathbf{m}\mathbf{m} + \mathbf{m}\mathbf{D} \cdot \mathbf{m} - 2\mathbf{m}\mathbf{m}(\mathbf{m}\mathbf{m}) : \mathbf{D}
\end{aligned} \tag{3.2.45}$$

which indicates that:

$$\overset{\nabla}{\mathbf{m}}\mathbf{m} + \mathbf{m}\overset{\nabla}{\mathbf{m}} = \mathbf{B} : \mathbf{D} \tag{3.2.46}$$

where

$$B_{ijkl} = \frac{1}{2} [(\delta_{ik}m_j + \delta_{jk}m_i)m_k + (\delta_{il}m_j + \delta_{jl}m_i)m_k] - 2m_i m_j m_k m_l \tag{3.2.47}$$

Substituting Eq. 3.2.42 and Eq.3.2.46 into Eq. 3.2.34 results in

$$\overset{\nabla}{\boldsymbol{\sigma}}^f = (1 + \varepsilon_0^m)(\sigma_0^m + G)(\mathbf{m}\mathbf{m}) : \mathbf{D}\mathbf{m}\mathbf{m} + \sigma^m \mathbf{B} : \mathbf{D} \quad (3.2.48)$$

or

$$\overset{\nabla}{\boldsymbol{\tau}}^f = \mathbf{J} \overset{\nabla}{\boldsymbol{\sigma}}^f = \mathbf{C}\mathbf{E}^f : \mathbf{D} \quad (3.2.49)$$

and finally,

$$\mathbf{C}\mathbf{E}^f = \frac{1}{\mathbf{J}} [(1 + \varepsilon_0^m)(\sigma_0^m + G)\mathbf{m}\mathbf{m}\mathbf{m}\mathbf{m} + \sigma^m \mathbf{B}] \quad (3.2.50)$$

To calculate $\overset{\nabla}{\boldsymbol{\sigma}}^{\text{ct}}$ and \mathbf{C}^{ct} , the following approach was used in this dissertation:

$$\overset{\nabla}{\boldsymbol{\tau}}^{\text{ct}} = \mathbf{C}\mathbf{E}^{\text{ct}} : \mathbf{D} \quad (3.2.51)$$

$$\mathbf{C}\mathbf{E}_{ijkl} = \mathbf{J}\mathbf{c}_{ijkl} + \delta_{ik}\tau_{jl} + \tau_{ik}\delta_{jl} \quad (3.2.52)$$

$$\mathbf{c}_{ijkl} = \mathbf{J}^{-1} \mathbf{F}_{iI} \mathbf{F}_{jJ} \mathbf{F}_{kK} \mathbf{F}_{lL} \mathbf{C}_{IJKL} \quad (3.2.53)$$

$$\mathbf{C}_{IJKL} = \lambda \delta_{IJ} \delta_{KL} + 2\mu \delta_{IK} \delta_{JL} \quad (3.2.54)$$

$$\mathbf{S}_{IJ} = \lambda \text{tr}(\mathbf{E}_{\mathbf{K}\mathbf{K}}) \mathbf{I} + 2\mu \mathbf{E}_{IJ} \quad (3.2.55)$$

where $\mathbf{C}\mathbf{E}$, \mathbf{c} , \mathbf{C} , and \mathbf{S} are Jaumann elasticity, spatial elasticity, standard material elasticity, and Second Piola-Kirchoff stress tensors, respectively (Bonet and Wood 2008). The identity tensor used in the second part of the Eq. 3.2.54 should be symmetric ($1/2 (\delta_{IK} \delta_{JL} + \delta_{IL} \delta_{JK})$), while the unsymmetric version is used in the equation. This doesn't affect the results because the symmetry of the strain tensor filters the skew-symmetric part of the unsymmetric fourth-order identity tensor.

Consequently, the overall linearization moduli of the muscle are the summation of the fiber and connective tissue linearization moduli:

$$\overset{\nabla}{\boldsymbol{\sigma}} \cong \frac{1}{J} (\mathbf{CE} : \mathbf{D}) \quad , \quad \mathbf{CE} = \mathbf{CE}^f + \mathbf{CE}^{ct} \quad (3.2.56)$$

Since the muscle tissue act as an incompressible material ($J = 1$), the derivatives of the constant term, J , were eliminated from the above equations. In addition, unlike the previous works that considered different deformation rate tensors (\mathbf{D}) for the fiber and connective tissues, it is assumed that $\mathbf{D} = \mathbf{D}^f = \mathbf{D}^{ct}$.

3.3 Summary of My Contribution

The ultimate goal of this chapter was to develop a new continuum method of muscle modeling to simulate active and passive behaviors of the skeletal muscles in only one element instead of modelling them using two discrete types of elements. This was achieved by developing a new constitutive model that was originally presented by Liang and his colleagues (2006). Later, Liang approach was developed by Spyrou and Aravas (2011) numerically, considering both parts of the muscle: fibers and connective tissue. However, there are some errors in their assumptions with regard to the stress and strain functions in the tissue, as well as some numerical mistakes from the continuum mechanics point of view.

First, similar to a composite material reinforced by the fibers, the skeletal muscle has two parts arranged in parallel: the fibers and connective tissue. The total strain or deformation of the muscle is equal to the strain in its individual components. Also, the total stress in the muscle is the summation of the stresses in the fibers and connective tissue. While, in the previous works,

both total stress and strain in the muscle were considered to be equal to the summation of the fiber and connective tissue ones, which is a wrong assumption from the physical point of view.

Second, some mistakes were observed in the numerical approaches used by the previous researchers which were corrected in this dissertation such as: considering different deformation rates for different parts of the muscle, whereas deformation rate is constant and equal for all parts of a composite material; and using Jaumann derivative to calculate the strain rate and assuming that it is equal to the deformation rate for each part of the muscle, while simple material derivative could be used and considered as deformation rate. Calculations done by Spyrou (2009) are presented in Appendix C.

CHAPTER FOUR: NUMERICAL IMPLEMENTATION, VERIFICATION AND VALIDATION OF THE MATERIAL MODEL

In this chapter, the implementation of the constitutive equations and their numerical formulation into the UMAT subroutine is presented. Subsequently, the UMAT is verified by conducting convergence tests; and finally, the material model of the muscle is validated against existing experimental data and numerical simulation studies of the extension of a squid fish (van Leeuwen and Kier, 1997).

4.1. UMAT Implementation

To implement the material model explained in Chapter Three, a user defined subroutine, UMAT, was developed. The UMAT was written in FORTRAN language, and was compiled into ABAQUS/Standard solver. The derived Cauchy stress and Jacobian (Elasticity) tensors were calculated at each integrated point at the end of each iteration. Before the developed material was inserted into the actual cervical spine model, it should be generally verified by conducting mesh convergence tests. To confirm the accuracy of the written UMAT, the stress and Jacobian tensors at the end of each increment were checked using a simple model with various numbers of elements. The elements size was decreased and the model was run again. The desired quantities such as strain and strain rate didn't change by more than 5%. Therefore, it was concluded that the mesh size is fine, and the model predictions and results don't depend on the mesh size. Moreover, the developed UMAT needed to be validated by comparing its predictions to the existing experimental data in the relevant literature. Experimental studies reported similarity between the tentacle and human musculature behavior (van Leeuwen and Kier, 1997). The ABAQUS Documentation User Subroutine Reference Manual (ABAQUS

Documentation 2013) was used as the main reference for developing the UMAT. The procedure is explained in the following sections.

UMAT subroutine is used to define material models that are not available in the ABAQUS material library. In the ABAQUS input file (.inp), under the material section, the “*User Material” command is used to call the UMAT for the set of elements that the UMAT is assigned to them. UMAT interface automatically transfers all the functions and parameters used in the code i.e., deformation gradient, stress, and time, at the beginning of each increment. The deformation gradient at the end of the increment (\mathbf{F}_{n+1} at $\text{time}(2) = \text{time}(1) + \Delta\text{time}$) is also calculated by ABAQUS. User should calculate the values of other quantities at the end of each increment as listed here (adopted from Spyrou and Aravas (2011), and based on the modified equations explained in Chapter Three):

$$\lambda_{m|n+1} = \sqrt{\mathbf{m}_0 \cdot \mathbf{F}_{n+1}^T \cdot \mathbf{F}_{n+1} \cdot \mathbf{m}_0} \quad (4.1)$$

$$\varepsilon_{0|n+1}^m = \lambda_{m|n+1} - 1 \quad , \quad \varepsilon_{m|n+1} = \ln \lambda_{m|n+1} \quad (4.2)$$

$$\mathbf{m}_{n+1} = \frac{1}{|\mathbf{F}_{n+1} \cdot \mathbf{m}_0|} \mathbf{F}_{n+1} \cdot \mathbf{m}_0 \quad (4.3)$$

$$\boldsymbol{\varepsilon}_{|n+1}^f = \frac{3}{2} \varepsilon_{m|n+1} (\mathbf{m}_{n+1} \mathbf{m}_{n+1} - \frac{1}{3} \boldsymbol{\delta}) \quad (4.4)$$

$$\dot{\varepsilon}_0^m = \frac{\varepsilon_{0|n+1}^m - \varepsilon_{0|n}^m}{\Delta t} \quad (4.5)$$

$$\sigma_{0|n+1}^m = \sigma_{\max} \left(f_a(t_{n+1}) f_l(\varepsilon_{0|n+1}^m) f_v(\dot{\varepsilon}_0^m) \right) + \sigma_{\text{pas}}^m(\varepsilon_{0|n+1}^m) \quad (4.6)$$

$$\sigma_{n+1}^m = (1 + \varepsilon_{0|n+1}^m) \sigma_{0|n+1}^m \quad (4.7)$$

$$\boldsymbol{\sigma}_{n+1}^f = \sigma_{n+1}^m \mathbf{m}_{n+1} \mathbf{m}_{n+1} \quad (4.8)$$

$$\boldsymbol{\sigma}_{n+1}^{\text{ct}} = \frac{1}{\det \mathbf{F}_{n+1}} \mathbf{F}_{n+1} \cdot \mathbf{S}_{n+1} \cdot \mathbf{F}_{n+1}^T \quad (4.9)$$

$$\boldsymbol{\sigma}_{n+1} = \boldsymbol{\sigma}_{n+1}^f + \boldsymbol{\sigma}_{n+1}^{\text{ct}} \quad (4.10)$$

The functions used in Eq. 4.6 were taken from van Leeuwen and Kier experimental and numerical work (1997), and are summarized here:

The activation function, f_a , is given by:

$$f_a = \begin{cases} 0 & t \leq t_d \\ \left[0.5 \left(1 - \cos \left(\frac{\pi(t - t_d)}{t_a - t_d} \right) \right) \right]^q & t_d < t < t_a + t_d \\ 1 & t \geq t_a + t_d \end{cases} \quad (4.11)$$

t_d is delay time, t_a is the time between the beginning of the activation and full activation ($f_a=1$), and q is a constant parameter used to modify the activation function profile. Fig. 4.1 shows an activation function profile based on Eq. 4.11 where $t_d=0$, $t_a=40$ millisecond, and q is set as 15. After full activation time, f_a remains constant.

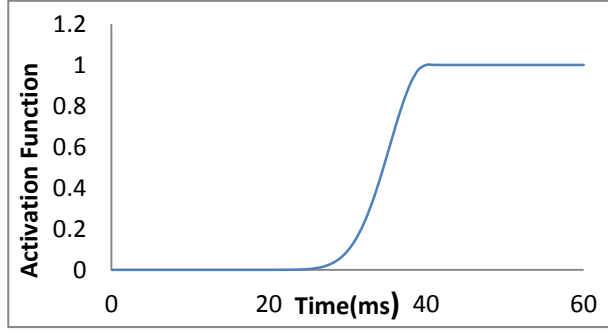


Figure 4.1 Activation function vs. time for the tentacle muscle.

Length function, f_l is derived from the experimental works done on the microstructures of the tentacle sarcomeres.

$$f_l = \begin{cases} f_5 + (f_4 - f_5)(\varepsilon_0^m - \varepsilon_5)/(\varepsilon_4 - \varepsilon_5) & \varepsilon_5 \leq \varepsilon_0^m < \varepsilon_4 \\ f_4 + (1 - f_4)(\varepsilon_0^m - \varepsilon_4)/(\varepsilon_3 - \varepsilon_4) & \varepsilon_4 \leq \varepsilon_0^m < \varepsilon_3 \\ 1 & \varepsilon_3 \leq \varepsilon_0^m < \varepsilon_2 \\ 1 - (\varepsilon_0^m - \varepsilon_2)/(\varepsilon_1 - \varepsilon_2) & \varepsilon_2 \leq \varepsilon_0^m < \varepsilon_1 \end{cases} \quad (4.12)$$

The characteristics parameters, f_l and ε_i are calculated as:

$$\varepsilon_1 = \frac{l_{myo} - (1/2)l_{bz}}{l_{0sarc}} \quad (4.13)$$

$$\varepsilon_2 = \frac{(1/2)l_{bz}}{l_{0sarc}} \quad (4.14)$$

$$\varepsilon_3 = -\frac{(1/2)l_{bz}}{l_{0sarc}} \quad (4.15)$$

$$\varepsilon_4 = \frac{l_{myo} - l_{act} - (1/2)l_{bz}}{l_{0sarc}} \quad (4.16)$$

$$\varepsilon_5 = -\frac{l_{min} - (1/2)l_{0sarc}}{l_{0sarc}} \quad (4.17)$$

$$f_4 = 1 - D_{act} \frac{l_{act} - l_{myo}}{l_{myo} - l_{bz}} \quad (4.18)$$

$$f_5 = 1 - D_{act} \frac{l_{act} + l_z - l_{min}}{l_{myo} - l_{bz}} - (D_{myo} + C_{myo}) \frac{l_{act} - l_{myo}}{l_{myo} - l_{bz}} \quad (4.19)$$

where l_{myo} is the length of myosin filament, l_{act} is the sum of the length of two opposing actin filaments in one sarcomere, l_{bz} is the length of the bare zone on the myosin, l_z is the width of Z-disc, the initial length of the sarcomere, $l_{0sarc} = l_{act} + l_z + (1/2)l_{bz}$, D_{act} and D_{myo} are parameters to account for cross-bridge losses owing to actin overlap and interaction between myosin filament and the Z-disc. Lastly, C_{myo} is introduced to count for resistive forces as a result of the collision of the myosin filaments with the Z-disc of the sarcomere (Liang et. al., 2006). The length function is shown in Fig. 4.2.

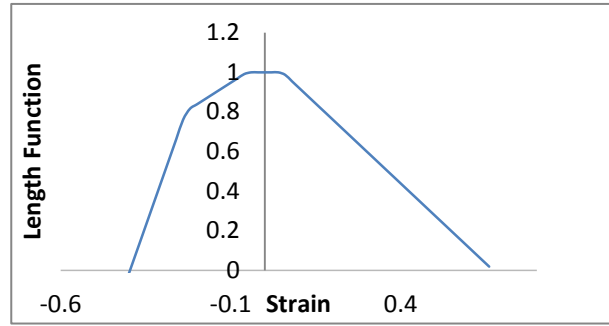


Figure 4.2 Length function vs. strain for the tentacle muscle.

Velocity function, f_v , is given as

$$f_v = \begin{cases} 1.8 - 1.8 \frac{1 + \dot{\epsilon}_m^*}{1 - 7.56\dot{\epsilon}_m^*/k} & \dot{\epsilon}_m^* < 0 \\ \frac{1 - \dot{\epsilon}_m^*}{1 + \dot{\epsilon}_m^*/k} & \dot{\epsilon}_m^* > 0 \end{cases} \quad (4.20)$$

where k is a constant, $\dot{\epsilon}_m^* = \dot{\epsilon}_m^0 / \dot{\epsilon}_{min}$, and $\dot{\epsilon}_{min}$ is a characteristic strain rate associated with the tentacle muscle. Fig. 4.3 describes a schematic velocity function against the strain rate of shortening (left side) or lengthening (right side) of the tentacle muscle.

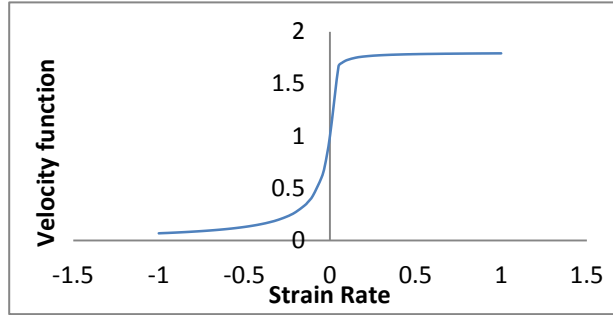


Figure 4.3 Velocity function vs. strain rate for the tentacle muscle.

Finally, the passive function is formulated as

$$\sigma_{pas}^m = \begin{cases} 0 & \epsilon_0^m \leq 0 \\ c_1(\epsilon_0^m)^{c_2} & 0 < \epsilon_0^m < \epsilon_c \\ c_3\epsilon_0^m + c_4 & \epsilon_0^m \geq \epsilon_c \end{cases} \quad (4.21)$$

Where ϵ_c is called critical strain. c_i are summarized in Table. 4.1.

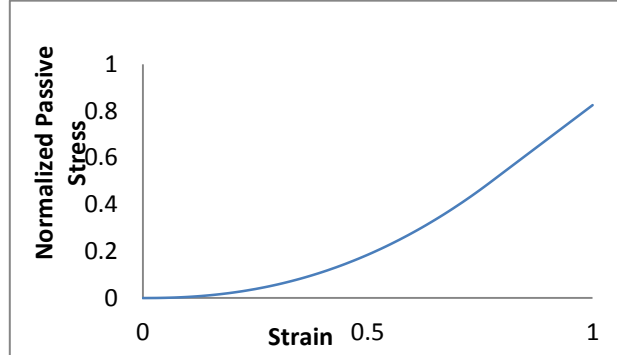


Figure 4.4 Normalized Passive Stress function vs. strain for the tentacle muscle.

All the parameters, functions, and equations used in this chapter to simulate the tentacle extension are from van Leeuwen and Kier work (1997).

Table 4.1 Constant muscle parameters used in this study, their units and values.

Parameter	Unit	Value	Parameter	Unit	Value
t_d	ms	0.0	ε_c	-	0.773
t_a	ms	40	ε_5	-	-0.4
ρ	Kg/m ³	1050	D_{act}	-	0.68
l_z	μm	0.06	D_{myo}	-	1.90
l_{bz}	μm	0.14	C_{myo}	-	0.44
c_1	kPa	0.887	q	-	15
c_3	kPa	1450	k	-	0.25
c_4	kPa	-625	c_2	-	2.26

Table 4.2 Parameters vary linearly from the base to the end of the stalk.

Parameter	Unit	At stalk base	At stalk end
σ_{max}	kPa	161	70
$\dot{\varepsilon}_{min}$	s ⁻¹	-30	-55
l_{act}	μm	1.21	0.73
l_{myo}	μm	0.97	0.5

4.2. UMAT Verification

To verify the UMAT and observe the material model behavior, two types of tests were performed:

- 1) Convergence test which was done by varying the number of elements in a FE model.
- 2) Same FE model was used to simulate the extension of a squid fish tentacle.

All analyses were performed using the dynamic implicit version of ABAQUS. Nonlinear Geometries Effects (NLGEOM) was considered in all simulations. And also, quadratic brick elements were used in the models.

4.2.1. Convergence Test

In the first step, a FE was generated as shown in Fig. 4.5 similar to Spyrou and Aravas (2011) test setup.

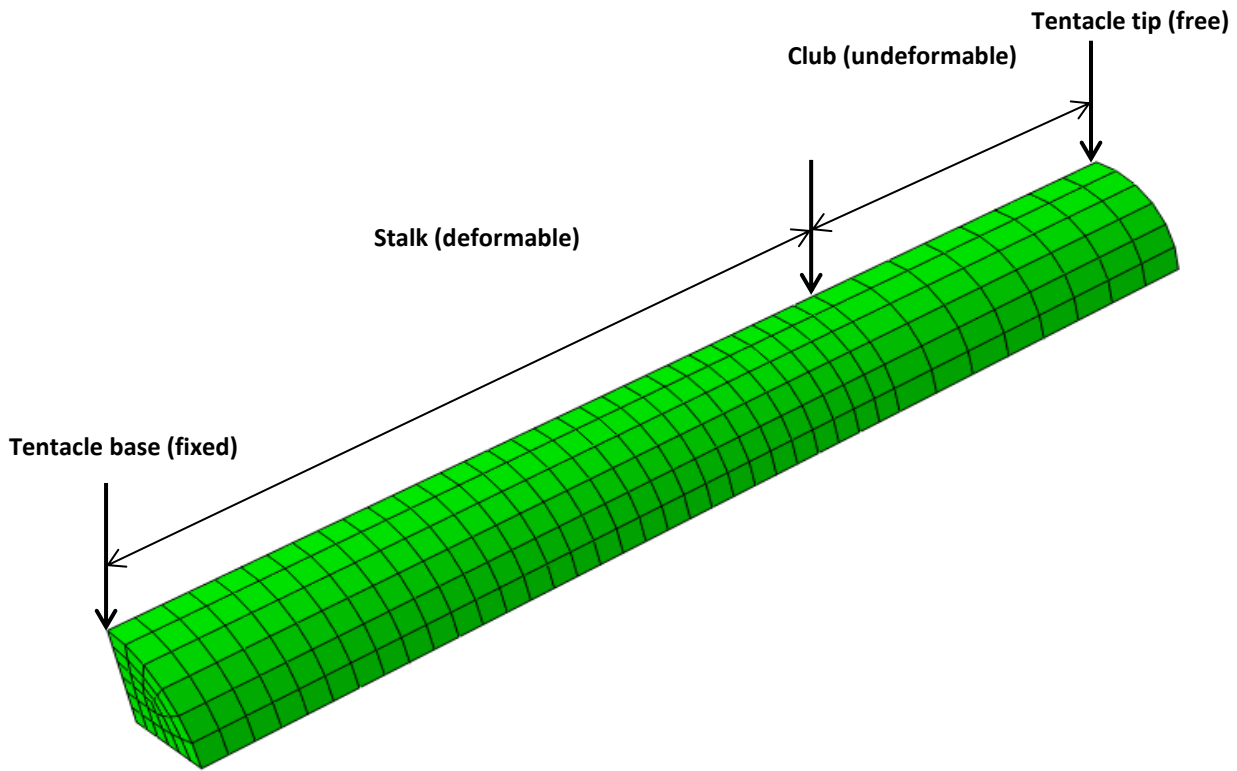


Figure 4.5 Squid fish tentacle test set-up. Tentacle base is fixed, while its end is free to extend. Club is considered as undeformable body, whereas stalk is deformable. Number of elements along the stalk length is changed to check the convergence of the developed material.

This model was also used in Section 4.2.2 to investigate the contraction of the tentacle muscle in the squid fish model. Tentacle consists of a deformable part called Stalk, and an undeformable part called Club. Tentacle base was fixed and its tip was free to contract or extend. UMAT was assigned to the stalk and elastic material properties were assigned to the club (High Young modulus was chosen to resemble the club as a rigid body in comparison to the stalk). Fig. 4.6 represents a schematic view of a squid fish in general, and its tentacle structure in particular.

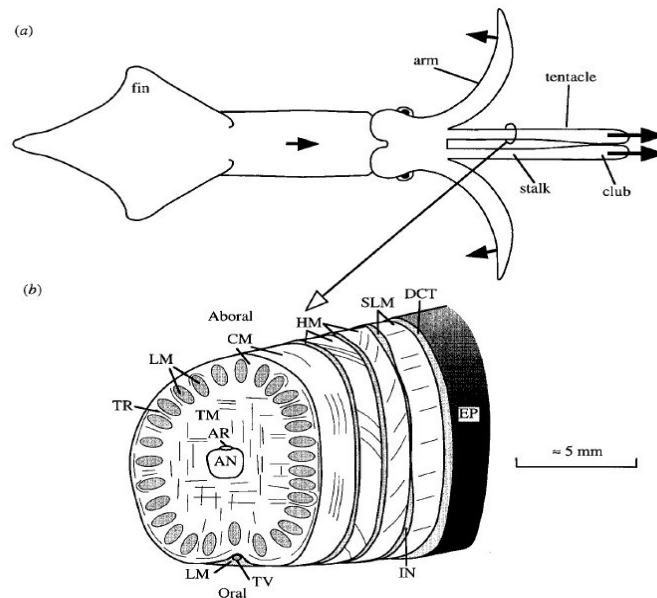


Figure 4.6 (a) Diagram of a squid. **(b)** Diagram of the morphology of the tentacular stalk in squid with its muscle groups (Van Leeuwen and Kier, 1997).

Symmetric boundary conditions were assigned to the model because only one quarter of the tentacle was modeled. No external load was applied to the tentacle and running time was 55 milliseconds.

To investigate the convergence of the material model, number of elements in the longitudinal direction of stalk was chosen to change. A path was defined from the tentacle base to its end (Fig. 4.7). Figs 4.8, 4.9 show the tentacle tip length and strain change along the defined path. As it is shown in Fig. 4.8, the tentacle displacement along the path remained constant by increasing the number of elements (decreasing mesh size). The velocity of tentacle along the path in the models with different numbers of elements followed the same pattern (Fig. 4.9).

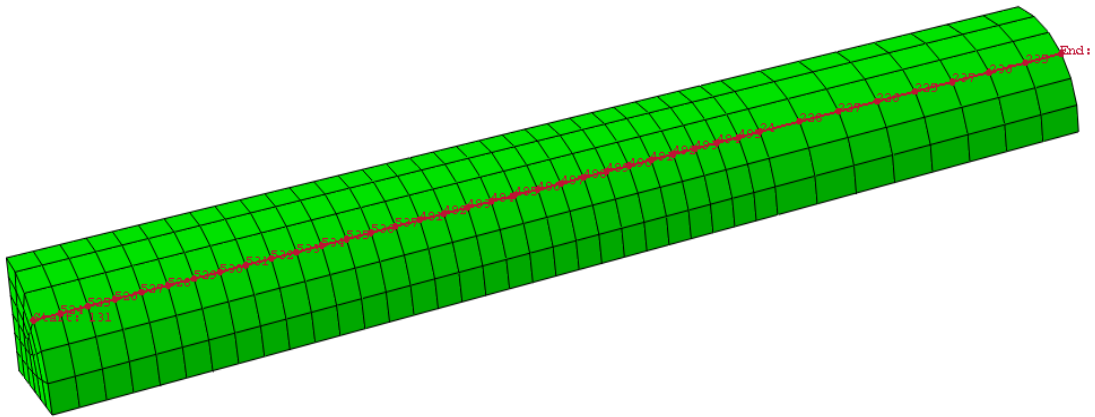


Figure 4.7 Defined path from tentacle base to the end.

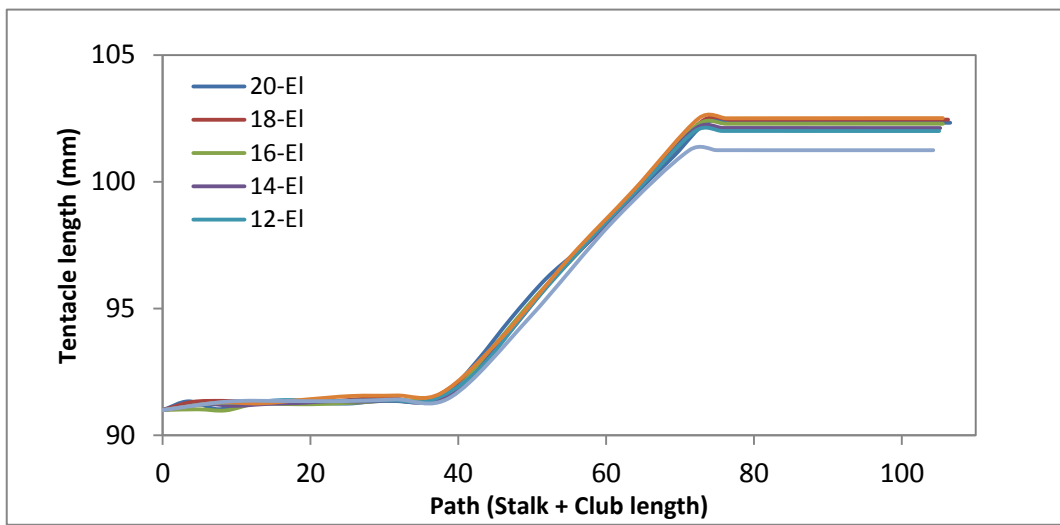


Figure 4.8 Position of the nodes along the defined path at t=55 msec.

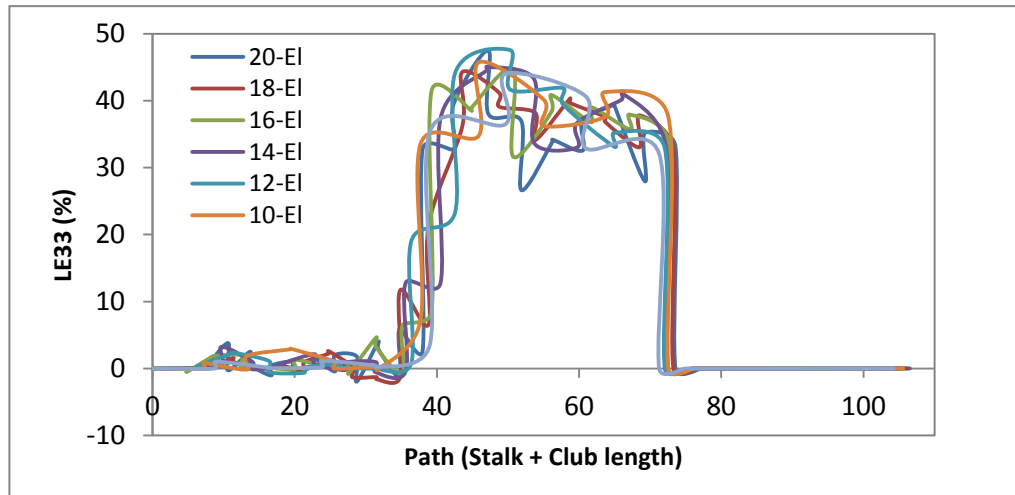


Figure 4.9 Tentacle tip longitudinal strain at $t=55$ msec along the defined path.

Providing the user with access to the level and pattern of activation of the muscle is one of the advantages of this continuum method of muscle modeling using UMAT subroutine. The maximum activation level (See Eq. 4.26 and Fig. 4.1) was changed from 0.25 (25%) to 1 (100%) and its effect on the total reaction force in the base of the tentacle is shown in Fig. 4.10. As the peak activation increased, maximum reaction force increased as well. Moreover, the force reached its maximum faster as the activation level increased.

The effect of different activation level on the tentacle tip displacement is also shown in Fig. 4.11. The tentacle tip extended more by increasing the activation level.

Regarding the activation function (pattern), Periodic activation pattern was used in this dissertation. See Spyrou thesis for linear activation pattern (Spyrou, 2009).

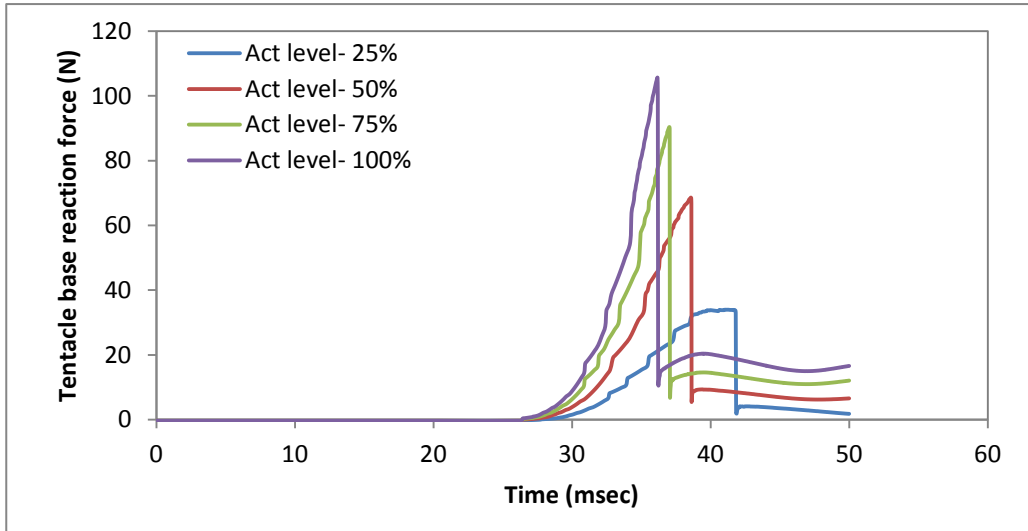


Figure 4.10 Reaction force in the tentacle base vs. time at different activation levels.

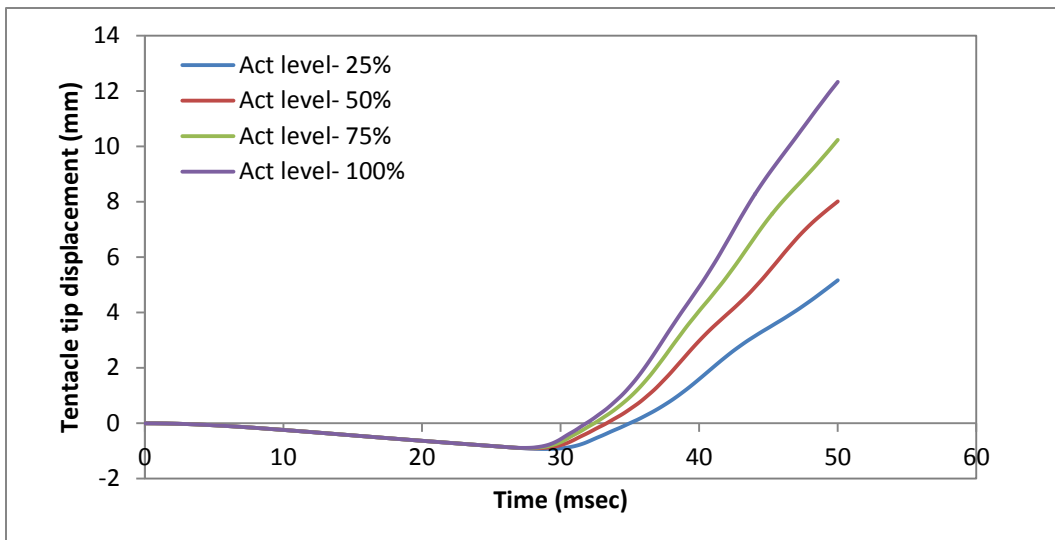


Figure 4.11 Tentacle tip displacement vs. time at different activation levels.

4.2.2. Extension of a Squid Tentacle: Validation Test

Due to the lack of experimental data about the human musculature microstructure and ethical concerns about *in-vivo* tests on human subjects, and also, due to the similarity between the extension of squid fish tentacle during the strike to catch a prey and the human muscle fiber's contraction mechanisms, the extension of the tentacle has been studied both experimentally

and numerically in the relevant literature (van Leeuwen and Kier, 1997; Liang et al., 2006; Spyrou and Aravas, 2011).

FE configuration of the tentacle was shown in Fig. 4.5. The stalk of the tentacle was modeled as deformable body with the properties described in Section 4.1.

The shear modulus and Poisson's ratio of the connective tissue were considered 5 kPa and 0.499, respectively. The club was not involved in the elongation of the tentacle. Therefore, it was modeled as undeformable passive, homogeneous and elastic material.

Due to the symmetry of the tentacle structure, only one quarter of it was modeled. The tentacle base remained fixed during the extension, while its tip was free to elongate. No other boundary condition was imposed to the model.

Figs. 4.12-4.13 show a comparison between the results of the simulations done in this study and the experimental data reported by van Leeuwen and Kier (1997). The evolution of the tentacle length during a strike to catch its prey (Fig. 4.12), and the history of the velocity of the tentacle tip contraction (Fig. 4.13) predicted by the current work fell within 5 and 10% of the above mentioned experimental, respectively.

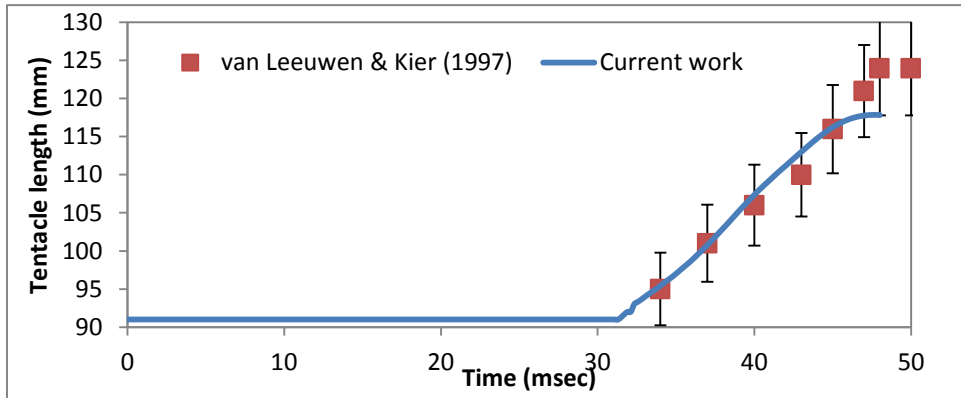


Figure 4.12 Tentacle length vs. time. Current work predictions fell within 5% of the experimental work done by van Leeuwen and Kier (1997).

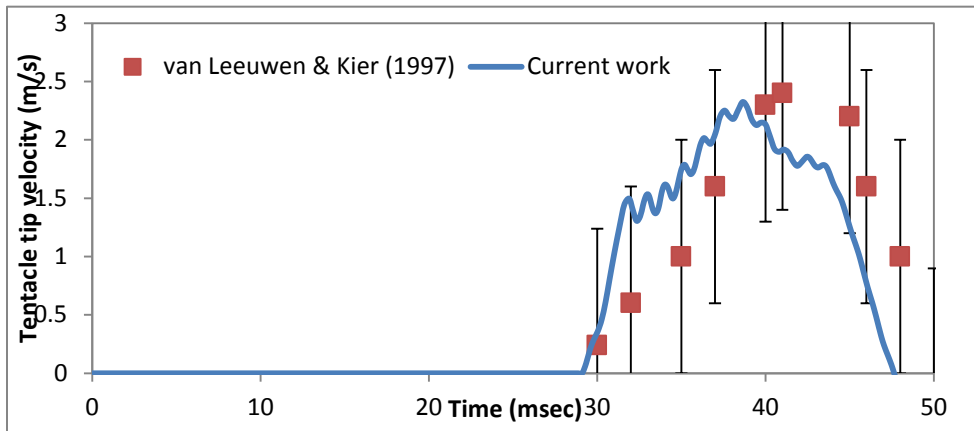


Figure 4.13 Tentacle tip velocity of contraction vs. time. Current work results are compared with the experimental data reported by van Leeuwen and Kier (1997).

Table 4.3 summarizes the values of the material properties (σ_{\max} , $\dot{\epsilon}_{\min}$) that were used in this dissertation. The difference between the values used in this work and those used in the previous works might be due to the changes that we made in the muscle constitutive law to make it adhere to the continuum mechanics basics as explained in Chapter Three. Other parameters are equal to the ones mentioned in Tables 4.1, 4.2

Table 4.3 Parameters vary linearly from the base to the end of the stalk (values used in this dissertation).

Parameter	Unit	At stalk base	At stalk end
σ_{\max}	kPa	-30	-16
$\dot{\epsilon}_{\min}$	s^{-1}	105	70

4.3. Summary of my Contribution

The developed UMAT in Chapter Three was used in this chapter. all the parameters used Section 4.1 were taken from the experimental and numerical works of van Leeuwen and Kier (1997). All the results presented in Section 4.2 were the original work of my dissertation. The tentacle validation set-up FE model (see Fig. 4.5) was adopted from Spyrou and Aravas (2011) model for the sake of validation.

CHAPTER FIVE: GEOMETRY RECONSTRUCTION, MESH GENERATION, AND MATERIAL PROPERTIES

The geometry of the cervical spine is usually reconstructed from Computed Tomography (CT) and Magnetic Resonance Imaging (MRI) of the spine. CT images are usually preferred for reconstruction of the hard tissues (cortical and cancellous bones), while MR images are more precise for the reconstruction of soft tissues (IVDs, ligaments, and muscles). To generate 3D geometry from 2D images, the image processing software Mimics (Mimics Research 17.0, Materialise, Leuven, Belgium) and geometric modeling package Geomagic (Geomagic Studio 2014, 3D Systems, USA) were used in this study. The geometry of the bony structures was reconstructed by master student Mr. Faisal Agah (Agah, 2016) from the CT and MR images of a 39-year old male subject provided by U.S. National Library of Medicine (the Human Visible Project: https://www.nlm.nih.gov/research/visible/visible_human.html) that were taken at 1 mm intervals in the axial plane. Further modifications in some parts were done by the author. For example, the collagen fibers were regenerated as well as the facets due to elements penetration problem. The MRI of the same subject was used to reconstruct the cervical muscles by the author. All the results presented in this chapter were based on the material properties and their units used on the published works of Mustafy and colleagues (Mustafy et al., 2014a, b; Mustafy et al., 2016). However, due to unit discrepancies in their work, stress unit was found to be wrong. To have a consistence set of units, stress unit must change from MPa to KPa.

5.1. Geometry Reconstruction

The CT or MR images were imported to the software Mimics. The boundaries of the tissues were selected from the images (segmentation process). By selecting the boundaries at each

slide, a mask was created. The contrast of soft tissues is usually insufficient comparing to the hard tissues. Therefore, it requires more accuracy and focus while selecting the boundaries. Otherwise, the penetration of nearby tissues may cause convergence problem in the FE solution. After editing the mask, the Calculate 3D feature was used to construct the geometry. Finally, in order to have a smooth and consistent surface, the geometry was imported to the Geomagic software. The spikes and holes were removed from the feature in the Geomagic environment.

5.2. Mesh Generation

The software Hypermesh (Hyperworks 12.0, Altair, USA) was used to mesh the cervical spine components.

5.2.1. Bony Structures

The vertebral bodies were modeled by separating the thin dense layer of the cortical bones (including endplates and facets) from the cancellous bone which has a spongy structure and is located at the core of each vertebra. 3-nodes shell elements (S3) with 1 mm thickness and 4-nodes solid elements (C3D4) were assigned to the cortical and cancellous bones, respectively (Fig. 5.1a). Also, 3- and 4-node shell elements (S3, S4) were assigned to the facets and endplates, respectively. Table (5.1) summarizes the number of elements in each bony component at different cervical spinal levels.

Table 5.1 Number of elements in bony components

	Skull	C1	C2	C3	C4	C5	C6	C7	T1
Cortical	34105	12192	12710	12929	14456	18744	14064	26401	39343
Facets	6123	10928	7432	3997	3218	3442	2548	3086	2098
Endplates	-	-	1848	3696	3696	3696	3696	3696	3696
Cancellous	-	119892	116035	100219	104828	132388	102872	187905	254617

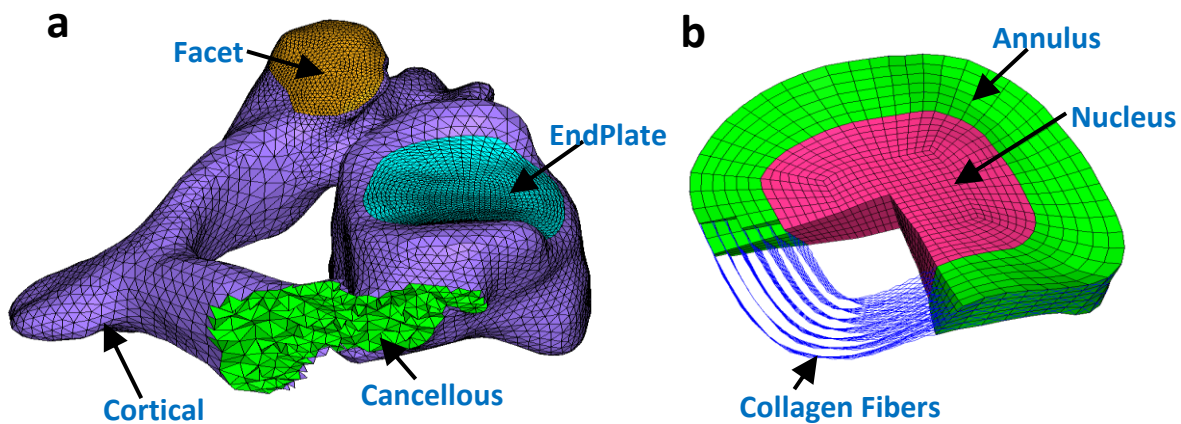


Figure 5.1 (a) Cervical vertebra bony components including cortical, cancellous, endplate, and facets. **(b)** The IVD components: annulus, nucleus, and 7 layers of collagen fibers.

5.2.2. Ligaments

The 2D geometry of the Upper Cervical Spine (UCS) ligaments: Anterior Atlanto-Occipital Membrane (AAOM), Alar, Apical, Posterior Atlanto-Axial Membrane (PAAM), Posterior Atlanto-Occipital Membrane (PAOM), and the Lower Cervical Spine ligaments: the Anterior Longitudinal (ALL), the Capsular (CL), the Ligamentum Flavum (LF), the Interspinal (ISL), the Intertransverse (ITL), the Posterior Longitudinal (PLL), and the Supraspinal (SSL) were constructed using surfaces connecting the origin and insertion points of the ligaments to the

surrounding bony components. The information about the mentioned points was found in the anatomical and histological studies (Panjabi *et al.*, 1991a,b; Yoganandan *et al.*, 2001). The ligaments were meshed with one layer of 4-node tensile resisting membrane elements (M3D4) of 1 mm consistent thickness (Fig. 5.2) (Agah, 2016). Table 5.2 (a, b) shows the number of elements in each ligament at different cervical spinal levels.

Table 5.2a Number of elements in UCS ligaments

UCS Ligaments	Alar	Apical	AAOM	PAAM	PAOM
No. of El.	64	30	230	270	350

Table 5.2b Number of elements in LCS ligaments at each cervical level

	C23	C34	C45	C56	C67	C7T1
ALL	56	144	180	160	130	192
CL	855	1300	1480	1434	1160	1600
ISL	77	300	168	143	208	260
ITL	56	76	68	76	78	64
LF	82	288	313	256	288	264
PLL	36	160	252	240	144	192
SSL	32	44	36	40	44	44

5.2.3. IVD

The disc mesh was generated by extruding seven layers of 8-node solid elements (C3D8) between the two adjacent endplates. The annulus ground comprised the seven circumferential outer layers, while the nucleus pulposus comprised the inner layers (Schmidt *et al.*, 2007; El-Rich *et al.*, 2009; Naserkhaki *et al.*, 2016). The annulus was filled with 7 layers of Collagen Fibers (CF) using unidirectional nonlinear springs resisting tensile load only and organized in

concentric lamellae with crosswise pattern close to $\pm 35^\circ$ (Schmidt *et al.*, 2007; El-Rich *et al.*, 2009; Naserkhaki *et al.*, 2016) (Fig. 5.1b). The percentage of the volume of the annulus and the nucleus in each disc at each cervical spinal level is summarized in Table (5.3). Despite their uneven volume at different levels, each component has the same number of elements at each

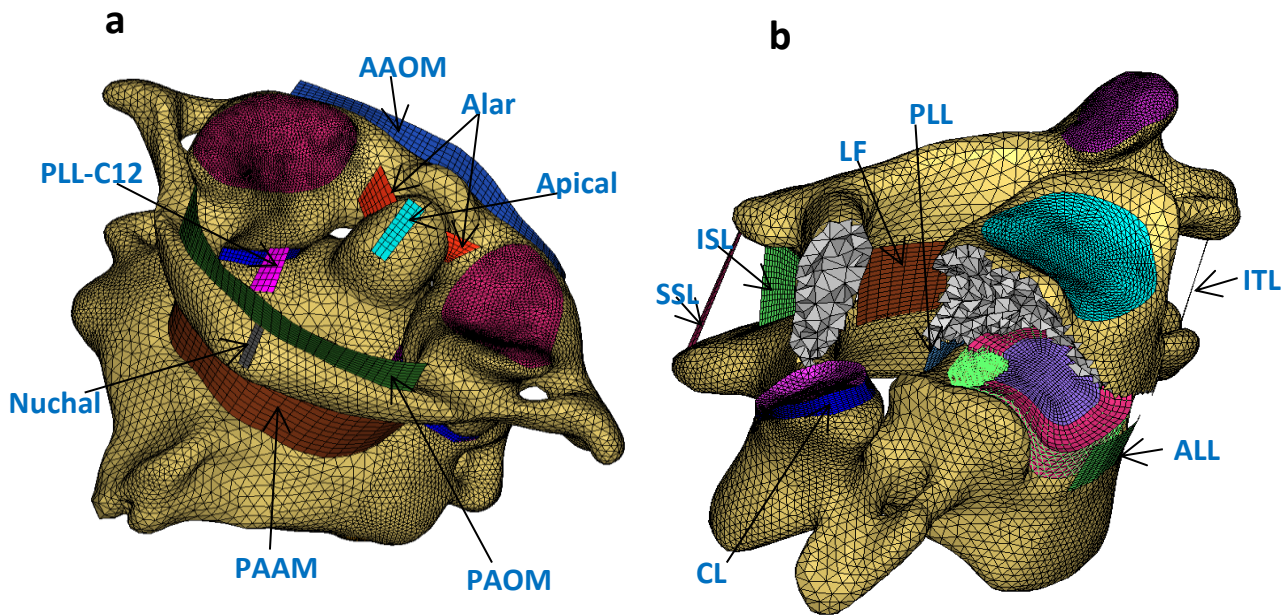


Figure 5.2 (a) The UCS ligaments: AAOM, Alar, Apical, Nuchal, PAAM, PAOM. **(b)** The LCS ligaments: ALL, CL, ISL, ITL, LF, PLL, SSL.

level (Table 5.4) (Agah, 2016).

Table 5.3 Percentage of annulus and nucleus volume out of disc volume (%)

Disc	Annulus	Nucleus
C23	41	59
C34	60	40
C45	49	51
C56	63	37
C67	58	42
C7T1	46	54

Table 5.4 Number of elements in disc components at different cervical spinal level

	C23	C34	C45	C56	C67	C7T1
Annulus	1680	1680	1680	1680	1680	1680
Nucleus	2490	2490	2490	2490	2490	2490
CF	3920	3920	3920	3920	3920	3920

5.2.4. Muscles and Tendons

The MR images of the same subject were used to reconstruct the cervical muscles. The 3D solid map feature of the software Hypermesh was used to create a solid by dragging the elements on the source geometry of the muscle (the muscle origin area or its attachment to the adjacent bone) to the elements on the destination surface (insertion area) along the surrounding surfaces. Three dimensional 8-node solid elements were assigned to the muscles. Due to the incompressible nature of the muscles, the Hybrid type of elements was used (C3D8H). The created muscles are upper Trapezius (TZ), Sternocleidomastoid (SCM), Splenius Capitis and Cervicis (SC), and Semispinalis Capitis and Cervicis (SSC) (Figs. 5.3a-5.3c). The Capitis and Cervicis are Latin words referring to the occipital bone and the neck. Therefore, the capitis muscles are attached to the head at their insertion points while the cervicis muscles are attached to the neck. In this study, the capitis and cervicis bodies of the Splenius and the Semispinalis muscle are combined but they are attached to their own insertion points via the tendons. Due to the poor quality of MR images existing in the Human Visible Project database, the deeper and smaller muscles were not constructed. However, the constructed muscles are among the biggest and most superficial spinal muscles comprising around 70% of the total mass of the cervical musculature as mentioned in Chapter Two. Moreover, the bigger the PCSA is, the

greater the amount of force produced by the skeletal muscle is. Therefore, the constructed muscles play more substantial role in the force generation process which is the main focus of this research than the deep ones.

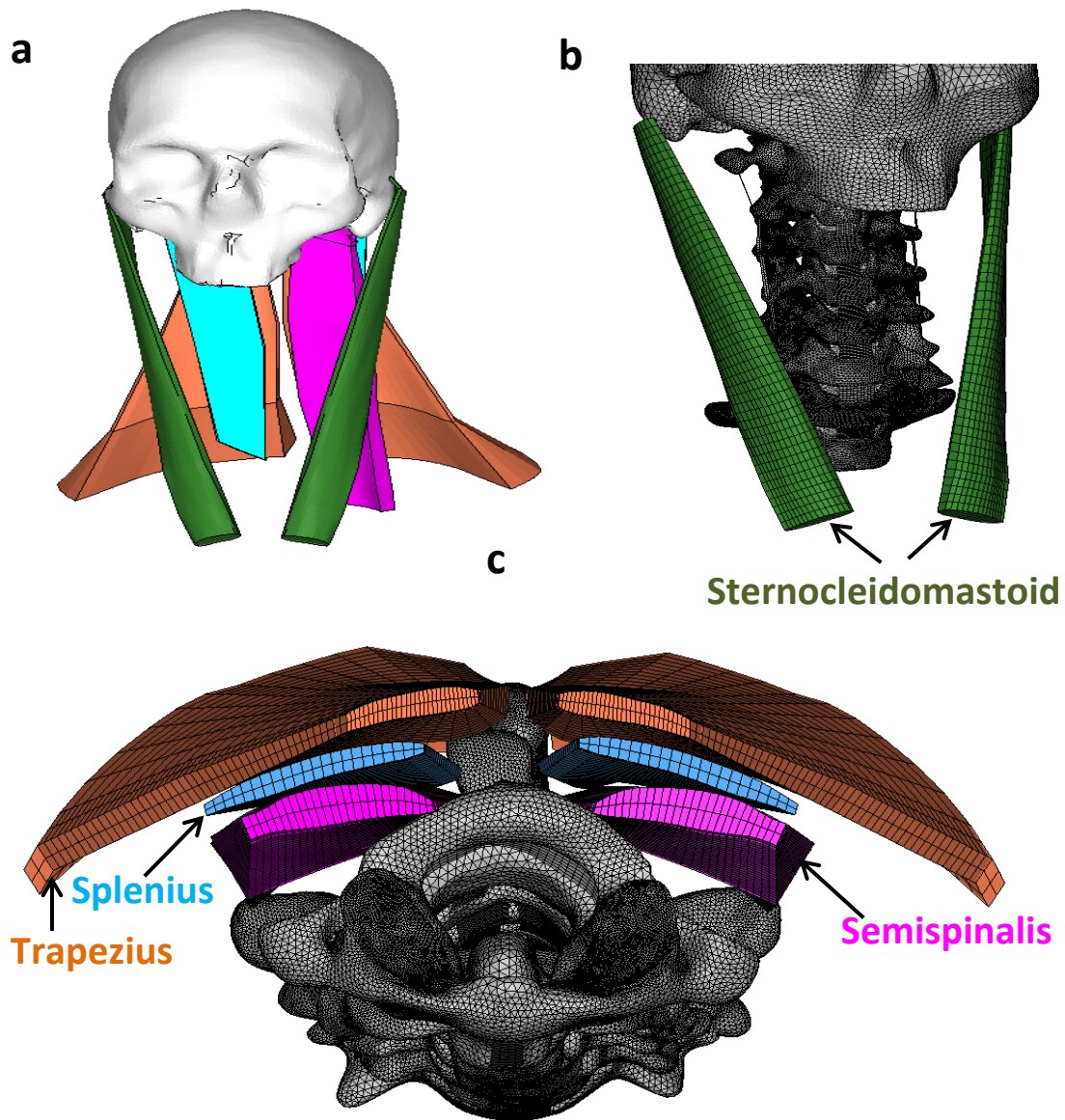


Figure 5.3 (a) An overall view of the cervical muscles. (b) Sternocleidomastoid (SCM) is located on the lateral sides of the cervical spine. (c) A schematic view of the cross sectional area of the muscles, Trapezius (TZ), Splenius (SC), and Semispinalis (SSC) located at the posterior side of the cervical spine.

The tendons were constructed as extensions to the constructed muscles in order to connect the muscles to the nearby bones, and were meshed using 4-node solid elements (C3D4).

Table 5.5 summarized the number of elements in each cervical muscle and the total number of elements in the tendons.

Table 5.5 Number of elements in the cervical muscles and tendons

Muscle	Trapezius	Sternocleidomastoid	Splenius (Capitis & Cervicis)	Semispinalis (Capitis & Cervicis)	Tendons
No. of El.	1440	1652	888	1696	1022

The whole ligamentous spine comprises of 1435765 elements, whereas the cervical spine with the muscles includes 1442463 elements in total.

The meshed geometry was next imported to the FE Solver ABAQUS (Simulia Inc.) for further analyses. The material properties were assigned to each section. Appropriate contact properties were defined and assigned to the various components. The boundary conditions and loading scenarios were also applied based on the existing experimental and numerical studies data that are explained in the next chapters with more details.

5.3. Material Properties

5.3.1. Vertebra

Johnson-Cook formulation for the isotropic symmetric strain rate-dependent elasto-plastic was assigned to all bony components:

$$\sigma = (a + b\varepsilon_p^n) \left\{ 1 + \ln \left(\frac{\dot{\varepsilon}}{\dot{\varepsilon}_0} \right) \right\} \quad (5.1)$$

where σ is the equivalent stress, a is the yield stress, b is the hardening modulus, n is the hardening exponent, ε_p is the plastic strain (true strain), $\dot{\varepsilon}$ is the current strain rate, and $\dot{\varepsilon}_0$ is the reference strain rate (Table 5.6). The Johnson-cook formulation is able to calculate von Mises hardening with ductile damage until potential rupture (El-Rich, *et al.*, 2009; Mustafy *et al.*, 2014). The equivalent stress behaves as a linear elastic material until it reaches the yield limit. At the onset of plastic deformation, it acts as a combination of both elastic and plastic materials.

Table 5.6 Material Properties of cervical spine bony components

Material Properties	Bony components					
	Cortical Ref.	Cancellous Ref.	Endplate Ref.			
Density (10^{-6} Kg/mm ³)	1.83	Lee et al., 2000	0.17	Ng and Teo, 2001	1.06	Panzer and Cronin, 2009
Young Modulus, E (MPa)	16800	Reilly et al., 1974	100		5600	
Poisson ratio, ν	0.3		0.29		0.3	
Yield stress, a (MPa)	110		1.92		6	
Hardening modulus, b (MPa)	100	El-Rich et al., 2009	20	El-Rich et al., 2009	100	El-Rich et al., 2009
Hardening exponent, n	0.1		1		1	
Failure plastic strain, (10^{-3}) ε_p	9.68		14.5		20	DeWit and Cronin, 2012
Max. stress (MPa)	155	Kopperdahl et al., 1998	2.23	Ochia et al., 2003	7.5	Kopperdahl et al., 1998
Strain rate coef., c	1	-	1	-	1	-

5.3.2. IVD

The linear homogenous isotropic elastic material properties were assigned to the nucleus and annulus in this study as presented in Table (5.7). The nonlinear elastic properties were also assigned to the collagen fibers (Shirazi-Adl *et al.*, 1986).

Table 5.7 Mechanical properties of disc components

	Density (10^{-6} Kg/mm^3)	Ref.	Young modulus, E, (MPa)	Ref.	Poisson 's ratio, v	Ref.
Nucleus	1	Lee <i>et al.</i>, 2000	1	Brolin and Halldin, 2004	0.4999	Brolin and Halldin, 2004
Annulus	1.2	Lee <i>et al.</i>, 2000	3	Kumaresan <i>et al.</i>, 1998	0.4	Kumaresan <i>et al.</i>, 1998
CF	Nonlinear elastic curve					Shirazi-Adl, <i>et al.</i>, 1986

5.3.3. Ligaments

An orthotropic nonlinear elastic material law was assigned to the UCS (Östh *et al.*, 2017; Mattucci *et al.*, 2013), and a viscoelastic material law, known as the Prony series, governed the LCS ligaments (Sadegh and Abraham, 2000; Mattucci *et al.*, 2012). The relaxation modulus is

$$G(t) = G_{\infty} + \sum_{i=1}^N G_i e^{-t/t_i} \quad (5.2)$$

where G_{∞} is the long-term shear modulus, G_i is the relaxation coefficient, and t_i is the time constants of the Maxwell elements. The progressive strain and stress failures were also considered for the ligaments (Tables 5.8a, 5.8b).

Table 5.8a Material properties of UCS ligaments

Orthotropic nonlinear elastic prop.	Density ($10^{-6}Kg/mm^3$)	Young modulus, E,(MPa)	Poisson's ratio, ν_{12}	Poisson's ratio, ν_{13}	Poisson's ratio, ν_{23}	Ref.
UCS ligaments	1	0.65-43	0.3	0.49	0.49	(Osth <i>et al.</i> , 2017; Mattucci <i>et al.</i> , 2012-15)

Table 5.8b Material properties of LCS ligaments

Viscoelastic Properties	Time dependent Prony series τ_i, G_i, t							Ref. (Sadegh and Abraham 2000)
	Young Modulus, E (MPa)	Poisson ratio, ν	Density ($10^{-6}Kg/mm^3$)	Update Coef., E1 (MPa/ms)	Update Coef., E2 (MPa)	Failure Strain, ϵ_1	Failure Strain, ϵ_2	
ALL	11.4	0.4	1	469.4	19	0.68	0.90	(Wagnac <i>et al.</i> 2012)
CL	7.7	0.39	1	3.6	0.6	1.75	1.85	(Yoganandan <i>et al.</i> , 1996; Wagnac <i>et al.</i> , 2012)
ISL	25.3	0.39	1	98.3	4.6	1.10	1.30	(Wagnac <i>et al.</i> , 2012; Kleinberger, 1993)
ITL	17.1	0.4	1	98.3	4.6	1.10	1.30	(Wagnac <i>et al.</i> , 2012; Yang and Kish, 1988)
LF	27.2	0.39	1	199.7	4.0	1.01	1.25	(Kleinberger, 1993; Wagnac <i>et al.</i> , 2012)
PLL	20.4	0.49	1	1432.1	83.5	0.38	0.50	(Kleinberger, 1993; Wagnac <i>et al.</i> , 2012)

5.4. Muscle and Tendon

The developed UMAT was used to govern the full musculature including both the active and passive behaviors of the muscle (the FMS model). The Ogden hyperelastic model governed the nonlinear stress-strain behavior of the passive musculature (the PMS model) (Hedenstierna and Halldin, 2008). In the Ogden material model, the strain energy function for the incompressible materials is expressed in terms of the principal stretches $\lambda_i, i = 1,2,3$.

$$W(\lambda_1, \lambda_2, \lambda_3) = \sum_{p=1}^N \frac{\mu_p}{\alpha_p} (\lambda_1^{\alpha_p} + \lambda_2^{\alpha_p} + \lambda_3^{\alpha_p} - 3) \quad (5.3)$$

where μ_p, α_p, N are material constants.

The tendons were elastic in this study (L. a. Spyrou and Aravas, 2011). Table (5.9) summarized the material properties of the passive muscles and the tendons.

Table 5.9 Material properties of passive musculature and tendons

Ogden Hyperelastic Parameters	μ_i	α_i	Ref.	Linear isotropic elastic properties	Young Modulus, E (MPa)	Poisson ratio, ν	Ref.
Passive Musculature	13337	14.5	Hedenstierna and Halldin, 2008	Tendons	1200	0.4999	Spyrou, 2009

CHAPTER SIX: LIGAMENTOUS CERVICAL SPINE RESPONSE (LOAD SHARING) UNDER FRONTAL AND REAR-END IMPACT LOADING SCENARIOS: A 3D FINITE ELEMENT STUDY

6.1 Problem Description

Finite Element (FE) studies allow for the investigation of how the cervical spine responds under different impact loading scenarios. The objective of this study is twofold: 1) to develop and validate a detailed ligamentous cervical spine; and, 2) to investigate how it responds to frontal and rear-end impacts. The 2D cervical ligaments constructed in this study allow for an evaluation of the distribution of stress and strain in the ligaments. The study also analyzes spinal tissues failure stress and strain. The concept of strain energy is used to represent the spinal load sharing among the cervical components at different spinal levels.

Chapter Five contained the geometry construction, mesh generation, and material properties of the cervical spine model. Fig. 6.1 provides an overall view of the model and its individual components. All the results presented in this chapter were based on the material properties and their units used on the published works of Mustafy and colleagues (Mustafy et al., 2014a, b; Mustafy et al., 2016). However, due to unit discrepancies in their work, stress unit was found to be wrong. To have a consistence set of units, stress unit must change from MPa to KPa.

6.2 Solution Techniques, Loading and Boundary Conditions

The Dynamic Implicit Solver of Abaqus (Abaqus 6.13-4, Dassault System Simulia, USA) was used to conduct the analyses in this study. Simulations were performed using Compute Canada facility (WestGrid, Jasper platform).

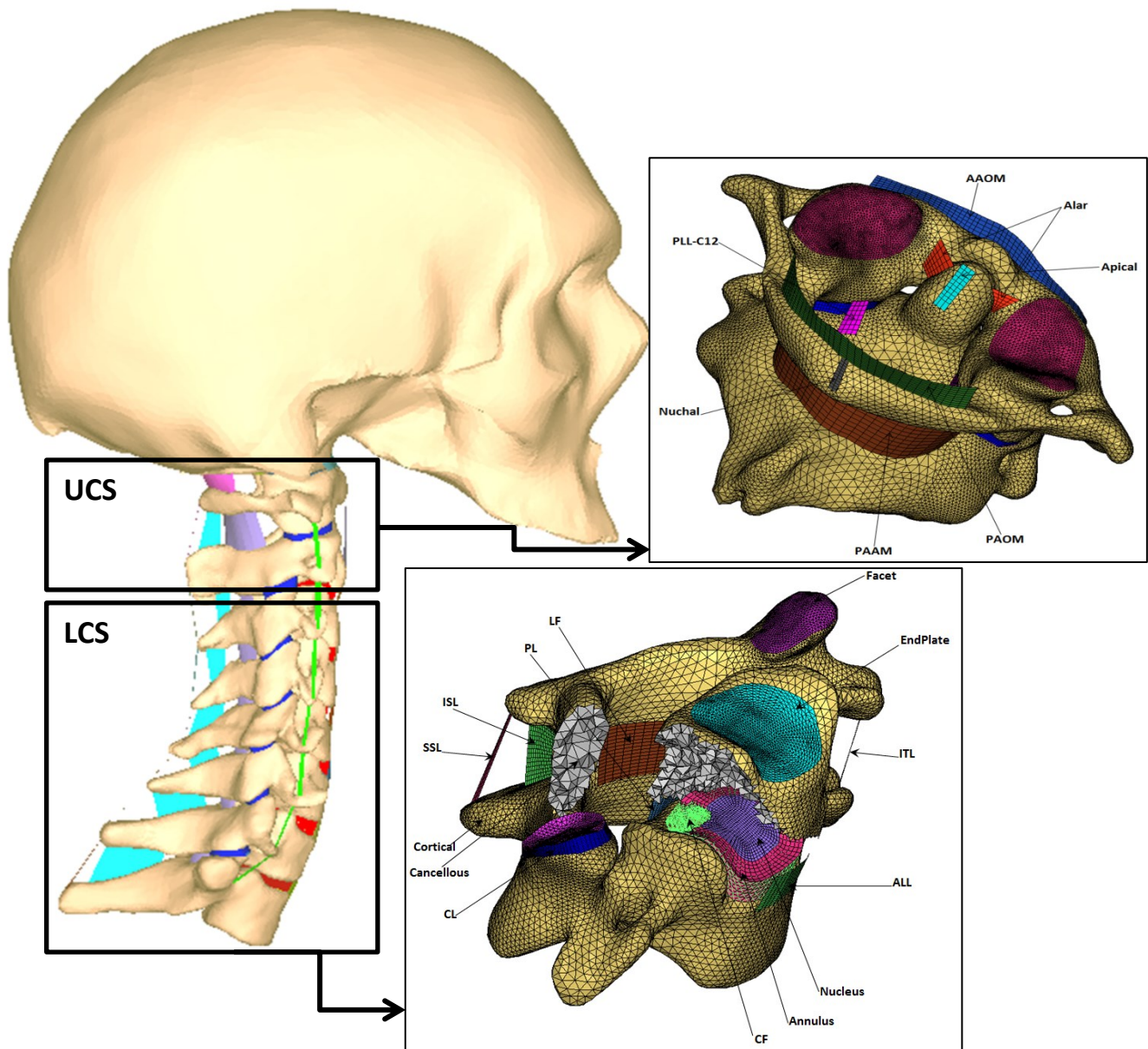


Figure 6.1 A general view of the cervical spine (left), a detailed view of the Upper Cervical Spine (UCS) and the Lower Cervical Spine (LCS) (right up and down, respectively).

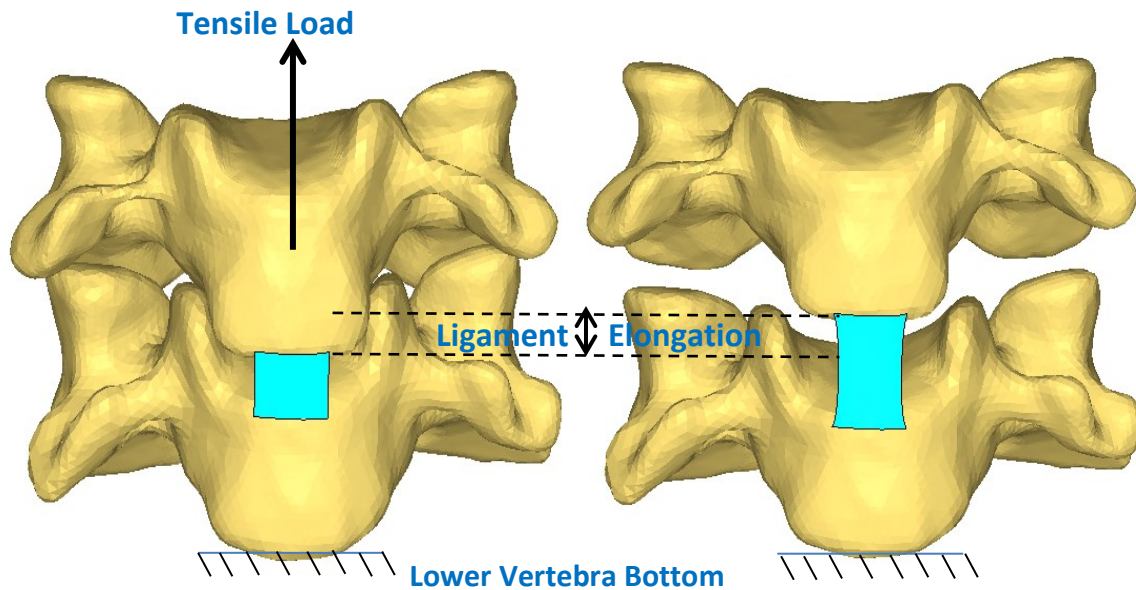


Figure 6.2 Loading test setup for the ligament validation test (ALL). Same setup is used of the other ligaments: CL, ISL, LF, and PLL.

6.2.1 Model Validation Tests

To validate the model, two types of analyses were performed. First, the force and strain in each cervical ligament at all cervical levels were predicted using FE models of Functional Spinal Units (FSU). The FSUs are made of bone-ligament-bone structure. Second, the overall kinematics of the head and the neck were validated using a detailed FE model of the entire head and neck.

6.2.1.1 FSU Validation

The force and elongation up to failure level for each ligament at each cervical spinal level at medium (20 s^{-1}), and high (150 s^{-1}) strain rates were determined by subjecting the cervical FSU to tensile load (Mattucci *et al.*, 2012; Mattucci and Cronin, 2015). Fig. 6.2 shows the C23 FSU used to assess the ALL ligament. The lower vertebra was fixed and the velocity was applied to the upper vertebra. In total, 25 FSUs were created and 50 analyses were completed in order

to investigate the effect of the medium and high strain rates on the behavior of the ligaments ALL, CL, ISL, LF, and PLL at cervical levels C23 to C67. The elongation of the ligament and the reaction force at the fixed endplate of the lower vertebra were measured and compared to the experimental values reported by Mattucci *et al.* (2012) (Fig. 6.3).

6.2.1.2 Cervical Spine Kinematics Validation

The ligamentous spine FE model was validated against existing data from various volunteer sled tests (Ewing *et al.*, 1976), Post Mortem Human Subject (PMHS) corridors (Stemper *et al.*, 2004), and numerical studies investigating head kinematics (Hedenstierna *et al.*, 2009; Östh *et al.*, 2017) under frontal and rear-end impact conditions. The loading scenarios consisted of:

- Frontal Impact of 15G peak acceleration (Ewing *et al.*, 1976)
- Rear-End Impact of 2.6 m/s (Stemper *et al.*, 2004).

To simulate rear-end and frontal impacts, periodic pulses were applied to the centroid of the T1 vertebra in anterior and posterior directions. The impulses were applied for 100 milliseconds. T1 was fixed to prevent movement in directions other than those under investigation. To avoid instability of the spine under compressive load in the absence of the cervical musculature, the gravity effect was ignored. However, a mass of 3.58 Kg was assigned to the centroid of the skull to consider the inertia effect (Carlsson *et al.*, 2014).

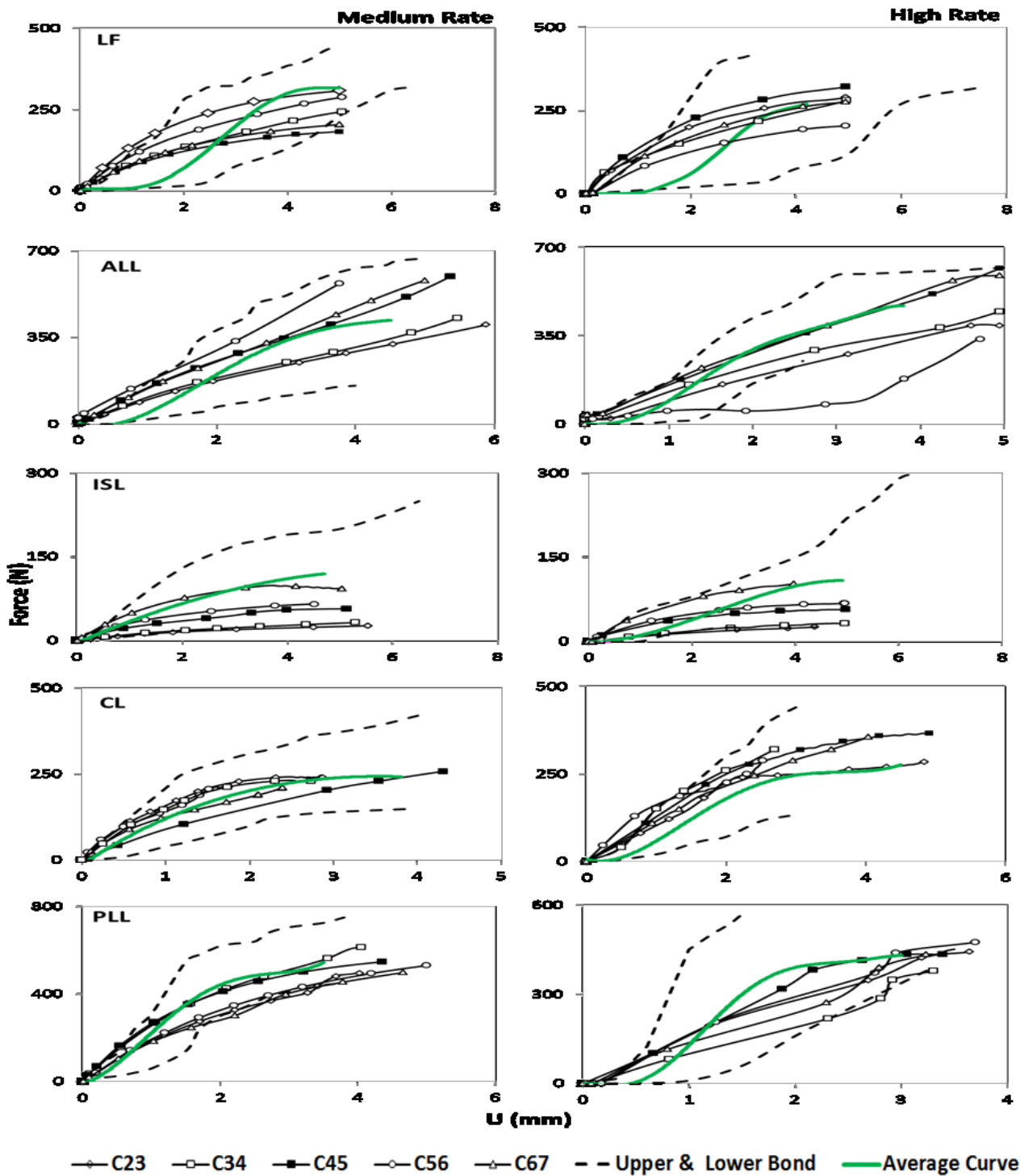


Figure 6.3 Failure force vs. elongation for the LF, ALL, ISL, CL, and PLL ligaments at medium ($20s^{-1}$), and high ($150s^{-1}$) strain rates. Average, Upper and Lower Bonds are from Mattucci experimental work (Mattucci et al. 2012). C23-C67 indicates the cervical spinal levels.

6.3 Results

6.3.1 FSU Validation Results

The nonlinear failure force and elongation curves of majority of the tested ligaments (ALL, CL, ISL, LF, and PLL) fell within the experimental corridors results reported by Mattucci *et al.* (2012) (Fig. 6.3).

6.3.2 Cervical Spine Validation in Frontal and Rear-End Impacts Results

The global head kinematics subjected to 15G frontal acceleration impact was compared with the volunteer corridors results (Figs. 6.4a, 6.4b). During the first 60 milliseconds, the anterior displacement of the head relative to the T1 is slightly stiffer than the experimental results. Specifically, within the time frame of 60 to 100 milliseconds the head moves steeper and faster than that reported in the volunteer sled test, and eventually goes beyond the upper bond of the experimental data as shown in Fig. 6.4a. The head rotation around x-axis with regard to T1 is roughly within the volunteer corridors upper bond (Fig. 6.4b).

The posterior displacement (Y-axis) and rotation of the head (X-axis) relative to the extension of the T1 were consistent with the results reported in PMHS tests (\pm SD) in 2.6 m/s rear-end impact condition (Figs. 6.4c, 6.4d).

6.3.3 Ligaments Injury Prediction using Stress Failure Criteria

To investigate ligament failure during frontal and rear-end impacts, the stress history of all ligaments at different spinal levels was measured and compared to the experimental data (Mattucci *et al.*, 2012). A comparison of the ligaments behavior in response to 15G frontal and rear-end impacts was undertaken. The results of these tests are shown in Figs. 6.5-6.9. The

thick blue horizontal lines in these figures show the failure level for each ligament reported by Mattucci and colleagues (Mattucci *et al.*, 2012). Additionally, the stress distribution of all elements for each ligament are plotted and presented in Appendix A to give the reader a sense of how multiple elements fail at specific times.

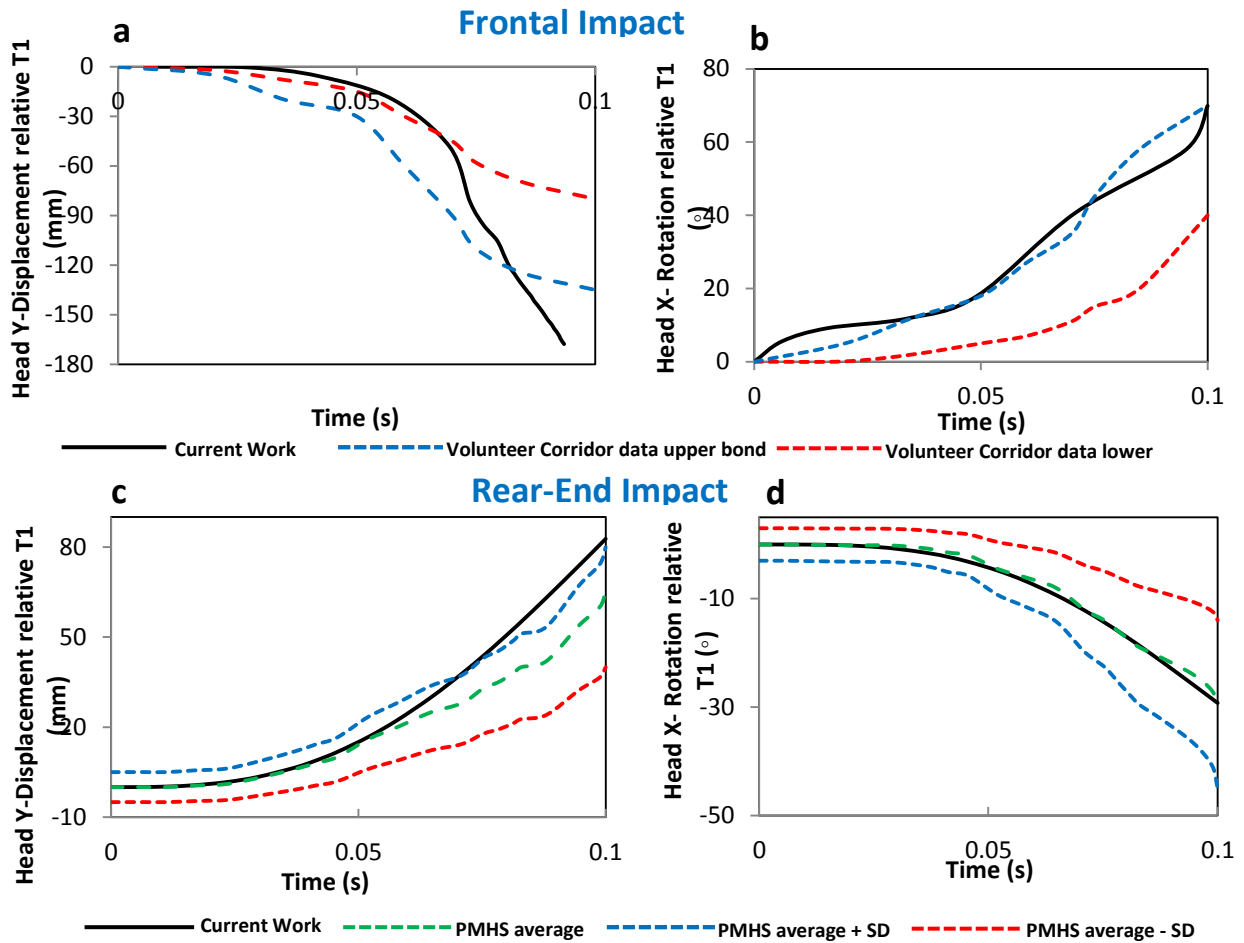


Figure 6.4 (a,b) Head relative T1 displacement (translation and rotation) results obtained from the current model validated against experimental data of the volunteer corridors (Ewing et al. 1976), and also is compared with the results reported in the previous numerical simulations during 15G frontal impact (Hedenstierna et al., 2009). **(c,d)** Head relative T1 displacement (translation and rotation) results obtained from the current model was validated against experimental data of Post Mortem Human Subject (PMHS) corridors (average response \pm 1 Standard Deviation (SD)) (Stemper et al., 2004), and also compared with previous numerical simulation results during a 2.6 m/s rear-end impact (Östh et al. 2017).

The model predicted no failure in the ALL ligament during the frontal impact, while during the rear-end impact, failure occurred at levels C45, C56, and C67. With the exception of level C23, the peak stresses for all levels resulting from rear impact were greater than values resulting from frontal impact (Fig. 6.5). The greatest stress was found at level C67 close to the end of the impact duration. Fig. 6.5 shows that levels C45, C56, and C67 reached failure at the same moment (83 milliseconds).

The CLL ligament reached failure at all cervical levels during both frontal and rear impacts. The maximum stresses occurred at levels C45 and C67 during frontal and rear-end impacts (250 MPa and 220 MPa, respectively). The upper levels reached failure earlier than the lower levels in both frontal and rear-end cases (Fig. 6.6).

The ISL ligament failed at all levels under the frontal impact, whereas failure only occurred at level C23 as a result of rear impact. At all levels, maximum stresses were higher for frontal impact than for rear impact. The peak stress occurred at level C56 in the frontal impact at 250 MPa. In addition, the upper levels experienced failure earlier (Fig. 6.7).

The LF ligament behavior was almost identical to that exhibited by the ISL ligament. Peak stress (150 MPa) occurred at level C23 at the end of the frontal impact (Fig. 6.8).

As a result of frontal impact, the PLL ligament failed at all levels; no failure was demonstrated as a result of rear impact. The maximum stress occurred at levels C34 and C45 (80 MPa). Level C34 reached failure first, followed by levels C45, C23, and C56, respectively (Fig. 6.9).

Figs. 6.10a, 6.10b contain the maximum stress values for the SSL and ITL ligaments at different spinal levels predicted by the current study. Results from the current study show that the SSL and ITL ligaments peak stresses are greater in conditions of frontal rather than rear impacts (the SSL ligament maximum stress is 90 MPa at level C45, and the maximum ITL stress is 34 MPa in the frontal impact). Experimental data on the failure stress values for these last two groups of ligaments does not exist.

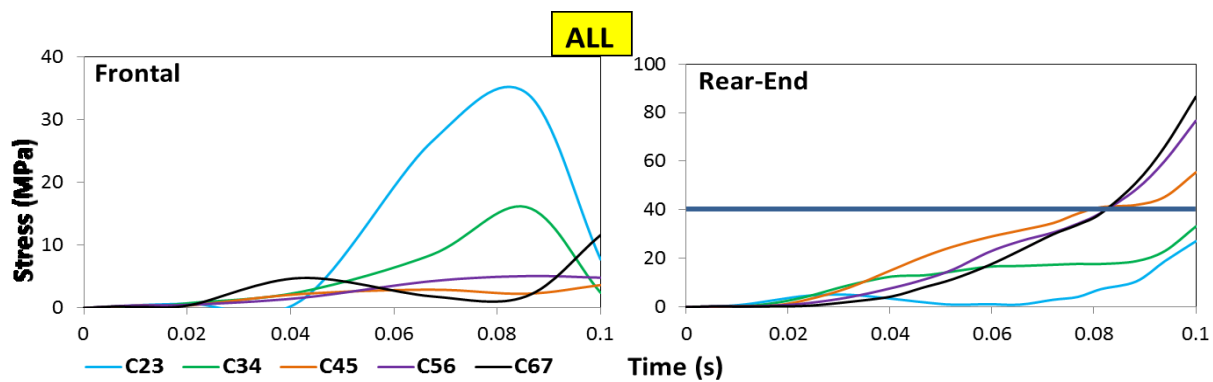


Figure 6.5 Sequences of failure in the ALL ligaments at different cervical spinal levels during 15G impact.

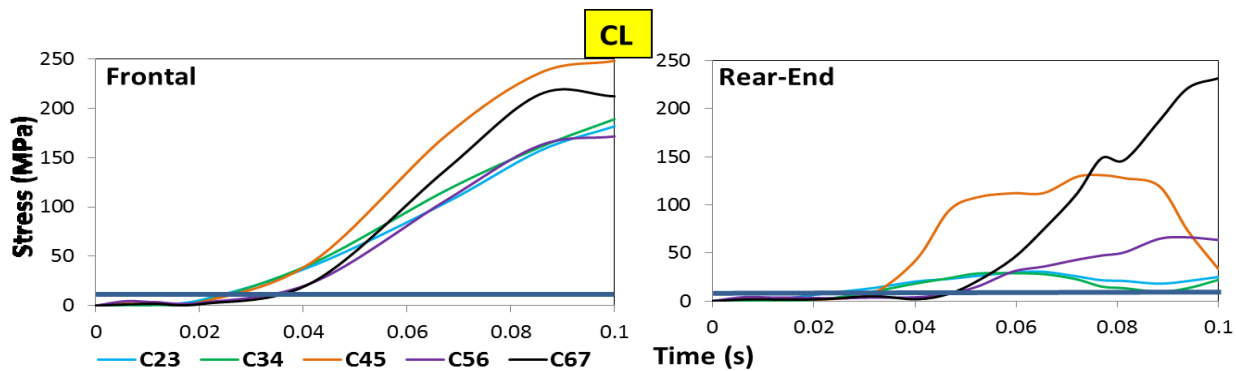


Figure 6.6 Sequences of failure in the CL ligaments at different cervical spinal levels during 15G impact.

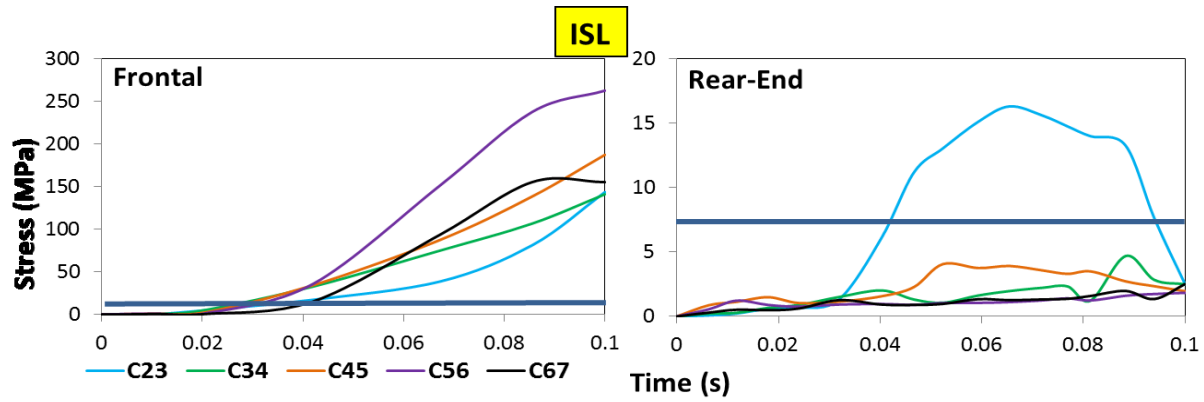


Figure 6.7 Sequences of failure in the ISL ligaments at different cervical spinal levels during 15G impact.

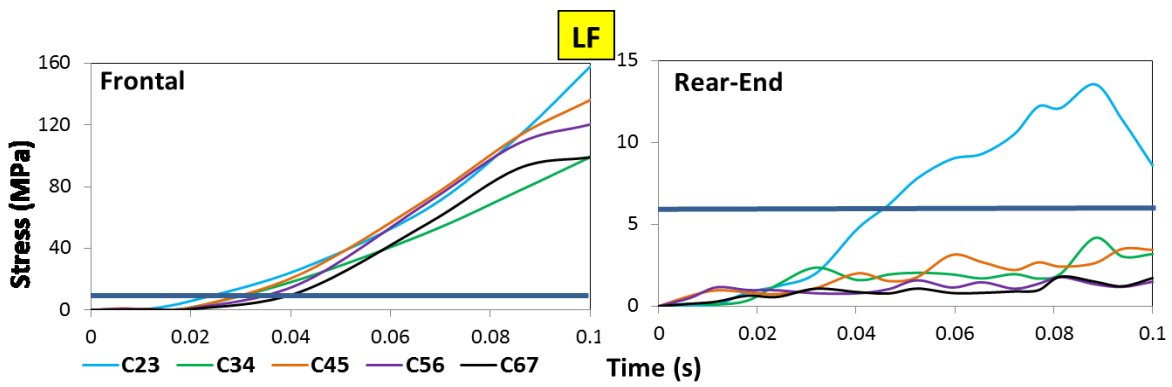


Figure 6.8 Sequences of failure in the LF ligaments at different cervical spinal levels during 15G impact.

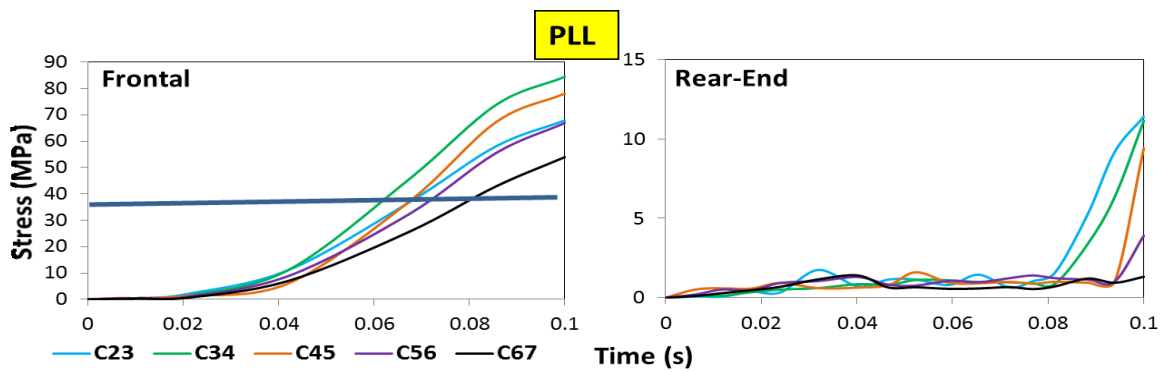


Figure 6.9 Sequences of failure in the PLL ligaments at different cervical spinal levels during 15G impact.

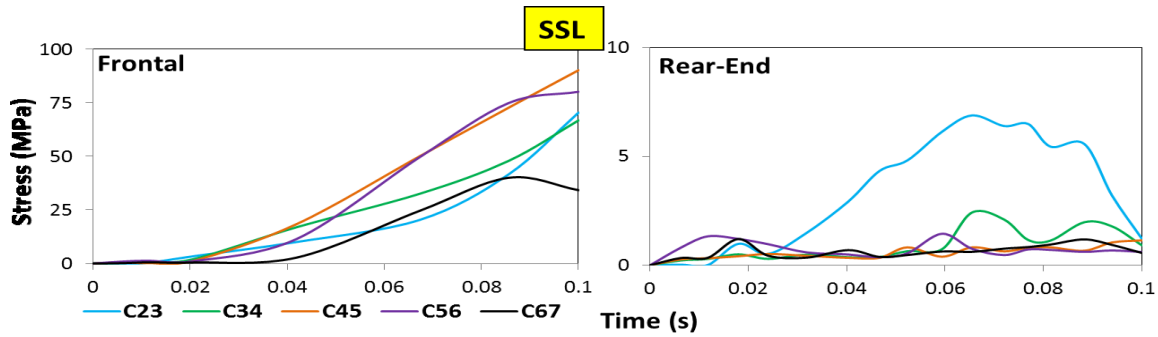


Figure 6.10 (a) The SSL ligaments peak stress at different cervical spinal levels during 15G impact.

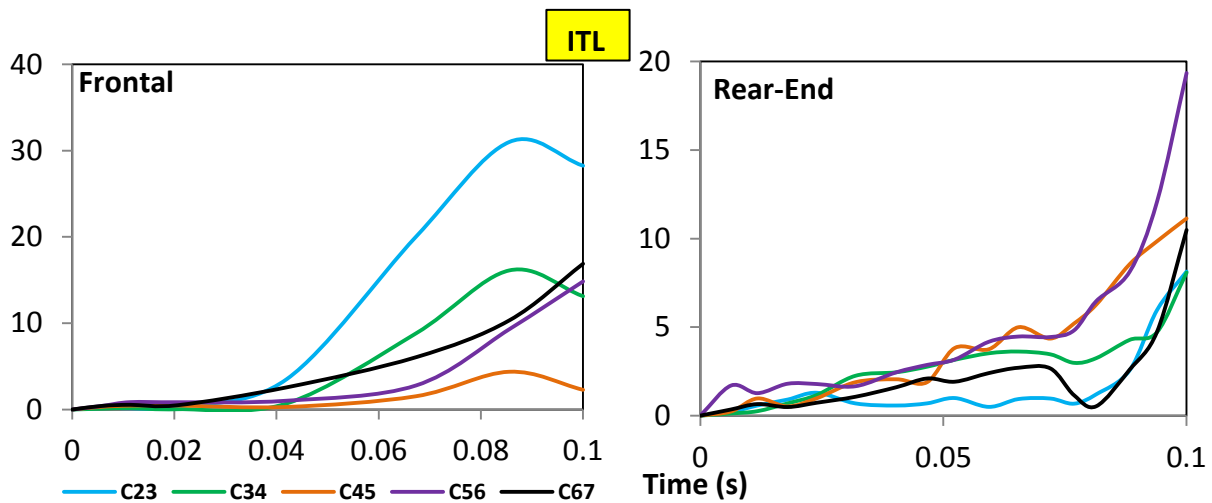


Figure 6.10 (b) The ITL ligaments peak stress at different cervical spinal levels during 15G impact.

6.3.4 Strain Distribution in Cervical Ligaments during 15G Frontal and Rear-End Impacts

For all ligaments, peak strains at different cervical levels were compared with numerical studies (Panzer *et al.*, 2011), see Fig. 6.11. Results of tests on all ligaments ALLs, PLLs, and ISLs (except at C67 level) show acceptable agreement with the reported values. The peak strain in the LF ligaments reported by Panzer and colleagues are greater than the values of the work herein discussed. As well, this model predicted higher values for the CL ligaments at all spinal levels than those reported by Panzer *et al.* (2011).

Unlike 1D spring elements, 2D elements show the distribution of stress and strain inside the ligaments. As shown in Figs. 6.12-6.15, the peak strain can occur in the middle of the ligament (not necessarily at the insertion points). The pictures on the left side were taken at the last increment in both frontal and rear impacts. The pictures located on the right side show the history of strain in each ligament at different spinal levels.

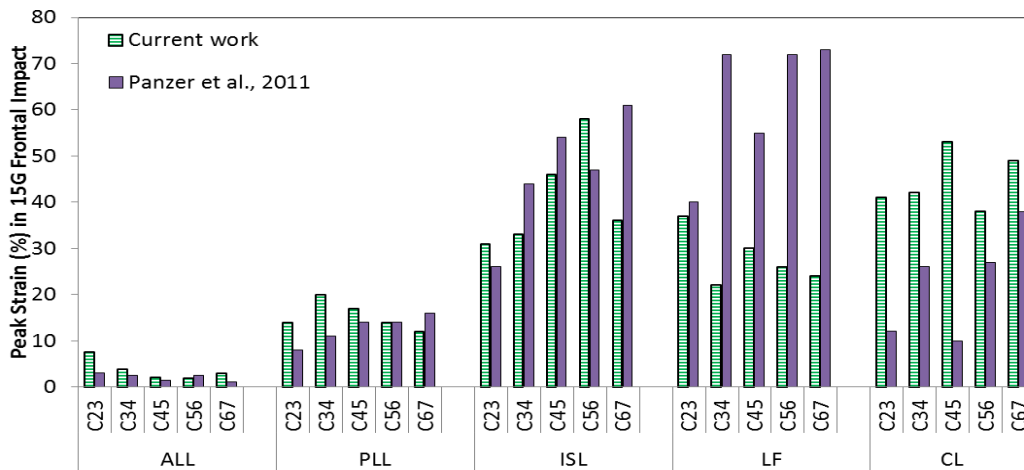


Figure 6.11 Peak strain in the cervical ligaments: the current work results are compared with Panzer et al. (2011) numerical study during 15G frontal impact loading scenario.

Maximum strain (%) in the ALL ligament was smaller during the frontal impact, than during the rear impact. Moreover, during the frontal impact the peak strain happened at level C23 at 85 milliseconds, whereas at level C67, the peak strain occurred at the end of rear impact (Fig. 6.12). Maximum strain for the CLL ligament at levels C45 and C67 happened at the end of the frontal and rear impacts, respectively (Fig. 6.13). Peak strain for the ISL ligaments occurred at level C56 during the end of the frontal impact duration. For level C23, this occurred at 75 milliseconds during the rear impact (Fig. 6.14). Level C23 was the site of maximum strain in the LF ligaments; this happened at the end of the frontal impact, and at 85 millisecond time point

during the rear impact (Fig. 6.15). The results for the peak strain of the other ligaments are presented in Appendix A.

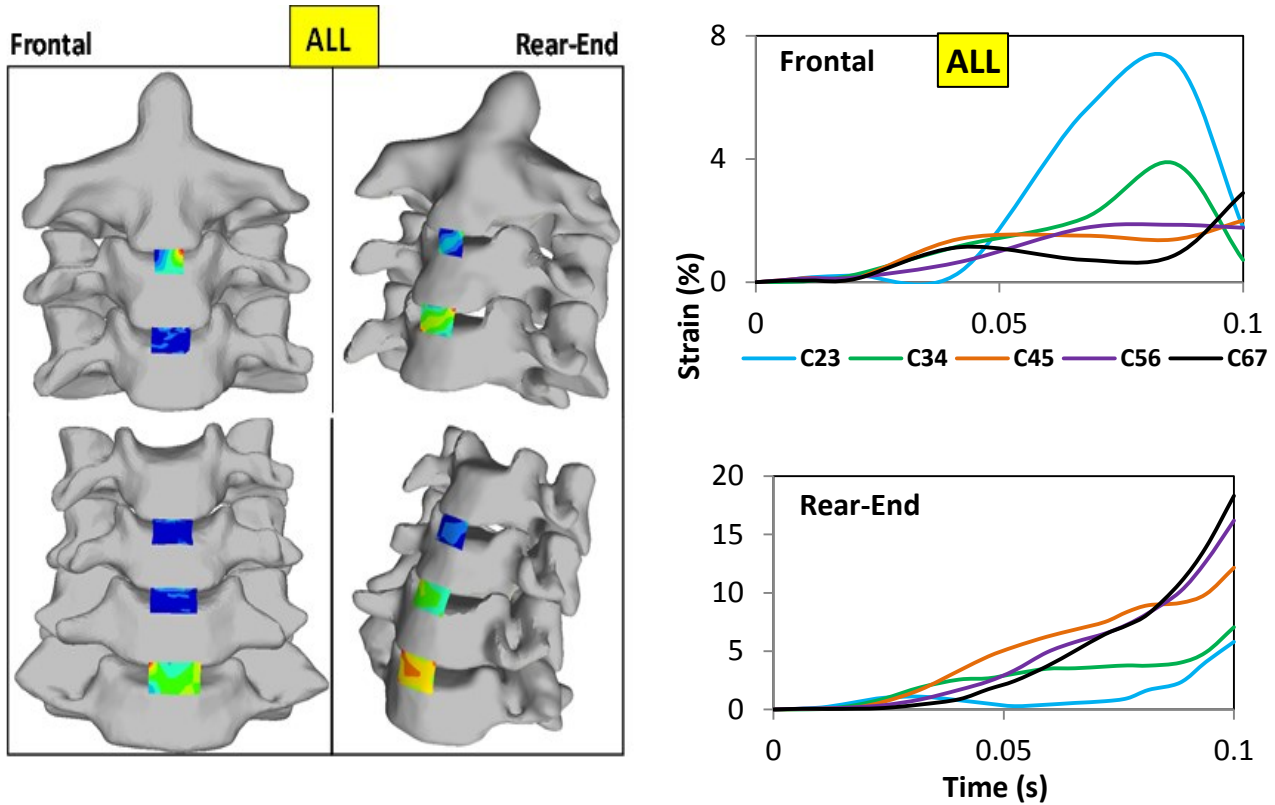


Figure 6.12 A schematic view of strain distribution in the ALL ligaments during 15G frontal and rear-end impacts captured at the time=0.1 s (Left side). Strain (%) vs. time in the ALL ligaments at different cervical levels during 15G frontal and rear-end impacts (Right side).

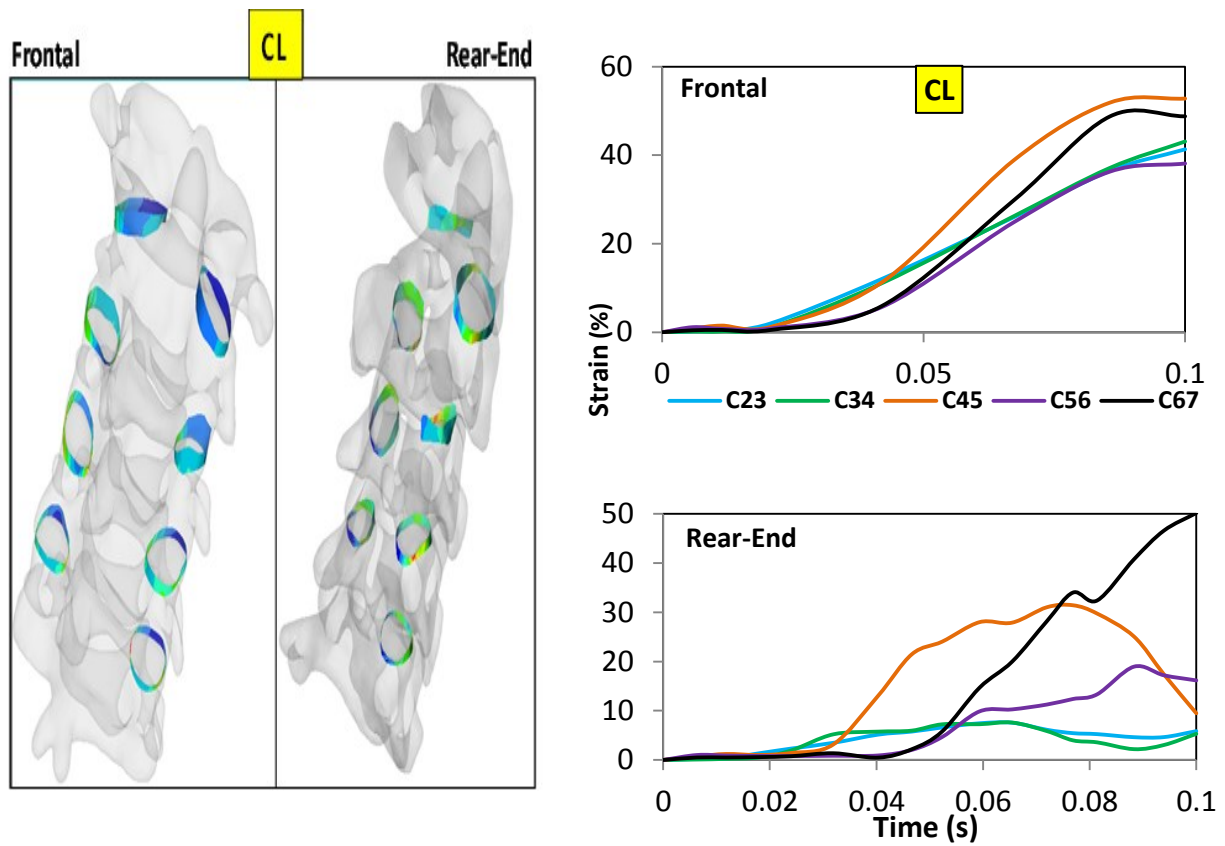


Figure 6.13 A schematic view of strain distribution in the CL ligaments during 15G frontal and rear-end impacts captured at the time=0.1s (Left side). Strain (%) vs. time in the ALL ligament at different cervical levels during 15G frontal and rear-end impacts (Right side).

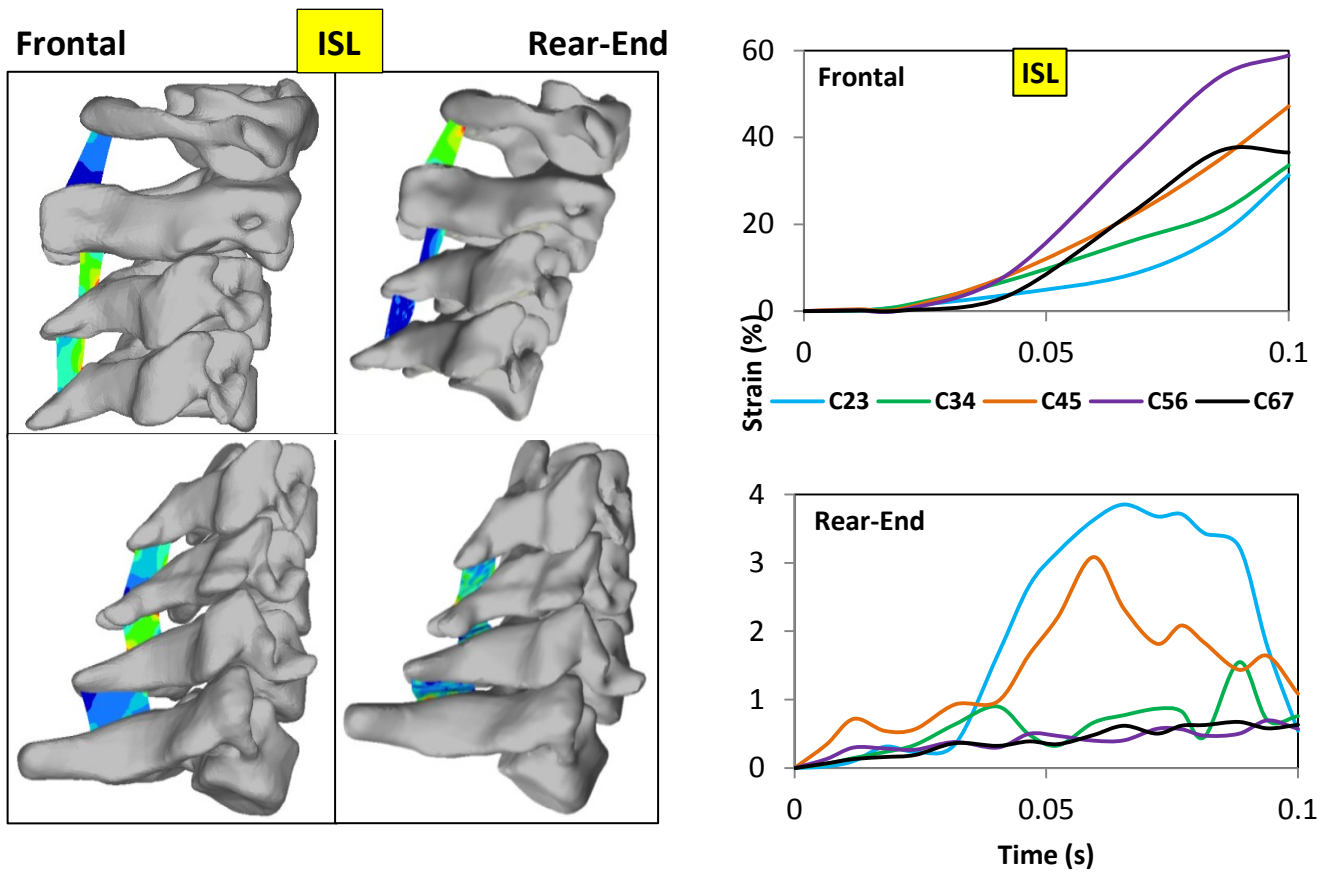


Figure 6.14 A schematic view of strain distribution in the ISL ligaments during 15G frontal and rear-end impacts captured at the time=0.1s (Left side). Strain (%) vs. time in the ALL ligaments at different cervical levels during 15G frontal and rear-end impacts (Right side).

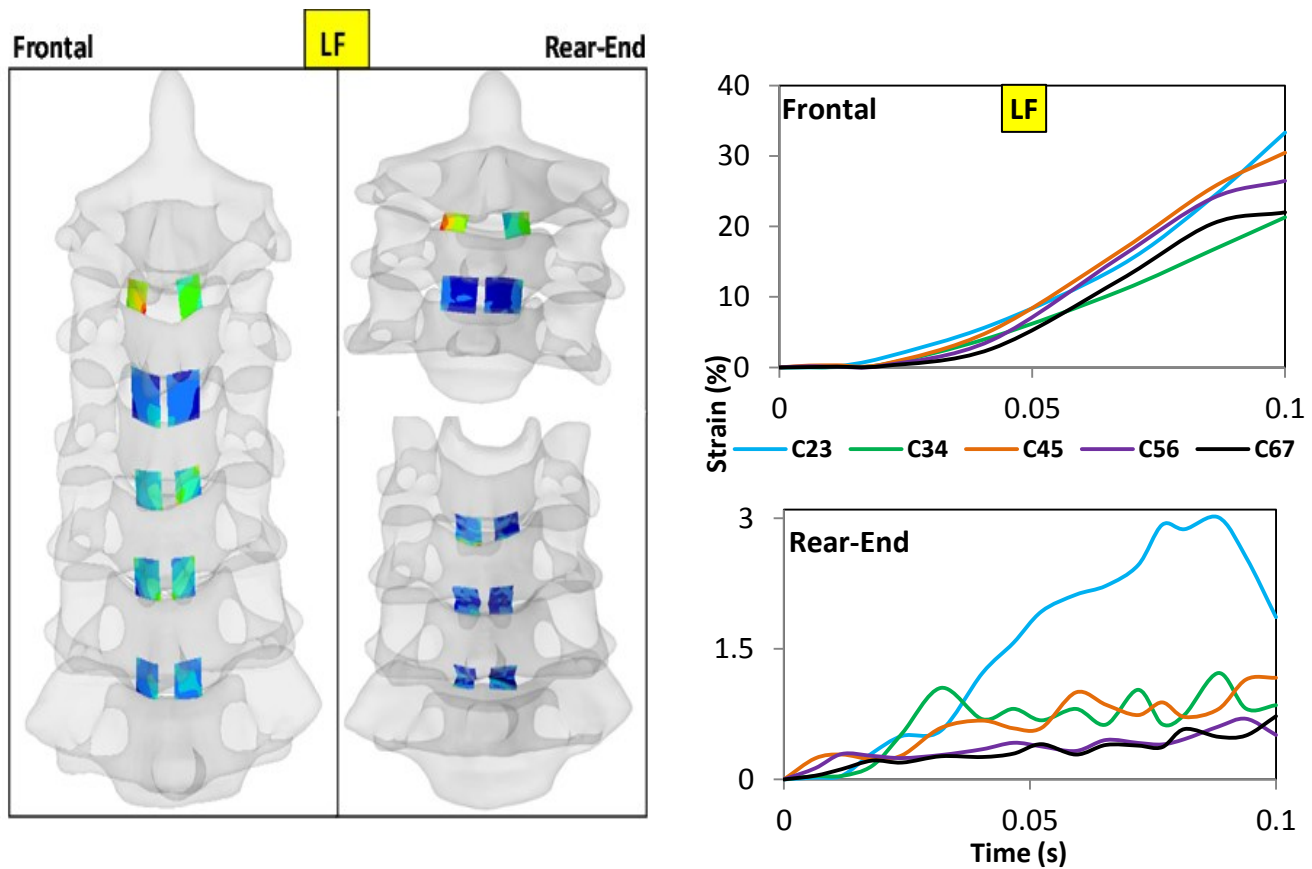


Figure 6.15 A schematic view of strain distribution in the LF ligaments during 15G frontal and rear-end impacts captured at the time=0.1s (Left side). Strain (%) vs. time in the ALL ligaments at different cervical levels during 15G frontal and rear-end impacts (Right side).

6.3.5 Contact Force and Pressure in Facet Joints

Contact force and pressure in Facet Joints (FJ) at various spinal levels were also measured during 15G frontal and rear-end impact scenarios (Fig. 6.16). The average contact pressure in the nodes that are in contact is reported here, as well as the peak contact pressure that occurred in those nodes. Measurements were taken in this way because the articular joint surfaces are not exactly parallel. No contact occurred at level C23 as a result of either frontal or rear impact. During the rear-end impact, contact occurred at all other levels. Conversely, as a result of frontal impact, no contact was found at levels C45, C67, or C7T1. Moreover, moving from level C12 toward the lower levels, peak contact force and pressure shifted to the end of the analysis time. The peak maximum contact pressure at level C12 at instant 61 milliseconds was 33.9 MPa, whereas the peak average contact pressure occurring in C56 level at 87 milliseconds was 4.65 MPa. Furthermore, the maximum contact force was 247 N; this occurred at level C7T1 at 87 milliseconds.

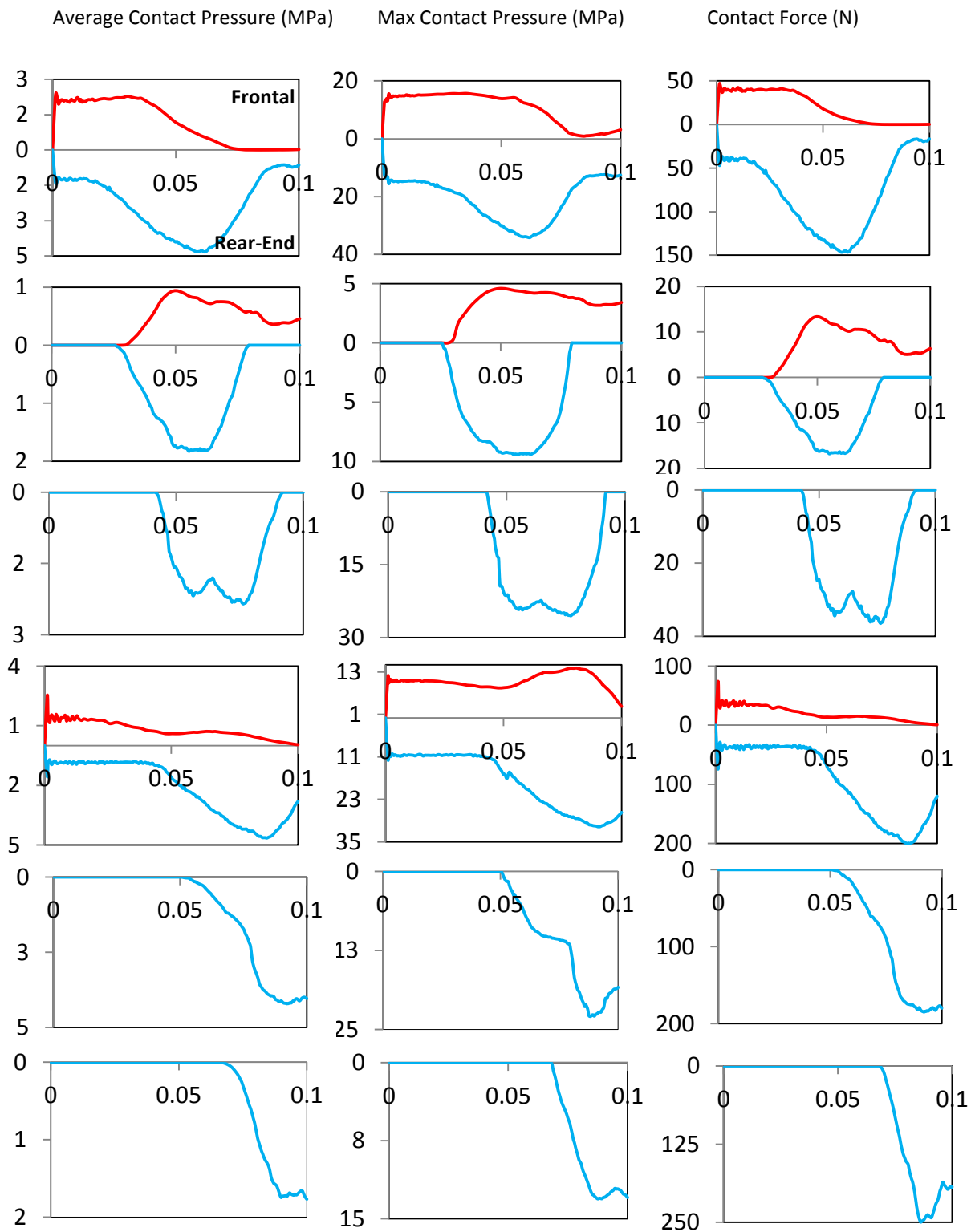


Figure 6.16 Average and maximum nodal contact pressures, as well as contact force in the cervical facet joints at different cervical spinal levels during 15 frontal and rear impacts.

6.3.6 Cervical Spinal Load Sharing

Unlike static loading conditions, impact is a dynamic loading scenario and is a function of time. Therefore, it is important that analysis results, such as those of stress or strain, be reported during the impact time span. In this study, the concept of Strain Energy (S.E.) was used to investigate load sharing in the cervical spine during the test duration of the frontal and rear impacts. The results are summarized in Figs. 6.17-6.23.

Strain energy is the internal energy which is stored in any material when it is loaded within its elastic limit. The applied external load causes deformation in the material. Because of the deformation, energy is stored in the material. The strain energy at zero deformation is set to zero. From continuum mechanics point of view, the area under stress-strain curve is termed strain energy:

$$\text{Strain energy increment} = \sum_{i,j=1}^3 \sigma_{ij} d\varepsilon_{ij} \quad (6.1)$$

Fig. 6.17 shows: the magnitude of S.E. in each cervical spinal level; the percentage of contribution of each level in comparison to all other levels resulting from 15G frontal and rear impacts; the magnitude and percentage of S.E. in each spinal tissue, in comparison to all other spinal tissues; the S.E. of each ligament group and its percentage compared to the other ligaments. The spinal level S.E. resulting from the frontal impact was almost three times greater than that resulting from the rear impact. At the beginning of both impacts, the highest S.E. was found at level C56, whereas at the mid-time point of impact, level C12 had the highest S.E. At

the end of the frontal impact, S.E. was similar at all levels. At the end of the rear impact, levels C67, C56, C45 showed the highest portions. Among the spinal tissues, ligaments showed the highest magnitudes of S.E. and this increased over time in both frontal and rear cases. The S.E. in discs and facet joints was small in comparison to the other spinal tissues. The contribution of disc S.E. in the frontal impact was almost zero, while it increased at the end of rear impact. The contribution of the facet joints S.E. was more significant at the beginning of both frontal and rear impacts, than it was at the end of impacts. While the cancellous bone played a major role at the beginning of the impact, its contribution decreased over time. The cortical bone contribution was almost zero at the beginning of the impact, then increased for 30 milliseconds, and finally dropped slightly until the end of impact. The CL ligament had the highest S.E. value, and had the most significant contribution in comparison to other ligaments at the beginning of the frontal and rear impacts. Its contribution decreased for 20 milliseconds sharply and stayed nearly constant for the rest of time. While the LF ligament took the most significant part of S.E. after the CL ligament in the frontal impact, the contribution of ALL ligament increased and was significant at the end of rear-end impact.

At level C12 (Fig. 6.18), the S.E. of the cervical tissues was significantly greater during the frontal rather than during the rear impact. During frontal impact the S.E. of all tissues, with exception of facets, increased over time. During the rear impact however, the maximum S.E. of each tissue occurred at the mid impact time (around 60 milliseconds). Moreover, the contribution of the cancellous bone was the highest at the beginning and decreased over time. The cortical bone contribution increased steeply from the beginning of impact for 25 milliseconds and decreased slightly following this. The facets contribution decreased over time, while the role of

the ligaments increased during the frontal impact. At the end of the rear impact, the role of ligaments decreased, while the role of cortical bone increased slightly. At level C12, the CL and LF ligaments had the most significant role in both frontal and rear impacts.

At level C23 (Fig. 6.19), disc contribution was more important during the end of the rear impact than it was during the frontal impact. While the ligaments were found to have most of the S.E. during the last 80 milliseconds of the frontal impact, cortical bone contribution was more significant during the rear impact. During frontal and rear impacts, the CL and LF ligaments were the major contributors, with the ALL ligament also contributing during the rear impact. In terms of frontal impact condition, S.E. magnitudes of CF, annulus, and nucleus were greater than those reported for the rear impact. In frontal and rear-end impacts, the nucleus had the lowest contribution whereas the CF had the highest.

From level C34 (Fig. 6.20) to level C67 (Fig. 6.23), the pattern of S.E. contained in the spinal tissues was similar to the levels reported above. During rear impact, the S.E. magnitude in discs increased and moved from levels C12 through C67 level. Furthermore, the contribution of the ALL ligament increased and moved from levels C12 through C67 during the rear-end impact.

Cervical Spine

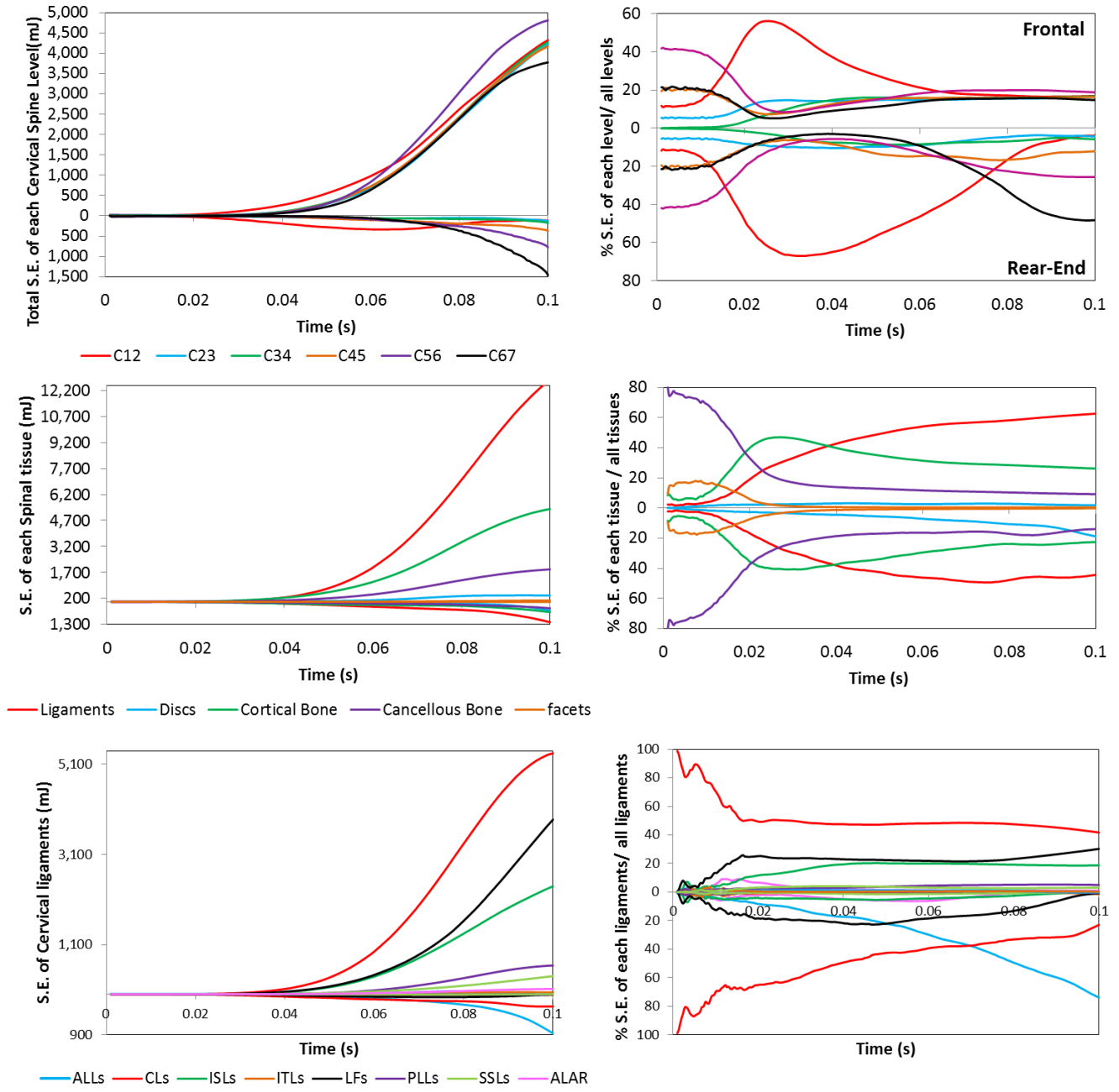


Figure 6.17 Cervical spinal load sharing based on Strain Energy (S.E.): The magnitude and percentage of contribution of S.E. of each spinal level, in comparison to all other levels; the magnitude and percentage of S.E. in each spinal tissue, in comparison to all other tissues, the S.E. of each ligament group and its percentage compared to the other ligaments, respectively, resulting from 15G frontal and rear-end impact scenarios.

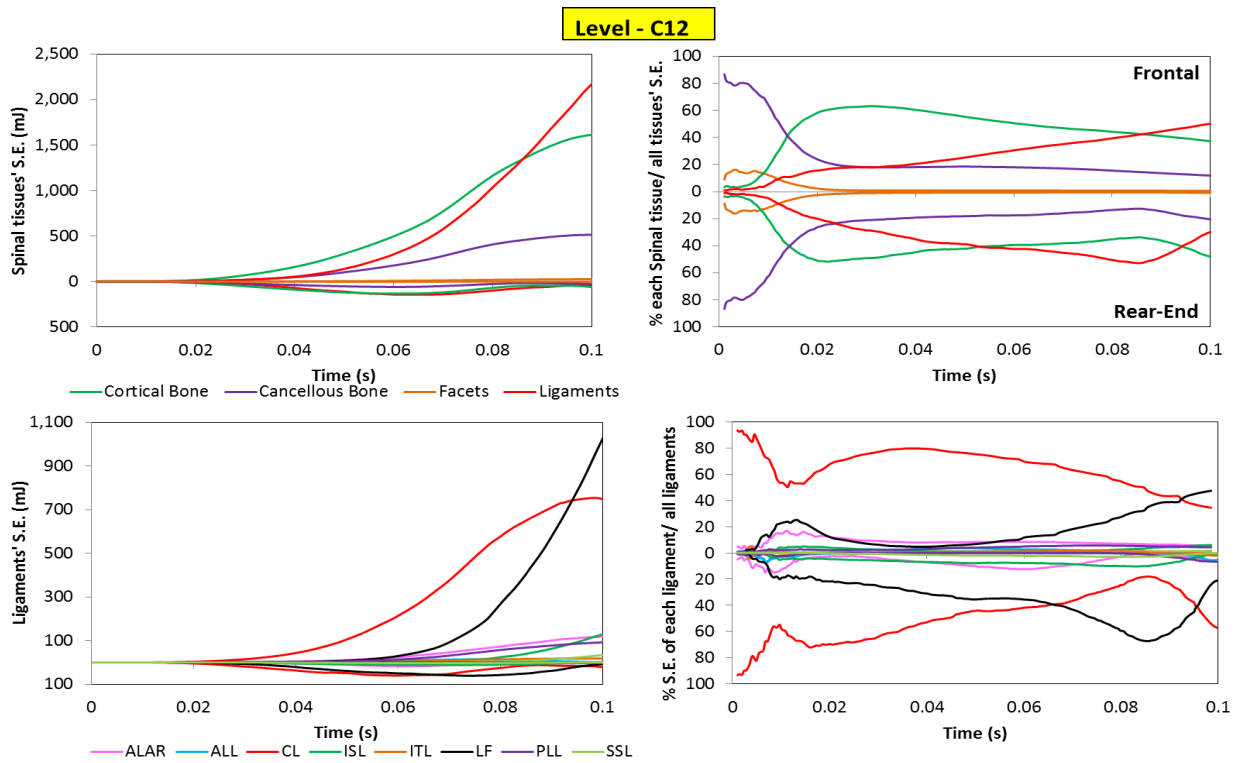


Figure 6.18 S.E. distribution in the spinal level C12 resulting from 15G frontal and rear-end impacts.

Level - C23

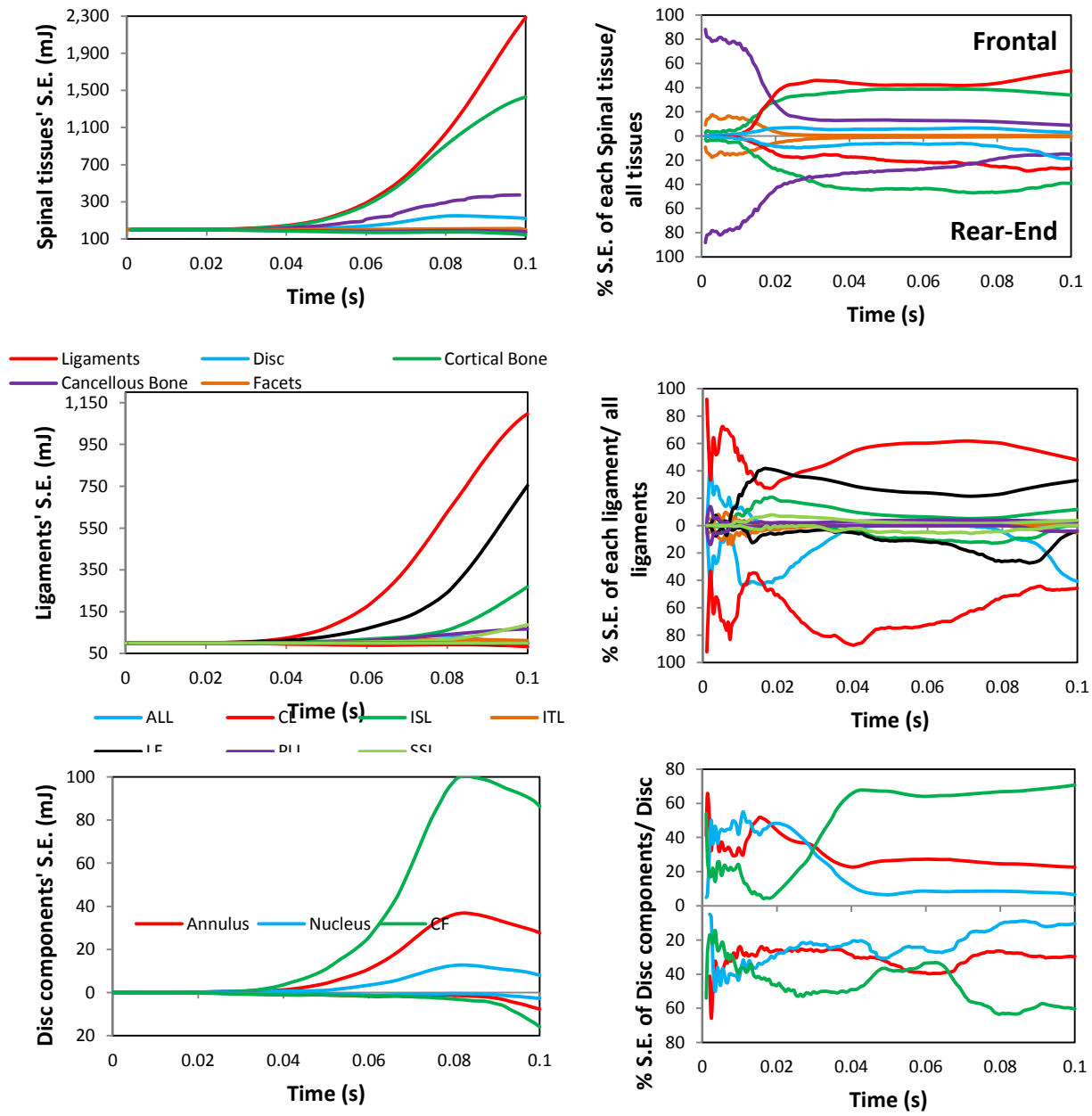


Figure 6.19 S.E. distribution in the spinal level C23 resulting from 15G frontal and rear-end impact conditions.

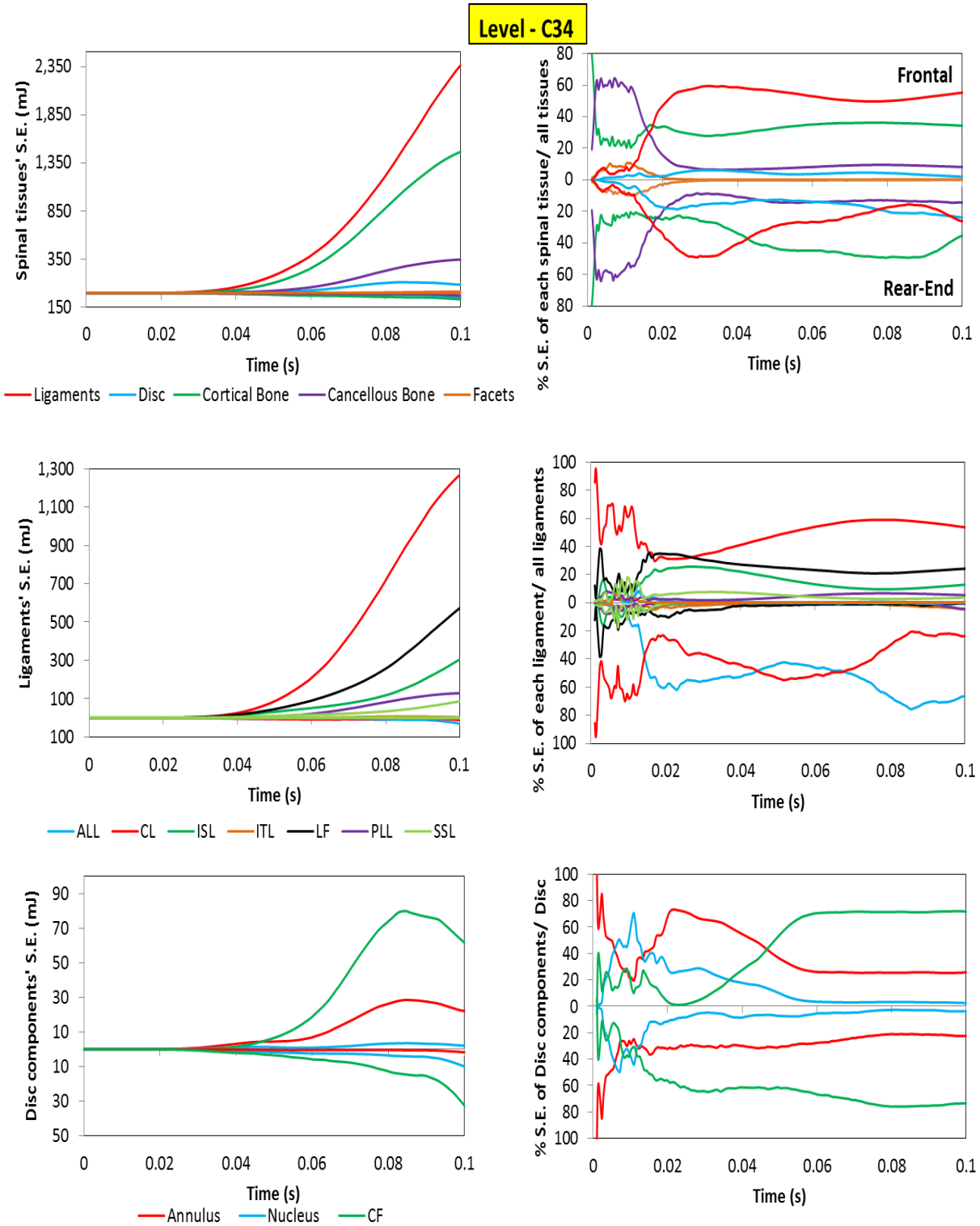


Figure 6.20 S.E. distribution in the spinal level C34 resulting from 15G frontal and rear-end impact conditions.

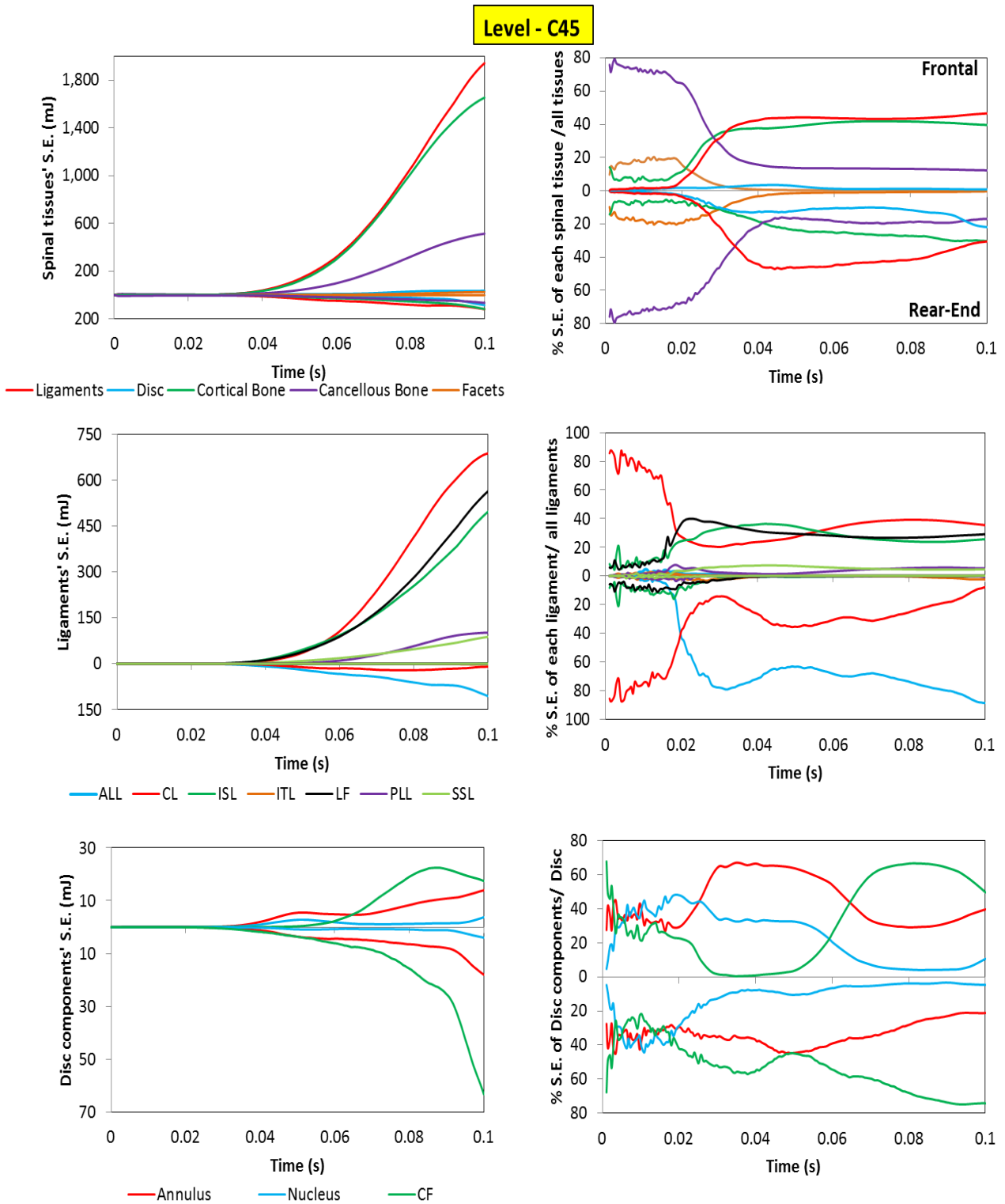


Figure 6.21 S.E. distribution in the spinal level C45 resulting from 15G frontal and rear-end impact conditions.

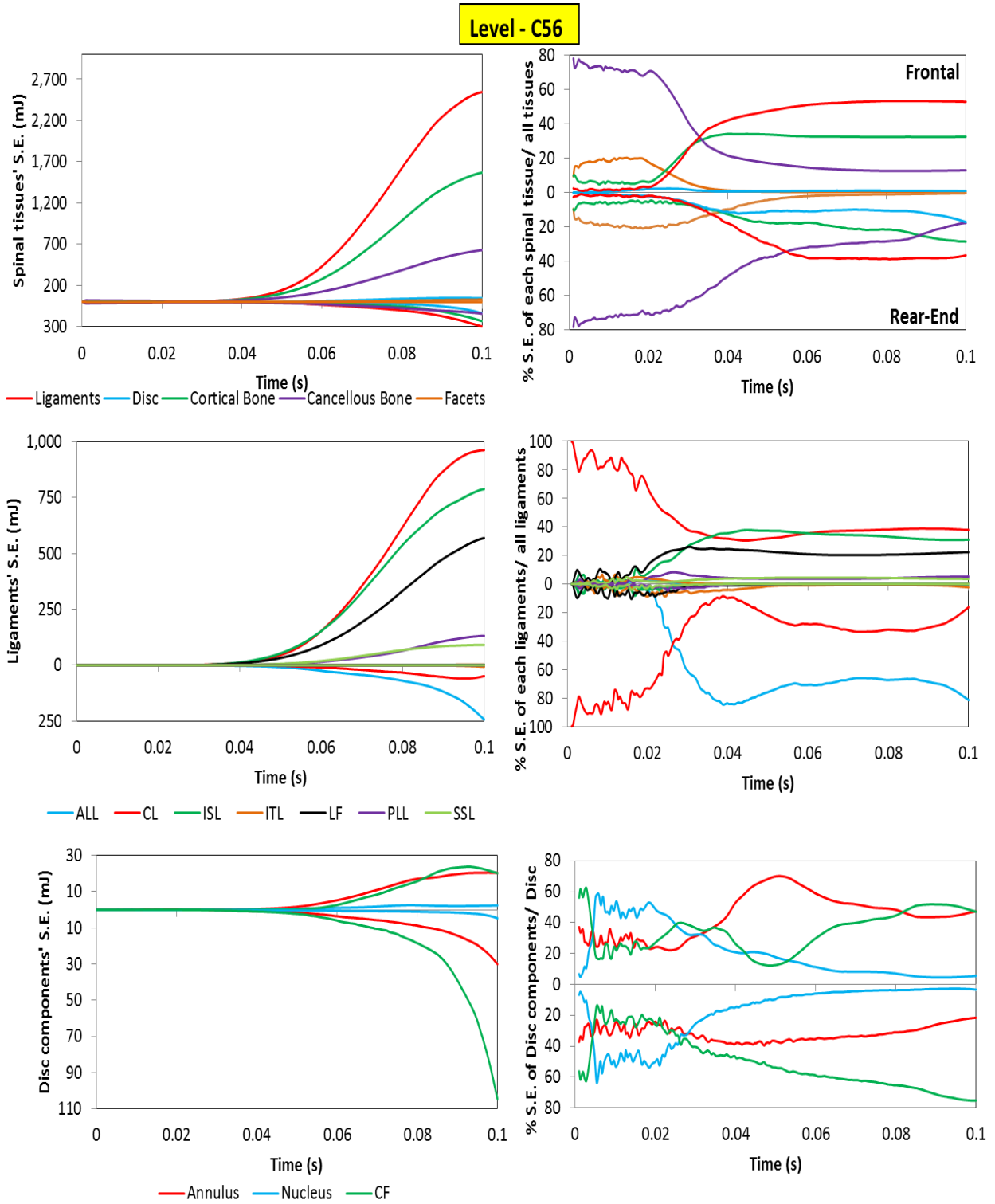


Figure 6.22 S.E. distribution in the spinal level C56 resulting from 15G frontal and rear-end impact conditions.

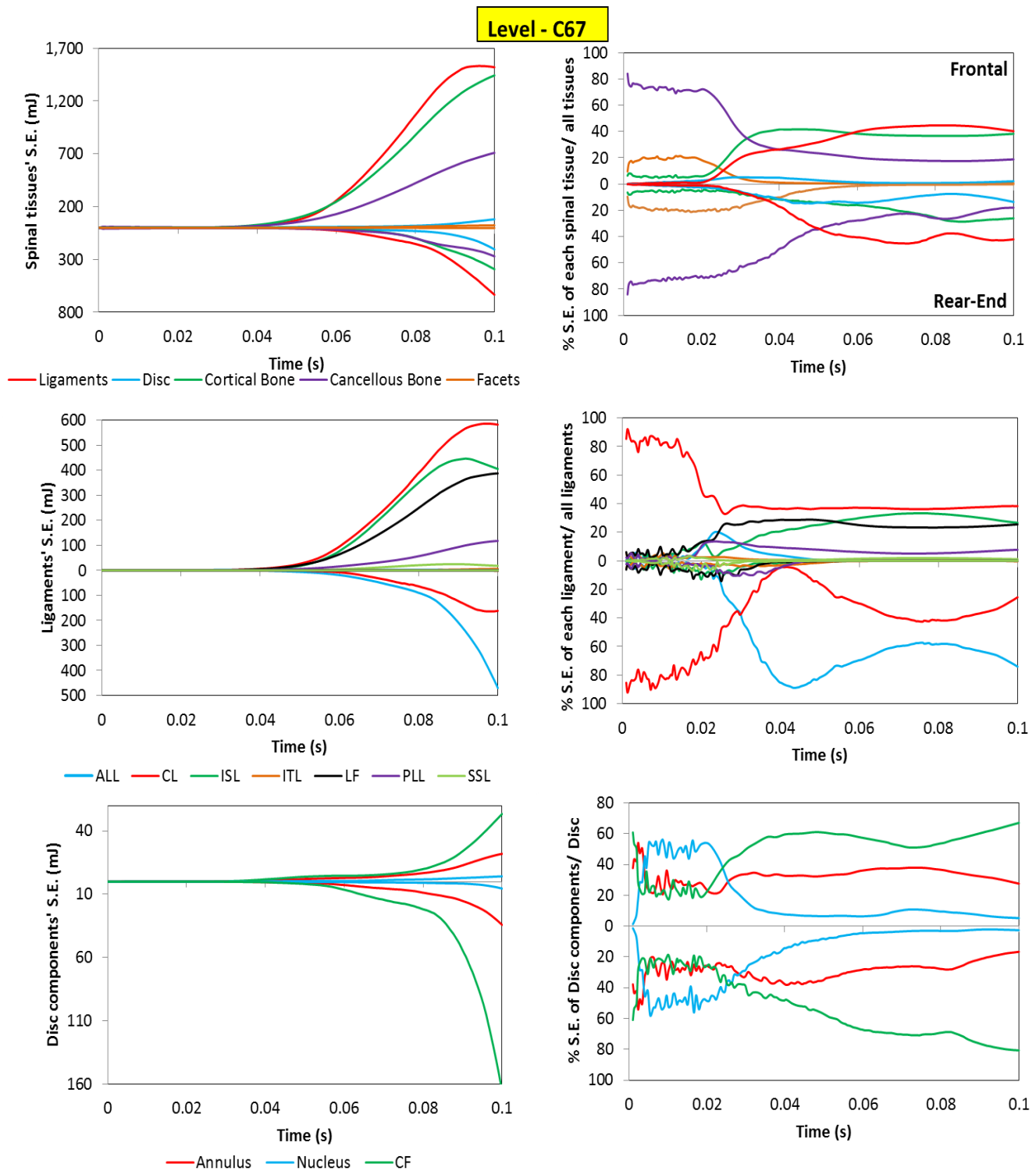


Figure 6.23 S.E. distribution in the spinal level C67 resulting from 15G frontal and rear-end impact conditions.

6.4 Discussion and Conclusion

As a step toward more accurate and realistic FE modelling of the cervical spine, a nonlinear detailed cervical spine model was employed to investigate spinal load sharing and predict stress and strain up to failure during frontal and rear-end impact conditions. The loading and boundary conditions were selected in order to as closely replicate those of the experimental and numerical studies reported in the literature (Hedenstierna *et al.*, 2009; Östh *et al.*, 2017; Ewing *et al.*, 1976; Stemper *et al.*, 2004). Under the 15G frontal and 2.6 m/s rear-end impact loading conditions, the anterior and posterior displacements, as well as the rotation (flexion or extension) of the head were in good agreement with the published works (Fig. 6.4). Due to the lack of cervical musculature in the FE model (which stabilizes and limits the range of motion for the head and neck), the displacement of the model in terms of translation and rotation was greater than those reported in the volunteer and PMHS results. This is especially the case during the end of either frontal or rear impacts.

The results explained in this chapter show that ligament failure depends on the location of the ligament in the cervical spine, as well as on the direction of impacts. The current model demonstrated that the CL ligament at level C45 had the highest stress among others which is in agreement with the previous studies (Östh *et al.*, 2017).

Moreover, the predicted results of the peak strain in the ALL, PLL, and ISL ligaments, at different levels were in good agreement with the previous experimental work done by Panzer and his colleague (2011). However, the model herein tested showed more strain in the CL ligaments and less strain in the LF ligaments in comparison to the previous work (Panzer *et al.*, 2011). This

could be because of the geometry of the 2D ligaments, as well as the location where the ligaments are attached.

The spinal load sharing results indicated that the direction of impact affects the amount of S.E. in the cervical spine. The S.E. was significantly higher during the frontal impact than the rear impact. Levels C56 and C67 had the greatest S.E. amongst the cervical spinal levels during the frontal and rear impacts, respectively. Among the cervical tissues, ligaments experienced the greatest S.E. during the middle and the end of impacts. Among the ligament groups, the CL and LF played the most significant role during frontal impact, while the contribution of the CL and ALL ligaments was more important during rear impact. The magnitude of S.E. in the IVDs at levels C23 and C34 under frontal impact was higher than those predicted under rear impact. The S.E. values in the IVDs at levels C45, C56, and C67 were greater as a result of rear impact in comparison to frontal impact.

The main limitation of the present study is the lack of cervical musculature in the FE cervical spine model. This required that the effect of gravity not be considered in order to avoid instability under the compression load. In addition, the elastic material properties assigned to the annulus and nucleus should be improved in future studies.

CHAPTER SEVEN: INVESTIGATING THE EFFECT OF 3D PASSIVE MUSCULATURE ON THE BEHAVIOR OF THE CERVICAL SPINE UNDER IMPACT LOADING SCENARIOS

7.1 Problem Description

Previous experimental and numerical works have identified the importance of the cervical musculature as stabilizer and force generator (Hedenstierna *et al.*, 2009; Kumar *et al.*, 2005; Brault, *et al.*, 2000). The objective of this study was to investigate the effects of passive cervical musculature on the response of the cervical spine tissues to impact loading conditions. This was done using a 3D continuum FE model. The results of the Ligamentous Spine (LS) model were compared to the results from a spine with passive musculature, a spine we have named the Passive Musculature Spine (PMS).

All the results presented in this chapter were based on the material properties and their units used on the published works of Mustafy and colleagues (Mustafy *et al.*, 2014a, b; Mustafy *et al.*, 2016). However, due to unit discrepancies in their work, stress unit was found to be wrong. To have a consistence set of units, stress unit must change from MPa to KPa.

7.2 Geometry and Material Properties of Cervical Musculature, Loading and Boundary Conditions, and Solution

The material parameters for the ligamentous spine were similar to those presented in Chapters Five and Six. The MR images of the same subject were used to reconstruct the cervical muscles explained in Section 5.2.4 (Fig. 7.1). The Ogden hyperelastic material law governed the musculature (Section 5.4). All the muscles were fixed at the T1 level. Finally, the same loading scenarios explained in Chapter Six were applied to the T1.

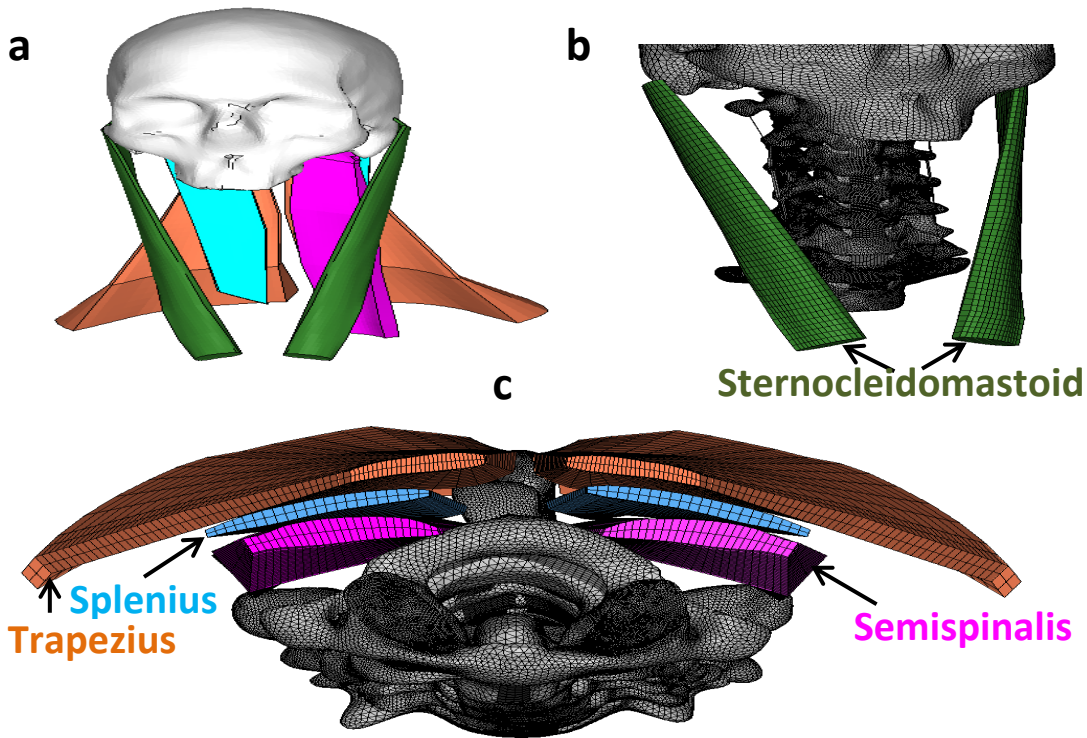


Figure 7.1 (a) An overall view of the cervical muscles. (b) Sternocleidomastoid (SCM) is located on the lateral sides of the cervical spine. (c) A schematic view of the cross sectional area of the muscles, Trapezius (TZ), Splenius (SC), and Semispinalis (SSC) located at the posterior side of the cervical spine.

7.3 Results

7.3.1 Ligaments Injury Prediction using Stress Failure Criteria

To investigate the effect of the musculature on the behavior of the other spinal tissues such as ligaments and discs, the stress history in all ligaments and IVDs at different spinal levels was compared in the LS and PMS models using 5G frontal and rear-end impact scenarios. The results were then compared to the existing experimental data (Mattucci *et al.*, 2012).

As shown in Figs. 7.2-7.6, the peak stress in the ligaments was greater in the LS model than the PMS model during the frontal impact, whereas during the rear impact, the peak stress was greater in the PMS model than the LS model.

No failure was noticed in the ALL ligament in either the LS or PMS models as a result of frontal or rear impact scenarios (Fig. 7.2).

The CL ligament failed in both the LS and PMS models during the frontal and rear impacts. During the frontal impact, level C45 failed first in both the LS and PMS models. The onset of failure was 40 milliseconds in the LS model, and 60 milliseconds in the PMS model. During the rear impact, levels C23, C34, and C45 failed almost at the same time in the LS model, whereas level C23 failed first followed by levels C34 and C45 in the PMS model. Adding the passive musculature to the spine model shifted the onset of the CL ligament failure toward the end of impact time (Fig. 7.3).

During frontal impact, the ISL ligament failed in both models at all levels but level C23. The failure occurred at levels C56 and C45 almost at the same time, followed by failure at levels C34 and C67 in the LS model. The failure occurred earlier in the LS model than in the PMS model (Fig 7.4). During the rear impact, the ISL ligament failed only in the PMS model, and at all levels excluding level C23. Failure occurred during the last instants of the impact. The sequences of failure were similar to the frontal impact (Fig 7.4).

The LF ligament failed in the LS model during the frontal impact, whereas the PMS model predicted the failure during the rear impact. Level C45 failed first in the frontal impact followed by levels C23 and C56, whereas level C23 failed first followed by level C45 during the rear impact (Fig. 7.5).

Stress in the PLL ligament did not reach the failure level (39.7 MPa) in either the frontal or rear impact scenarios. In both models the peak stress was observed at level C34 as a result of both impact scenarios (Fig. 7.6).

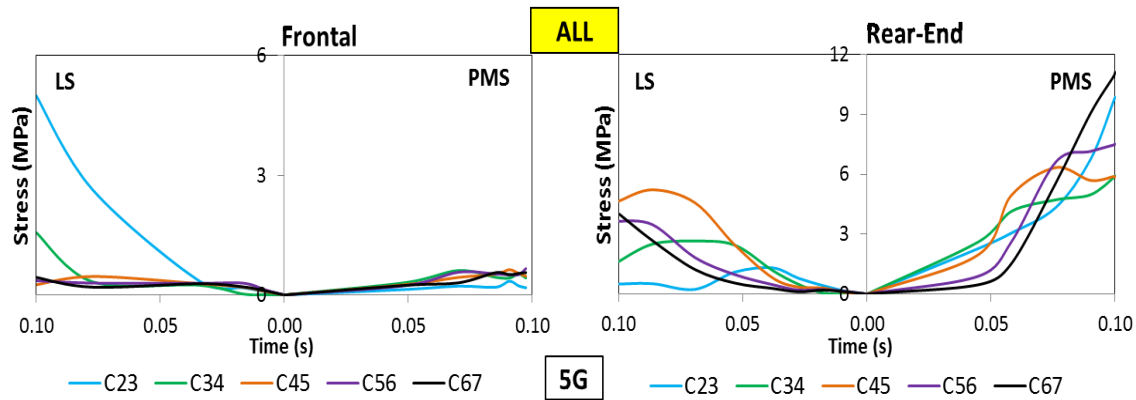


Figure 7.2 Sequences of failure in the ALL ligaments at different cervical spinal levels in the LS and PMS models during 5G frontal and rear-end impact scenarios.

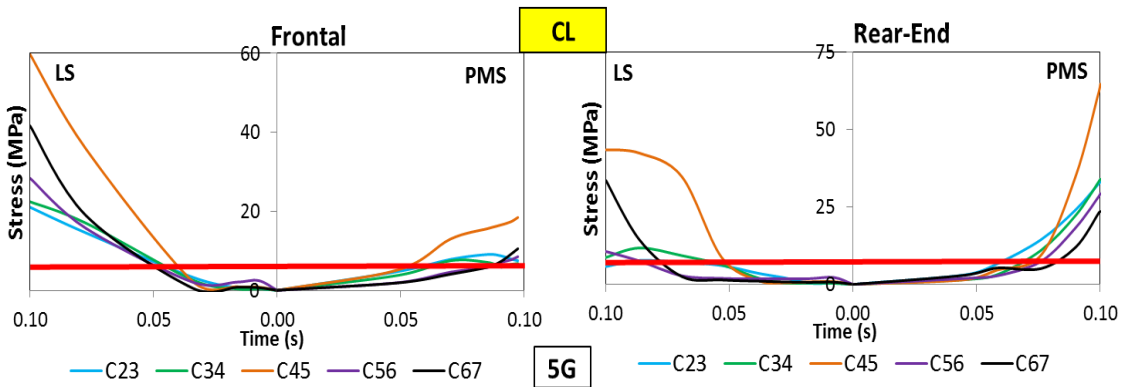


Figure 7.3 Sequences of failure in the CL ligaments at different cervical spinal levels in the LS and PMS models during 5G frontal and rear-end impact scenarios.

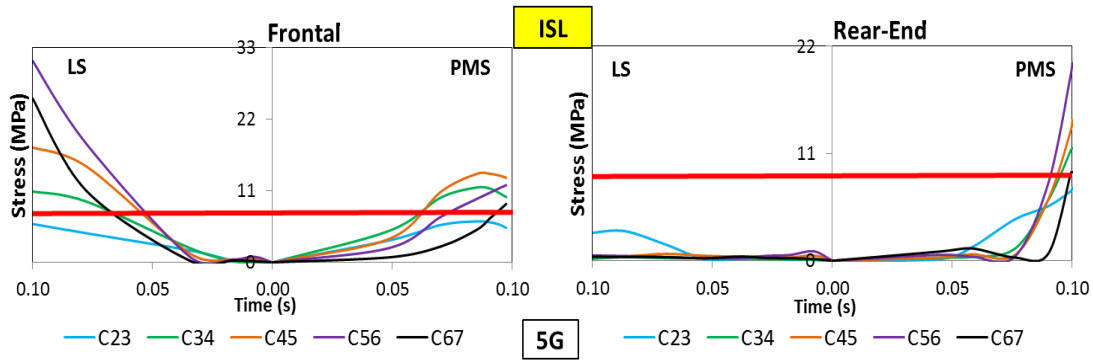


Figure 7.4 Sequences of failure in the ISL ligaments at different cervical spinal levels in the LS and PMS models during 5G frontal and rear-end impact scenarios.

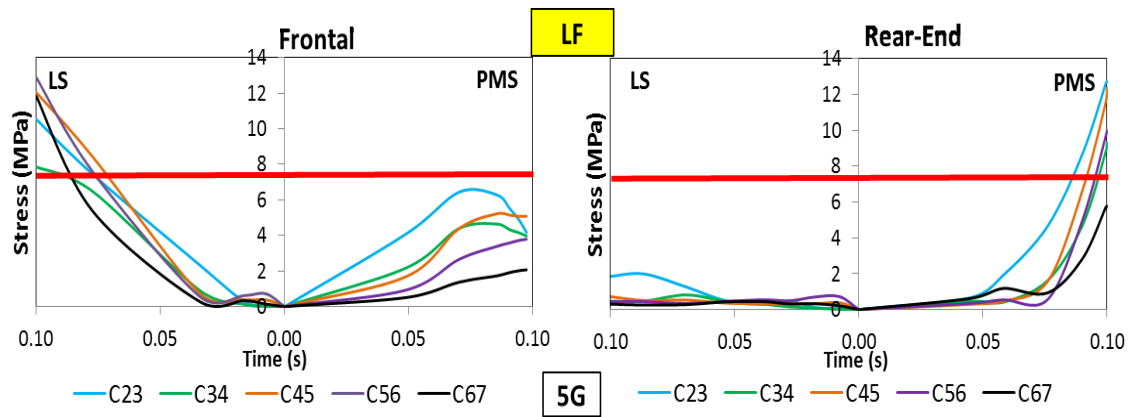


Figure 7.5 Sequences of failure in the LF ligaments at different cervical spinal levels in the LS and PMS models during 5G frontal and rear-end impact scenarios.

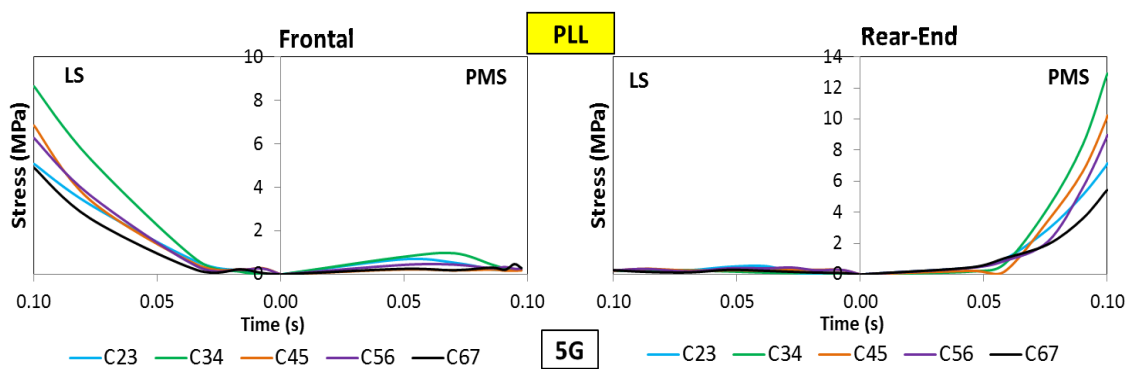


Figure 7.6 Sequences of failure in the PLL ligaments at different cervical spinal levels in the LS and PMS models during 5G frontal and rear-end impact scenarios.

7.3.2 Effect of the Musculature on Strain Distribution in the Cervical Spine Soft Tissues

The peak strains for all ligaments, at different levels were predicted by both the LS and PMS models. These predictions were then compared with the values reported in the experimental and numerical studies (Panjabi *et al.*, 2004; Panzer *et al.*, 2011). This comparison was accomplished using an 8G frontal impact loading scenario (Fig. 7.7). Nearly all ligaments showed stiffer behavior at all levels in the PMS model than in the LS model. Overall, the PMS model results are in closer agreement with those reported in the previous researches.

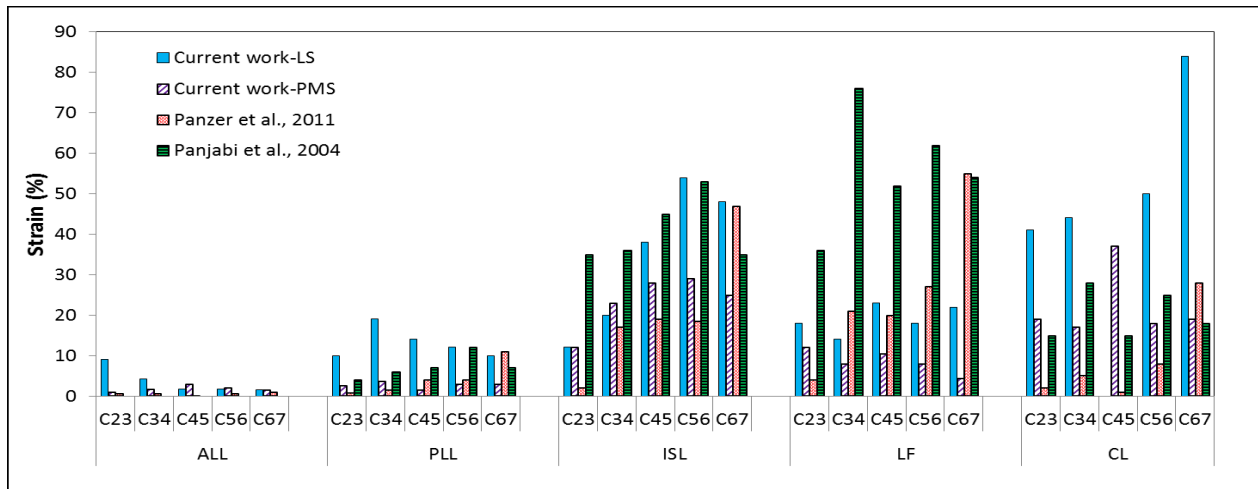


Figure 7.7 Strain distributions in the cervical ligaments during 8G frontal impact. The LS and PMS models predictions were compared with the numerical and experimental studies results.

Peak shear strain in the anterior and posterior parts of the IVDs were also measured and compared to the relevant experimental and numerical studies that had used an 8G frontal impact scenario (Ito *et al.*, 2005; Panjabi *et al.*, 2004; Panzer *et al.*, 2011) (Fig. 7.8). To see the effect of passive musculature on the peak shear strain at the anterior and posterior parts of the

discs, the LS and PMS models predictions were compared with the experimental works done by Panjabi and colleagues (Panjabi et al., 2004). The results are summarized below:

At level C23, the LS and PMS models predictions were 51% and 74% less than the experiment data in the anterior parts; whereas they were 67% and 68% less than the experiment results in the posterior part, respectively. At level C34, the LS and PMS models predictions were 250% and 30% higher than those reported in the experiment in the anterior part; while they were 120% and 46% greater than the experimental results in the posterior part, respectively. Also, at level C45, the peak strain predicted by the LS and PMS models were less than the experimental data (33% and 16%) in the anterior part. The LS model result was 7% below the experiment, while the PMS model result was above 25% it in the posterior part of the disc. At level C56, the LS and PMS models predictions were 62% and 5% greater than those of the experimental data, respectively in the anterior part; while they were 8% and 25% higher than the experimental data in the posterior part. Moreover, at level C67 in the anterior part of the disc, the LS model result was 7% higher than the experiment, whereas the PMS model result was 20% smaller than the experimental data. While in the posterior part of the disc, the LS and PMS modes predictions were 20% and 15% smaller than the experimental data, respectively (Fig. 7.8).

To investigate the effect of the passive musculature on the ligaments strain, the history of the strain in all ligaments at all cervical levels was compared in the LS and PMS models using 5G frontal and rear-end impact scenarios.

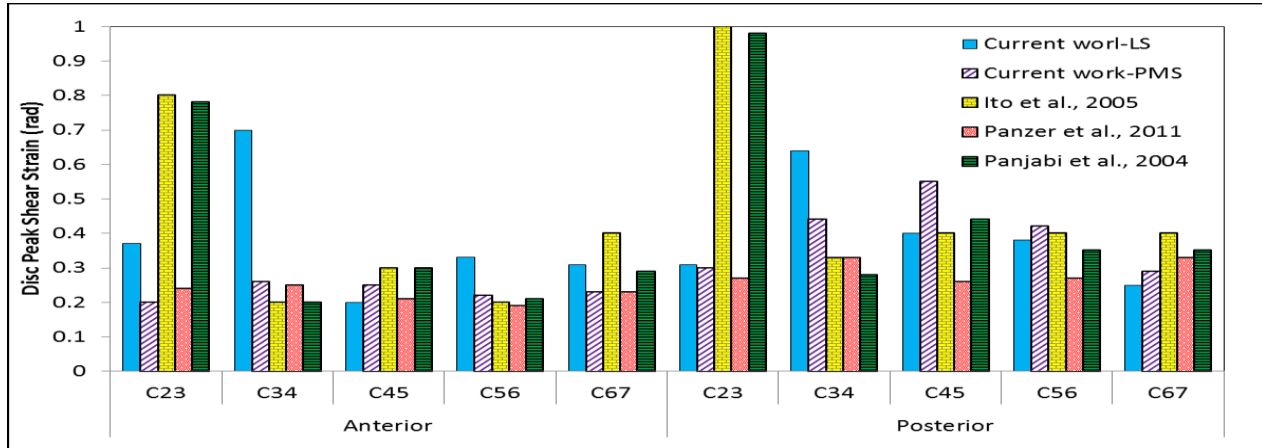


Figure 7.8 Strain distributions in the anterior and posterior parts of IVDs during 8G frontal impact. The LS and PMS models predictions were compared with the numerical and experimental studies results.

Maximum strain in the ALL ligaments was experienced at level C23 in the LS model, whereas during the frontal impact, it occurred at level C67 in the PMS model during the rear-end impact (Fig. 7.9).

Peak strain in the CL ligaments was predicted at C45 level in both the LS and PMS models during frontal and rear-end impacts (Fig. 7.10).

The ISL ligaments at level C56 experienced maximum strain in the LS model during the frontal impact, and in the PMS model during the rear-end impact (Fig. 7.11).

During the frontal impact, the LF ligament at level C56 experienced the highest strain in the LS model; while during the rear-end impact, the LF ligament at level C23 had the maximum strain (Fig. 7.12).

Maximum strain in the PLL ligaments was predicted at level C34 by the LS model during the frontal impact, and the PMS model during the frontal impact (Fig. 7.13).

Among the upper cervical ligaments, the Alar ligament had the greatest strain in both the LS and PMS models during the frontal and rear impacts (Fig. 7.14).

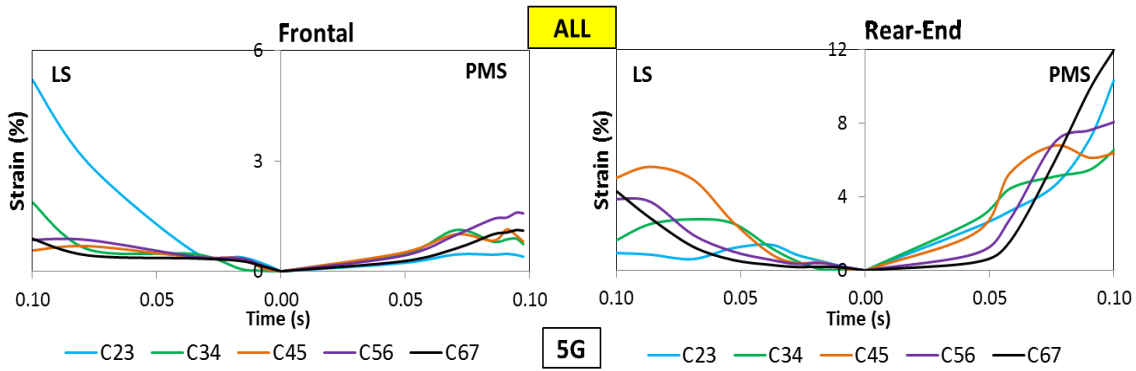


Figure 7.9 History of strain (%) in the ALL ligaments over time in the LS and PMS models during 5G frontal and rear-end impact scenarios.

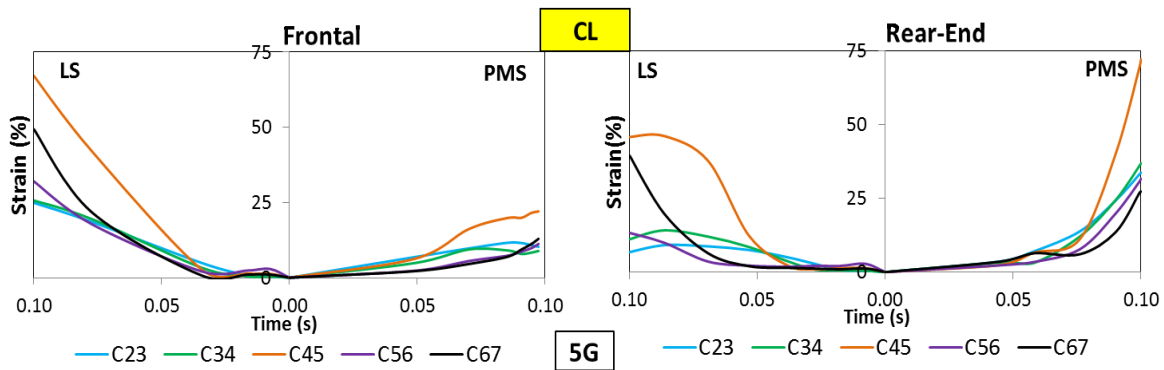


Figure 7.10 History of strain (%) in the CL ligaments over time in the LS and PMS models during 5G frontal and rear-end impact scenarios.

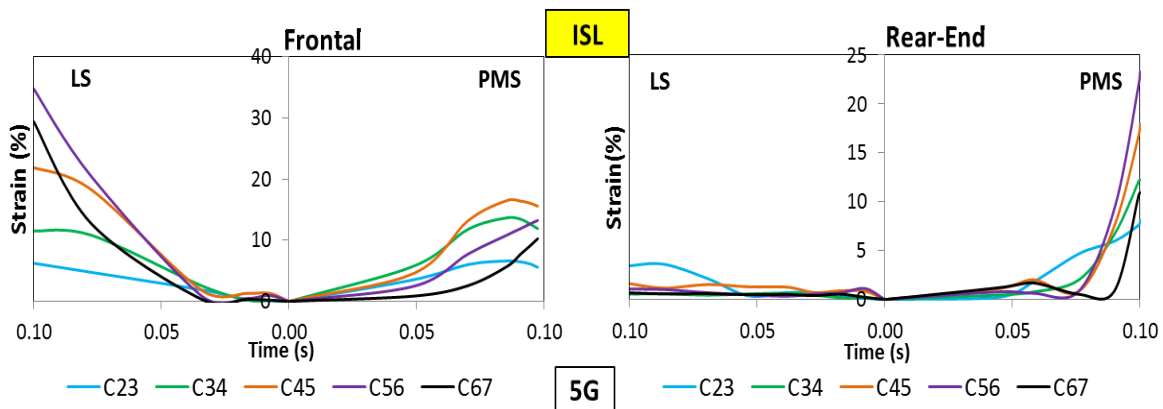


Figure 7.11 History of strain (%) in the ISL ligaments over time in the LS and PMS models during 5G frontal and rear-end impact scenarios.

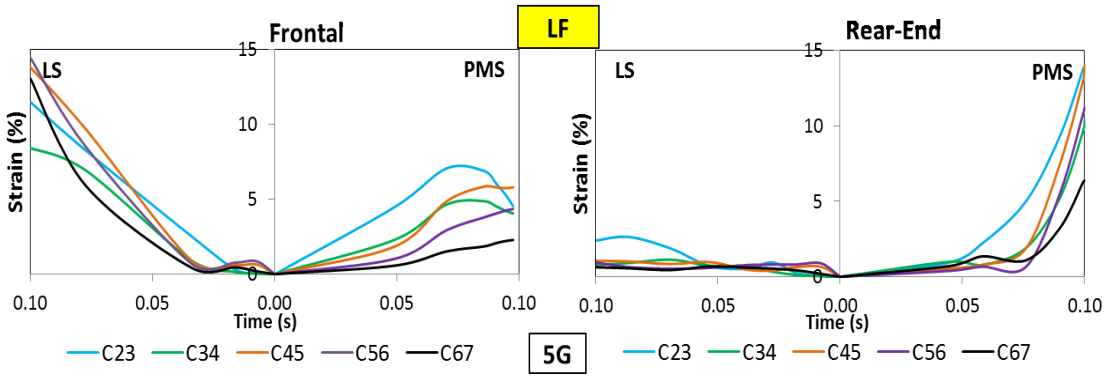


Figure 7.12 History of strain (%) in the LF ligaments over time in the LS and PMS models during 5G frontal and rear-end impact scenarios.

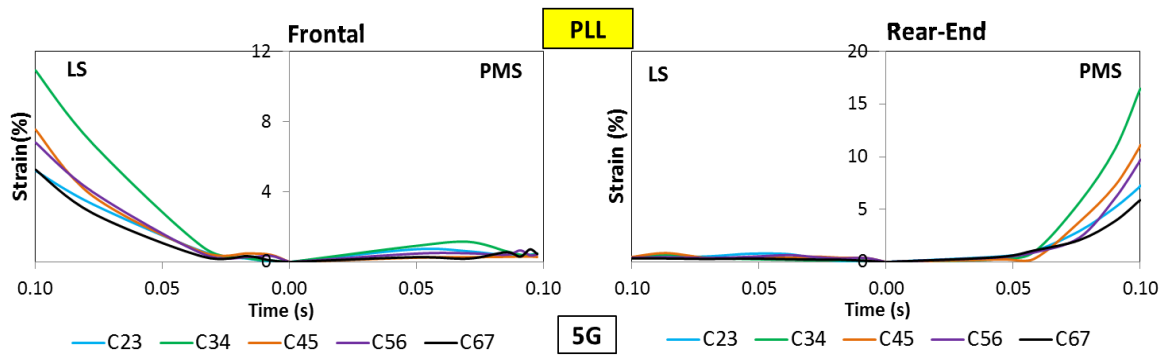


Figure 7.13 History of strain (%) in the PLL ligaments over time in the LS and PMS models during 5G frontal and rear-end impact scenarios.

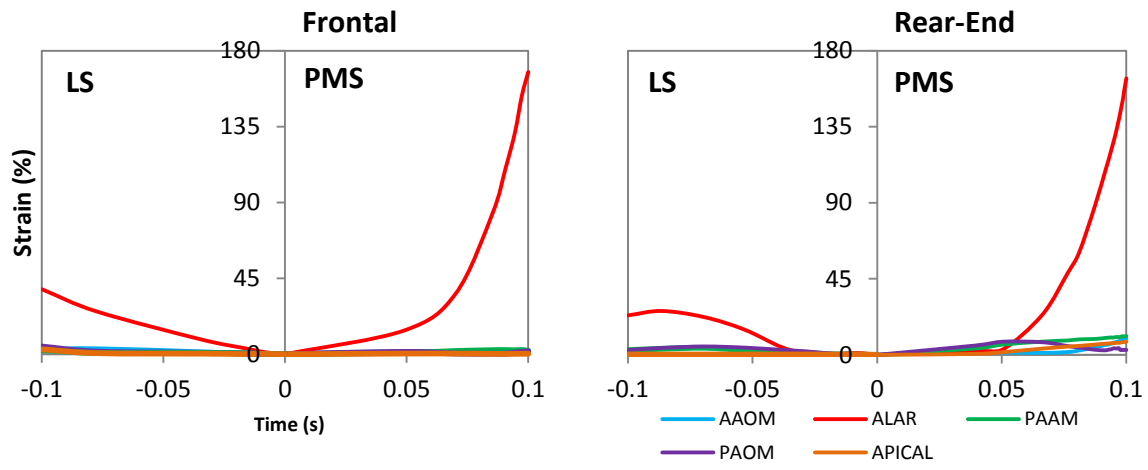


Figure 7.14 History of strain (%) in the UCS ligaments over time in the LS and PMS models during 5G frontal and rear-end impact scenarios.

7.3.3 Contact Force and Pressure in Facet Joints

The contact force and pressure in the Facet Joints (FJ) at different levels were also measured in the LS and PMS models during 5G and 8G frontal and rear-end impact conditions (Figs. 7.15, 7.16).

During the 8G rear-end impact, contact occurred at all cervical levels in the LS model, whereas in the PMS model, contact only occurred at levels C34 and C7T1. The magnitude of contact force and pressure decreased with the presence of muscles. During the 8G frontal impact, the PMS model predicted contact in the FJs of levels C23, C34 and C67, while the LS model predicted contact at levels C12, C34, and C56. In addition, the patterns of contact, and the peak contact pressure and force at all levels were different in the LS and PMS models.

In comparison to the 8G frontal impact, the PMS model predicted contact would occur at more cervical levels during the 5G frontal impact, whereas opposite was found during the rear-end impact.

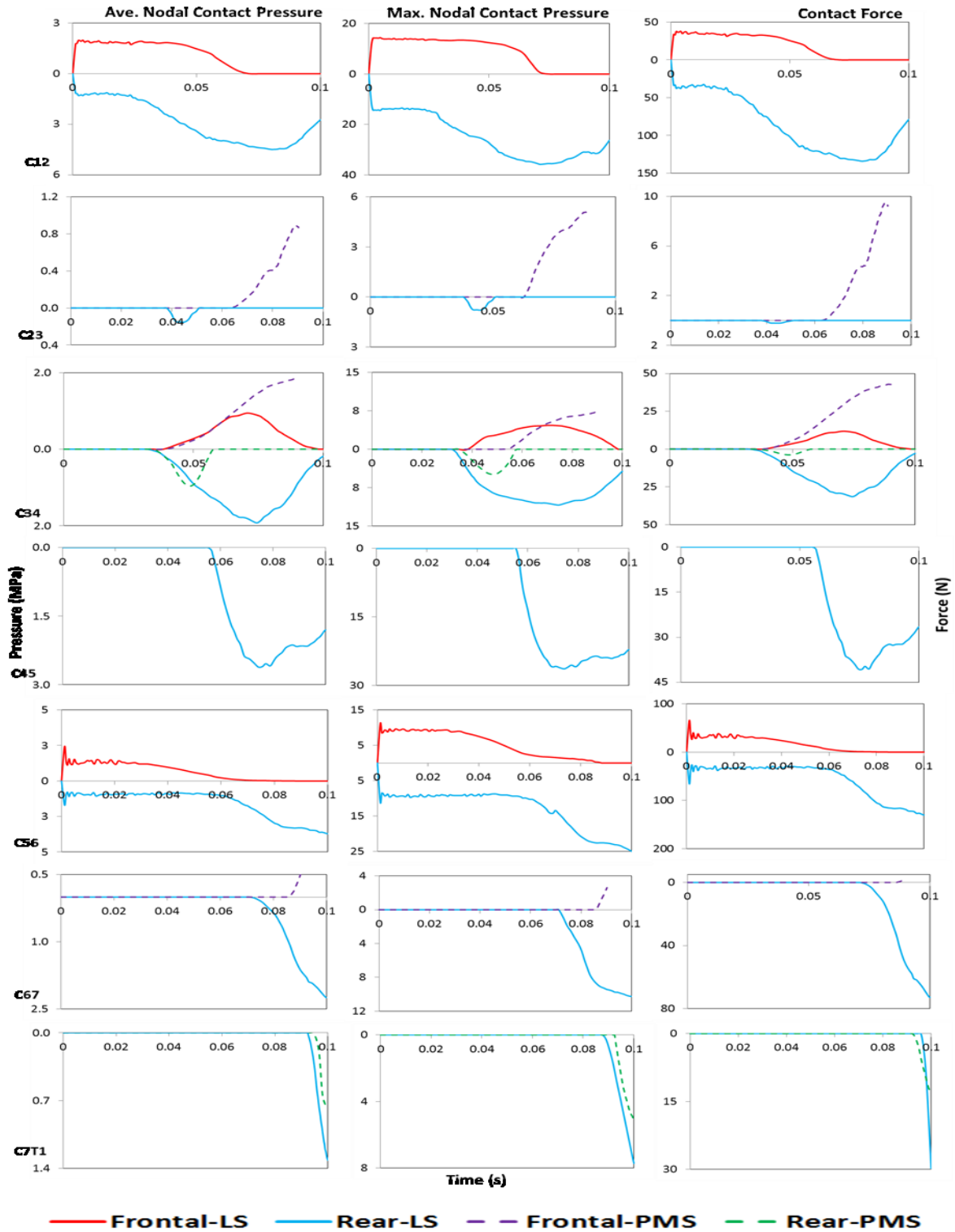


Figure 7.15 Average and maximum contact pressures and contact force in the FJs at different spinal levels during 8G frontal and rear impact scenarios.

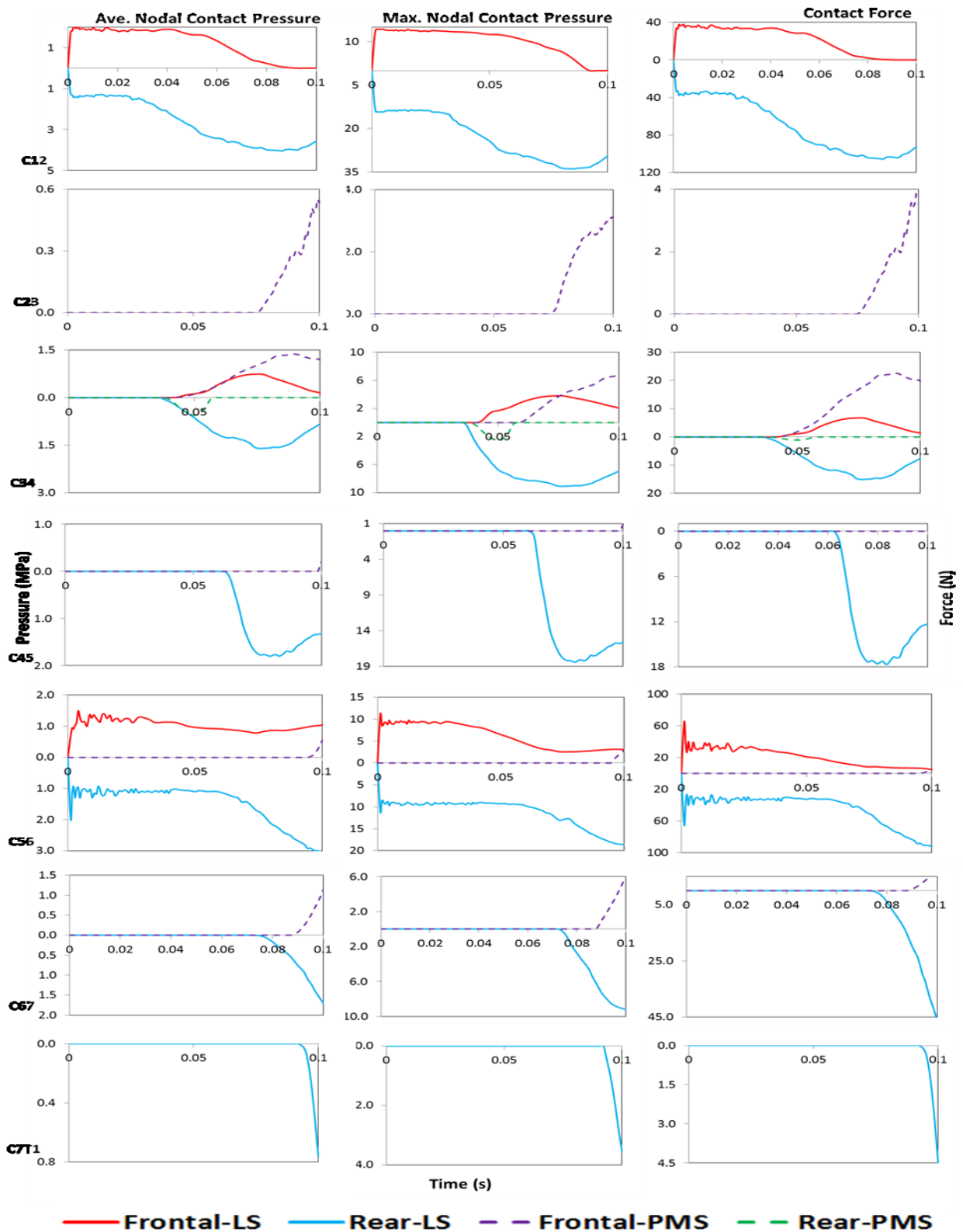


Figure 7.16 Average and maximum contact pressures and contact force in the FJs at different spinal levels during 5G frontal and rear impacts.

7.3.4 Cervical Spine Load Sharing

Similar to the method discussed in Chapter Six, Section 6.3.6, the concept of Strain Energy (S.E.) was used to investigate effects of the passive musculature on the spinal load sharing during frontal and rear-end impact scenarios. To achieve this goal, results of the LS and PMS models were compared (Figs. 7.17-7.23 show the compared results of the LS and PMS models during 5G frontal impact. Figs. 7.24-7.30 show the compared predictions of the LS and PMS models during 5G rear-end impact).

7.3.4.1 Frontal Impact Load Sharing Results

The S.E. predicted in the cervical levels of the LS model was greater than those predicted in the PMS model. In the LS model, levels C56, C67, and C45 had the greatest contribution for resisting load at the beginning of the impact, and the role of level C12 increased until the 50 millisecond time point. At the end of the impact all spinal levels had the same contribution. In the PMS model, level C12 had the highest S.E. at the beginning of the impact. The S.E. for level C12 decreased over time until the 80 millisecond time point and then increased after this time point (Fig. 7.17). The ligaments showed the highest contribution amongst the cervical tissues in both the LS and PMS models. Specific to the ligaments, the CL ligament featured the most significant contribution in the LS model, whereas in the PMS model the Alar ligament played a more larger role than the CL ligament at the end of the impact. However, it should be noted that the CL ligament played a major role during the majority of the impact time for both models. In addition, in the PMS Model, the IVD at level C23 showed the highest contribution for the first 50 milliseconds of the impact, whereas the roles of levels C34 and C45 exceeded C23 at the end of the impact. In the LS model, the IVD at levels C67 and C56 had the greatest contribution at

the beginning of the impact, while the role of the upper cervical levels became more significant during the end of impact (Fig. 7.17).

At level C12, the role of the ligaments increased during the impact period. In comparison to other tissues and ligaments, the CL ligament was the main contributor in the majority of time in both models. Only at the end of impact did the contribution of the Alar ligament exceed that of the CL ligament (Fig. 7.18).

From levels C23 to C67, the ligaments contribution increased over time in the LS model, whereas in the PMS model, the IVDs played a more significant role over time (Figs. 7.19-7.23).

Specific to the cervical ligaments, and despite the CL ligament being the main contributor in the LS model, the ISL and LF ligaments exceeded that of the CL ligament over the course of impact and at all cervical levels (Figs. 7.18-7.23).

The role of disc components varied along the spine. While in the LS model, the annular fibers (CF) were the main contributor followed by the annulus, the contribution of the annular fibers was most pronounced at the end of impact. In the PMS model, the annulus played the main role, followed by the nucleus. The role of the CF was not significant in this model (Figs. 7.19-7.23).

7.3.4.2 Rear-End Impact Load Sharing Results

Unlike the frontal impact, the S.E. predicted by the PMS model was greater at all cervical levels than that predicted by the LS model during the rear-end impact. Level C12 experienced the highest S.E. in both the LS and PMS models during the majority of impact time. Furthermore,

ligaments had the highest contribution amongst the cervical tissues. In addition, the contribution of the CL ligament was the most significant in both models, followed by the LF and ALL ligaments. Within the IVDs at different spinal levels, in the PMS model the IVD at level C23 had the highest contribution at the beginning of impact, and the IVD at level C67 had highest contribution at the end of impact. In the LS model, the IVD at level C56 had the highest contribution at the beginning of impact, while the IVDs at levels C67, C34, and C56 had the greatest contribution at the end of impact (Fig. 7.24).

The LS model predicted the role of IVD components differently than did the PMS model prediction. In the LS model, the CF and annulus had equal contributions. Furthermore, these contributions were more significant than that of the nucleus. In the PMS model, the CF, the annulus, and the nucleus had the highest contributions, respectively (Figs. 7.25-7.30).

In addition, among the ligaments, the CL and ALL ligaments had the highest contributions in both models (Figs. 7.25-7.30).

Moreover, the LS model predicted that the contribution of the cancellous bone would be greater than that of other spinal tissues at most of cervical levels. Of the spinal tissues, the ligaments and the IVDs were predicted by the PMS model to have the greatest contributions (Figs. 7.25-7.30).

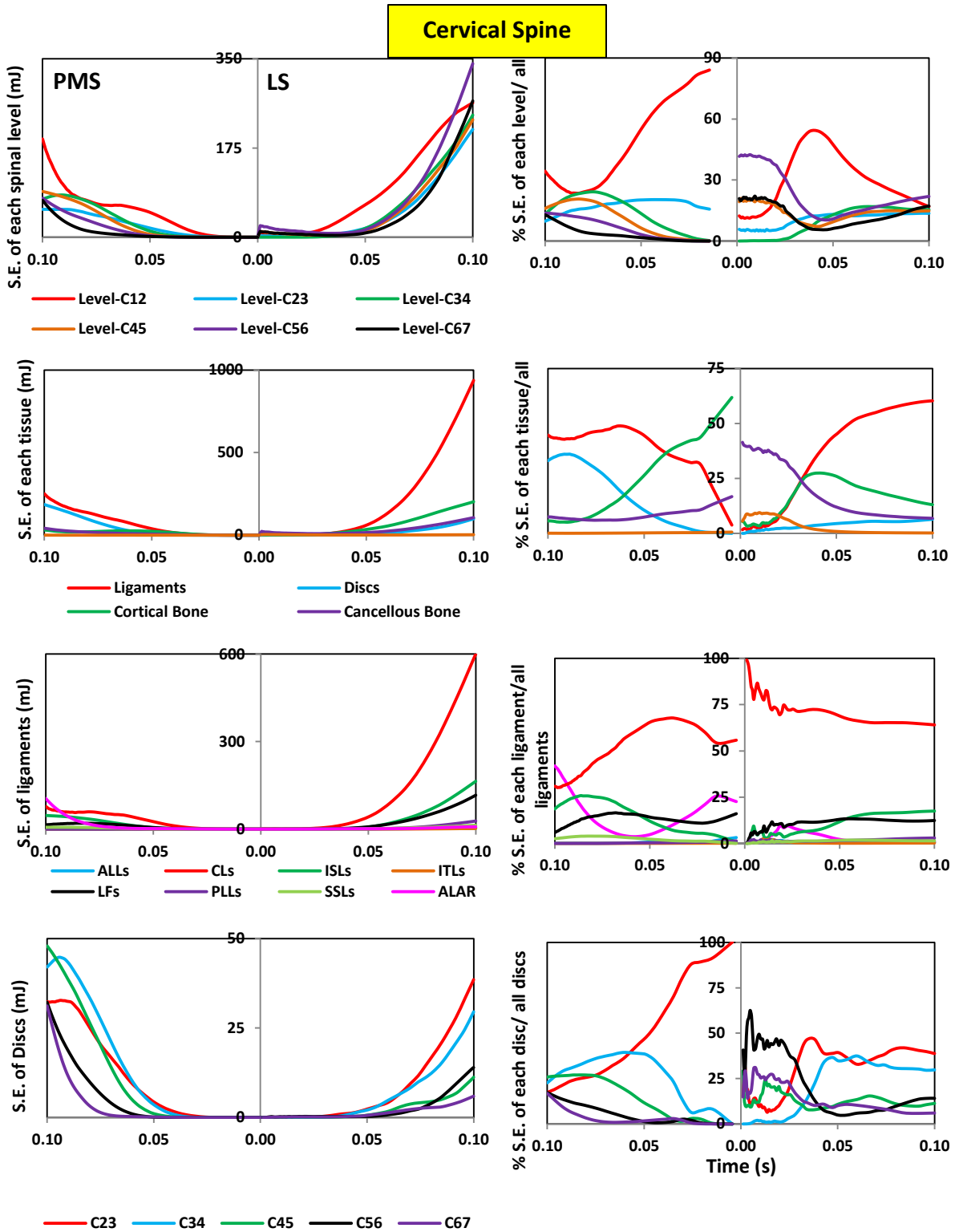


Figure 7.17 Cervical spinal load sharing based on Strain Energy (S.E.): The magnitude and percentage of contribution of S.E. of each spinal level in comparison to all other levels; the magnitude and percentage of S.E. in each spinal tissue and in comparison to all other tissues, the S.E. of each ligament group and its percentage compared to the other ligaments, respectively, predicted by the LS and PMS models resulting from 5G frontal impact.

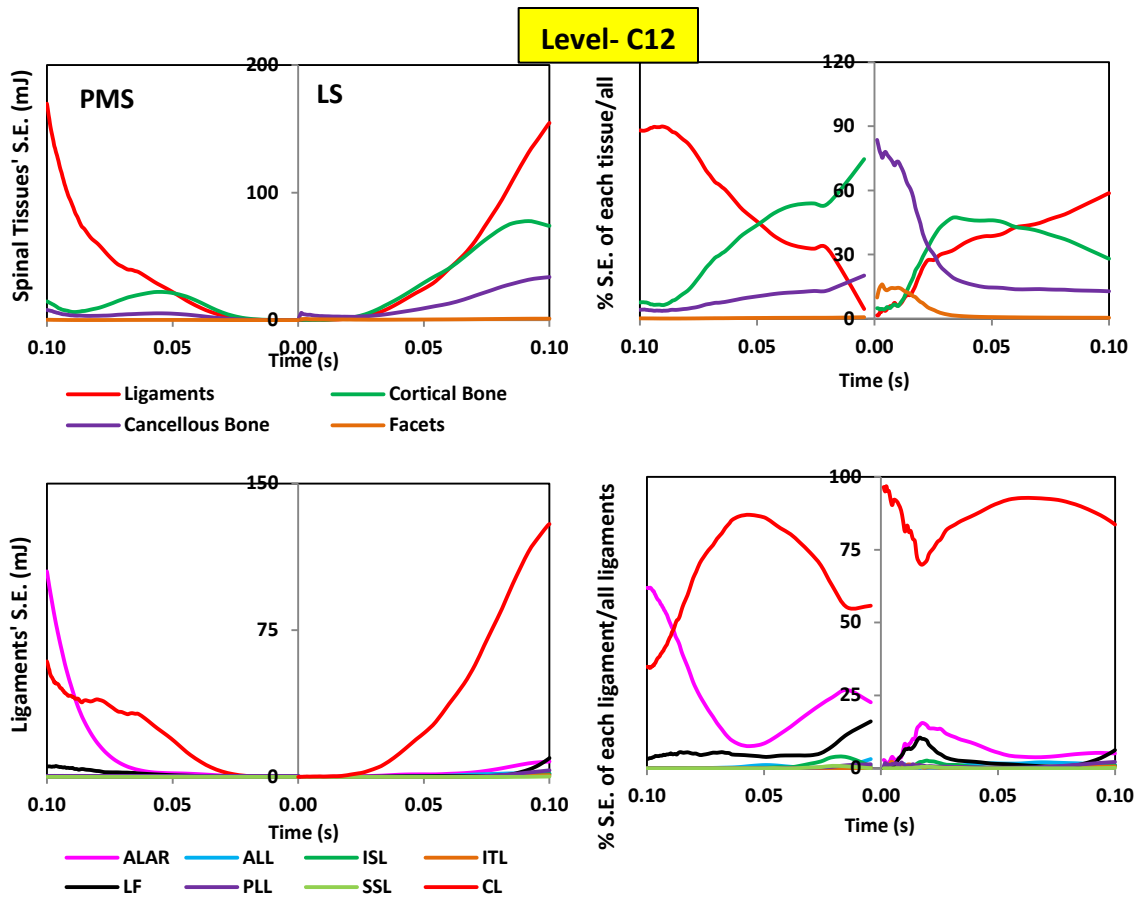


Figure 7.18 S.E. distribution in the spinal level C12 predicted by the LS and PMS models during 5G frontal impact.

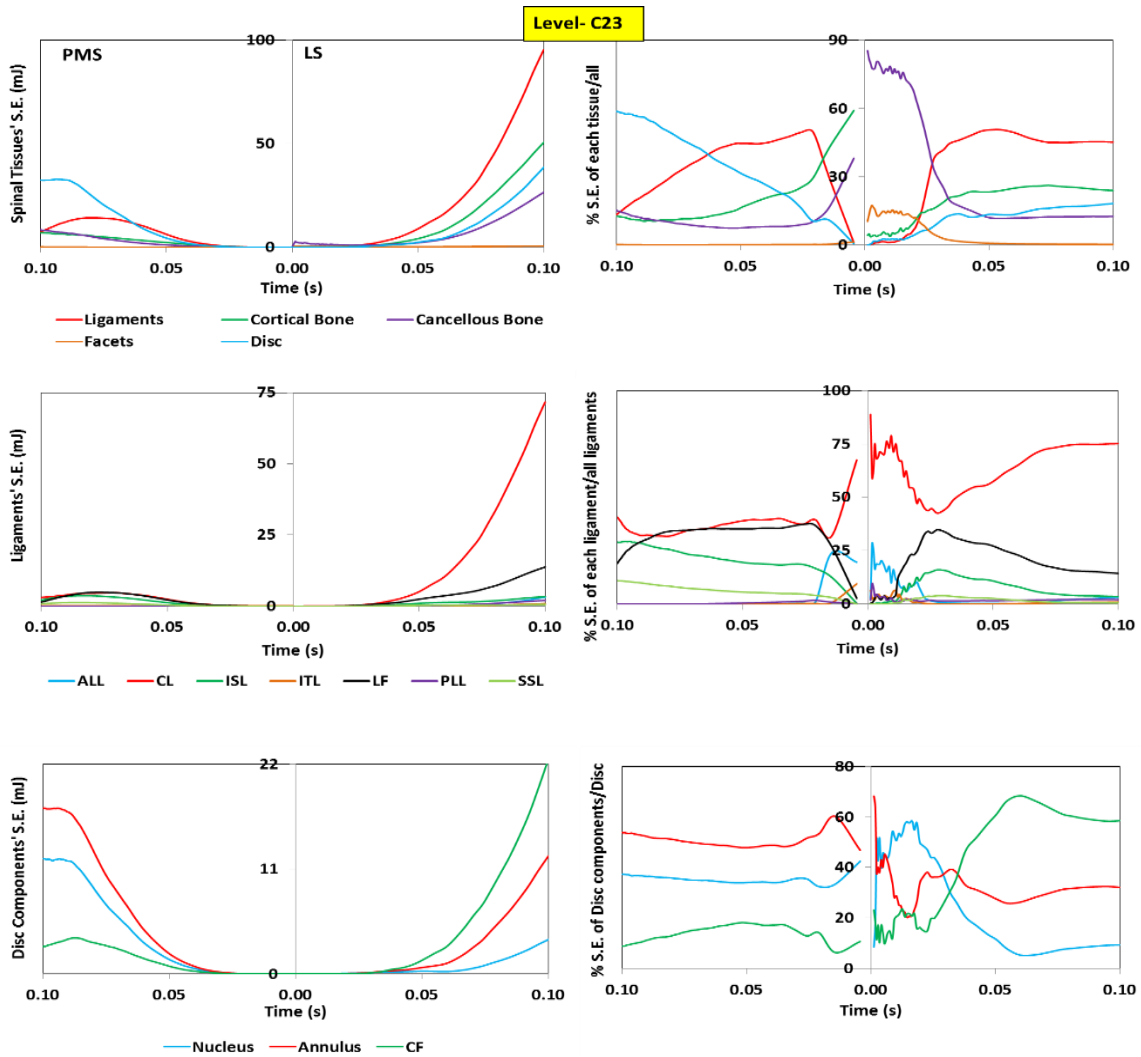


Figure 7.19 S.E. distribution in the spinal level C23 predicted by the LS and PMS models during 5G frontal impact.

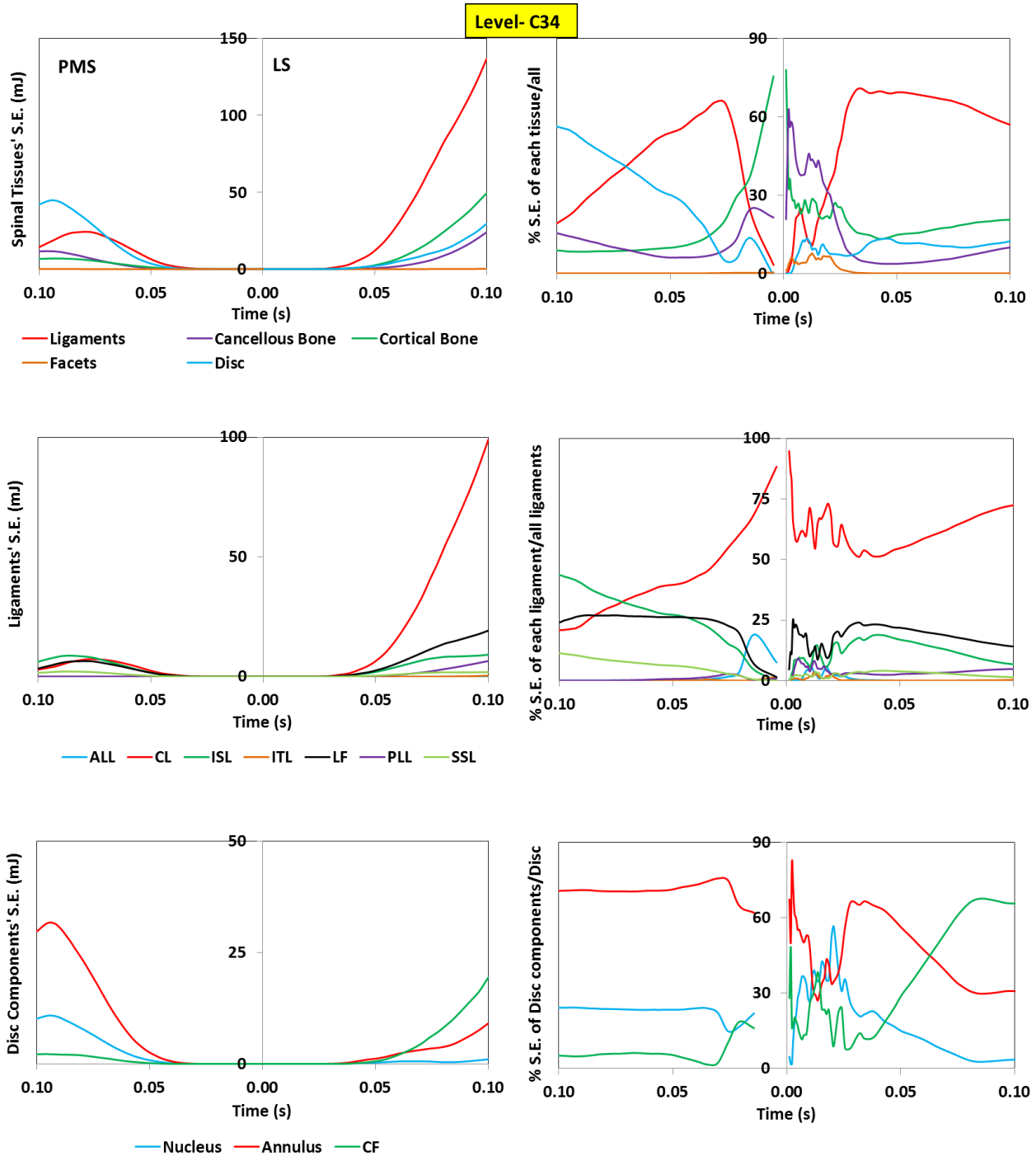


Figure 7.20 S.E. distribution in the spinal level C34 predicted by the LS and PMS models during 5G frontal impact.

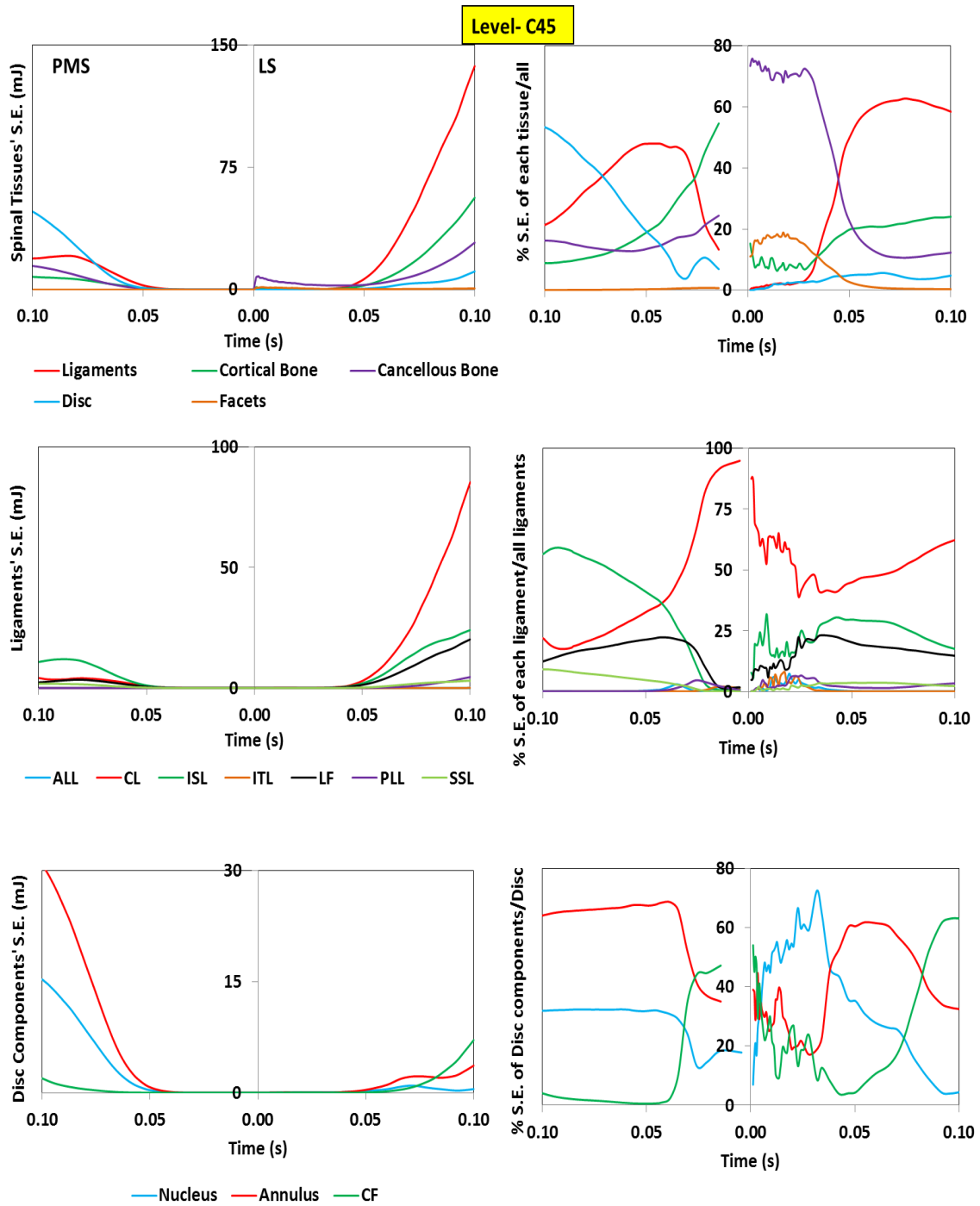


Figure 7.21 S.E. distribution in the spinal level C45 predicted by the LS and PMS models during 5G frontal impact.

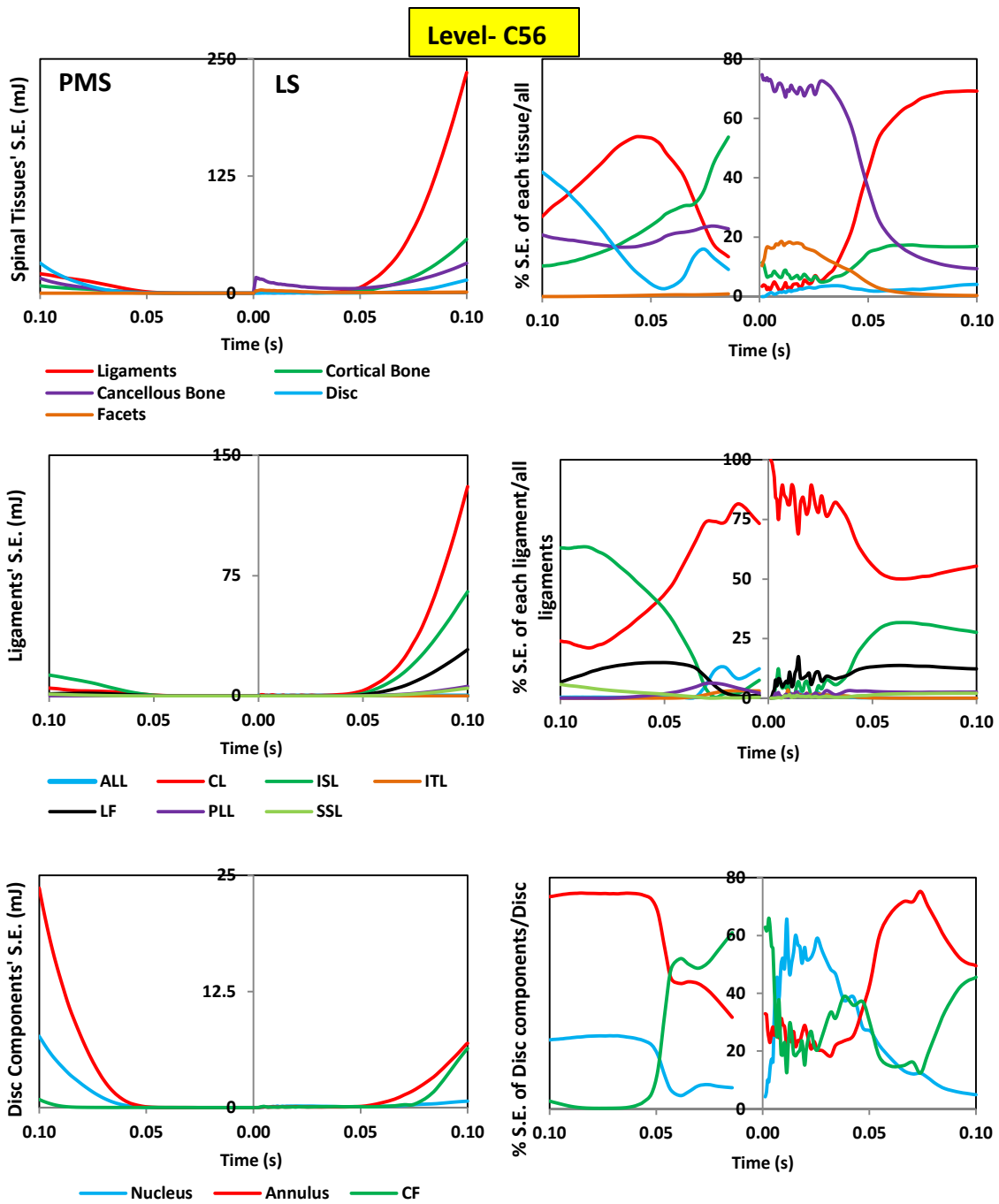


Figure 7.22 S.E. distribution in the spinal level C56 predicted by the LS and PMS models during 5G frontal impact.

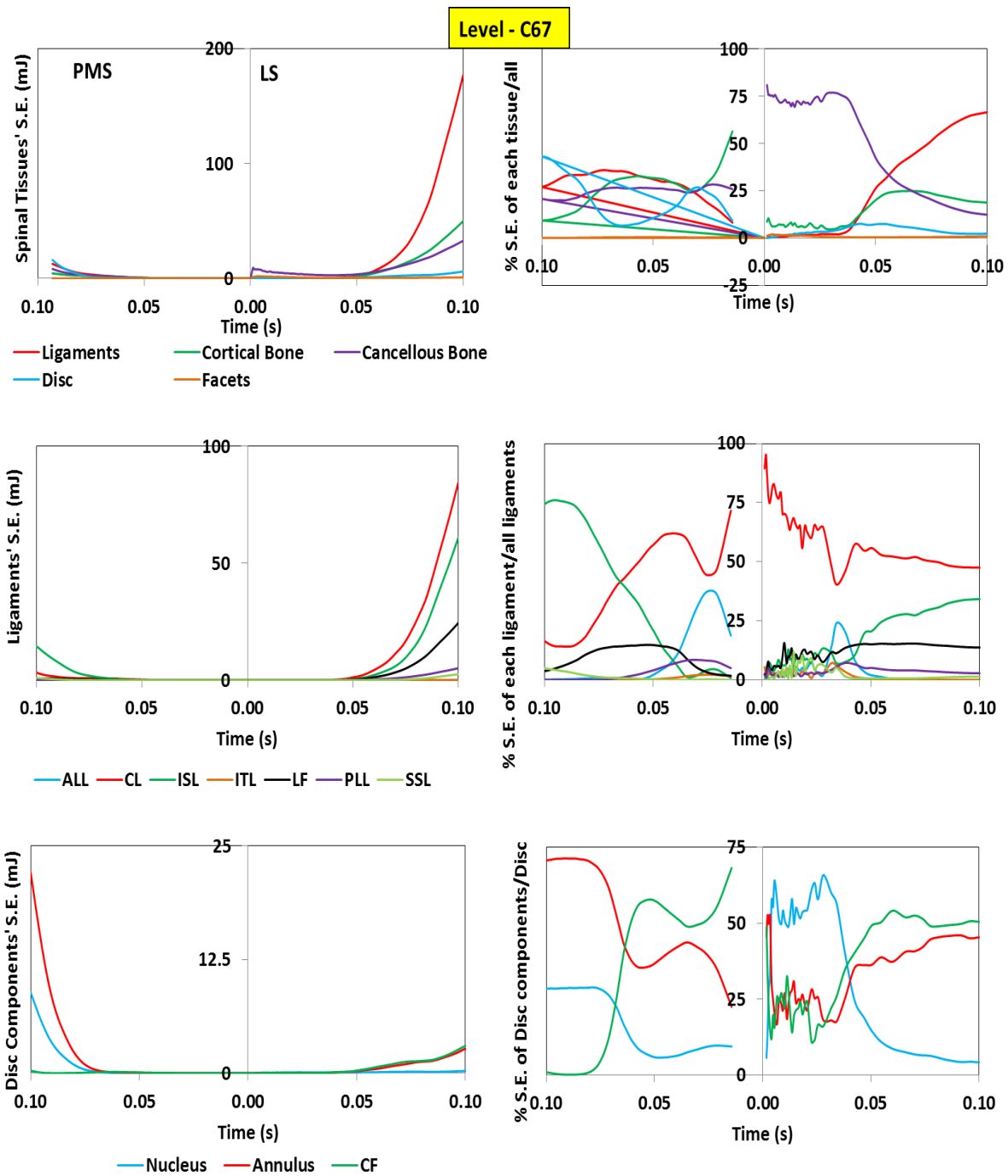


Figure 7.23 S.E. distribution in the spinal level C67 predicted by the LS and PMS models during 5G frontal impact.

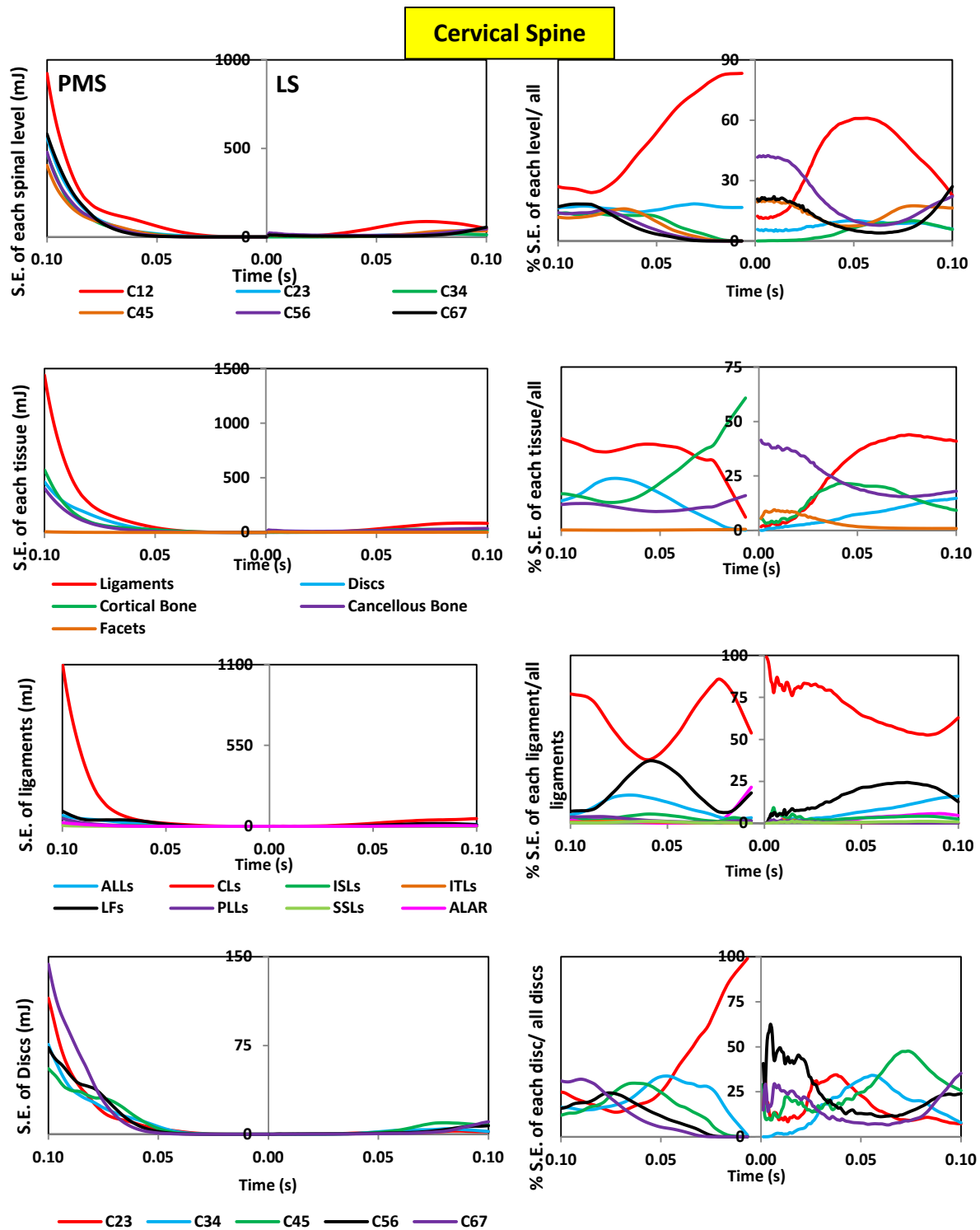


Figure 7.24 Cervical spinal load sharing based on Strain Energy (S.E.): The magnitude and percentage of contribution of S.E. of each spinal level in comparison to all other levels; the magnitude and percentage of S.E. in each spinal tissue and in comparison to all other tissues, the S.E. of each ligament group and its percentage compared to the other ligaments, respectively, predicted by the LS and PMS models resulting from 5G rear-end impact.

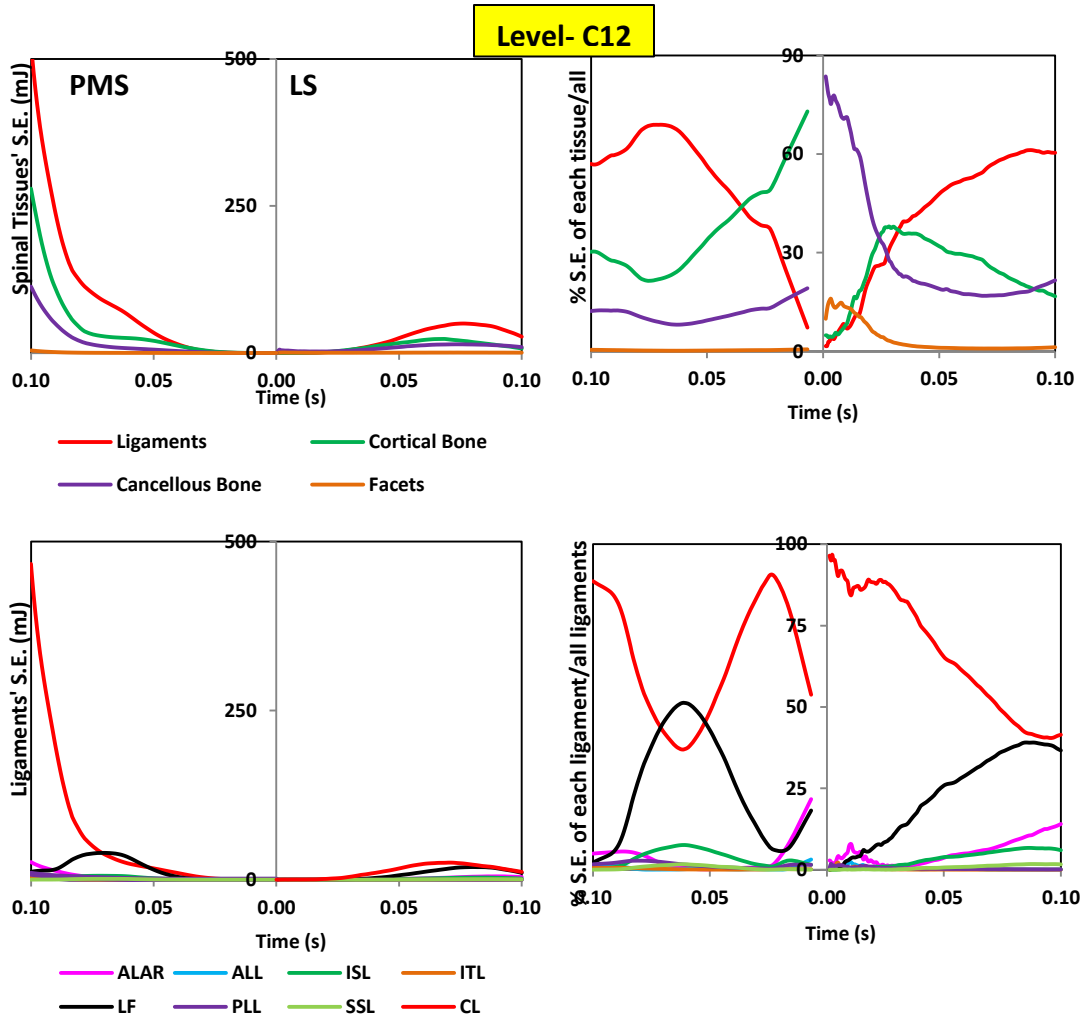


Figure 7.25 S.E. distribution in the spinal level C12 predicted by the LS and PMS models during 5G rear-end impact.

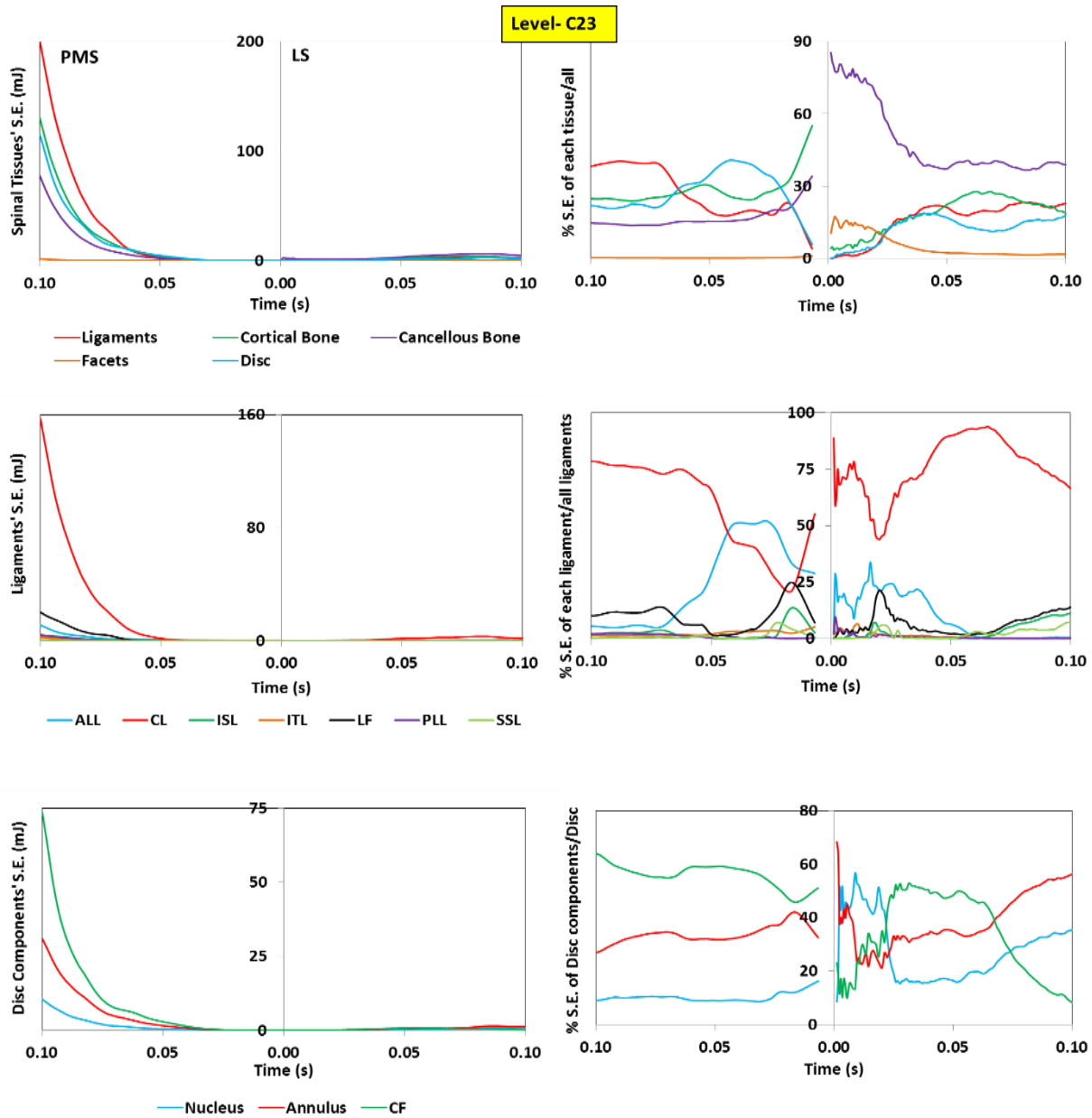


Figure 7.26 S.E. distribution in the spinal level C23 predicted by the LS and PMS models during 5G rear-end impact.

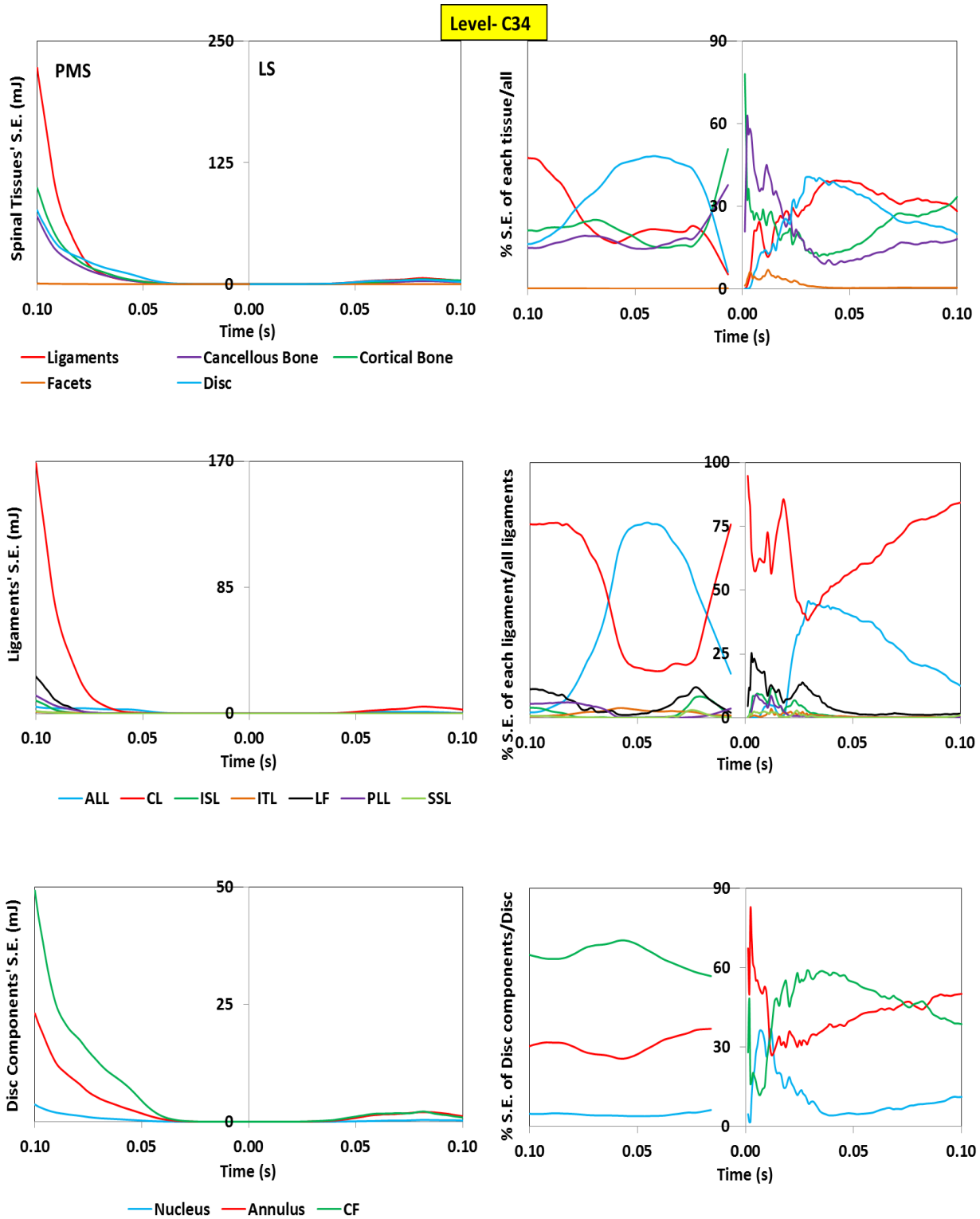


Figure 7.27 S.E. distribution in the spinal level C34 predicted by the LS and PMS models during 5G rear-end impact

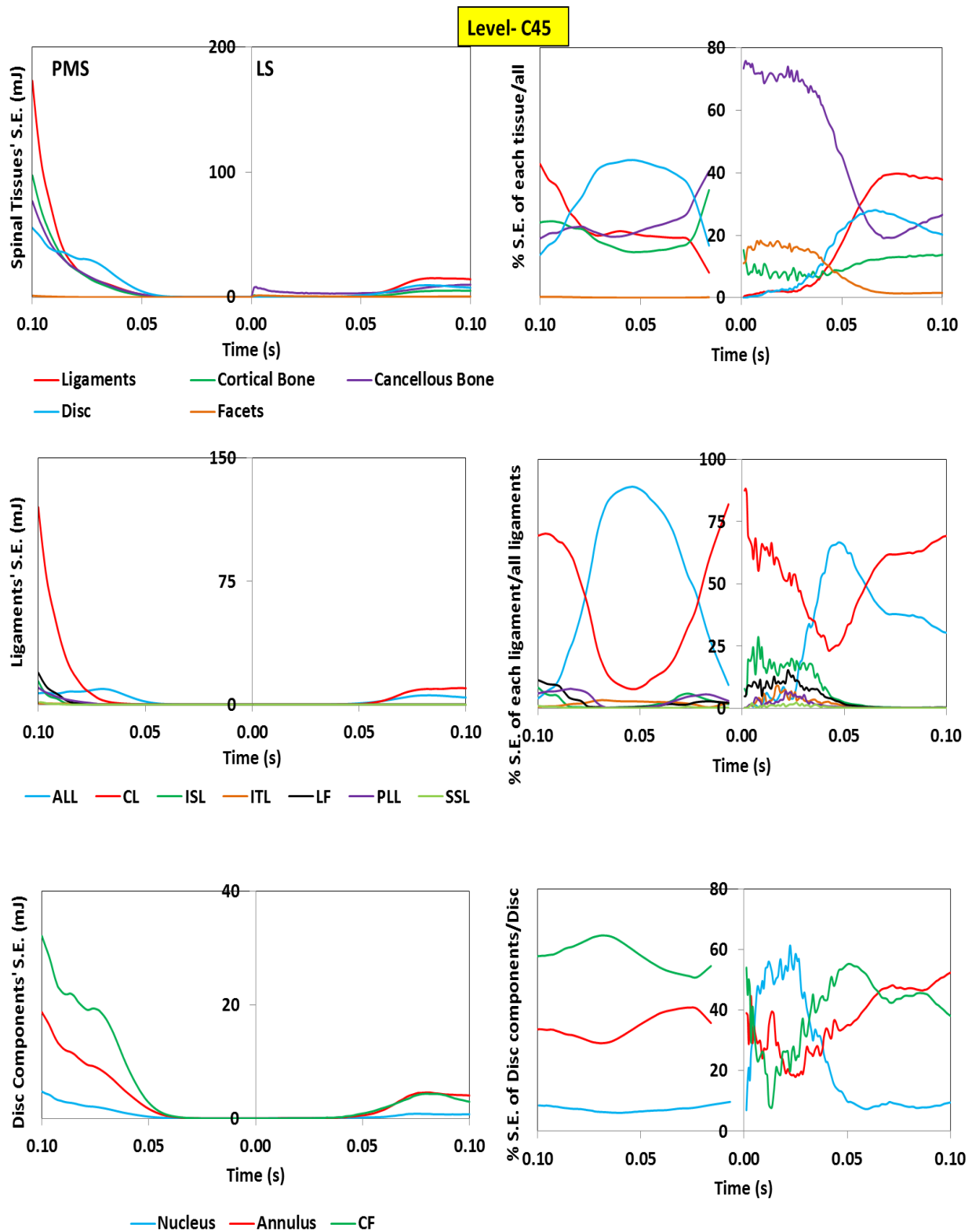


Figure 7.28 S.E. distribution in the spinal level C45 predicted by the LS and PMS models during 5G rear-end impact.

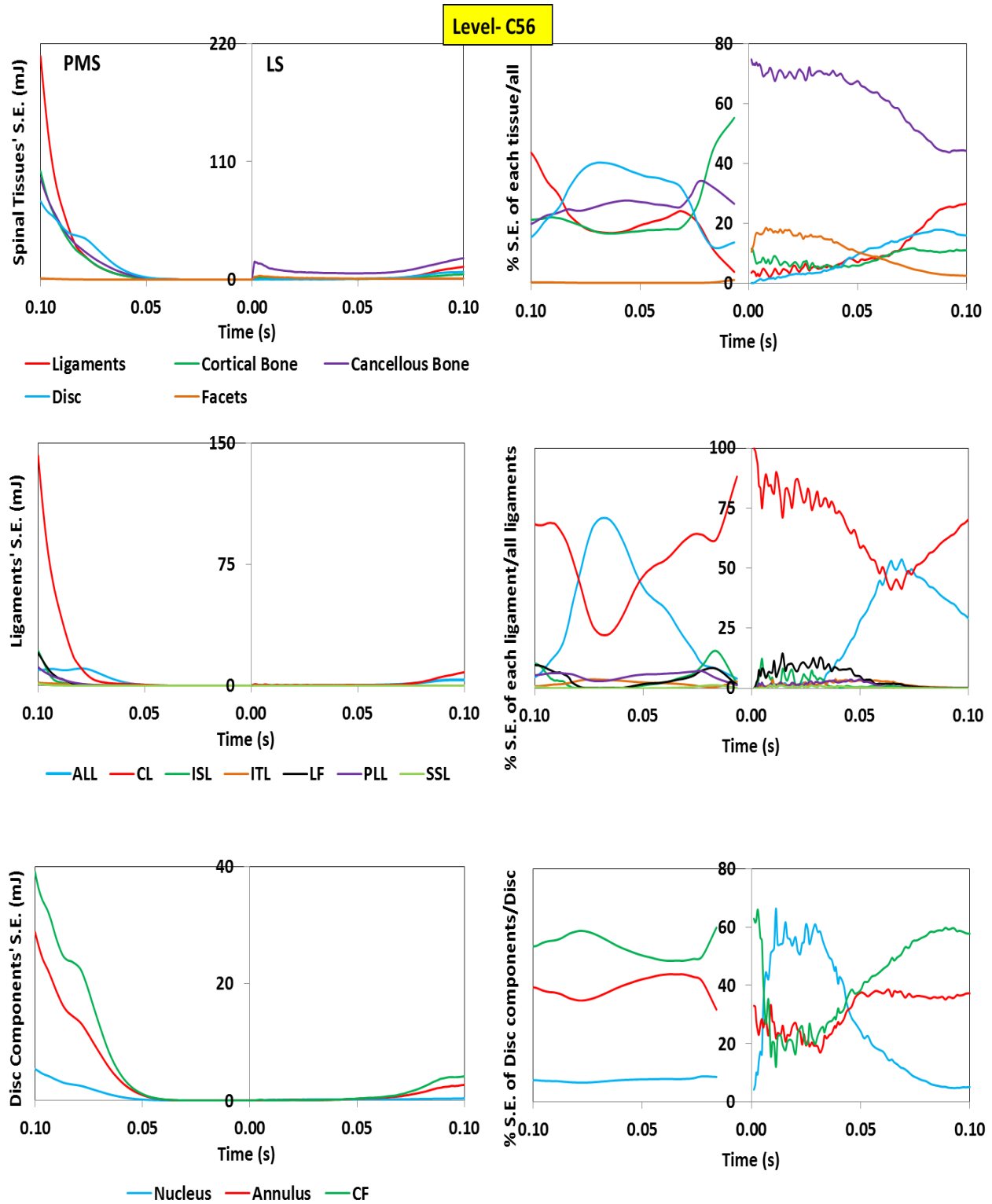


Figure 7.29 S.E. distribution in the spinal level C56 predicted by the LS and PMS models during 5G rear-end impact.

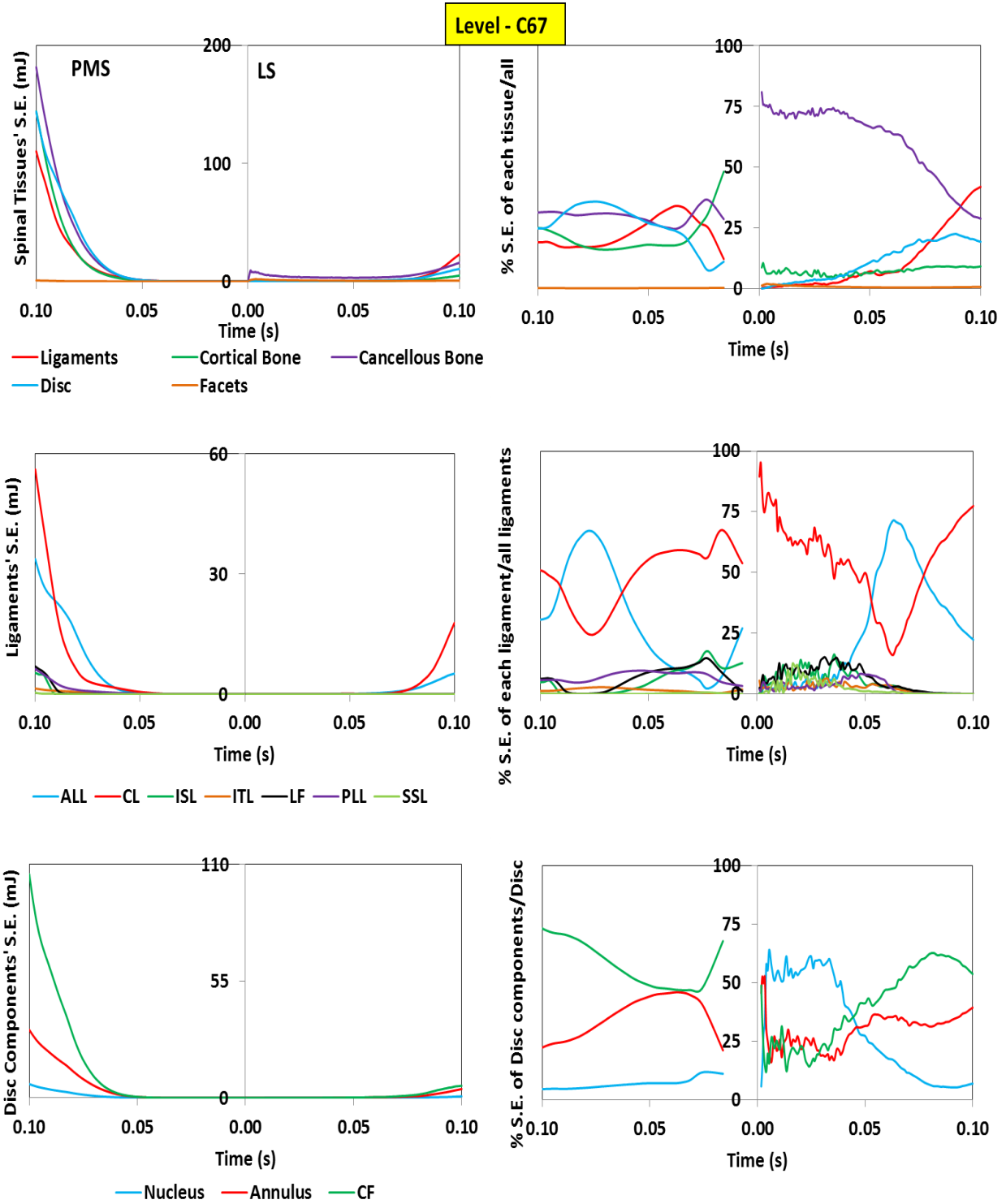


Figure 7.30 S.E. distribution in the spinal level C67 predicted by the LS and PMS models during 5G rear-end impact.

7.3.5 Energy Distribution in the Cervical Muscles

The energy distribution in the cervical muscles during frontal impacts of different peak accelerations, from 1G to 8G, was plotted and compared to the results reported by Hedenstierna and colleagues (Hedenstierna *et al.*, 2009) (Fig. 7.31). The current work predicted less energy in the splenius than did the previous study by Hedenstierna and colleagues. Furthermore, the sternocleidomastoid and semispinalis energies predicted here are greater than the values reported in the aforementioned work. Trapezius energy was also smaller at most of the time points.

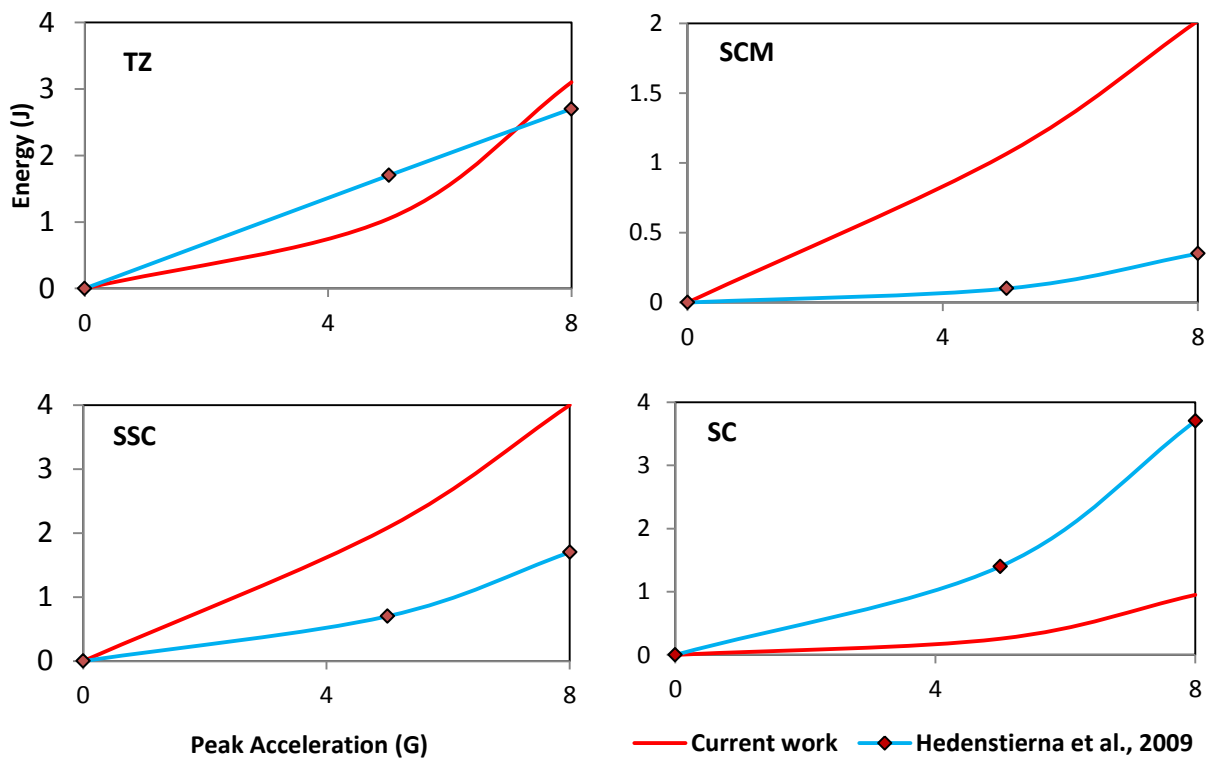


Figure 7.31 Peak muscle energy vs. peak acceleration during frontal impact scenarios. The current model results for Trapezius (TZ), Sternocleidomastoid (SCM), Splenius (SC), and Semispinalis (SSC) were compared with the results reported by Hedenstierna *et al.* (2009).

In addition, table (7.1) summarized the percentage of the energy in each muscle in comparison to the energy contained in all muscles during the frontal and rear impact scenarios. The peak of the accelerations did not affect the percentage of contribution of each muscle during the impact, whereas the direction of impact did.

During the frontal impacts, the contribution of the TZ and SSC muscles were equivalent to one another and had the highest contributions. During the rear impact scenarios however, the contribution of the TZ muscle was significantly greater than other muscles.

Table 7.1 %Energy in each muscle/All muscles

Muscle	8G		5G	
	Frontal	Rear-end	Frontal	Rear-end
TZ	34.3	48.4	36.5	49.8
SCM	19	18.8	18.5	19.2
SC	8.9	6.7	8.9	6.4
SSC	37.7	25.9	36.1	24.8

7.4 Discussion and Conclusion

The main objective and contribution of this case study was to add the 3D cervical passive musculature to the validated ligamentous spine that was explained in Chapter Six. To assess the effects of passive musculature on the spinal response to frontal and rear-end impact loading conditions, the stress and strain distributions in the UCS and LCS ligaments were measured and compared against previous experimental and numerical studies (Panjabi *et al.*, 2004; Panzer *et al.*, 2011) (Fig. 7.7). Adding the passive musculature reduced the peak stress and strain in some ligaments such as the CL ligament and brought the results of the current model closer to the

predictions reported in previous studies. However, results of the LF ligament were smaller than those previously published. The strain distributions in the anterior and posterior parts of IVDs were in good agreement with the previous studies (Ito *et al.*, 2005; Panjabi *et al.*, 2004; Panzer *et al.*, 2011) (Fig. 7.8).

Moreover, the contact pressure and force magnitudes in the FJs decreased when the musculature added to the LS model. Severity and direction of impact affects the magnitude and pattern of contact pressure and force in the FJs at different cervical levels.

Analyzing the energy distribution in each muscle revealed that the magnitude of the peak acceleration did not affect the percentage of each muscle contribution in comparison to all muscles. While the SSC and TZ muscles had the highest contribution in the frontal impact scenarios, the TZ contribution was significantly greater than other muscles during the rear impact scenarios (Table 7.1).

It should also be noted that because the origin and insertion of the constructed muscle are located at various locations along the cervical spine (Table 2.3), the constructed muscles do not have an origin and insertion point at every cervical spinal level. The muscles were therefore, not considered in the S.E. load sharing calculations. Instead, a comparison of the predictions contained in the LS and PMS models allowed for investigating the effects of the muscles on the load sharing along the cervical spine.

The main limitation of this study was the small number of constructed muscles. Due to the poor quality of MR images derived from the Visible Human Project, only the largest posterior muscles that had the largest Physiological Cross Sectional Area (PCSA) were constructed (TZ,

SCM, SC, SSC). This limitation might affect the cervical spine Range of Motion (ROM) in frontal and rear-end impact conditions. This limitation may also affect the percentage of the contribution of each muscle, and the magnitude of energy in each muscle. The S.E. of the spinal levels, as well as the S.E. of the entire spine predicted by the LS model were greater than the values predicted by the PMS model during frontal impact; the opposite was found in rear-end impact scenarios. This could be due to the posterior location of the constructed muscles which facilitated the movement of the spine in the posterior direction during the rear-end impact. The constructed muscles were also shown to reduce the ROM during the frontal impact.

CHAPTER EIGHT: INVESTIGATING THE EFFECT OF THE CERVICAL MUSCULATURE ON THE BEHAVIOR OF THE CERVICAL SPINE USING A NEW 3D CONTINUUM CONSTITUTIVE MODEL CONSIDERING BOTH ACTIVE AND PASSIVE MECHANICAL PROPERTIES OF THE CERVICAL MUSCULATURE

8.1 Problem Description

In the preceding research, the effect of the passive musculature on the cervical spine response during impact loading conditions was investigated. However, the effect of both active and passive behaviors of the musculature on the cervical spine response has not been studied yet. In fact, a 3D continuum computational model suitable for study of the spinal musculature is still a challenge. The objective of this study was to investigate the effect of the muscle activation on the overall kinematics of the spine and its individual tissues response to various impact loading conditions. This was done using a developed and validated continuum muscle model including both active and passive parts of the skeletal muscle (explained in Chapters Three and Four). The results predicted by the PMS model were compared to the results predicted by a spine with the new muscle model, a spine we have named the Full Musculature Spine (FMS).

All the results presented in this chapter were based on the material properties and their units used on the published works of Mustafy and colleagues (Mustafy et al., 2014a, b; Mustafy et al., 2016). However, due to unit discrepancies in their work, stress unit was found to be wrong. To have a consistence set of units, stress unit must change from MPa to KPa. Moreover, the UMAT developed and published by Spyrou and Aravas (2011) was used as material model for simulating the spinal muscle.

8.2 Material Properties, Loading and Boundary Conditions

For convenience, a brief summary of the developed continuum material model for the muscle, and also the validation procedure of the cervical spine under rear-end impact loading condition is presented here.

8.2.1 Cervical Muscle Material Properties

The muscle fibers generate two types of forces: active and passive. While the active force is a function of the activation level, fiber length, and velocity of contraction, the passive force is just a function of the fiber length.

$$\sigma_{\text{muscle fibers}} = \sigma^{\text{active}} + \sigma^{\text{passive}} \quad (8.1)$$

$$\sigma^{\text{active}} = \sigma_{\text{max}} f_a(t) \cdot f_l(\epsilon^f) \cdot f_v(\dot{\epsilon}^f) \quad (8.2)$$

$$\sigma^{\text{passive}} = f_p(\epsilon^f) \quad (8.3)$$

where σ_{max} is the maximum isometric stress in the fiber, f_a is the activation function that relates the pattern of the activation to time, f_l is the length function that shows the relation between the active stress and the fiber nominal longitudinal strain, ϵ^f , and finally, f_v is the velocity function that shows the effect of velocity of contraction or nominal longitudinal strain rate on the overall nominal longitudinal stress of the fiber.

Central Nervous System (CNS) sends electrochemical stimulation signals down to receptors in the muscles and causes the muscle contraction in response to external stimuli. Sending the signals down to the muscle receptors takes some time called the delay time. Each muscle reaches full activation level at a specific instance. The full activation time depends on the severity and direction of the external loads, the time duration of applying the external load, the

location of the muscle in the spine, and its synergy with other muscles. Furthermore, Electromyography (EMG) is a common way to measure the percentage of activation of each muscle amongst all the involved muscles in a specific movement (Kumar *et al.*, 2002; Kumar *et al.*, 2004; Siegmund and Inglis, 2016; Gabriel *et al.*, 2004; Siegmund *et al.*, 2007; Hedenstierna *et al.*, 2009). In this study, the delay time and the full activation time for all the constructed muscles (TZ, SSC, SC, and SCM) were assumed to be zero and 40 milliseconds, respectively. The activation function, f_a , includes all the aforementioned information (see Chapter Four).

Muscle fibers are surrounded by fatty components called connective tissue. Similar to the fibers, the connective tissue produces the passive force. An isotropic linear hyperelastic material model governed the connective tissue in this work (Spyrou and Aravas, 2011).

$$\boldsymbol{\sigma}_{\text{connective tissue}} = \frac{1}{J} \mathcal{L}^e : \boldsymbol{\varepsilon}^{\text{ct}} \quad (8.4)$$

where J is the determinant of the deformation gradient tensor, and \mathcal{L}^e is the elasticity tensor which related the stress to the strain the connective tissue to the connective tissue.

and finally, total stress in the muscle is assumed to be the sum of stresses in the fibers and the connective tissue:

$$\boldsymbol{\sigma} = \boldsymbol{\sigma}_{\text{muscle fibers}} + \boldsymbol{\sigma}_{\text{connective tissue}} \quad (8.5)$$

See Chapters Three and Four for more information about this material model. Subroutine UMAT was used to implement the developed material into the software ABAQUS. Due to the high strain rate of the muscle fibers (high contraction velocity) the muscle elements experienced large deformation within a small period of time. To avoid instability and numerical

convergence problems that encountered during the running time, the FMS model was subjected to low energy impact loading scenarios (up to 4G frontal and rear-end impact conditions).

8.2.2 Cervical Spine Kinematics Validation during Rear-End Impact

The FMS model was validated against existing data from volunteer corridors (Davidsson *et al.*, 2001; Ewing *et al.*, 1976) and previous numerical studies investigating head kinematics (Hedenstierna *et al.*, 2007) under 4G rear-end impact loading scenario.

To simulate the impact, periodic pulse was applied to the centroid of the T1 vertebra in anterior direction. T1 was fixed to prevent movement in directions other than the one under investigation. To avoid instability of the spine under compressive load in the absence of the muscle activation at the beginning of the impact, the gravity effect was ignored. However, a mass of 3.58 Kg was assigned to the centroid of the skull to consider the inertia effect (Carlsson *et al.*, 2014).

8.3 Results

8.3.1 Cervical Spine Validation during Rear-End Impact Results

The global head kinematics subjected to 4G rear-end acceleration impact was validated against existing data from volunteer corridors and previous numerical studies investigating head kinematics (Davidsson *et al.*, 2001; Ewing *et al.*, 1976; Hedenstierna *et al.*, 2007) (Figs. 8.1a, 8.1b).

Although the posterior displacement of the head relative to the T1 predicted by the FMS model was stiffer than that predicted by the PMS model, the results predicted by both models were

consistent with the results reported in the volunteer corridors during the majority of the impact time. Moreover, the models herein tested showed more acceptable agreement with the volunteer corridors results in comparison to the previous numerical study (Hedenstierna *et al.*, 2007) (Fig. 8.1a).

The rotation of the head around the x-axis relative to the extension of T1 predicted by the FMS was consistent with the data reported in the volunteer corridors in the majority of the impact time, while the PMS model predicted more rotation for the head (Fig. 8.1b).

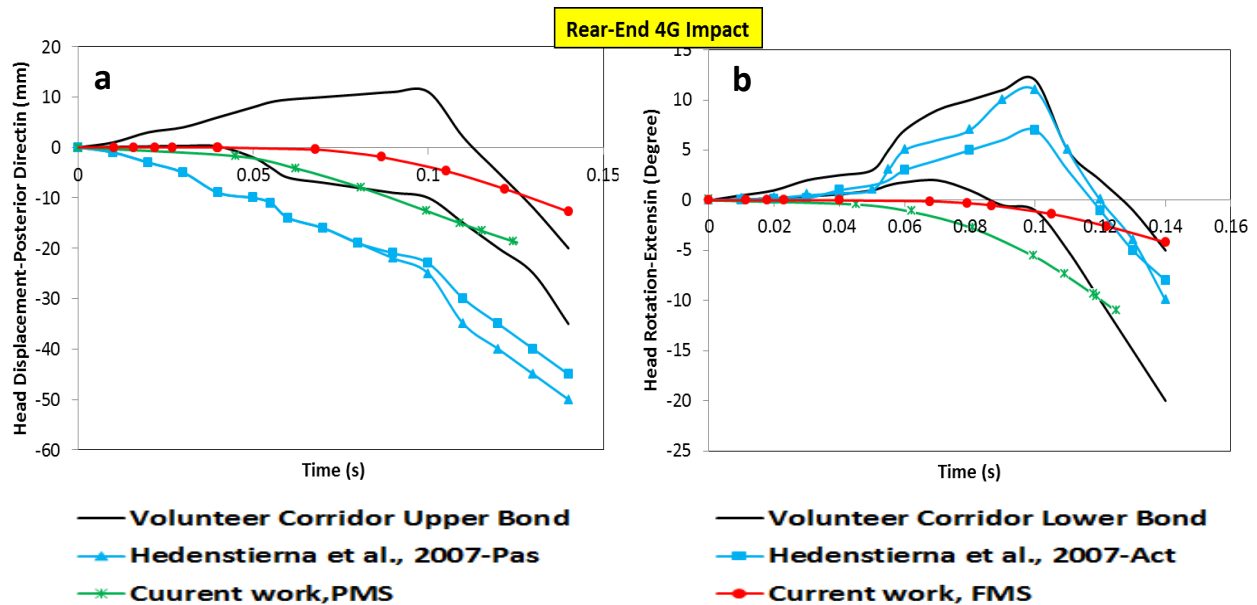


Figure 8.1 (a,b) Posterior displacement of the head relative to the T1 and rotation of the head around the x-axis relative to the extension of T1 predicted by the FMS and PMS models are validated against volunteer corridors, and compared to results reported by a numerical study.

8.3.2 Effect of Muscles Contraction-only on the Spinal Tissues Behaviour

To see the effect of muscle contraction on the behaviour of spinal tissues, the cervical muscles were contracted for 40 milliseconds without applying any external load. The skull was fixed. The delay time and fully contraction time were considered as zero and 40 milliseconds, respectively.

Fig 8.2 shows the maximum pressure in the IVDs at different spinal levels. Maximum pressure occurred in the IVD at level C45 (0.125 MPa). Figs 8.3, 8.4 also show the peak strain and stress in the ligaments groups at different levels. The CL ligaments at levels C56 and C45 experienced the highest strain and stress amongst the ligament groups followed by the ISL ligaments at levels C34 and C45.

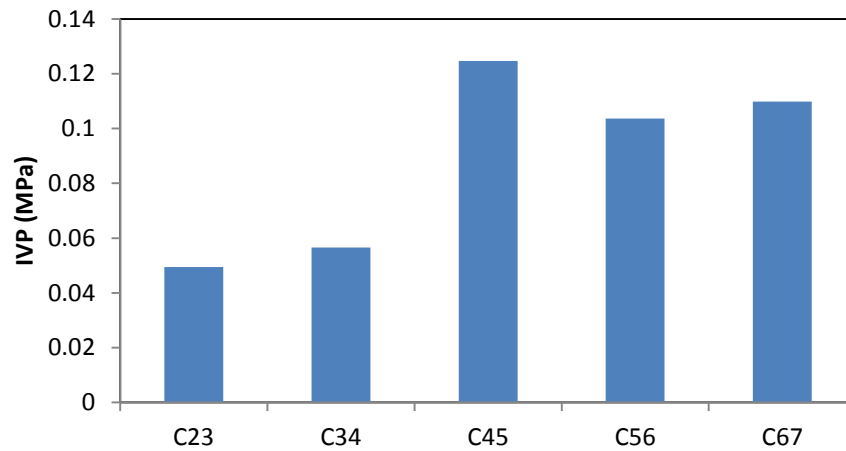


Figure 8.2 Peak pressure in the IVDs at different cervical spinal levels.

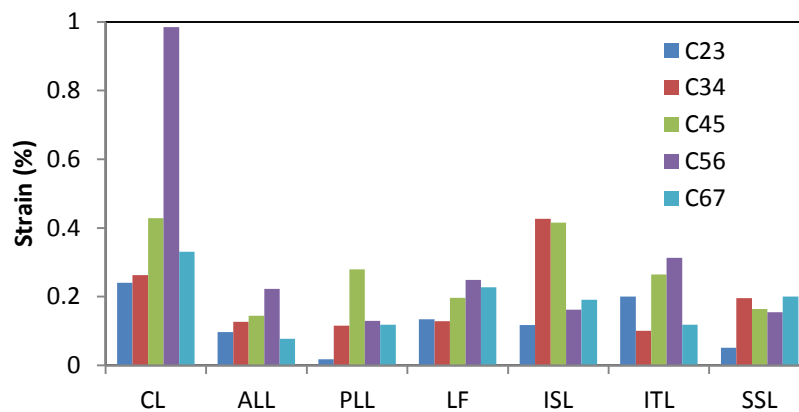


Figure 8.3 Maximum Strain (%) in the ligament groups at different cervical spinal levels.

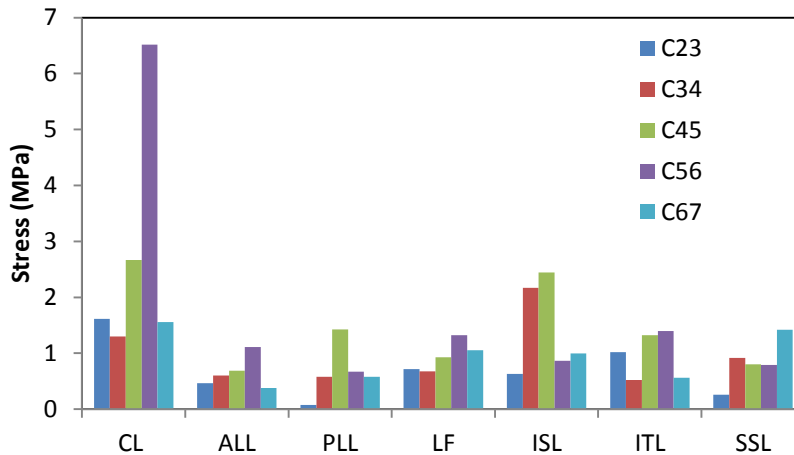


Figure 8.4 Maximum Stress (MPa) in the ligament groups at different cervical spinal levels.

8.3.3 Load Distribution in the Cervical Muscles

The peak force generated by the cervical muscles during 1G frontal impact was compared to the results reported by Hedenstierna and colleagues (Hedenstierna, *et al.*, 2009) (Fig. 8.5). During the frontal impact, the force produced in the splenius (SC) and the trapezius (TZ) muscles was greatest, respectively. During the rear-end impact, the sternocleidomastoid (SCM) generated the highest force amongst the muscles. These findings coincided with EMG results reported by Kumar and colleagues (Kumar *et al.*, 2002), and Schuldt and Harms-ringdahl (Schuldt and Harms-ringdahl 1988).

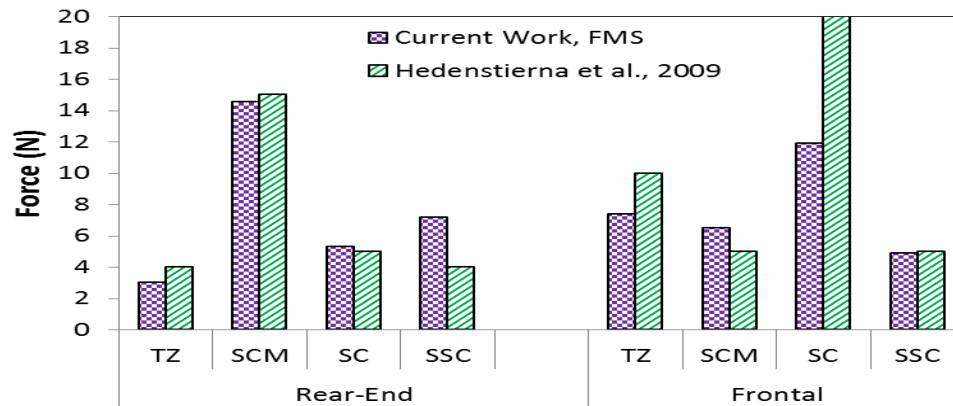


Figure 8.5 Peak force in the cervical muscles predicted by the FMS model and the results reported by Hedenstierna and colleagues during 1G frontal and rear-end impact loading scenarios (Hedenstierna et al., 2009).

8.3.4 Strain and Stress Distributions in the Cervical Ligaments

To investigate the effect of muscle activation on the behavior of the spinal ligaments, the peak stress and strain in the ALL, CL, ISL, LF, PLL, ITL, and SSL ligaments at different cervical spinal levels were compared in the PMS and FMS models during 2G frontal and rear-end impact scenarios. The stress results were also compared to the existing *in-vitro* experimental data (Mattucci *et al.*, 2012).

As shown in Figs. 8.3-8.9, the peak stress and strain in the ligaments were greater in the PMS model than in the FMS model during the rear-end impact, whereas during the frontal impact the peak stress and strain were greater in the FMS in most of the ligaments than in the PMS model. It should be noted that the peak stress and strain values in each ligament at different spinal levels predicted by the PMS and FMS models did not occur at the same instant. Additionally, the thick horizontal blue line indicates the stress failure levels obtained from experimental data (Mattucci *et al.*, 2012).

No failure was noticed in the ALL ligament in either the FMS or PMS as a result of frontal or rear impact scenarios (Fig. 8.6). With the exception of level C23, the peak stress and strain for all levels predicted by the PMS model were greater than those predicted by the FMS model during both frontal and rear-end impact scenarios.

With the exception of level C56 in the PMS model, the CL ligament failed in both PMS and FMS models at all cervical level during the frontal impact. During the rear-end impact, all cervical levels failed in the PMS model, while only level C45 failed in the FMS model. The muscle activation increased the risk of failure at the majority of cervical levels during the frontal impact, while opposite was found during the rear-end impact. Moreover, the highest values of both stress and strain were occurred in the PMS model at level C45 during the rear impact. Level C45 also experienced the greatest stress and strain in the FMS model during the frontal impact (Fig. 8.7).

During the frontal impact, the FMS model predicted failure in the ISL ligament only at level C56, whereas, during the rear-end impact; the PMS model predicted the failure at all levels with the exception of level C23 (Fig. 8.8).

The LF ligament did not fail in both the PMS and FMS models during the frontal impact. During the rear impact, the PMS predicted failure at all cervical levels but C34, whereas the FMS model predicted no failure in the LF ligaments (Fig. 8.9).

No failure was predicted in the PLL ligament by FMS and PMS models during impact scenarios (Fig. 8.10).

No failure stress level was reported for the ITL and SSL ligaments in the aforementioned experimental study. Fig. 8.11 and Fig. 8.12 show the peak stress and strain in the ITL and SSL ligaments predicted by both PMS and FMS models during both impact scenarios.

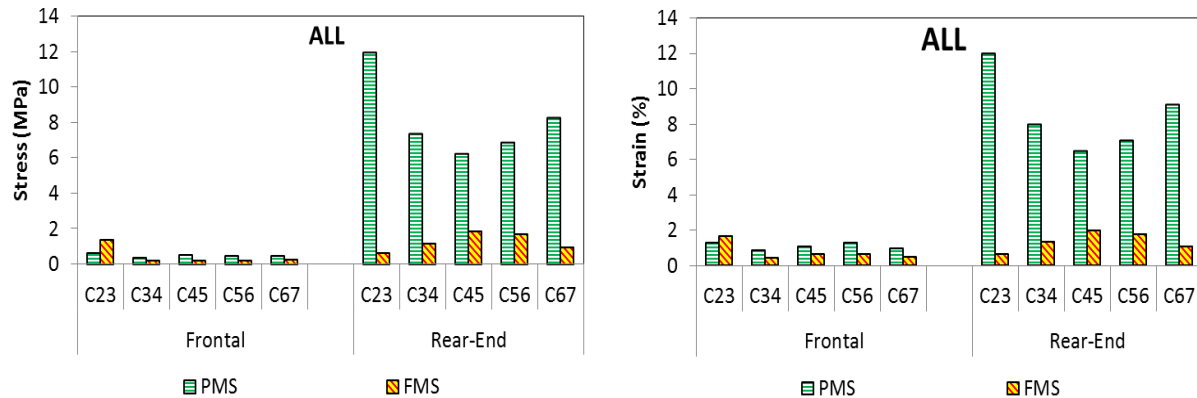


Figure 8.6 Peak stress and strain in the ALL ligaments at different cervical levels predicted by the PMS and FMS models during 2G frontal and rear impacts.

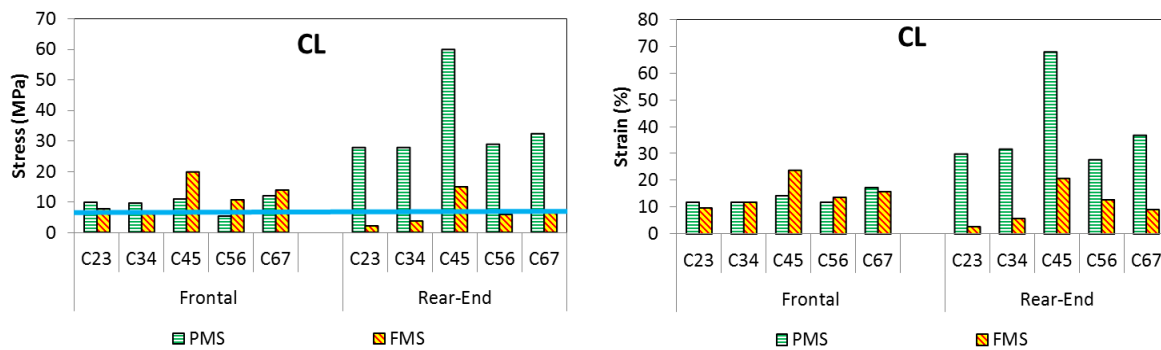


Figure 8.7 Peak stress and strain in the CL ligaments at different cervical levels predicted by the PMS and FMS models during 2G frontal and rear impacts. The thick blue horizontal line indicates the failure stress level obtained from in vitro experimental tests (Mattucci et al., 2012).

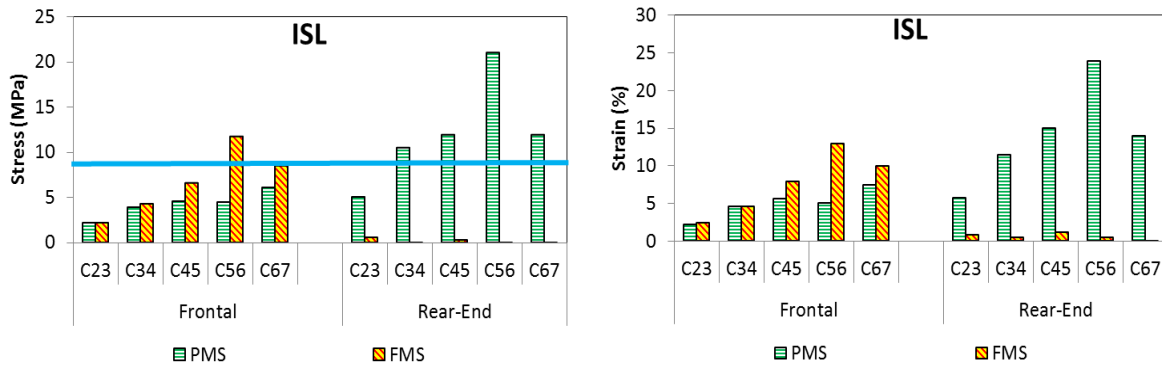


Figure 8.8 Peak stress and strain in the ISL ligaments at different cervical levels predicted by the PMS and FMS models during 2G frontal and rear impacts. The thick blue horizontal line indicates the failure stress level obtained from in vitro experimental tests (Mattucci et al., 2012).

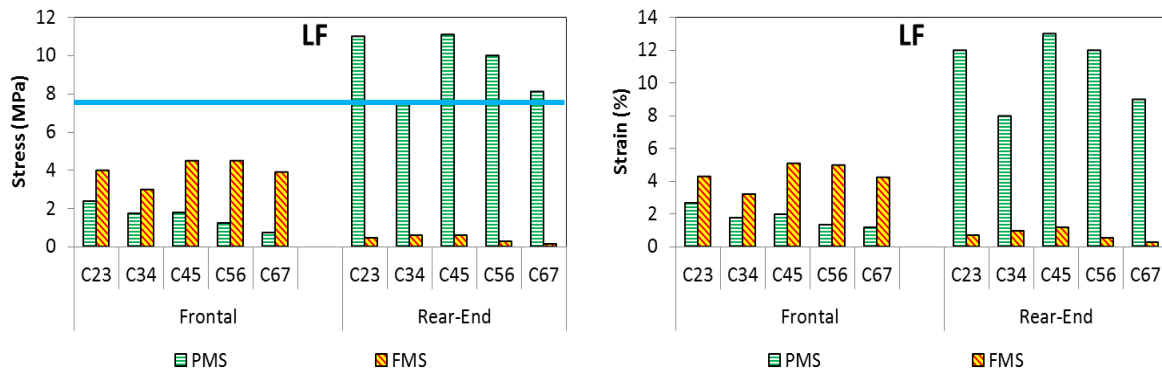


Figure 8.9 Peak stress and strain in the LF ligaments at different cervical levels predicted by the PMS and FMS models during 2G frontal and rear impacts. The thick blue horizontal line indicates the failure stress level obtained from in vitro experimental tests (Mattucci et al., 2012).

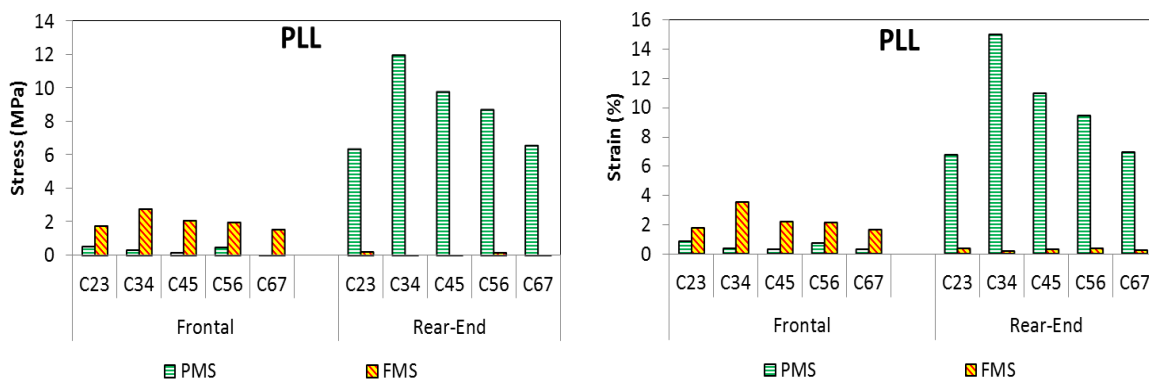


Figure 8.10 Peak stress and strain in the PLL ligaments at different cervical levels predicted by the PMS and FMS models during 2G frontal and rear impacts.

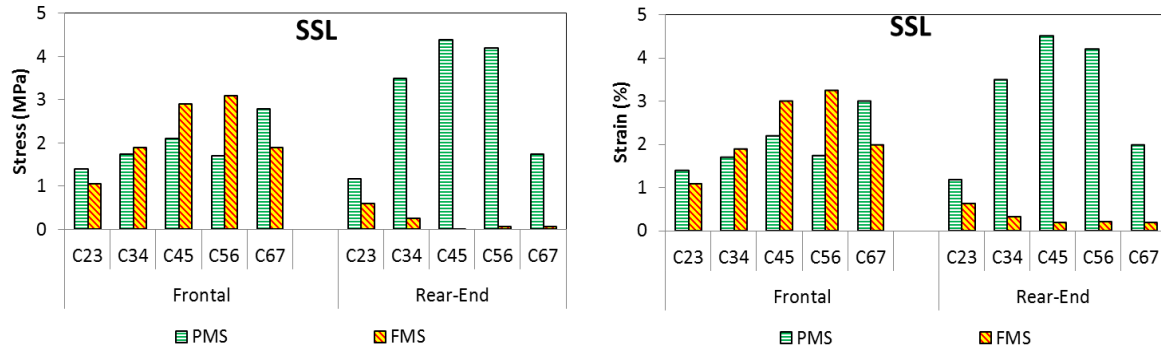


Figure 8.11 Peak stress and strain in the SSL ligaments at different cervical levels predicted by the PMS and FMS models during 2G frontal and rear impacts.

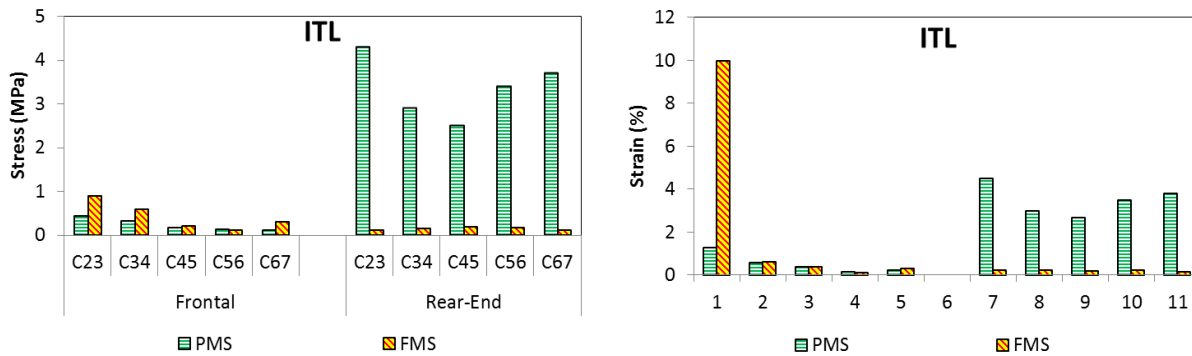


Figure 8.12 Peak stress and strain in the ITL ligaments at different cervical levels predicted by the PMS and FMS models during 2G frontal and rear impacts.

8.3.5 Effect of Muscle Activation on the Pressure Distribution in the Intervertebral Discs

Maximum pressure in the IVDs was measured and compared in both FMS and PMS models during 2G and 4G frontal and rear impacts (Fig. 8.13). During frontal impacts, the PMS model predicted higher pressure in the IVDs than those predicted by the FMS model at all cervical levels; whereas the opposite was predicted in rear-end impact scenarios. Peak pressure occurred in the PMS model at levels C34 and C23 during frontal impact scenarios, respectively. Level C56 experienced the greatest pressure in the FMS model during rear-end impact

scenarios. Fig. 8.14 shows the pressure distribution, the location and the magnitude of the maximum pressure in both models during 4G frontal and rear impact scenarios.

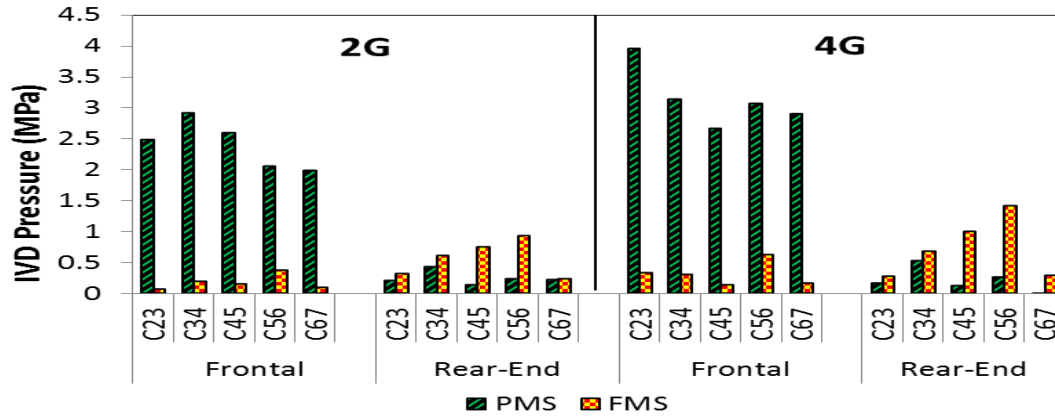


Figure 8.13 Peak pressure in the IVDs at different cervical levels predicted by the FMS and PMS models during 2G and 4G frontal and rear impact loading scenarios.

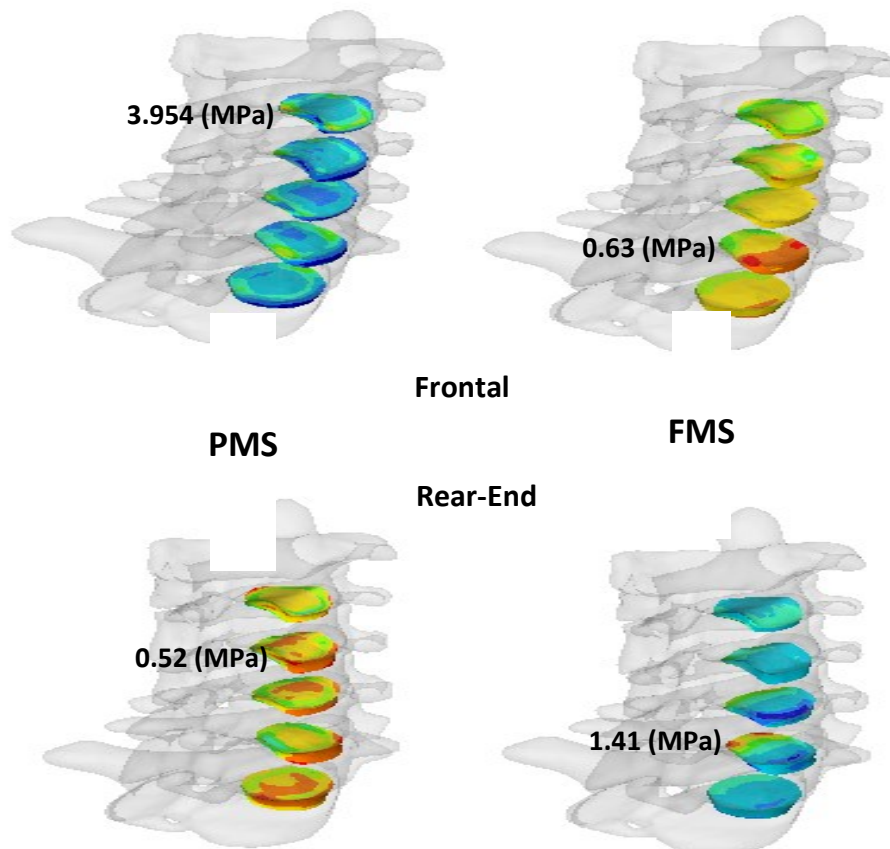


Figure 8.14 A schematic view of the location of the maximum pressure in the IVDs under 4G impact scenarios predicted by the PMS and FMS models.

8.3.6 Contact Force and Pressure in Facet Joints

The contact force and pressure in the Facet Joints (FJ) at different levels were also measured in the PMS and FMS models during 4G frontal and rear-end impact loading scenarios (Fig. 8.15).

During the frontal impact, contact occurred at levels C23, C34, C45, C67, and C7T1 in the PMS model, whereas contact only occurred at level C34 in the FMS model. The magnitude of contact force and pressure decreased with the presence of the muscle activation.

During the rear-end impact, the PMS model predicted contact in the FJs at level C34, while in the FMS model, contact occurred at levels C34, C45, and C67. In addition, the patterns of contact in the PMS and FMS models were different.

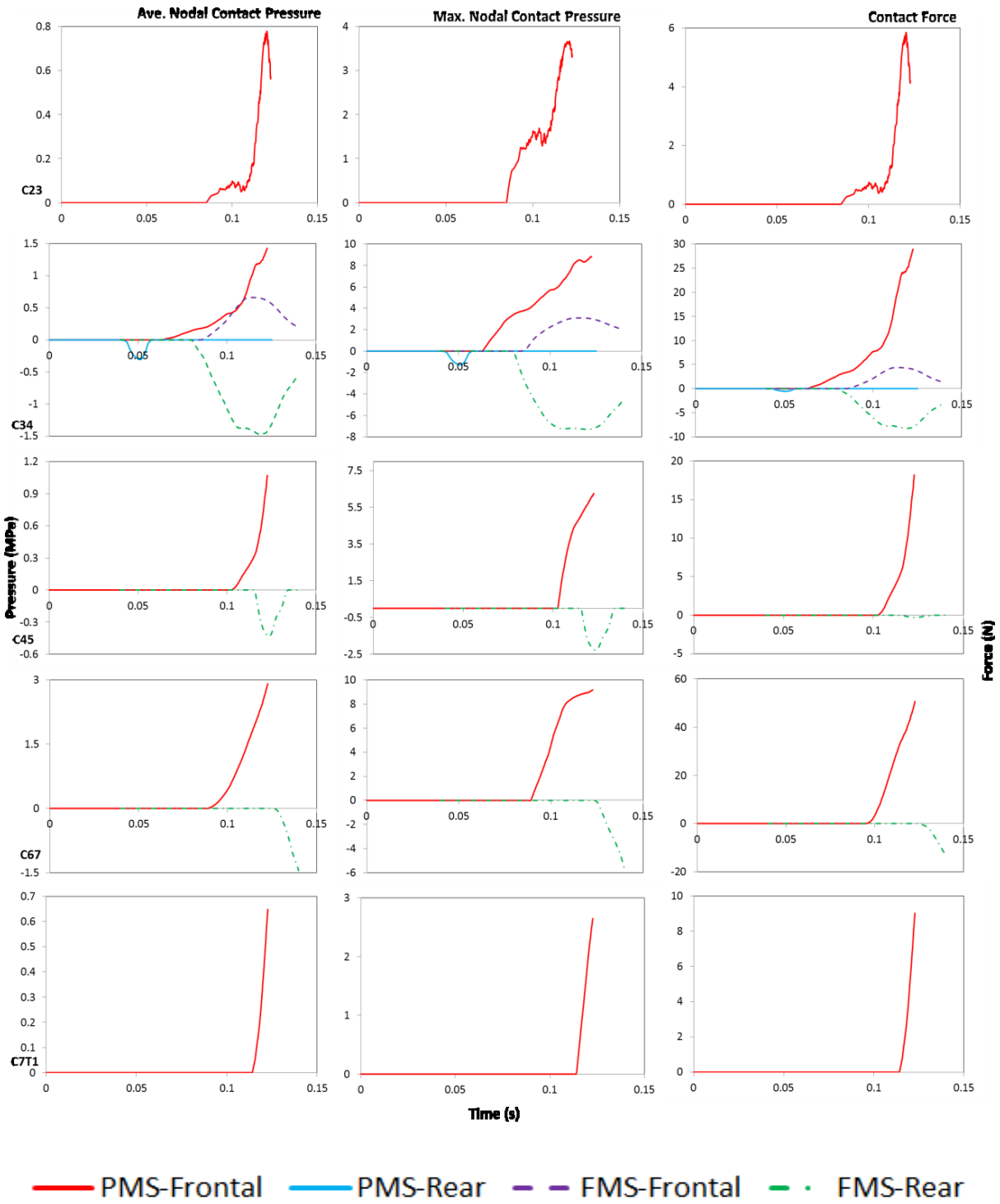


Figure 8.15 Contact average and maximum pressures and contact force at the FJs at different spinal levels during 4G frontal and rear impact loading scenarios. The results predicted by the PMS and FMS models are compared.

8.3.7 Cervical Spinal Load Sharing

Similar to the method discussed in Chapter Six, Section 6.5.7, and Chapter Seven, Section 7.3.4, the concept of Strain Energy (S.E.) was used to investigate effect of the continuum muscle model including both active and passive parts of the muscle on the spinal load sharing during frontal and rear-end impact scenarios. To achieve this goal, results of the PMS and FMS models were compared during 2G frontal and rear-end impacts (Figs. 8.16-8.29). It should be noted that the percentage of contribution of spinal levels and tissues was similar in the PMS and FMS models. Therefore, in this section only the magnitude of the S.E. in the PMS and FMS models were compared. (See Chapter Seven, Section 7.3.4 for the information about the percentage of contribution of the spinal components).

8.3.7.1 Frontal Impact Load Sharing Results

The S.E. predicted in the cervical levels by the FMS model was smaller than those predicted by the PMS model (Fig. 8.16). Moreover, the S.E. of the entire cervical spine predicted by the PMS model was greater than that predicted by the FMS model. Level C12 had the greatest S.E. in comparison to other spinal levels in the PMS model, whereas level C56 had the greatest S.E. in the FMS model at the end of the impact. The ligaments showed the highest S.E. amongst the cervical tissues in both the FMS and PMS models. Specific to the ligaments, the Alar ligament featured the most significant contribution followed by the CL ligament in the PMS model, whereas the CL ligament played a more larger role in the FMS model. In addition, the IVD at levels C23 and C34 had the highest S.E. values in the FMS models at the end of the impact, whereas the IVD at level C67 played the major role in the PMS model (Fig. 8.16).

At level C12, the role of the ligaments increased during the impact period followed by the cortical and cancellous bones in both models. Specific to the ligament, the Alar ligament had the greatest S.E. value during the majority of the impact period, while the S.E. value of the LF ligament exceeded that of the Alar ligament at the end of the impact time in the FMS model. However, the Alar and SSL ligaments had the greatest contributions amongst other ligament in the PMS model (Fig. 8.17).

From levels C23 to C67, the ligaments contribution increased over time in the FMS model, whereas in the PMS model, the IVDs played a more significant role over time (Figs. 8.15-8.19). Specific to the cervical ligaments, and despite the CL ligaments being the main contributor in the FMS model, the contribution of the ISL ligaments exceeded that of the CL ligaments at the majority of the impact time at all cervical levels in the PMS model. However, the CL ligaments had the greatest S.E. values at the end of impact time in both models (Figs. 8.18-8.22).

The role of disc components varied along the spine. While in the FMS model, the annulus and the annular fibers (CF) were the main contributors; in the PMS model, the annulus and the nucleus contribution was more significant than that of the CF at all cervical levels (Figs. 8.18-8.22).

8.3.7.2 Rear-End Impact Load Sharing Results

Similar to the frontal impact, the S.E. predicted by the PMS model was greater at all cervical levels than that predicted by the FMS model in the rear impact. While level C12 experienced the highest S.E. in the PMS model over the impact time period, in the FMS model, the S.E. value at the level C12 decreased after 120 millisecond time point. Furthermore, the contribution of

the CL ligament was the most significant amongst the ligaments in both models. Among the IVDs at different spinal levels, the IVD at level C56 had the highest S.E. value at the end of the impact in the FMS model, and the IVD at level C23 had the greatest value at the end of the impact in the PMS model (Figs. 8.23-8.29).

With the exception of level C23, the FMS model predicted the contribution of the ligaments would be greater than that of other spinal tissues at the majority of impact time followed by the IVDs, the cortical and the cancellous bones, respectively. Similar to the FMS, the PMS model predicted that the ligaments had the highest value of S.E. amongst the cervical tissue. However, the PMS model predicted small contribution of the IVDs in comparison to the one predicted by the FMS model (Figs. 8.23-8.29).

In addition, among the ligaments, the CL ligament had the highest S.E. in both models followed by the ALL and the LF ligaments in the FMS and PMS models, respectively (Figs. 8.23-8.29).

Moreover, specific to the IVD components, both models predicted higher S.E. values for the annulus and the CF than the nucleus during the majority of impact time (Figs. 8.23-8.29).

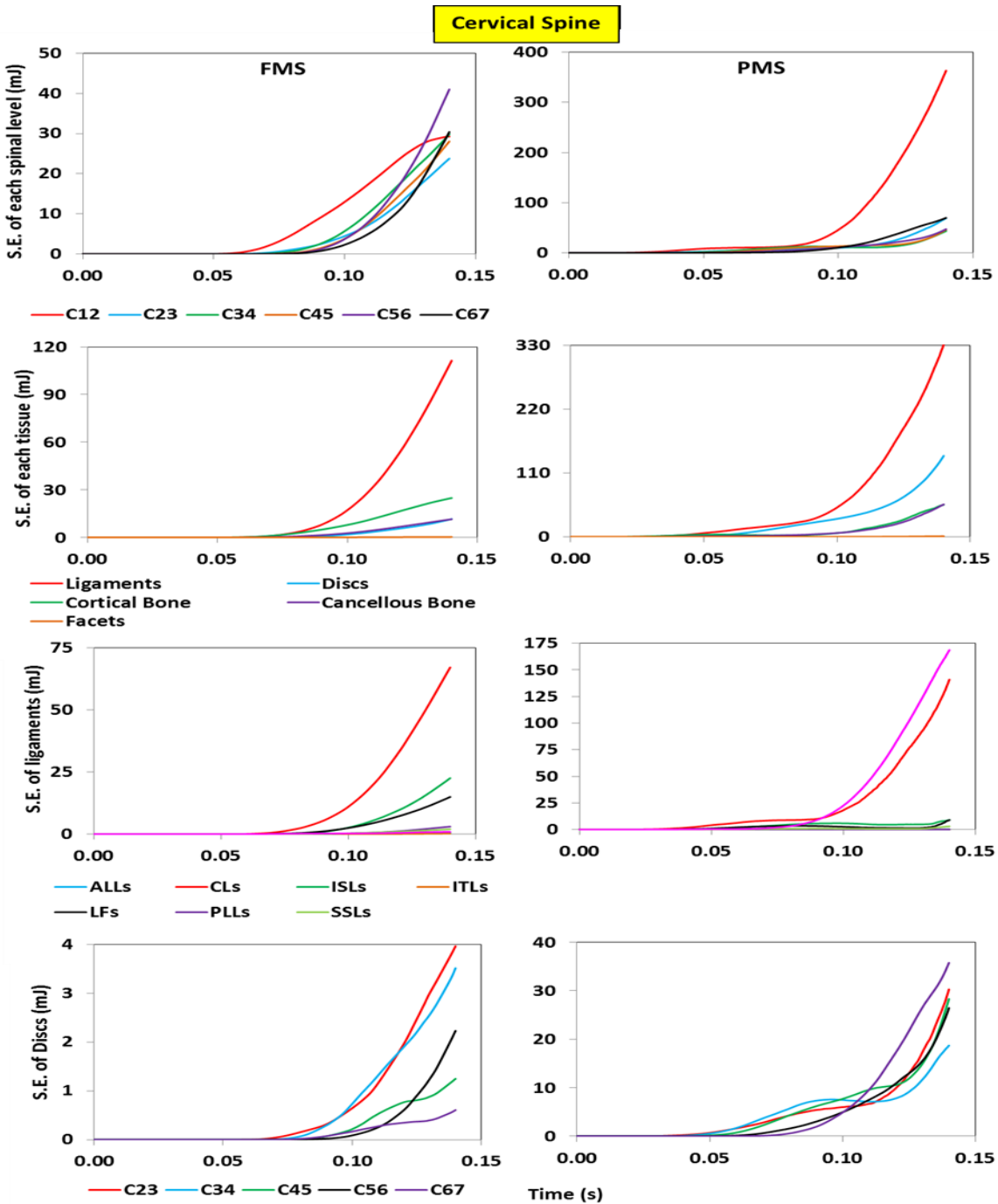


Figure 8.16 Cervical spinal load sharing based on Strain Energy (S.E.). Magnitude of S.E. in each spinal level, Magnitude of S.E. in each spinal tissue, magnitude of cervical ligaments S.E., and magnitude of S.E. in discs at different levels, respectively, predicted by the FMS and PMS models during 2G frontal impact.

Level- C12

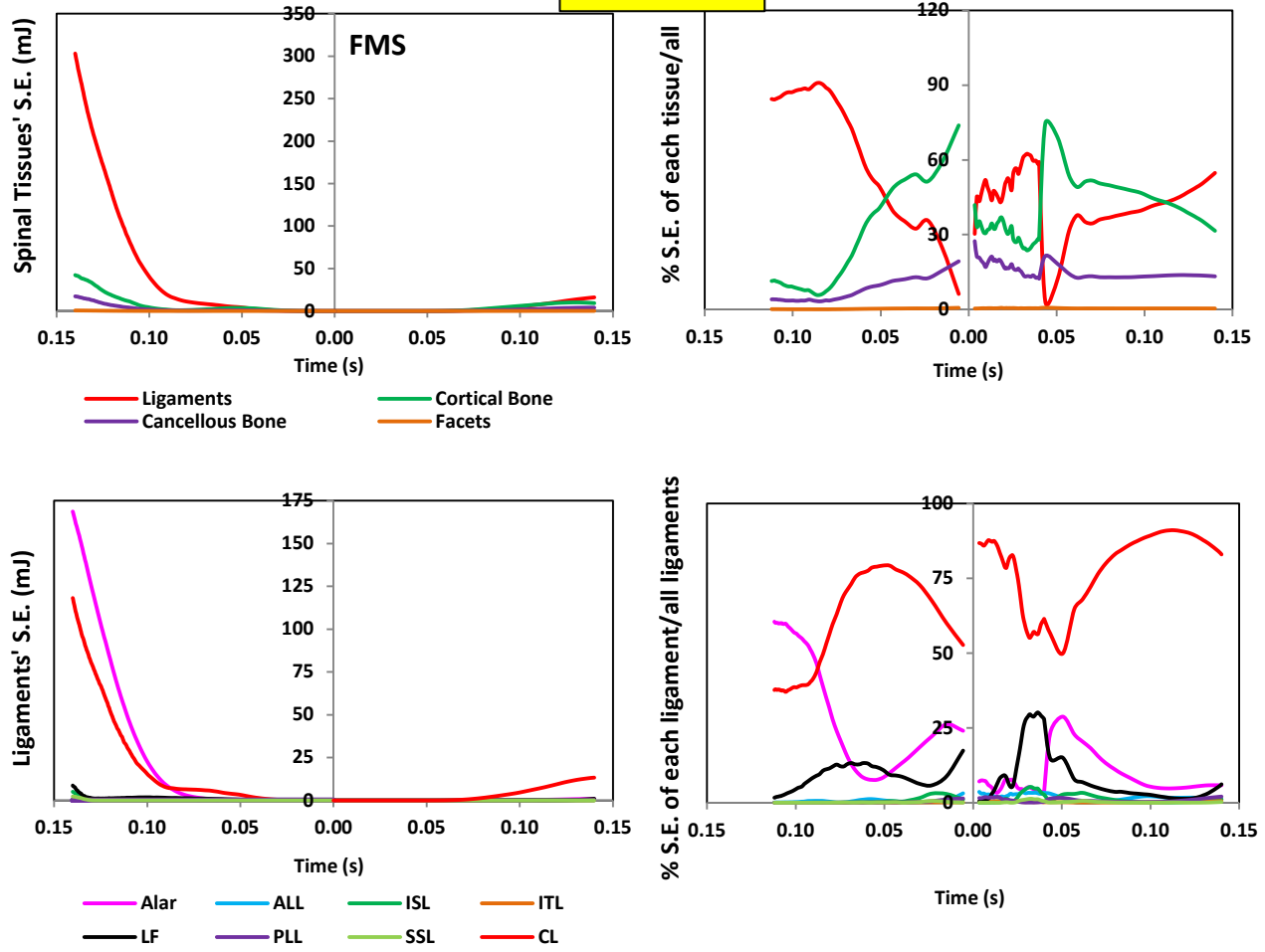


Figure 8.17 S.E. distribution in the spinal level C12 during 2G frontal impact.

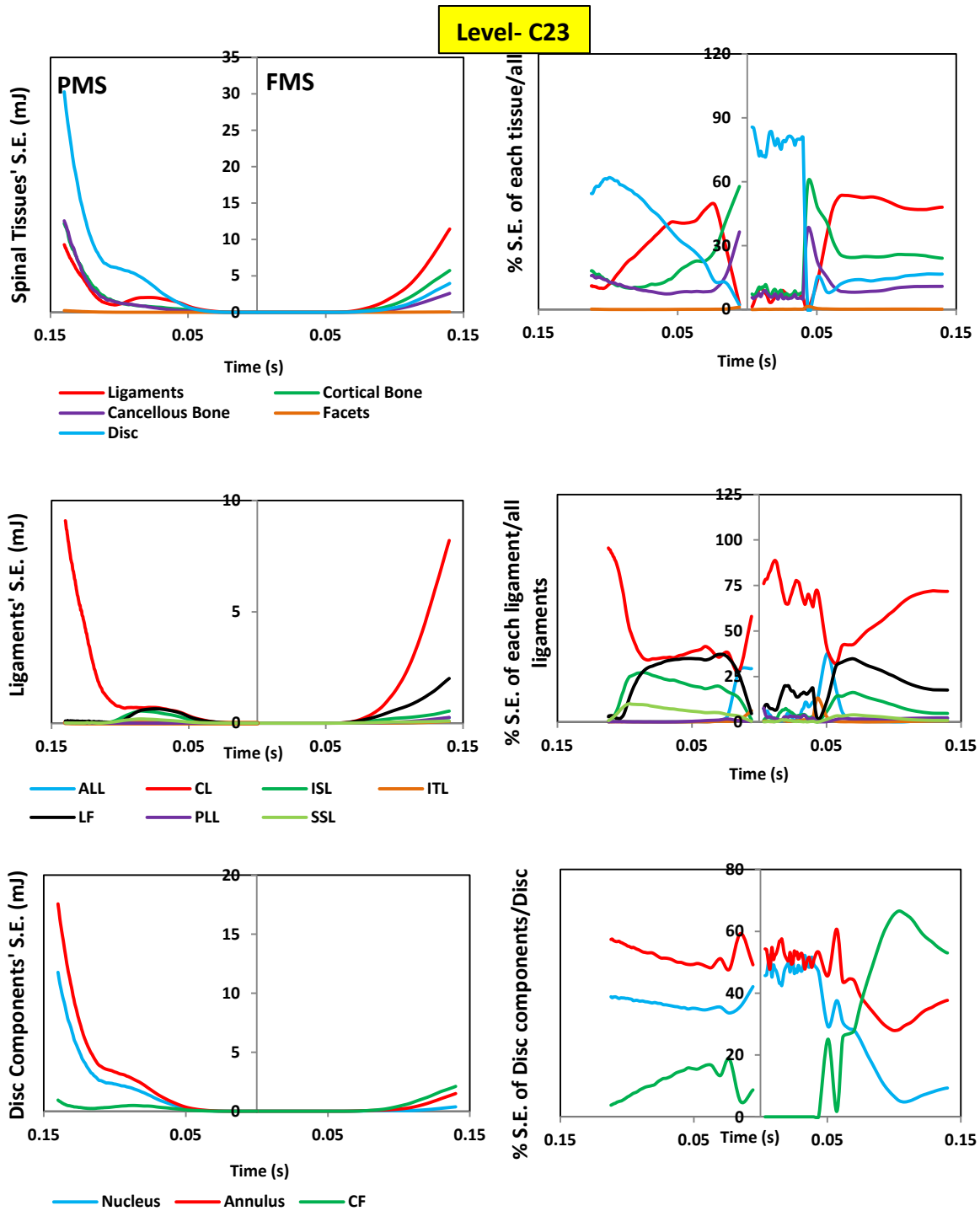


Figure 8.18 S.E. distribution in the spinal level C23 during 2G frontal impact.

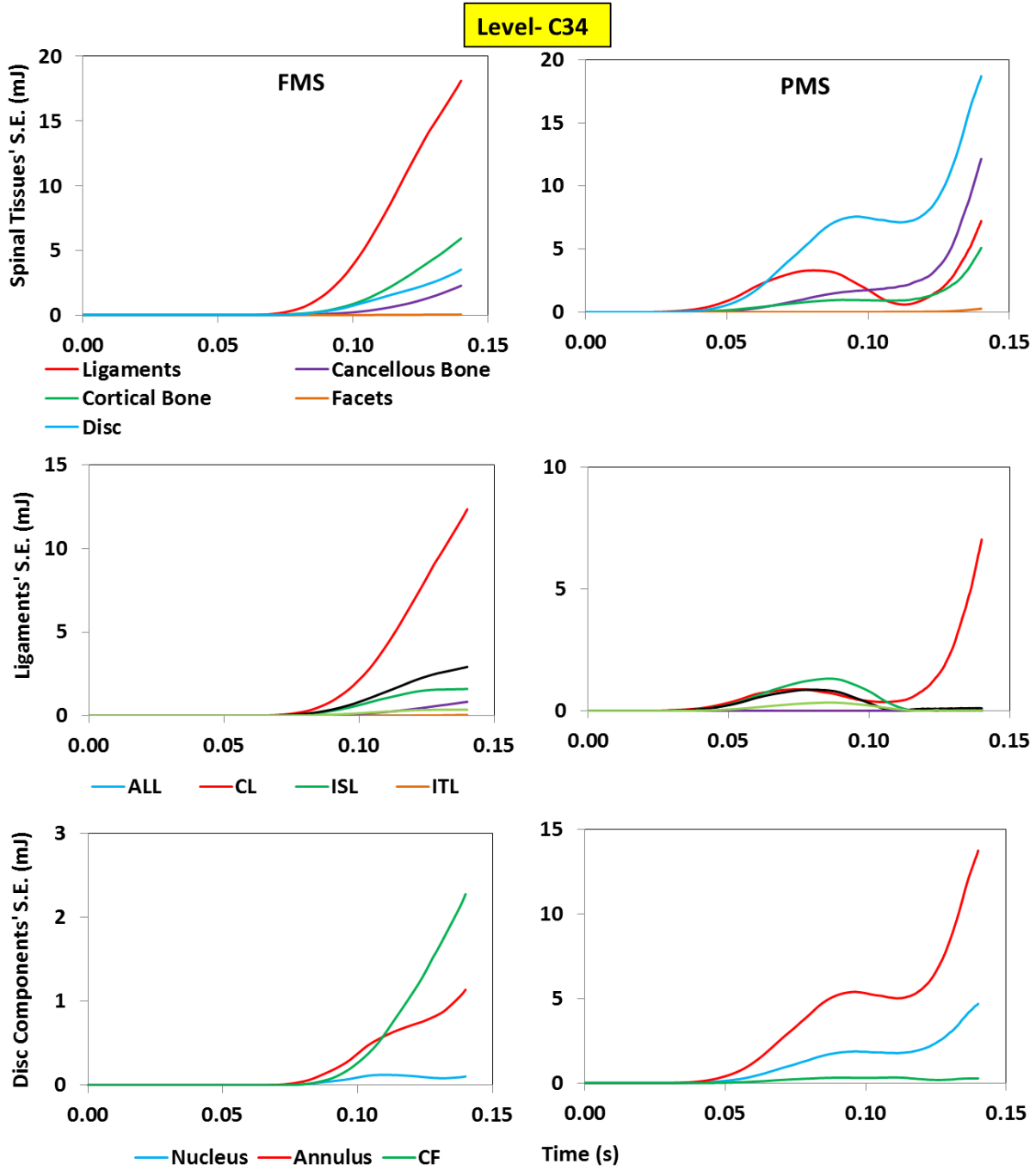


Figure 8.19 S.E. distribution in the spinal level C34 during 2G frontal impact.

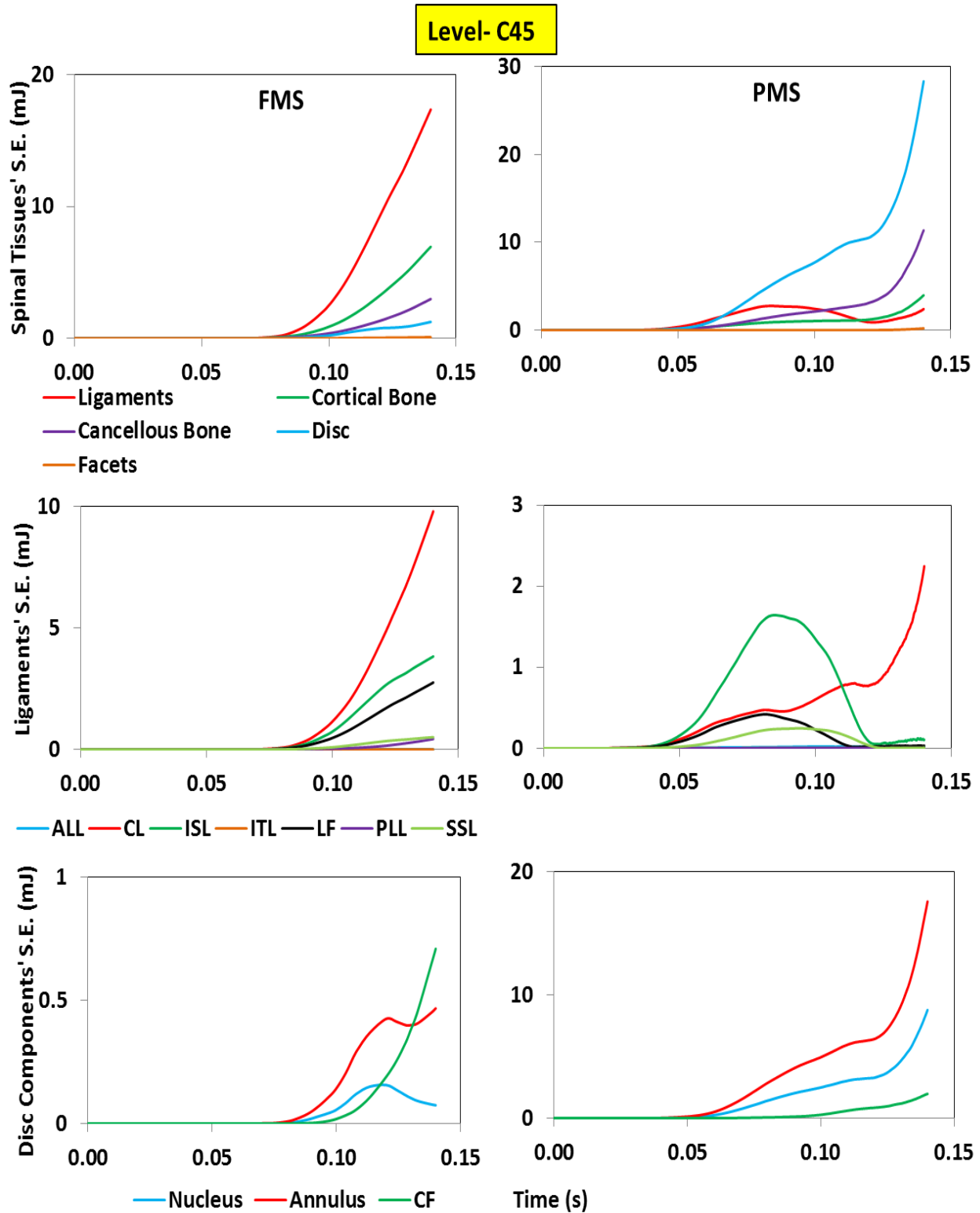


Figure 8.20 S.E. distribution in the spinal level C45 during 2G frontal impact.

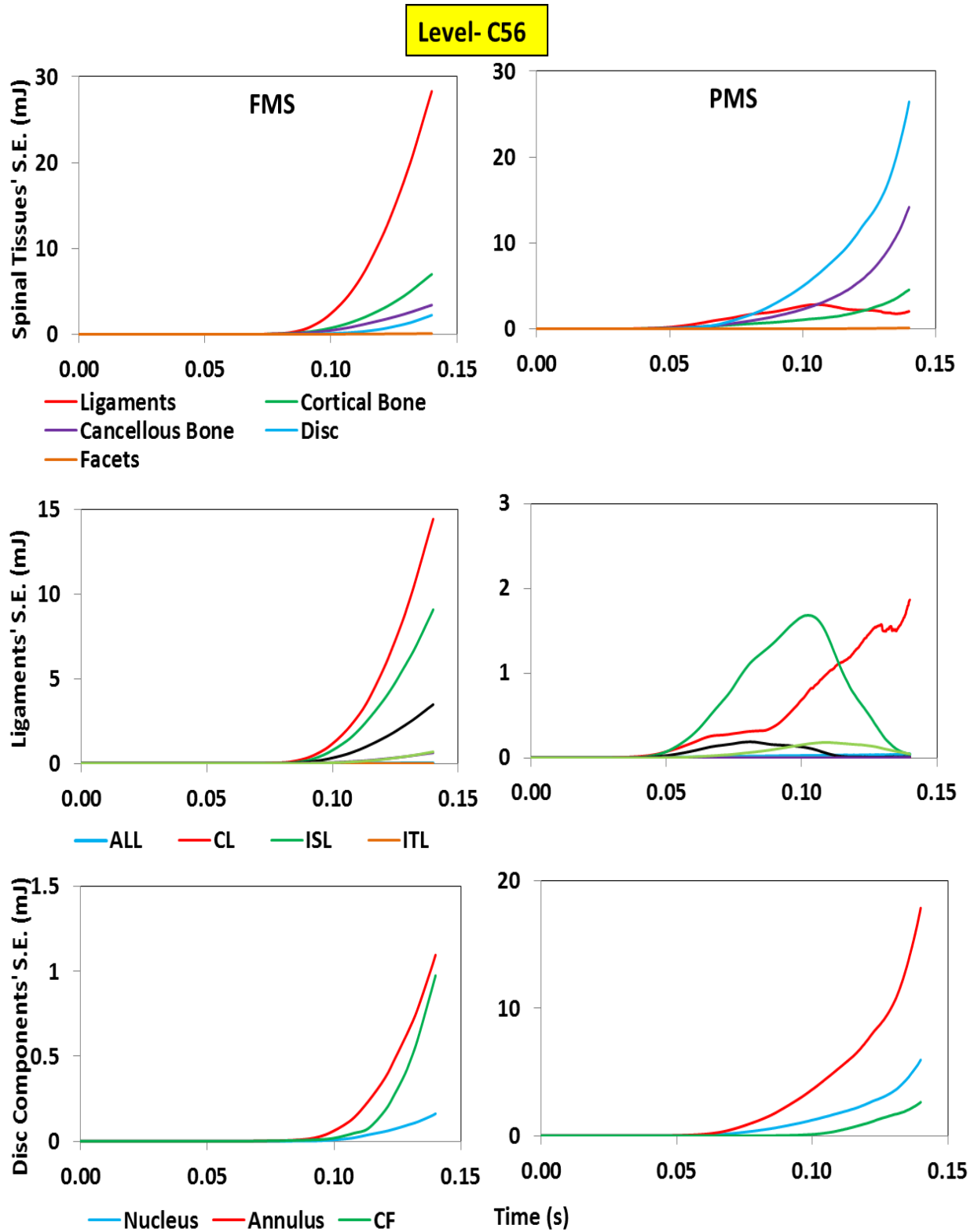


Figure 8.21 S.E. distribution in the spinal level C56 during 2G frontal impact.

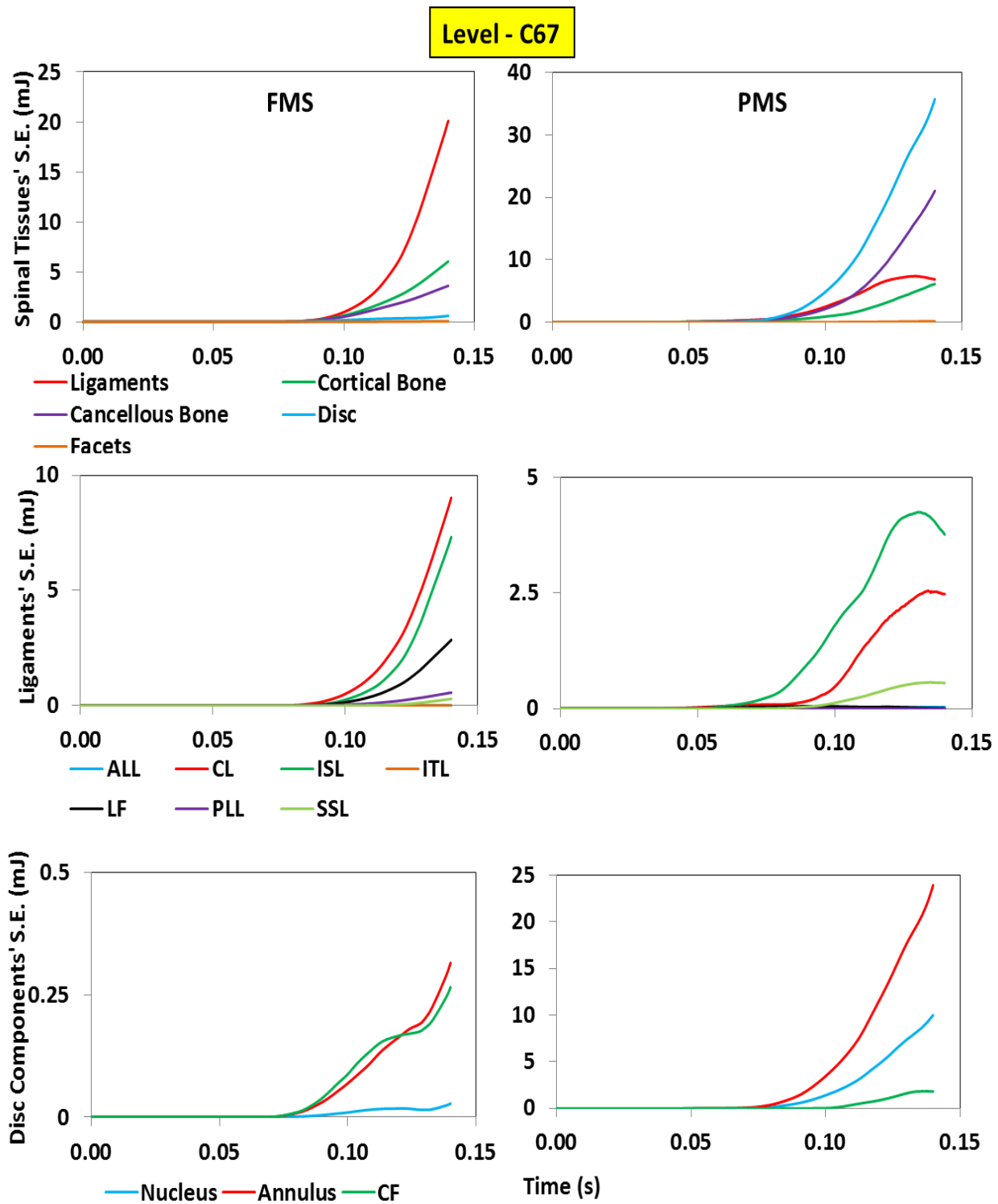


Figure 8.22 S.E. distribution in the spinal level C67 during 2G frontal impact.

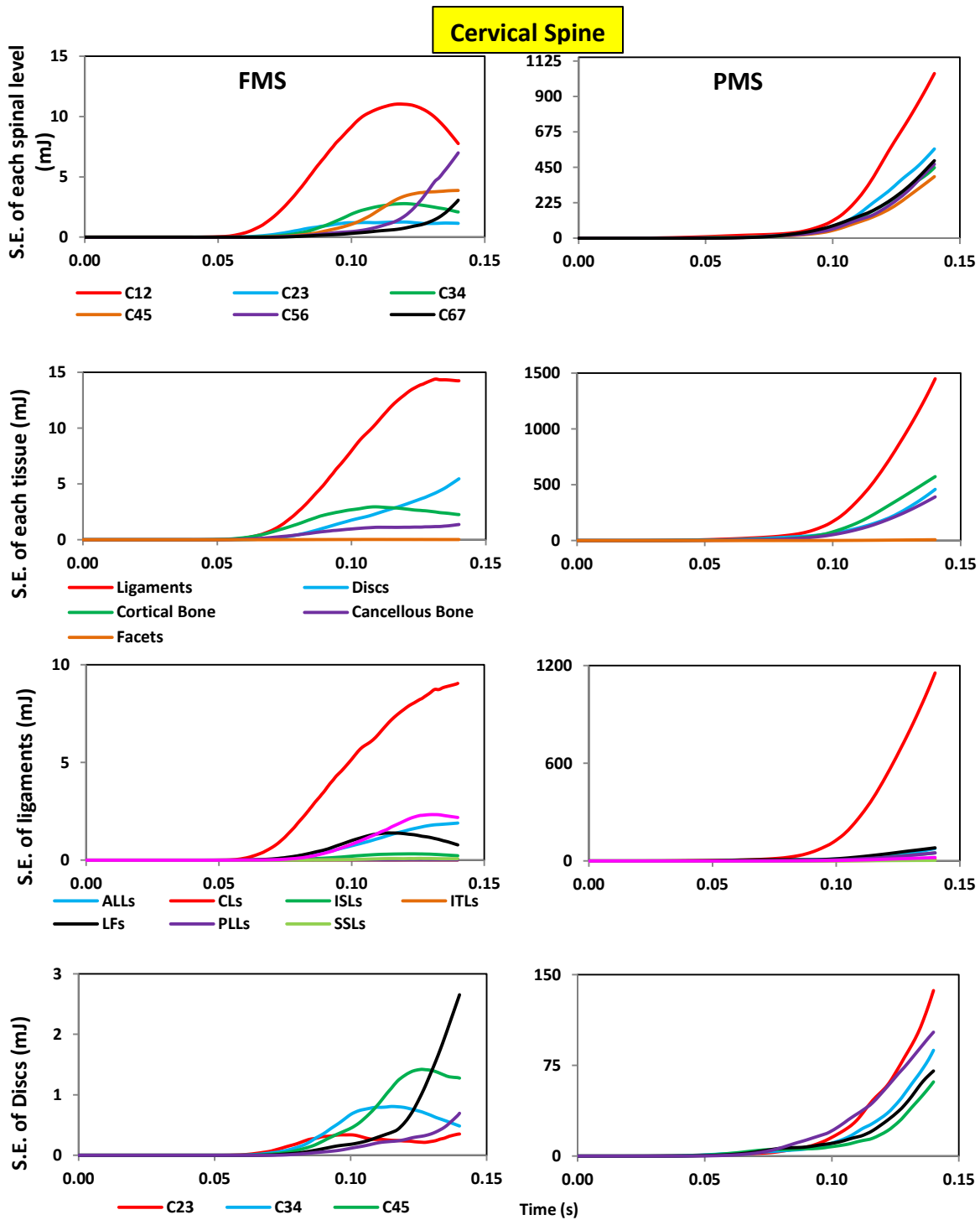


Figure 8.23 Cervical spinal load sharing based on Strain Energy (S.E.). Magnitude of S.E. in each spinal level, Magnitude of S.E. in each spinal tissue, magnitude of cervical ligaments S.E., and magnitude of S.E. in discs at different levels, respectively, predicted by the FMS and PMS models during 2G rear impact.

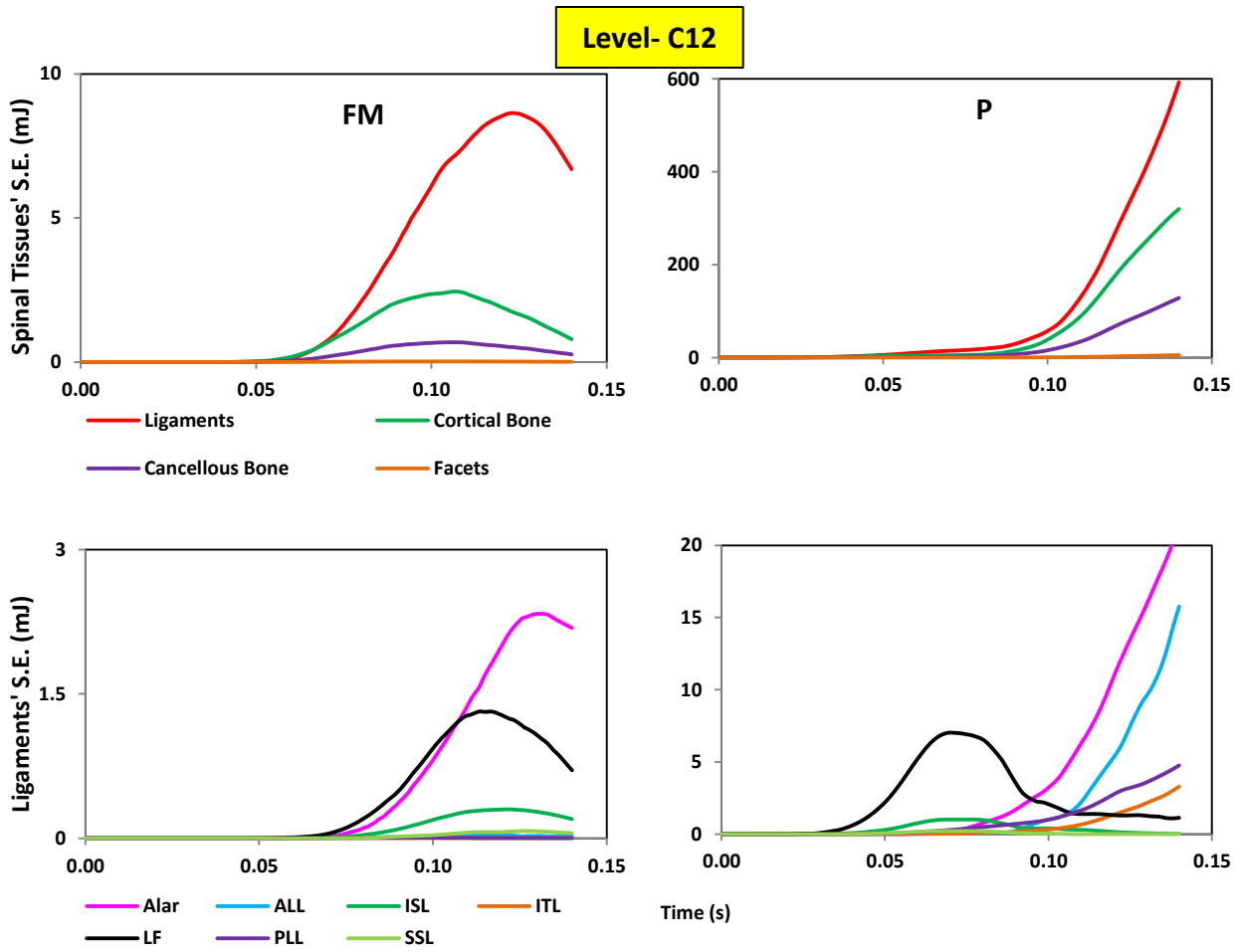


Figure 8.24 S.E. distribution in the spinal level C12 during 2G rear impact.

Level- C23

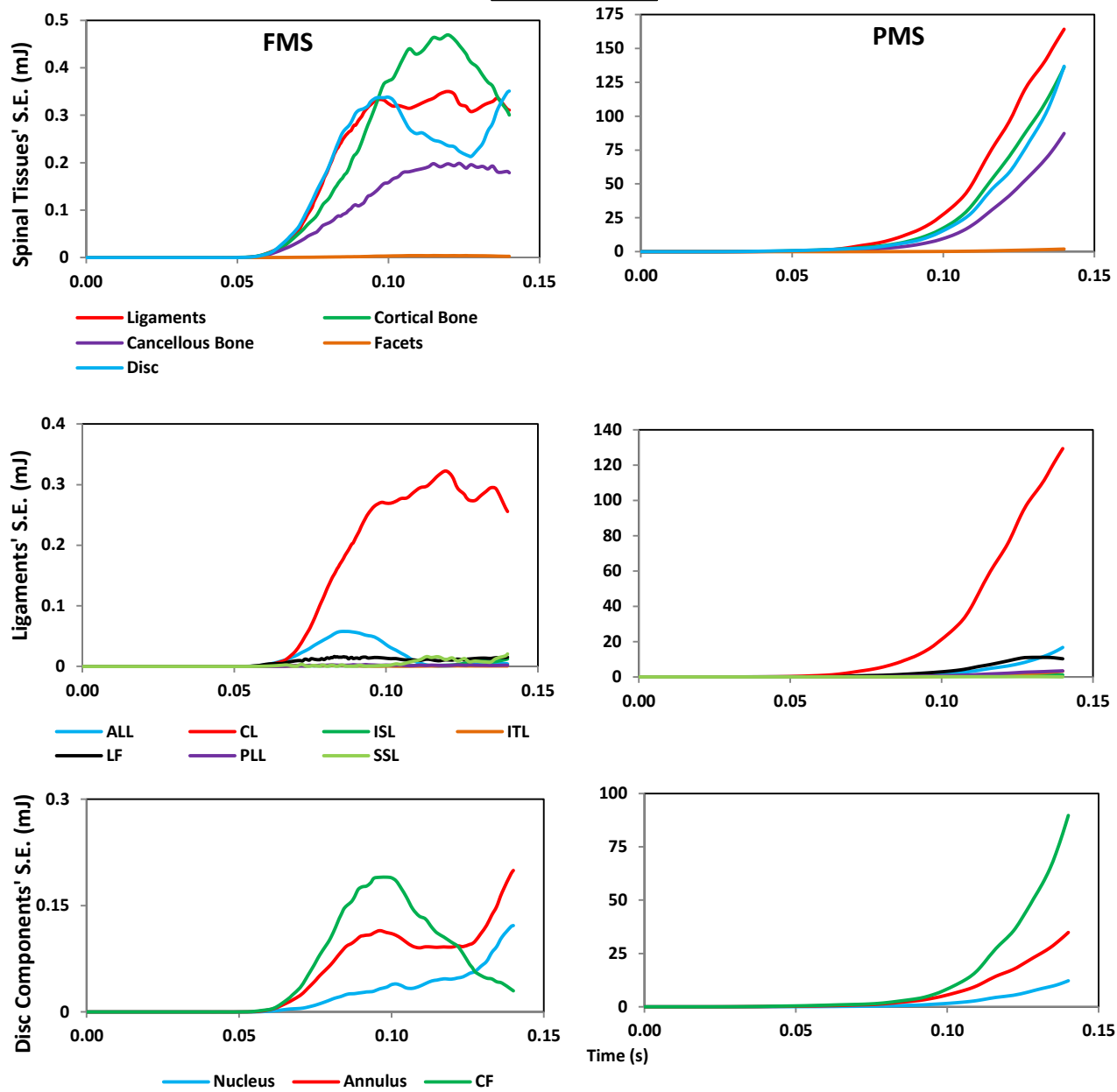


Figure 8.25 S.E. distribution in the spinal level C23 during 2G rear impact.

Level- C34

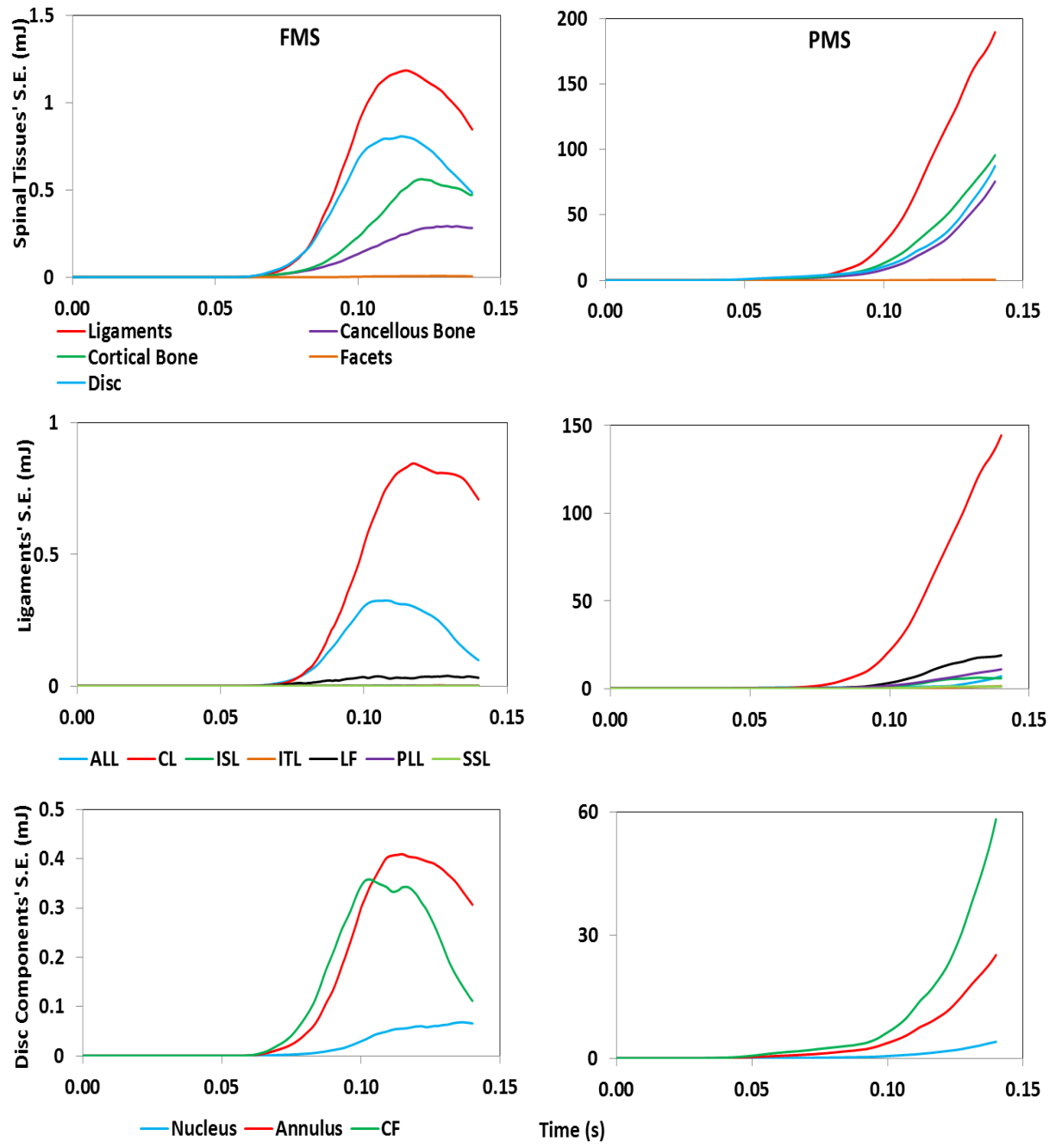


Figure 8.26 S.E. distribution in the spinal level C34 during 2G rear impact.

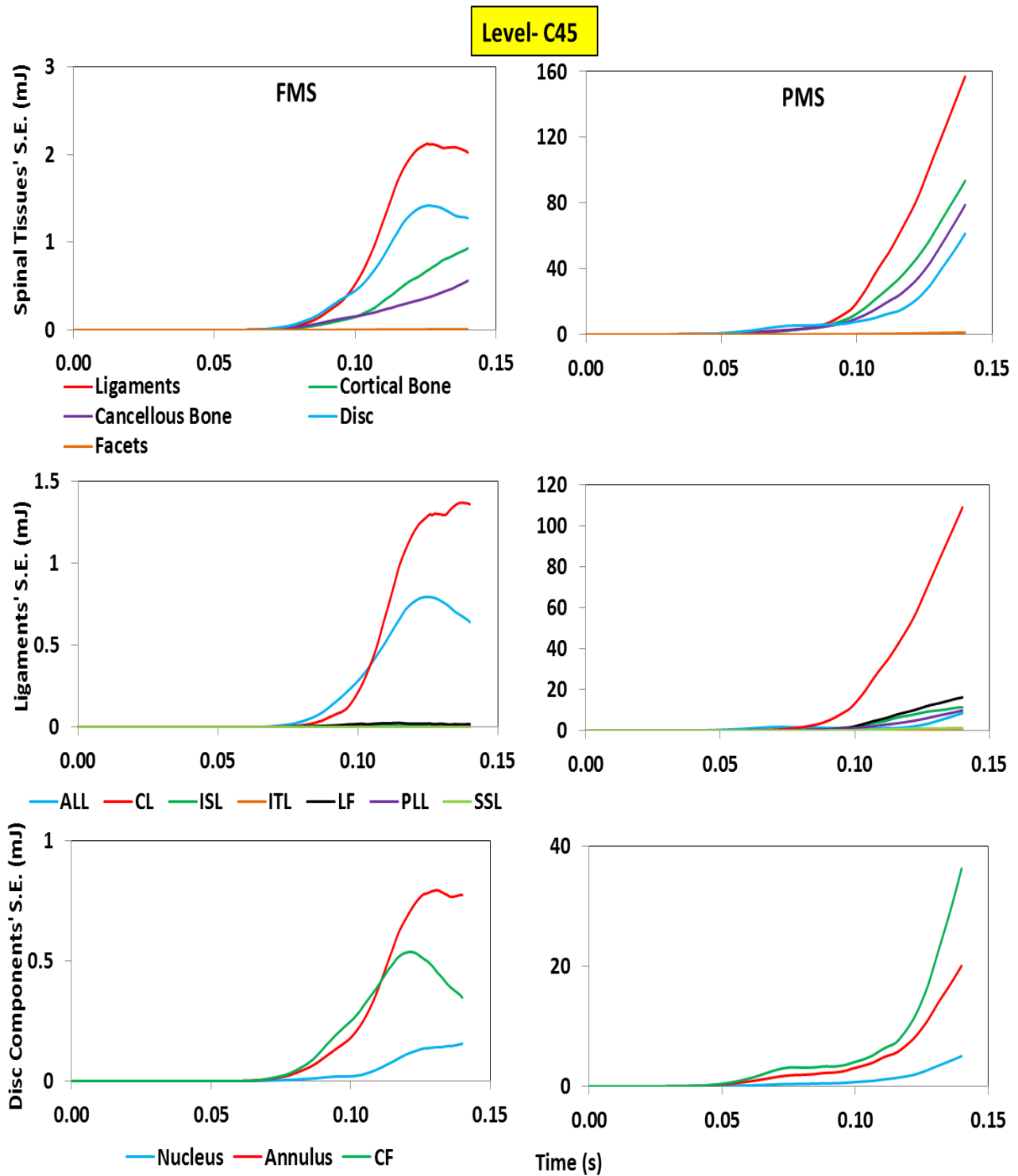


Figure 8.27 S.E. distribution in the spinal level C45 during 2G rear impact.

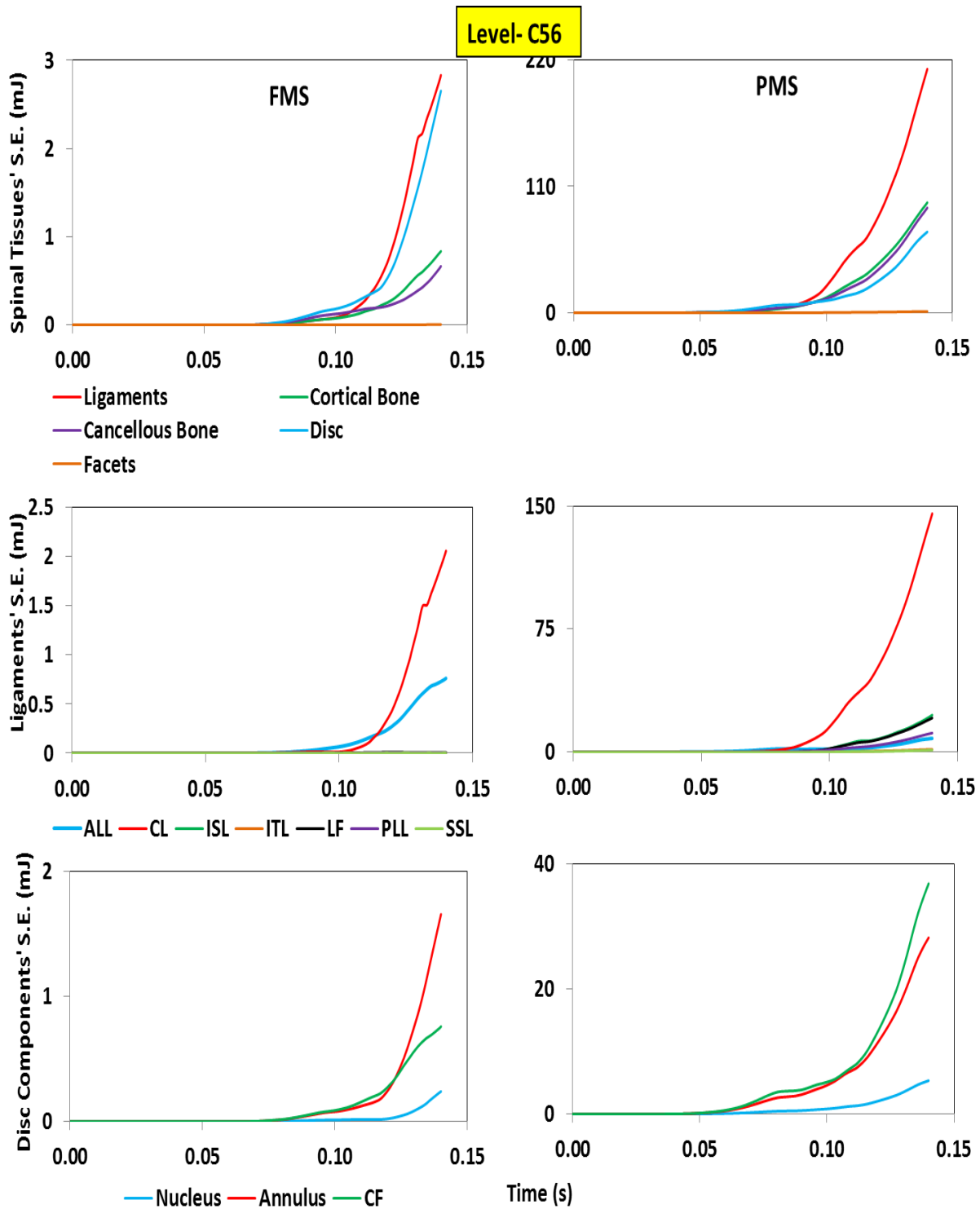


Figure 8.28 S.E. distribution in the spinal level C56 during 2G rear impact.

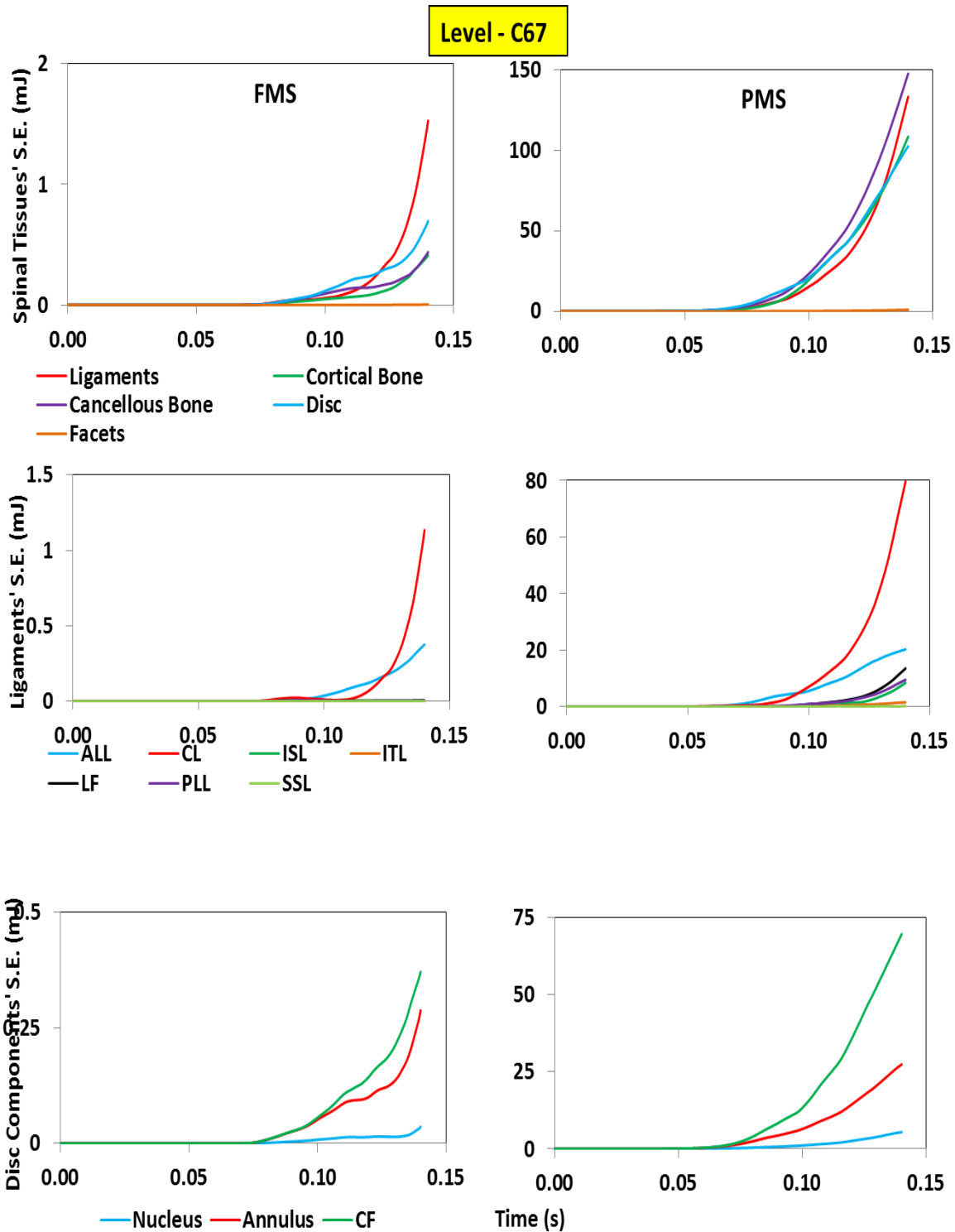


Figure 8.29 S.E. distribution in the spinal level C67 during 2G rear impact.

8.4 Discussion and Conclusion

A 3D continuum model was developed to simulate the active and passive behavior of the skeletal muscles in one element instead of using two discrete elements to represent active and passive parts of the muscle separately. This study is the first computational model that uses this approach of muscle modeling in the simulation of the spinal musculature. A user defined FORTRAN subroutine, UMAT, was developed to implement the constitutive behavior of the muscle tissue into the FE software (Chapter Three).

Prior to implementation in the spine model, the developed UMAT was verified in different loading and boundary conditions. A single solid element was used to verify the stress-strain relationship of the muscle obtained from UMAT. In addition, the UMAT was able to simulate the squid fish tentacle behavior while trying to catch the prey as the previous studies showed the similarities between the tentacle behavior and the human skeletal muscles contraction (Chapters Four).

In-vivo and *in-vitro* experimental measurements in the literature were used to partially validate the FMS model results. In particular, head kinematics during rear-end impact was compared with the experiments. Moreover, the predictions of this study were compared to those reported by other numerical studies.

The predicted head posterior displacement and extension relative to the T1 were in good agreement with *in-vivo* volunteer corridors experimental data (Davidsson *et al.*, 2001; Ewing *et al.*, 1976) and relevant numerical studies (Hedenstierna *et al.*, 2007-2009) (Fig. 8.1).

Moreover, consistent with the *in-vivo* EMG studies of the neck muscles performed by Kumar *et al.* (2002) and Schuldt *et al.* (1988), as well as aforementioned numerical FE studies done by Hedenstierna *et al.* (2007-2009), during the frontal impact, the force produced in the splenius (SC) and the trapezius (TZ) muscles was greatest, respectively. Furthermore, the sternocleidomastoid (SCM) generated the highest force amongst the muscles during the rear-end impact (Fig. 8.5).

In addition, the maximum stress and strain in the cervical ligaments obtained from the FMS model were compared with the results predicted by the PMS model to investigate the effect of muscle activation on the cervical ligaments behavior under 2G frontal and rear-end impact loading scenarios (Figs. 8.6-8.12). The PMS model predicted higher strain and stress in all ligaments at different cervical levels than those predicted by the FMS model during the rear-end impact, while the opposite was found during the frontal impact. It means the muscle activation reduced the amount of stress and strains (range of motion) in the ligaments during the rear-end impact, whereas the activation did the opposite during the frontal impact. The PMS model predicted failure in the CL, ISL, and LF ligaments at the majority of the spinal levels during the rear-end impacts based on the *in-vitro* experimental failure stress data reported by Mattucci *et al.* (2012), while the FMS did not predict the failure in the above ligaments.

Maximum pressure in the IVDs predicted by the FMS was smaller than that predicted by the PMS model during the frontal impact, while opposite was found during the rear-end impact. It means the muscle activation had different effects on the pressure distribution in the IVDs during the frontal and rear impacts. While the activation decreased the maximum pressure in

the IVDs at all cervical levels during the frontal impact, it increased the maximum pressure in the IVDs during the rear-end impact (Fig 8.13). During the frontal impact, the maximum pressure predicted by the PMS model was occurred in the IVD at level C23 (3.954 MPa), and the maximum pressure predicted by the FMS model occurred in the IVD at level C56 (0.63 MPa). During the rear impact, the IVD at level C34 experienced the highest pressure (0.52) amongst the IVDs in the PMS model, and the IVD at level C56 experienced the greatest pressure (1.41 MPa) amongst the IVDs in the FMS model (Fig. 8.14).

Moreover, during the rear-end impact and in the presence of the muscle activation, the pressure in the IVDs increased, whereas the stress in the ligaments decreased. However, the muscle activation had the opposite effect during the frontal impact.

During the frontal impact, contact in the FJs at levels C23-C7T1 was predicted by the PMS model with the exception of the level C56, while the FMS model predicted contact only would occur in the FJ at level C34. Therefore, the muscle activation not only reduced the number of spinal levels which experienced contact, but also reduced the peak value of the contact pressure (both average and maximum pressures) and force (Fig. 8.15). During the rear-end impact, however, the muscle activation caused opposite effect than that of the frontal impact. More spinal levels experienced contact (C34, C45, and C67) in the FMS model than the PMS model (only C34). The magnitude of the contact pressure and force also increased in the presence of the activation during the rear impact.

The results observed from the comparison between the cervical spinal load sharing in the PMS and FMS models during all impact loading scenarios showed that the muscle activation reduced

the magnitude of S.E. in the entire cervical spine as well as each spinal level and tissues. Among the spinal tissues, the FMS model predicted the higher values of S.E. in the ligaments, while the PMS models predicted the higher values would occur in the IVDs during the frontal impact. During the rear-end impact, both FMS and PMS models predicted the highest value of S.E. occurred in the ligaments (Figs. 8.16-8.29).

During the frontal impact, the FMS model predicted the CL ligaments had the highest contribution followed by the ISL ligaments, while the PMS model predicted the ISL played the main role during the majority of impact time, but at the end of impact the CL ligament contribution exceeded the ISL contribution (Figs. 8.16-8.22).

During the rear impact, the CL ligament had the highest contribution amongst other ligaments, followed by the ALL and LF ligaments in the FMS and PMS models, respectively (Figs. 8.23-8.29).

CHAPTER NINE: SUMMARY, CONCLUSIONS, LIMITATIONS, AND FUTURE DIRECTIONS

9.1 Summary

The main objective of this study was to develop a 3D FE model of the cervical spine including a 3D continuum musculature governed by a new material model. This material model simulates both active and passive parts of the muscle. The active and passive behaviors of the muscle was numerically formulated and a user defined FORTRAN subroutine, UMAT, was developed to implement the material model into the FE software ABAQUS (Simulia Inc.). CT and MR images of a 39-year old male subject were used to construct the 3D geometry of ligamentous spine. MRI of the same subject was then used to construct 3D cervical muscles. This new thorough cervical spine model was used to investigate the overall kinematics of the head and neck as well as the mechanical responses of the cervical tissues i.e. muscles, ligaments, discs and bony structures to various dynamic loading conditions. In addition, the responses of the Ligamentous Spine (LS) and a spine with only the Passive Musculature (PMS) were compared to the response of a spine with both active and passive musculature (FMS) to investigate the effect of the 3D cervical musculature, and the muscle activation in particular, in the cervical spine modelling, and also on the overall behavior of the cervical spine and its individual tissues.

The cervical spine overall kinematic response to various loading conditions was investigated. The mechanical response of each tissue such as stress and strain distribution in the intervertebral discs (IVD), the vertebrae, the 2D ligaments, and contact force and pressure in the Facet Joints (FJ) in a validated ligamentous spine model was compared with the outcomes of the model that includes the passive cervical musculature (PMS). Ogden hyperelastic material

law was assigned to the passive muscles. The loading scenarios were selected in accordance with the relevant numerical and experimental studies to simulate frontal and rear-end car crash impact scenarios. In addition, mechanical behaviors of the individual cervical muscles i.e. the amount of force that each one can produce, as well as stress and strain distribution within them were investigated. Next, the developed UMAT was assigned to the constructed cervical muscles and various dynamic loads were applied to our main and final model that contains both active and passive properties of the muscle (FMS). The results predicted by the FMS model were compared to those of the LS and PMS models to investigate the effect of muscle activation on the overall behavior of the spine and its individual tissues.

It should be noted that, both strain and stress have been used as the spinal injury criteria in the previous studies, as well as in the current dissertation. However, the spinal load sharing was decided to be based on the strain energy concept. The strain energy is a combination of both stress and strain.

9.2. Conclusions

9.2.1 Significance of the Severity and Direction of Impact – *Chapter Six*

The predicted spinal load sharing results of the ligamentous spine (LS) indicated that the severity and direction of impact loading scenarios significantly affect the behavior of the spine and individual spinal tissues. The S.E. magnitude of the spine during the 15G frontal impact (22J) was greater than that during the rear-end impact (4J). The results also showed that the magnitude of the S.E. increased by increasing the severity (peak acceleration) of the impact. Moreover, the spinal levels C56 and C67 had the greatest S.E. at the end of 15G frontal and

rear-end impact conditions, respectively (4.7J and 1.5J). Furthermore, the ligaments had the highest S.E. amongst the spinal tissues. Specific to the ligaments, the CL ligament had the greatest value of the S.E. Therefore, levels C56 and C67 amongst the spinal levels; the ligament amongst the spinal tissues; and the CL ligament in the group of ligaments are the potential sites of injury based on the predictions of the current study.

9.2.2 Importance of the Passive Musculature - *Chapter Seven*

The obtained results indicated the important role of the passive cervical musculature in the cervical spine behavior under impact loading scenarios. Adding the passive musculature to the LS model not only restricted the movement of the head and neck, which was in agreement with the published studies (*in-vivo* and *in-vitro*), but also altered the stress and strain distribution in the cervical tissues. It also shifted the onset of failure in the ligaments to the end of impact duration (postponed the failure process).

In addition, the S.E. magnitude of the spine predicted by the PMS model was greater than that predicted by the LS during the rear-end impact, whereas opposite was found during the frontal impact condition. This may indicate that similar to other passive tissues in the spine model, the location of the passive musculature in the spine affects its contribution during different impact directions. The constructed muscles were mainly located in the posterior site of the spine, so they facilitated the movement of the head and neck posteriorly, while restricted their anterior movement.

9.2.3 Significance of the Muscle Activation – *Chapter Eight*

The present study indicated that active musculature plays an important role in the response of the cervical spine to the external perturbations. In fact, it was found that the activation reduces the range of motion of the head and neck. Therefore, it increases the stability of the spine significantly. These findings were consistent with the experimental data (*in-vivo* and *in-vitro*). Furthermore, unlike the passive musculature model (PMS), the muscle activation reduced the magnitude of S.E. during both frontal and rear-end impact scenarios.

It has been reported that the muscle activation in general protects the cervical tissues by reducing the head deflection during car crashes (Hedenstierna *et al.*, 2007). However, in statistical data, it has been found that occupants who tensed their neck and shoulder muscles at the time of impact were at a significant higher risk of neck injury symptoms compared to occupants not tensing their muscles (Jakobsson and Noring, 2000). This could be a consequence of exaggerated muscle active forces together with high strain and strain rates.

One advantage of the employed muscle continuum material model in this work is that the user has control over the percentage of the muscle activation. Therefore, exaggerated active force can be eliminated in the crash simulation. This is a step toward a better understanding of the muscle injury mechanism, and preventing neck pain due to acute strain in a tensed muscle from vehicle accidents.

Finally, the new continuum muscle model was able to predict strain, force, and energy distribution in the muscles and indicated which muscle bears the major role during a specific

impact loading scenario. The results coincided with the experimental data (EMG) and previous numerical studies.

The UMAT developed by Spyrou and Aravas (2011) was used to model the cervical muscles in this chapter.

9.3 Modeling Considerations, Limitations, and Future Directions

Like all computational modelling, there are several limitations and simplifications associated with the assumptions in the current FE study. These limitations and simplifications with the suggestions to eliminate them in future studies are listed below:

- Simplification associated with Geometry Construction:

Constructing an accurate geometry for the cervical spine, and its musculature in particular, is an essential step toward a more realistic and biofidelic spine FE modeling. However, due to the poor quality of the MR images used to reconstruct the cervical musculature, only a small number of the cervical muscles with simplified geometry were constructed. Furthermore, the constructed muscles were mainly located in the posterior side of the cervical spine, with the exception of the sternocleidomastoid muscle. Therefore, using a high quality MRI to construct more muscles around the cervical spine with accurate geometry in future studies will improve the accuracy of the FE model.

- Simplification and Discrepancies associated with Material Properties

Material properties of the tissues highly affect the accuracy of the constitutive models. Due to the numerical instability and convergence problems that encountered during running the

model, the IVD was decided to be governed by a linear isotropic elastic material law, while it has been reported that the IVD shows hyperelastic and rate-dependent viscoelastic behaviors. This limitation might affect the behavior of the IVDs, and consequently the entire spine behavior. In addition, the results of the current work showed that the viscoelastic material law governing the cervical ligaments was not able to predict an acceptable behavior for some ligament groups such as the LF and CL ligaments (not an acceptable agreement with the experimental and numerical data). Moreover, hyperelastic and linear elastic material laws were assigned to the passive musculature and the connective tissue, respectively; while experimental studies revealed rate-dependent (viscoelastic) behavior for them. Therefore, the material properties of the spinal tissues must improve in future studies.

- Simplification associated with Loading and Boundary Conditions

The effect of gravity was ignored in this dissertation to avoid the numerical instability caused by the absence of the muscle activation at the beginning of the impact scenario. Although previous studies showed that adding the gravity increases the head rotation and displacement only up to 5% (Van der Horst, 2002), adding the gravity load to the model in future studies improves the accuracy of the model predictions, and is a step toward more realistic modeling.

In addition, it was assumed in this dissertation that the muscles are fixed at the shoulder level, while in reality the shoulder is not fixed, and so the muscles move with the entire spine when subjected to external loads.

- Numerical Convergence and Computational Cost

The computation of the current user defined material, UMAT, in the complicated nonlinear cervical spine model is extremely time-consuming. One reason is that the active stress is a function of time which requires calculating the results for thousands of time increments. Another obstacle is the convergence difficulties associated with the 2D membrane ligaments which remarkably reduces the convergence rate and adds to the running time. Moreover, impact, as a fast loading scenario, will result in slow numerical convergence. Even for a short duration as hundred milliseconds.

From the computational cost point of view, finding a suitable computational facility to run the current models was challenging. The Jasper platform (Compute Canada, WestGrid) was used to perform the simulations. However, there were several limitations using the Jasper platform. First, the queue time (the amount of time that a submitted job to the Jasper facility remains in the line before running the simulation) was long most of the time. Second, the current model required the maximum computational capacity of the Jasper platform which is three nodes (each node takes 12 CPUs and 2GB of RAM). In addition, the maximum allocated time to a job is 72 hours. Moreover, the number of ABAQUS licenses was limited. In order to run a model with these limitations, only few outputs i.e. stress, strain, and displacement was requested in the input file (.inp file). And also, the intermuscular contact that caused slow convergence rate was ignored. Therefore, to eliminate these computational obstacles, facilities with higher performance should be used in future studies.

- UMAT is applicable only in Low Energy Impact Scenarios

Due to the high strain rate of the muscle fibers (high contraction velocity) the muscle elements experienced large deformation within a small period of time. To avoid instability and numerical convergence problems that encountered during the running time, the FMS model was subjected to slow velocity impact scenarios. To eliminate this limitation, the UMAT should be improved in future considerations.

- Uncertainty associated with EMG Data and its correlation with FEM

Muscle strain (change in the length of the muscle) is caused by: 1) external load, 2) internal muscle contraction. The internal strain coincides with the external strain during the eccentric contraction, while opposite happens during concentric contraction. Despite EMG is widely used in analyzing the muscle activity, force, strain, and energy; it cannot differentiate between the external and internal strains. Moreover, the normalization procedure used in EMG is based on peak stress generating during the maximum voluntary contraction, while due to synergy between muscles groups involved in a specific movement, each muscle may not reach the maximum contraction. Therefore, due to the aforementioned uncertainties associated with the EMG data, it cannot be used as direct input to the FE modeling. Some ultrasound-based clinical techniques such as Tissue Velocity Imaging (TVI) and Position Emission Tomography (PET) can be used as a link between EMG and FEM. TVI is able to distinguish between the external and internal strains in the muscles (Peolsson *et al.*, 2008). PET is able to visualize a tissue amongst a group of muscles and the area of inflammation. Therefore, it can be used to correlate between FE predictions of high load areas and detected areas of inflamed muscle tissue in patients

(Linnman, 2008). As a future direction, the correlation between FEM (numerical approaches), EMG (experimental approaches), and clinical approaches can be investigated.

- Discrepancies in the units of the Material Properties

Finally, all the results presented in Chapters Six-Eight were based on the material properties and their units used on the published works of Mustafy and colleagues (Mustafy et al., 2014a, b; Mustafy et al., 2016). However, due to unit discrepancies in their work, stress unit was found to be wrong. To have a consistence set of units, stress unit must change from MPa to kPa. It is expected that by changing unit of stress, the results do change quantitatively, not qualitatively.

Bibliography

- Agah, Faisal. 2016. "Detailed Finite Element Modeling of the Human Ligamentous Cervical Spine." University of Alberta.
- Bernhard, Michael, Andr?? Gries, Paul Kremer, and Bernd W. B??ttiger. 2005. "Spinal Cord Injury (SCI) - Prehospital Management." *Resuscitation* 66(2): 127–39.
- Blackburn, J. Troy, Darin A. Padua, Bryan L. Riemann, and Kevin M. Guskiewicz. 2004. "The Relationships between Active Extensibility, and Passive and Active Stiffness of the Knee Flexors." *Journal of Electromyography and Kinesiology* 14(6): 683–91.
- Blemker, Silvia S., Peter M. Pinsky, and Scott L. Delp. 2005. "A 3D Model of Muscle Reveals the Causes of Nonuniform Strains in the Biceps Brachii." *Journal of Biomechanics* 38(4): 657–65.
- Brault, John R, Gunter P Siegmund, and B Wheeler. 2000. "Cervical Muscle Response during Whiplash : Evidence of a Lengthening Muscle Contraction." 15: 426–35.
- Brault, JR, GP Siegmund, and JB. Wheeler. 2000. "Cervical Muscle Response during Whiplash: Evidence of a Lengthening Muscle Contraction." *Clin Biomech* 15: 426–35.
- Brolin, K. et al. 2008. "The Importance of Muscle Tension on the Outcome of Impacts with a Major Vertical Component." *International Journal of Crashworthiness* 13(5): 487–98.
- Brolin, Karin et al. 2006. "The Effect of Muscle Activation on Neck Response." (July 2014): 37–41.
- Brolin, Karin, and Peter Halldin. 2004. "Development of a Finite Element Model of the Upper Cervical Spine and a Parameter Study of Ligament Characteristics." *SPINE* 29(4): 376–85.
- Carlsson, Anna et al. 2014. "Anthropometric Specifications, Development, and Evaluation of EvaRID-A 50(th) Percentile Female Rear Impact Finite Element Dummy Model." *Traffic injury prevention* 9588(May 2016): 855–65. <http://www.ncbi.nlm.nih.gov/pubmed/24484526>.
- Chancey, Valeta Carol, Roger W Nightingale, Chris A Van Ee, et al. 2003. "Improved Estimation of Human Neck Tensile Tolerance : Reducing the Range of Reported Tolerance Using Anthropometrically ... Improved Estimation of Human Neck Tensile Tolerance : Reducing the Range Physiologic Initial Conditions." (July 2014).
- Chancey, Valeta Carol, Roger W Nightingale, Chris a Van Ee, et al. 2003. "Improved Estimation of Human Neck Tensile Tolerance: Reducing the Range of Reported Tolerance Using Anthropometrically Correct Muscles and Optimized Physiologic Initial Conditions." *Stapp car crash journal* 47(October): 135–53. <http://www.ncbi.nlm.nih.gov/pubmed/17096248>.
- Chancey, VC et al. 2003. "Improved Estimation of Human Neck Tensile Tolerance: Reducing the Range of Reported Tolerance Using Anthropometrically Correct Muscles and Optimized Physiologic Initial Conditions." *Stapp Car Crash J.* 47: 135–53.
- Chazal, J. et al. 1985. "Biomechanical Properties of Spinal Ligaments and a Histological Study of the Supraspinal Ligament in Traction." *Journal of Biomechanics* 18(3): 167–76.
- Cheung, Jason Tak Man, Ming Zhang, Aaron Kam Lun Leung, and Yu Bo Fan. 2005. "Three-Dimensional Finite Element Analysis of the Foot during Standing - A Material Sensitivity Study." *Journal of Biomechanics*.
- Clausen, J. D., V. K. Goel, V. C. Traynelis, and J. Scifert. 1997. "Uncinate Processes and Luschka Joints Influence the Biomechanics of the Cervical Spine: Quantification Using a Finite Element Model of the C5-C6 Segment."

Journal of Orthopaedic Research.

- Davidsson, John et al. 2001. "A Comparison of Volunteer, BioRID P3 and Hybrid III Performance in Rear Impacts." *Journal of Crash Prevention and Injury Control* 2(3): 203–20.
<http://www.tandfonline.com/doi/abs/10.1080/10286580108902565>.
- Davis, Jennifer, Kenton R Kaufman, and Richard L Lieber. 2003. "Correlation between Active and Passive Isometric Force and Intramuscular Pressure in the Isolated Rabbit Tibialis Anterior Muscle." 36: 505–12.
- Deng, Y. C., and W. Goldsmith. 1987. "Response of a Human Head/neck/upper-Torso Replica to Dynamic Loading-I. Physical Model." *Journal of Biomechanics*.
- Dibb, Alan T et al. 2013. "Tension and Combined Tension-Extension Structural Response and Tolerance Properties of the Human Male Ligamentous Cervical Spine." 131(August 2009): 1–11.
- Dreischarf, M. et al. 2014. "Comparison of Eight Published Static Finite Element Models of the Intact Lumbar Spine: Predictive Power of Models Improves When Combined Together." *Journal of Biomechanics* 47(8): 1757–66.
<http://dx.doi.org/10.1016/j.jbiomech.2014.04.002>.
- Ejima, Susuma, Koshiro Ono, Koji Kaneoka, and Makoto Fukushima. 2005. "Development and Validation of the Human Neck Muscle Model under Impact Loading." In *IRCOBI Conference, Prague (Czech Republic)*.
- El-Rich, Marwan et al. 2009. "Finite Element Investigation of the Loading Rate Effect on the Spinal Load-Sharing Changes under Impact Conditions." *Journal of Biomechanics* 42(9): 1252–62.
- Ewing, C.L. et al. 1976. "The Effect of Duration, Rate of Onset, and Peak Sled Acceleration on the Dynamic Response of the Human Head and Neck." In *20th Stapp Car Crash Conference*, , 3–41.
- Frechede, B et al. 2005. "Computer Methods in Biomechanics and Biomedical Engineering Finite Element Model of the Human Neck during Omni-Directional Impacts. Part II: Relation between Cervical Curvature and Risk of Injury Finite Element Model of the Human Neck during Omni- Directi."
<http://www.tandfonline.com/action/journalInformation?journalCode=gcmb20>.
- French, Dustin D et al. 2007. "Health Care Costs for Patients with Chronic Spinal Cord Injury in the Veterans Health Administration." *The journal of spinal cord medicine* 30(5): 477–81.
<http://www.ncbi.nlm.nih.gov/pubmed/18092564><http://www.pubmedcentral.nih.gov/articlerender.fcgi?artid=PMC2141733>.
- Gabriel, D A et al. 2004. "Multidirectional Neck Strength and Electromyographic Activity for Normal Controls." *Clinical Biomechanics* 19(7): 653–58.
- Garo, Anaïs, Pierre Jean Arnoux, Eric Wagnac, and Carl Eric Aubin. 2011. "Calibration of the Mechanical Properties in a Finite Element Model of a Lumbar Vertebra under Dynamic Compression up to Failure." *Medical and Biological Engineering and Computing*.
- Gordon, a. M., a. F. Huxley, and F. J. Julian. 1966. "The Variation in Isometric Tension with Sarcomere Length in Vertebrate Muscle Fibres." *The Journal of Physiology* 184(1): 170–92.
<http://www.pubmedcentral.nih.gov/articlerender.fcgi?artid=1357553&tool=pmcentrez&rendertype=abstract>.
- Guyton, Arthur C., and John E. Hall. 2011. xPharm: The Comprehensive Pharmacology Reference *TEXTBOOK OF Medical Physiology*. 11th ed. Philadelphia, Pennsylvania: Elsevier Inc.
- Hedenstierna, S, P Halldin, and K Brolin. 2008. "Evaluation of a Combination of Continuum and Truss Finite Elements in a Model of Passive and Active Muscle Tissue." *Computer methods in biomechanics and*

- biomedical engineering* 11(January 2016): 627–39.
- Hedenstierna, Sofia. 2008. *3D Finite Element Modeling of Cervical Musculature and Its Effect on Neck Injury Prevention* Royal Institute of Technology School of Technology and Health Division of Neuronic Engineering.
- Hedenstierna, Sofia, and Peter Halldin. 2008. "How Does a Three-Dimensional Continuum Muscle Model Affect the Kinematics and Muscle Strains of a Finite Element Neck Model Compared to a Discrete Muscle Model in Rear-End, Frontal, and Lateral Impacts." *Spine* 33(8): E236-45. <http://www.ncbi.nlm.nih.gov/pubmed/18404093>.
- Hedenstierna, Sofia, Peter Halldin, and Karin Brodin. 2007. "Development and Evaluation of a Continuum Neck Muscle Model." In *6th European LS-DYNA Users' Conference*, , 89–100.
- Hedenstierna, Sofia, Peter Halldin, and Gunter P Siegmund. 2009. "Neck Muscle Load Distribution in Lateral, Frontal, and Rear-End Impacts: A Three-Dimensional Finite Element Analysis." *Spine* 34(24): 2626–33. <http://www.ncbi.nlm.nih.gov/pubmed/19910765>.
- Hill, A. V. 1938. "The Heat of Shortening and the Dynamic Constants of Muscle." In *Proceedings of The Royal Society of London. Series B, Biological Sciences*, , 136–93.
- Hill, A. V. 1970. *First and Last Experiments in Muscle Mechanics*. Cambridge, Cambridge: Cambridge University Press.
- van der Horst, M.J. 2002. "Human Head Neck Response in Frontal, Lateral and Rear End Impact Loading. (PhD Thesis)." Eindhoven University of Technology, Eindhoven.
- van der Horst, Mj et al. 1997. "The Influence of Muscle Activity on Head-Neck Response during Impact." *41st Stapp Car Crash Conference*: 487–507. <http://alexandria.tue.nl/repository/freearticles/603676.pdf>.
- Huxley, Andrew F. 1957. "Muscle Structure and Theories of Contraction."
- Ito, Shigeki, Paul C Ivancic, Manohar M Panjabi, and Bryan W Cunningham. 2004. "Soft Tissue Injury Threshold During Simulated Whiplash A Biomechanical Investigation." 29(9): 979–87.
- de Jager, Mj. 1996. "Mathematical Head-Neck Models for Acceleration Impacts." *Thesis, Eindhoven University of Technology*: 144.
- Jakobsson, L., and H. Noring. 2000. "Parameters Influencing the Risk of AISI Neck Injuries in Frontal and Side Impacts." In *International IRCOBI Conference, Montpellier (France)*.
- Johansson, T, P Meier, and R Blickhan. 2000. "A Finite-Element Model for the Mechanical Analysis of Skeletal Muscles." *J. theor. Biol* 206: 131–49. <http://www.idealibrary.com>.
- Jost, R, and G N Nurick. 2000. "Development of a Finite Element Model of the Human Neck Subjected to High G-Level Lateral Deceleration." *Journal of Crashworthiness* 5(3): 259–70.
- Kleinberger, M. 1993. "Application of Finite Element Techniques to the Study of Cervical Spine Mechanics." In *37th Stapp Car Crash Conference*, , 261 – 272.
- Kumar, S, R Ferrari, and Y Narayan. 2005. "Kinematic and Electromyographic Response to Whiplash Loading in Low-Velocity Whiplash Impacts—a Review." *Clin Biomech* 20: 343–56.
- Kumar, Shrawa, Yogesh Narayan, Tyler Amell, and Robert Ferrari. 2002. "Electromyography of Superficial Cervical Muscles with Exertion in the Sagittal , Coronal and Oblique Planes." *Eur Spine J* 11: 27–37.
- Kumar, Shrawan, Robert Ferrari, and Yogesh Narayan. 2004. "Electromyographic and Kinematic Exploration of

- Whiplash-Type Neck Perturbations in Left Lateral Collisions." *SPINE* 29(6): 650–59.
- Kumar, Shrawan, Yogesh Narayan, and Tyler Amell. 2004. "An Electromyographic Study of Low-Velocity Rear-End Impacts." 27(10): 1044–55.
- Kumaresan, S. 1997. "Finite Element Modeling of Cervical Laminectomy with Graded Facetectomy." *Journal of Spinal Disorders* 10: 40–46.
- Kumaresan, Srirangam, Narayan Yoganandan, Frank A. Pintar, and Dennis J. Maiman. 1999. "Finite Element Modeling of the Cervical Spine: Role of Intervertebral Disc under Axial and Eccentric Loads." *Medical Engineering and Physics* 21(10): 689–700.
- Langenderfer, Joseph et al. 2004. "Musculoskeletal Parameters of Muscles Crossing the Shoulder and Elbow and the Effect of Sarcomere Length Sample Size on Estimation of Optimal Muscle Length." *Clinical Biomechanics*.
- Lee, C.K. et al. 2000. "Impact Response of the Intervertebral Disc in a Finite-Element Mode." *Spine* 25: 2431–2439.
- Van Leeuwen, J L, and W M Kier. 1997. "Functional Design of Tentacles in Squid: Linking Sarcomere Ultrastructure to Gross Morphological Dynamics." *Phil. Trans. R. Soc. Lond. B* 352: 551–71.
- Liang, Y., R. M. McMeeking, and A. G. Evans. 2006a. "A Finite Element Simulation Scheme for Biological Muscular Hydrostats." *Journal of Theoretical Biology*.
- Liang, Y, R. M McMeeking, and A. G Evans. 2006b. "A Finite Element Simulation Scheme for Biological Muscular Hydrostats." *Journal of Theoretical Biology* 242(1): 142–50.
- Lieber, Richard L, and Jan Fridé N. 2000. "FUNCTIONAL AND CLINICAL SIGNIFICANCE OF SKELETAL MUSCLE ARCHITECTURE." *Muscle Nerve* 23: 1647–66.
- Linnman, C. 2008. "Imaging Chronic Pain and Inflammation; Positron Emission Studies of Whiplash Associated Disorder." Uppsala University.
- Maganaris, C.N, and J.P. Paul. 1999. "In Vivo Human Tendon Mechanical Properties." *Journal of Physiology* 521(1): 307–13.
- Maganaris, Constantinos N., Panagiotis Chatzistergos, Neil D. Reeves, and Marco V. Narici. 2017. "Quantification of Internal Stress-Strain Fields in Human Tendon: Unraveling the Mechanisms That Underlie Regional Tendon Adaptations and Mal-Adaptations to Mechanical Loading and the Effectiveness of Therapeutic Eccentric Exercise." *Frontiers in Physiology*.
- Maiman. 1983. "Compression Injuries of the Cervical Spine: A Biomechanical Analysis." *Neurosurgery*.
- Mattucci, Stephen F E, and Duane S. Cronin. 2015. "A Method to Characterize Average Cervical Spine Ligament Response Based on Raw Data Sets for Implementation into Injury Biomechanics Models." *Journal of the Mechanical Behavior of Biomedical Materials* 41: 251–60. <http://dx.doi.org/10.1016/j.jmbbm.2014.09.023>.
- Mattucci, Stephen F E, Jeffrey A. Moulton, Naveen Chandrashekar, and Duane S. Cronin. 2012. "Strain Rate Dependent Properties of Younger Human Cervical Spine Ligaments." *Journal of the Mechanical Behavior of Biomedical Materials* 10: 216–26. <http://dx.doi.org/10.1016/j.jmbbm.2012.02.004>.
- Mattucci, Stephen, Moulton, Jeffery, Chandrashekar, Naveen, Cronin, Duane . 2013. "Strain Rate Dependent Properties of Human Craniovertebral Ligaments." *Journal of the Mechanical Behavior of Biomedical Materials* 23: 71–79. <http://dx.doi.org/10.1016/j.jmbbm.2013.04.005>.
- Maurel, N, De Biomtcanique, F Lavaste, and W Skalli. 1997. "A THREE-DIMENSIONAL PARAMETERIZED FINITE

- ELEMENT MODEL OF THE LOWER CERVICAL SPINE . STUDY OF THE INFLUENCE OF THE POSTERIOR." 30(9).
- McHugh, M. P., and D. E. Hogan. 2004. "Effect of Knee Flexion Angle on Active Joint Stiffness." *Acta Physiologica Scandinavica* 180(3): 249–54.
- Milne, N. 1991. "The Role of Zygapophysial Joint Orientation and Uncinate Processes in Centrolling Motion in the Cervical Spine." *J. of Anatomy* 178: 189–201.
- Mustafy, Tanvir, Marwan El-rich, Wissal Mesfar, and Kodjo Moglo. 2014. "Investigation of Impact Loading Rate Effects on the Ligamentous Cervical Spinal Load-Partitioning Using Finite Element Model of Functional Spinal." *Journal of Biomechanics* 47(12): 2891–2903. <http://dx.doi.org/10.1016/j.jbiomech.2014.07.016>.
- Mustafy, Tanvir, Marwan El-Rich, Wissal Mesfar, and Kodjo Moglo. 2014. "Investigation of Impact Loading Rate Effects on the Ligamentous Cervical Spinal Load-Partitioning Using Finite Element Model of Functional Spinal Unit C2-C3." *Journal of Biomechanics* 47(12): 2891–2903. <http://dx.doi.org/10.1016/j.jbiomech.2014.07.016>.
- Mustafy, Tanvir, Kodjo Moglo, Samer Adeeb, and Marwan El-Rich. 2016. "Injury Mechanisms of the Ligamentous Cervical C2-C3 Functional Spinal Unit to Complex Loading Modes: Finite Element Study." *Journal of the Mechanical Behavior of Biomedical Materials* 53: 384–96. <http://dx.doi.org/10.1016/j.jmbbm.2015.08.042>.
- Myklebust, J.B. et al. 1988. "Tensile Strength of Spinal Ligaments." *Spine* 13: 526–31.
- Naserkhaki, Sadegh, Jacob L. Jaremko, Samer Adeeb, and Marwan El-Rich. 2016. "On the Load-Sharing along the Ligamentous Lumbosacral Spine in Flexed and Extended Postures: Finite Element Study." *Journal of Biomechanics* 49(6): 974–82. <http://dx.doi.org/10.1016/j.jbiomech.2015.09.050>.
- Naserkhaki, Sadegh, Jacob L Jaremko, Samer Adeeb, and Marwan El-rich. 2016. "On the Load-Sharing along the Ligamentous Lumbosacral Spine in Flexed and Extended Postures : Finite Element Study." *Journal of Biomechanics* 49(6): 974–82. <http://dx.doi.org/10.1016/j.jbiomech.2015.09.050>.
- Nightingale, Roger W. et al. 1997. "The Dynamic Response of the Cervical Spine: Buckling, End Conditions, and Tolerance in Compressive Impact." In *41st Stapp Car Crash Conference*,.
- Östh, Jonas et al. 2017. "A Female Head – Neck Model for Rear Impact Simulations." *Journal of Biomechanics* 51: 49–56. <http://dx.doi.org/10.1016/j.jbiomech.2016.11.066>.
- Osth, Jonas, Karin Brolin, and Astrid Linder. 2017. "A Female Ligamentous Cervical Spine Finite Element Model Validated for Physiological Loads." 138(June 2016): 1–9.
- Otten, E. 1987. "A Myocybernetic Model of the Jaw System of the Rat." *Journal of Neuroscience* 21: 287–302.
- Panjabi, Manohar M et al. 2004. "Cervical Spine Ligament Injury during Simulated Frontal Impact." *Spine* 29(21): 2395–2403.
- Panjabi, Manohar M, T Oxland, and E Parks. 1991. "Quantitative Anatomy of Cervical Spine Ligaments. Part I. Upper Cervical Spine." *J Spinal Disord* 4(3): 270–76.
- Panzer, Matthew B., Jason B. Fice, and Duane S. Cronin. 2011. "Cervical Spine Response in Frontal Crash." *Medical Engineering and Physics* 33(9): 1147–59. <http://dx.doi.org/10.1016/j.medengphy.2011.05.004>.
- Park, Won Man, Kyungsoo Kim, and Yoon Hyuk Kim. 2013. "Effects of Degenerated Intervertebral Discs on Intersegmental Rotations, Intradiscal Pressures, and Facet Joint Forces of the Whole Lumbar Spine." *Computers in Biology and Medicine*.
- Peolsson, M., B. Larsson, L.A. Brodin, and B. Gerdle. 2008. "A Pilot Study Using Tissue Velocity Ultrasound Imaging (TVI) to Assess Muscle Activity Pattern in Patients with Chronic Trapezius Myalgia." *BMC Musculoskeletal*

Disord 9(1): 127.

- Priebe, Michael M. et al. 2007. "Spinal Cord Injury Medicine. 6. Economic and Societal Issues in Spinal Cord Injury." *Archives of Physical Medicine and Rehabilitation* 88(3 SUPPL.1): 84–88.
- Robertson, Angus, Toby Branfoot, Ian F Barlow, and Peter V Giannoudis. 2002. "Spinal Injury Patterns Resulting from Car and Motorcycle Accidents." *Spine* 27(24): 2825–30.
<http://www.ncbi.nlm.nih.gov/pubmed/12486355>.
- Sadegh, Ali M, and Tchako Abraham. 2000. "Vertebral Stress of a Cervical Spine Model under Dynamic Load." *Technology and health care : official journal of the European Society for Engineering and Medicine* 8: 143–54.
- Schmidt, H. et al. 2007. "Intradiscal Pressure, Shear Strain, and Fiber Strain in the Intervertebral Disc under COmbined Loading." 32(7).
- Schmidt, Hendrik et al. 2007. "Intradiscal Pressure, Shear Strain, and Fiber Strain in the Intervertebral Disc Under Combined Loading." *SPINE* 32(7): 748–55.
- Schuldt, K, and K Harms-ringdahl. 1988. "Activity Levels during Isometric Test Contractions of Neck and Schulter Muscles." *Scand J Rehabil Med* 20: 117–27.
- Sekhon, L H, and M G Fehlings. 2001. "Epidemiology, Demographics, and Pathophysiology of Acute Spinal Cord Injury." *Spine (Phila Pa 1976)* 26(24 Suppl): S2-12.
- SHIRAZI-ADL, A, ABDUL M. AHMED, and SURESH C. SHRIVASTAVA. 1986. "Mechanical Response of a Lumbar Motion Segment in Axial Torque Alone and Combined with Compression." *Spine* 11(9): 914–27.
<http://content.wkhealth.com/linkback/openurl?sid=WKPTLP:landingpage&an=00007632-198611000-00012>.
- Siegmund, GP et al. 2009. "The Anatomy and Biomechanics of Acute and Chronic Whiplash Injury." *Traffic Inj Prev.* 10(2): 101–12.
- Siegmund, Gunter P et al. 2007. "Electromyography of Superficial and Deep Neck Muscles during Isometric, Voluntary, and Reflex Contractions." *Journal of biomechanical engineering* 129(1): 66–77.
- Siegmund, Gunter P, and J Timothy Inglis. 2016. "Electromyography of Superficial and Deep Neck Muscles During Isometric , Voluntary , and Reflex." 129(February 2007).
- Spyrou, L. a., and N. Aravas. 2011. "Muscle and Tendon Tissues: Constitutive Modeling and Computational Issues." *Journal of Applied Mechanics* 78(4): 41015.
- Spyrou, L A, and N Aravas. 2011. "Muscle and Tendon Tissues : Constitutive Modeling and." 78(July 2011): 1–10.
- Spyrou, Leonidas A. 2009. "Muscle and Tendon Tissues: Constitutive Modeling, Numerical Implementation and Applications." (September): 18264.
- Stemper, BD, N Yoganandan, and FA Pintar. 2004. "Validation of a Head–neck Computer Model for Whiplash Simulation." *Med Biol Eng Comput* 42: 333–38.
- Teo, Ee Chon, Qing Hang Zhang, and Russel C. Huang. 2007. "Finite Element Analysis of Head-Neck Kinematics during Motor Vehicle Accidents: Analysis in Multiple Planes." *Medical Engineering and Physics*.
- Vasavada, Anita N, John R Brault, and Gunter P Siegmund. 2007. "Musculotendon and Fascicle Strains in Anterior and Posterior Neck Muscles During Whiplash Injury." *Spine* 32: 756–65.
- Wagnac, Eric et al. 2012. "Finite Element Analysis of the Influence of Loading Rate on a Model of the Full Lumbar Spine under Dynamic Loading Conditions." *Med Biol Eng Comput* 50: 903–15.

- White, A. A., and M. M. Panjabi. 1990. *Clinical Biomechanics of the Spine*. Lippincott, Philadelphia, PA.
- Winters, Jack M, and KL. Star. 1988. "Estimated Mechanical Properties of Synergistic Muscles Involved in Movements of a Variety of Human Joints." *Journal of Biomechanics* 21: 1027–1041.
- Wittek, Adam. 2000. "Mathematical Modeling of the Muscle Effects on the Human Body Responses under Transient Loads [PhD Thesis]." Chalmers University of Technology.
- Yang, K.H., and V.L. Kish. 1988. "Compressibility Measurement of Human Intervertebral Nucleus Pulposus." *Journal of Biomechanics* 21(10).
- Yang, King H. et al. 1998. "Development of a Finite Element Model of the Human Neck." In *Stepp Car Crash Conference*,.
- Yoganandan, N et al. 1989. "Dynamic Response of Human Cervical Spine Ligaments." *Spine* 14(10): 1102–10. <http://www.ncbi.nlm.nih.gov/pubmed/2588060>.
- Yoganandan, N. et al. 1996. "Human Head- Neck Biomechanics under Axial Tension." *Medical Engineering Physics* 18: 289–94.
- Yoganandan, Narayan, S Kumaresan, and Frank a Pintar. 1996. "Finite Element Applications in Human Cervical Spine Modeling.pdf."
- Yoganandan, Narayan, Srirangam Kumaresan, and Frank A Pintar. 2001. "Biomechanics of the Cervical Spine Part 2 . Cervical Spine Soft Tissue Responses and Biomechanical Modeling." 16.
- Zajac, F.E. 1989. *Muscle and Tendon: Properties, Models, Scaling, and Application to Biomechanics and Motor Control*. In *CRC Critical Reviews in Biomedical Engineering*. CRC Press, Boca Raton.

Appendix A

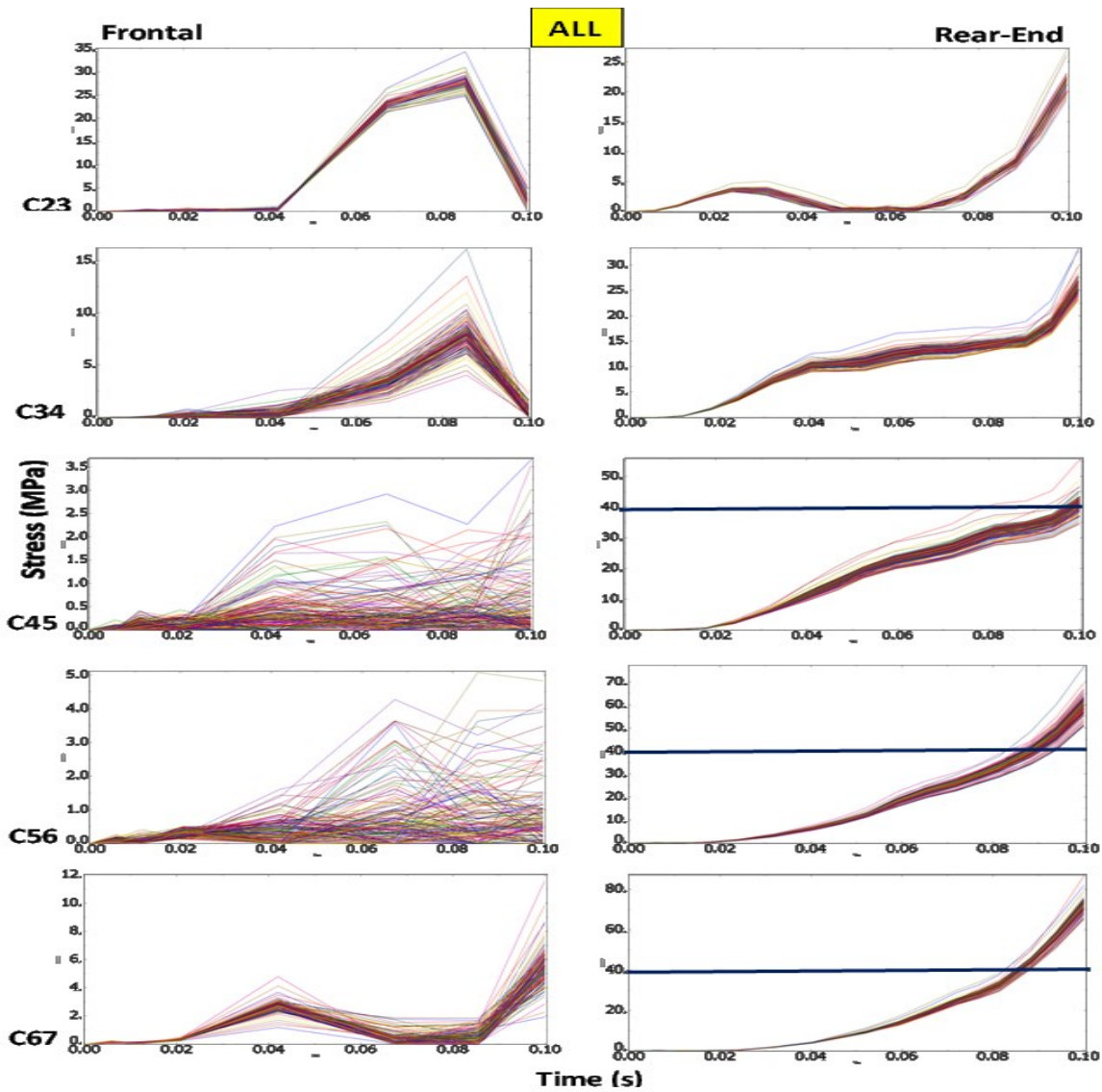


Figure A.1 Stress distribution vs. time in the ALL elements at different cervical spinal levels in 15G frontal (left) and rear-end (right) impacts. The thick horizontal line indicates the catastrophic stress failure level (Mattucci et al., 2012).

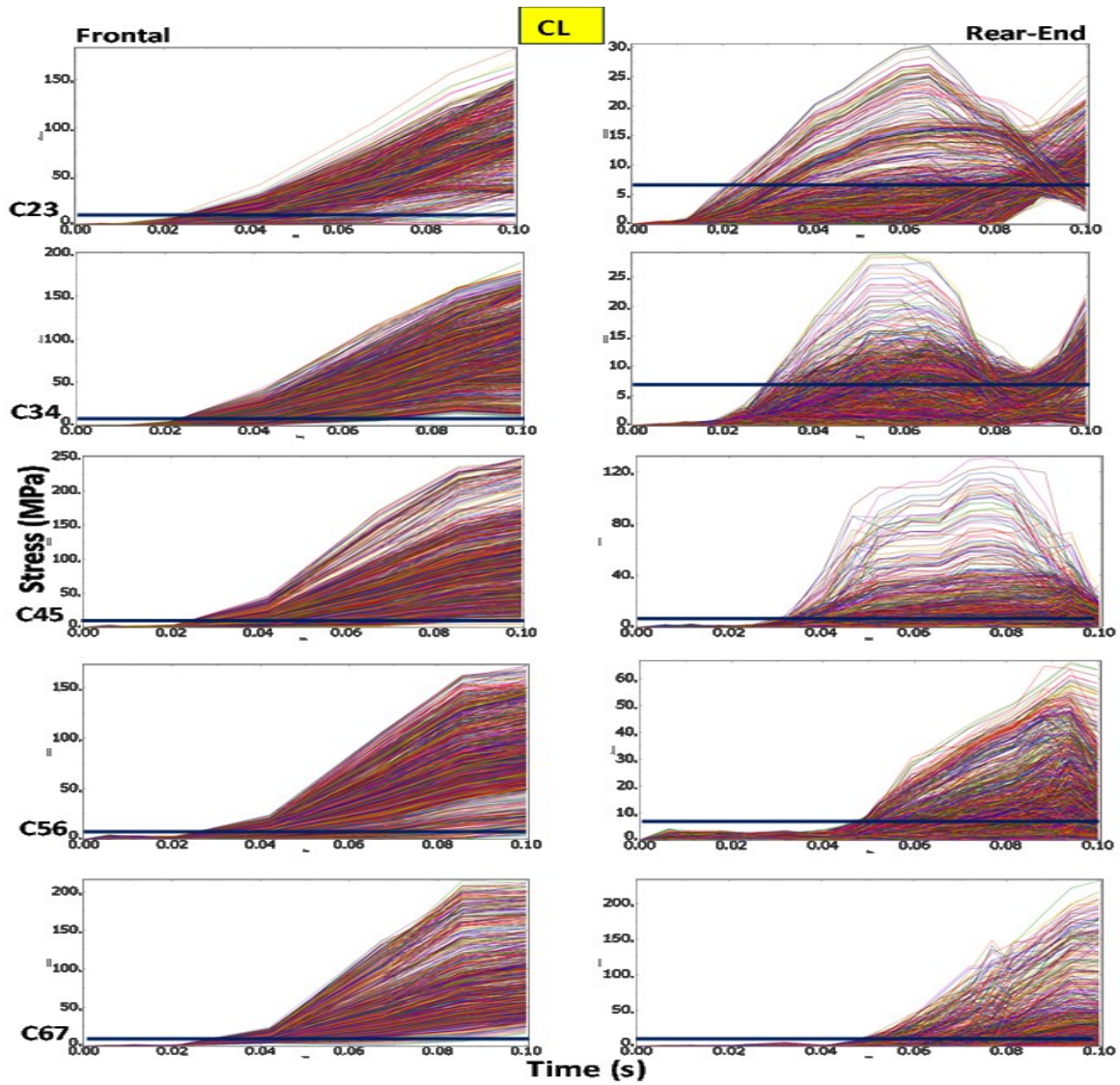


Figure A.2 Stress distribution vs. time in the CL elements at different cervical spinal levels in 15G frontal (left) and rear-end (right) impacts. The thick horizontal line indicates the catastrophic stress failure level (Mattucci et al., 2012).

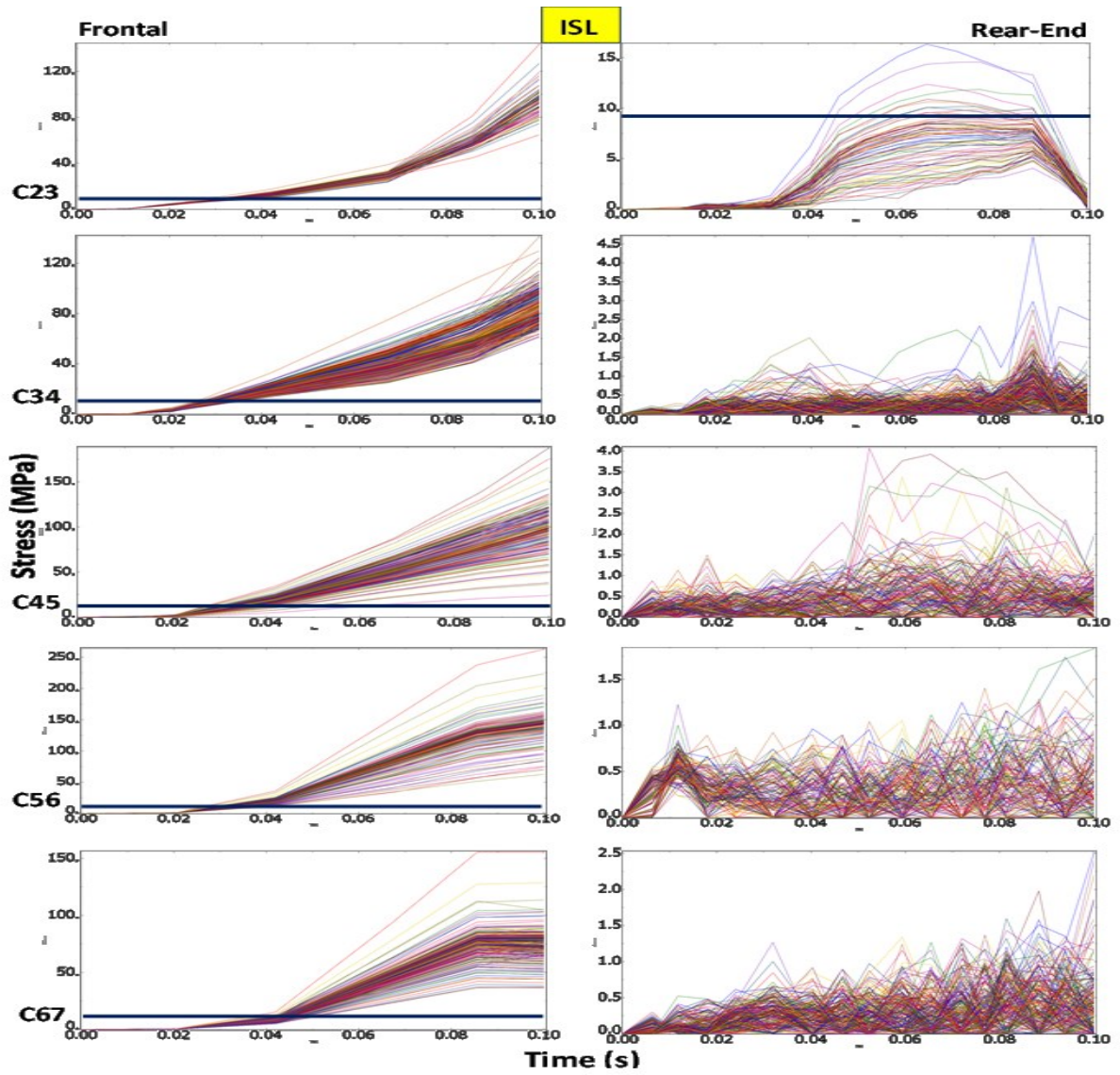


Figure A.3 Stress distribution vs. time in the ISL elements at different cervical spinal levels in 15G frontal (left) and rear-end (right) impacts. The thick horizontal line indicates the catastrophic stress failure level (Mattucci et al., 2012).

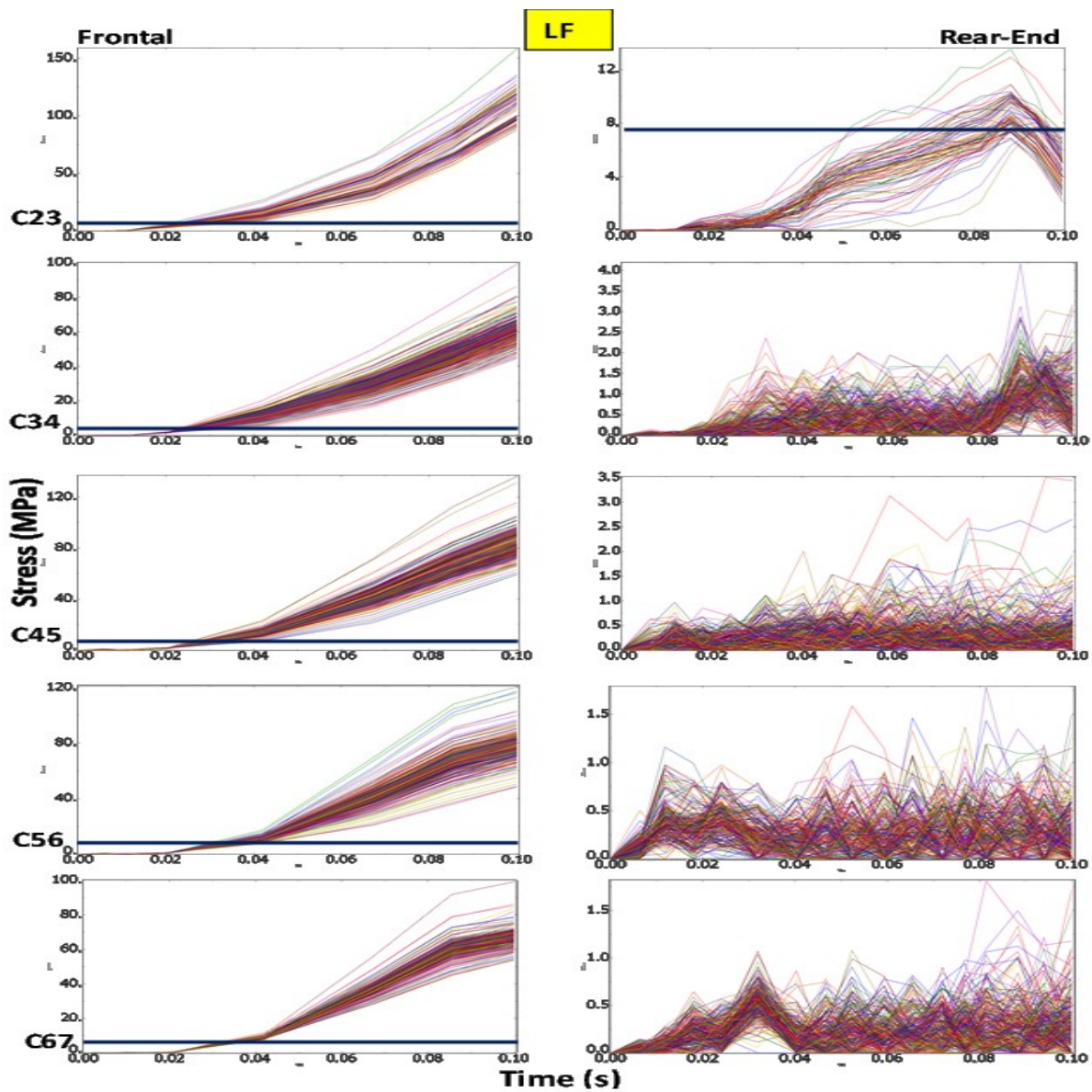


Figure A.4 Stress distribution vs. time in the LF elements at different cervical spinal levels in 15G frontal (left) and rear-end (right) impacts. The thick horizontal line indicates the catastrophic stress failure level (Mattucci et al., 2012).

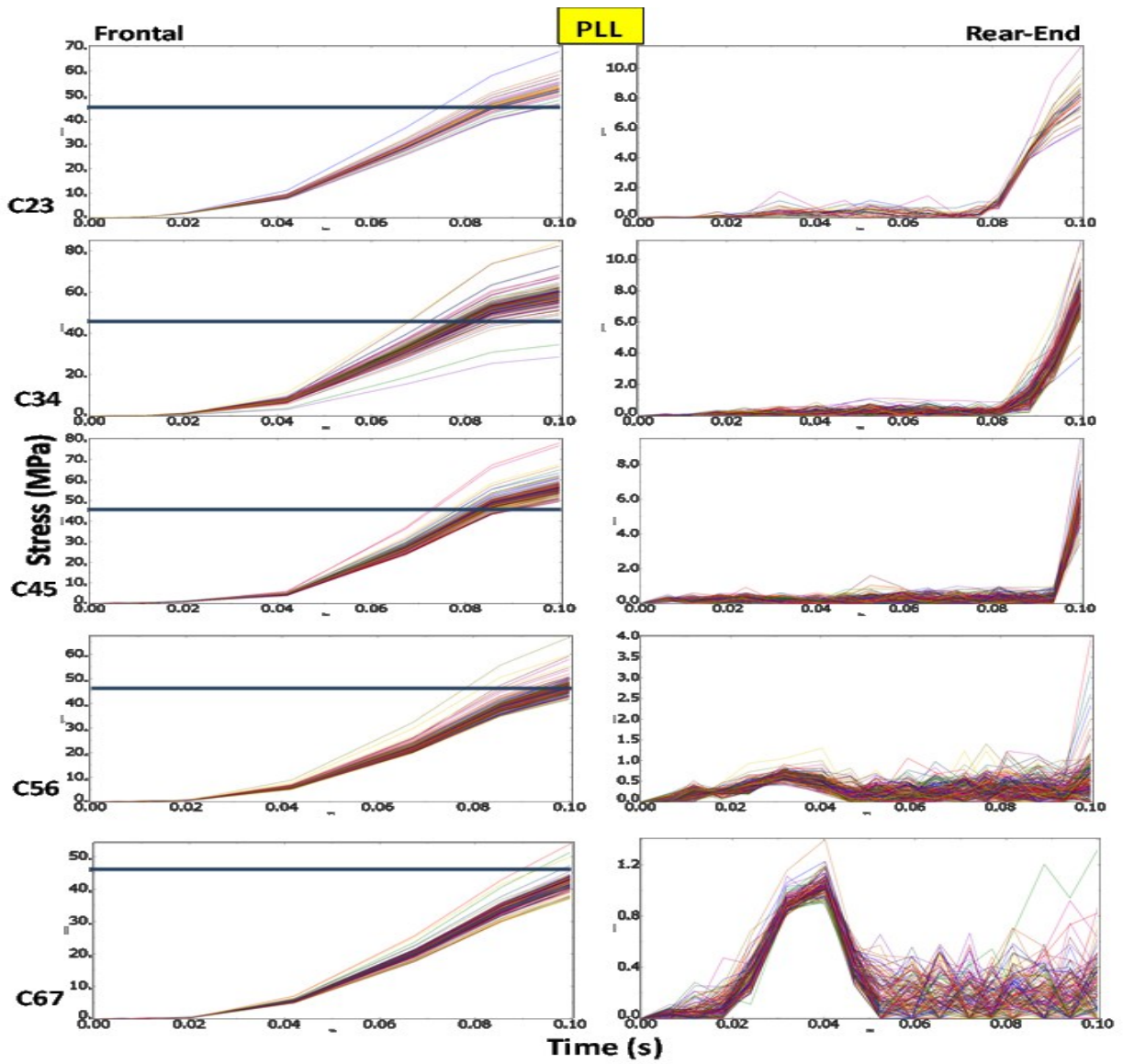


Figure A.5 Stress distribution vs. time in the PLL elements at different cervical spinal levels in 15G frontal (left) and rear-end (right) impacts. The thick horizontal line indicates the catastrophic stress failure level (Mattucci et al., 2012).

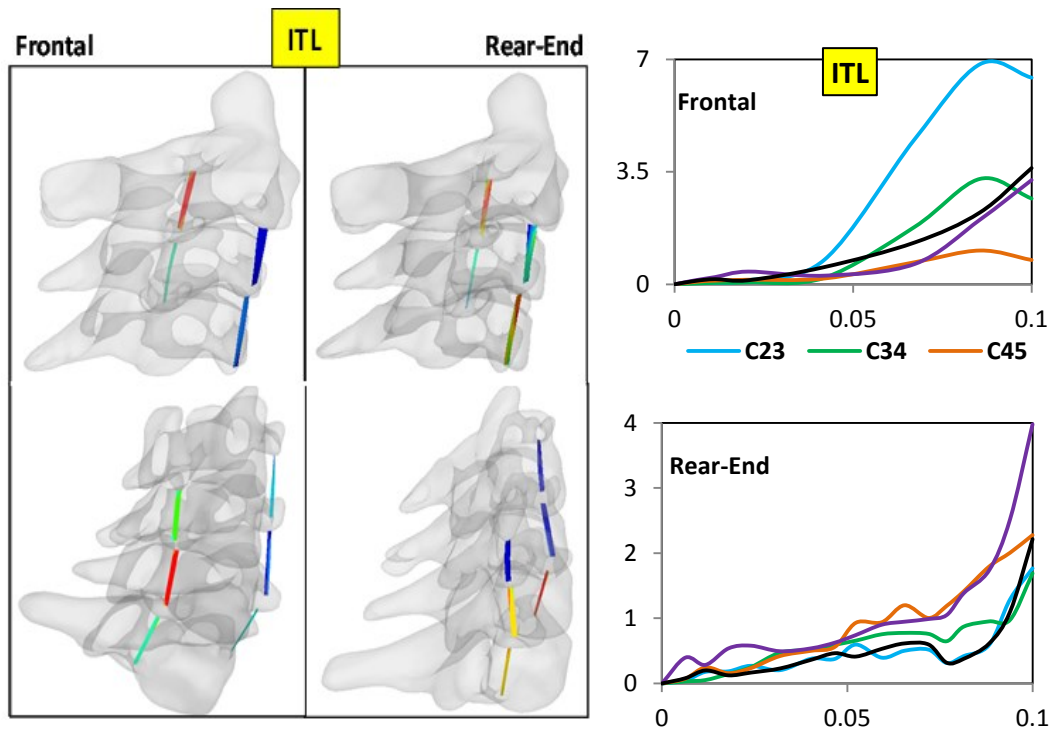


Figure A.6 A schematic view of strain distribution in the ITL ligaments in 15G frontal and rear-end impact captured at the time=0.1s (Left side). Strain (%) vs. time in ALLs at different cervical levels in 15G frontal and rear-end impacts (Right side).

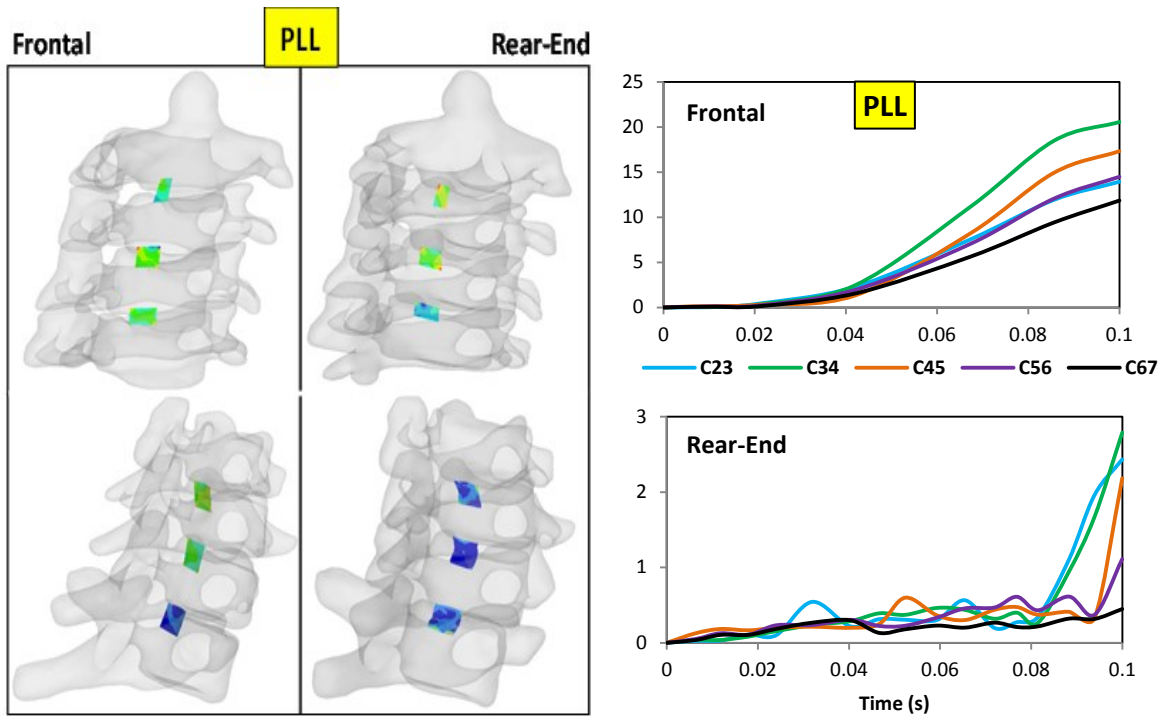


Figure A.7 A schematic view of strain distribution in the PLL ligaments in 15G frontal and rear-end impact captured at the time=0.1s (Left side). Strain (%) vs. time in ALLs at different cervical levels in 15G frontal and rear-end impacts (Right side).

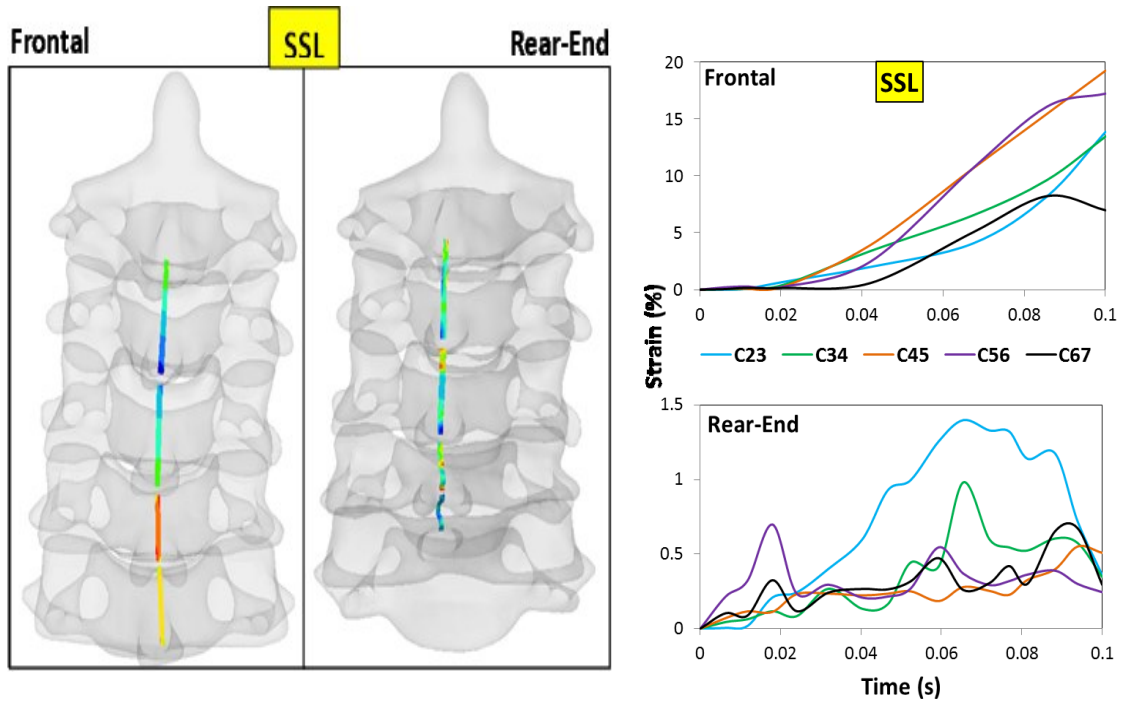


Figure A.8 A schematic view of strain distribution in SSLs in 15G frontal and rear-end impact captured at the time=0.1s (Left side). Strain (%) vs. time in the SSL ligaments at different cervical levels in 15G frontal and rear-end impacts (Right side).

Appendix B

UMAT Developed in This Dissertation

```
*****
**  UMAT FOR ABAQUS/STANDARD  **
*****
*USER SUBROUTINE
  SUBROUTINE UMAT (STRESS, STATEV, DDSDD, SSE, SPD, SCD,
1  RPL, DDSDDT, DRPLDE, DRPLDT,
2  STRAN, DSTRAN, TIME, DTIME, TEMP, DTEMP, PREDEF, DPRED, CMNAME,
3  NDI, NSHR, NTENS, NSTATV, PROPS, NPROPS, COORDS, DROT, PNEWDT,
4  CELENT, DFGRD0, DFGRD1, NOEL, NPT, LAYER, KSPT, KSTEP, KINC)
C
  INCLUDE 'ABA_PARAM.INC'
C
  CHARACTER*80 CMNAME
C
  DIMENSION STRESS (NTENS), STATEV (NSTATV),
1  DDSDD (NTENS, NTENS), DDSDDT (NTENS), DRPLDE (NTENS),
2  STRAN (NTENS), DSTRAN (NTENS), TIME (2), PREDEF (1), DPRED (1),
3  PROPS (NPROPS), COORDS (3), DROT (3, 3), DFGRD0 (3, 3), DFGRD1 (3, 3)
C
C
  PARAMETER ZERO=0.D0, ONE=1.D0, TWO=2.D0, THREE=3.D0, NINE=9.D0
  PARAMETER SIX=6.D0, FOUR=4.D0, HALF=ONE/TWO, PI=3.14D0
C
  INTEGER i, j, NTENS, NSTATV, NPROPS
  REAL*8 STM, STM0, ESM0A, DESMODT, ESM, ESM0, LAMDA, LAMDA1, TEMP1, KK
  REAL*8 STMAX, FLEN, FRAT, FACT, STMPAS, TD, TA, G, GG, KB, NU, E, GE
  REAL*8 q, ES5, ES4, ES3, ES2, ES1, F5, F4, DENSITY
  REAL*8 L_myo, L_bz, L_0sarc, L_act, L_min, L_z, D_act, D_myo, C_myo
  REAL*8 ESMR_ST, ESMOR, ESR_MIN, KKK, ESC, C1, C2, C3, C4
  REAL*8 DFRATDES, TD0, DET, DFLENDES
  REAL*8 F, FT, V, V1, PROPS, ES, M0, M0FT, FM0, M, MM, DELTA, ESF, ESCT
  REAL*8 DFGRD0, DFGRD1, DTIME, IDEN, TIME, STF, LE, DDFGRD, LE1
  REAL*8 mmmm, B, mo, STCT, ST, CECT, CEF
  REAL*8 STRESS, STATEV, DDSDD, DDSDDT, DRPLDE, STRAN, DSTRAN
  REAL*8 PREDEF, DPRED, COORDS, DROT, dfpassdesm0
  REAL*8 STMACT, ABESM0, FTF, LAME1, LAME2, SPK, KCT, EKK, FS, FSFT, TCT
C
  DIMENSION F (3, 3), FT (3, 3), V1 (3, 3), V (3, 3)
  DIMENSION m0 (3), m0FT (3), Fm0 (3), GE (3, 3)
  DIMENSION m (3), mm (3, 3), DELTA (3, 3), ESF (3, 3), LE1 (9, 9)
  DIMENSION ESCT (3, 3), STF (3, 3), TD0 (6, 6), FTF (3, 3)
  DIMENSION LE (9, 9), STCT (3, 3), ST (3, 3)
  DIMENSION B (9, 9), CEF (9, 9), DDFGRD (3, 3)
  DIMENSION IDEN (9, 9), CECT (9, 9), mmmm (9, 9)
  DIMENSION SPK (3, 3), KCT (3, 3), FS (3, 3), FSFT (3, 3), TCT (3, 3)
C
  *****SPECIFIED MATERIAL PROPERTIES*****
  G=SHEAR MODULUS
  K=BULK MODULUS
  DFGRD0=deformation gradient tensor at the beginning of each increment
  DFGRD1=deformation gradient tensor at the end of each increment
  ES= muscle total strain array
  m0= initial vector of fiber direction
  m=fiber direction vector at each increment
  mm= m*m(attention: it is vector product Not dot product of vectors)
```

```

C      ESM0= nominal strain(engineering strain)in m direction
C      DESM0DT= time drivative of ESM0 in each incriment
C      ESM= muscle true strain in m direction
C      DELTA= 3*3 Identity matrix
C      ESF= fiber strain matrix
C      ESCT= connective tissue strain matrix
C      ESM0A= active ESM0
C      STM0= nominal stress in m direction
C      STM= true stress in m direction
C      STF= true stress array of fiber
C      STCT= true stress tensor of connective tissue
C      ST= STF + STCT
C      *****CONSTANTS USED IN DIFF PARTS OF EQUATIONS*****
C      KK= a constant in used calculation of ESM0A
C      STMAX= max stress in the muscle tissue
C      C      FLEN= length function which shows how muscle force is related to its
C      strain or length variation
C      FRAT= strain rate function which shows dependance of muscle force on its strain
rate
C      FACT= activation function which shows dependance of muscle force on the
activation level
C      STMPAS= passive part of muscle stress
C      L_act= length of 2 opposing actin filaments in 1 sarcomere
C      L_min
C      L_z= width of Z-disc
C      C      D_act= parameter to account for cross-bridge loses owing to actin overlap
C      D_myo= parameter to account for interaction between filament and Z-disc
C      C_myo= parameter to account for resistive forces as a result of collision
of myosin with Z-disc
C      ESMR_ST= muscle strain rate
C      ESM0R= nominal muscle strain rate
C      ESR_MIN= minimum(unloaded)muscle strain rate
C      KKK= constant
C      ESC= critical strain above which the relationship is linear
C      C1,C2,C3,C4= constants
C      TD= Delay time
C      TA= full activation time
C      q= constant
C      L_myo= myosin filament length
C      L_bz= length of bare zone on myosin filament
C      ES5= (L_min - L_0sarc)/ L_0sarc
C      *****
E=PROPS(1)
NU=PROPS(2)
STMAX=PROPS(3)
ESR_MIN=PROPS(4)
L_act=PROPS(5)
L_myo=PROPS(6)
GG=E/ (TWO* (ONE+NU) )
LAME1=E*NU/ ( (ONE+NU) * (ONE-TWO*NU) )
LAME2=GG
L_z=0.06D-3
D_act=0.68D0
D_myo=1.90D0
C_myo=0.44D0
KKK=25D-2
KK=15.0D-2
ESC=0.773D0
C1=887.0D-3
C2=2.26D0
C3=-55.0d0
C4=-625.0d0
TD=0.0d0

```

```

TA=0.04d0
q=15.D0
L_bz=0.14D-3
L_0sarc= L_act + L_z + HALF * L_bz
ES5=-0.4D0
L_min=ES5*L_0sarc+L_0sarc
ES4= (L_myo - L_act - HALF*L_bz) / L_0sarc
ES3= - HALF*L_bz / L_0sarc
ES2= HALF*L_bz / L_0sarc
ES1= (L_myo - HALF*L_bz) / L_0sarc
F5= ONE - D_act*(L_act + L_z - L_min)/(L_myo - L_bz)
1 - (D_myo + C_myo)*(L_act + L_z - L_min)/(L_myo - L_bz)
F4= ONE - D_act*(L_act - L_myo)/(L_myo - L_bz)
C *****STRESS FORMULATION*****
DO i=1,3
  DO j=1,3
    F(i,j)=DFGRD1(i,j)
  END DO
END DO
C *****TRANSPOSE (DFGRD1) *****
DO i=1,3
  DO j=1,3
    FT(i,j)=F(j,i)
  END DO
END DO
C *****STRAIN CALCULATION*****
m0(1)=0.0d0
m0(2)=0.0d0
m0(3)=1.0d0
C
DO i=1,3
  DO j=1,3
    m0FT(i)=m0(j)*FT(j,i)
  END DO
END DO
C
DO i=1,3
  DO j=1,3
    Fm0(i)=F(i,j)*m0(j)
  END DO
END DO
C
LAMDA1= m0FT(1)*Fm0(1)+ m0FT(2)*Fm0(2)+ m0FT(3)*Fm0(3)
LAMDA= SQRT(abs(LAMDA1))
C *****NOMINAL STRAIN (ENGINEERING) *****
TEMP1=ZERO
ESM0=(LAMDA-ONE)
C *****TRUE STRAIN *****
ESM=(log(ABS(LAMDA)))
C *****FIBER DIRECTION*****
DO i=1,3
mo=SQRT(Fm0(1)**TWO+Fm0(2)**TWO+Fm0(3)**TWO)
m(i)=(ONE/mo)*Fm0(i)
END DO
C *****mm calculation*****
mm(1,1)= m(1)*m(1)
mm(1,2)= m(1)*m(2)
mm(1,3)= m(1)*m(3)
mm(2,1)= m(2)*m(1)
mm(2,2)= m(2)*m(2)
mm(2,3)= m(2)*m(3)
mm(3,1)= m(3)*m(1)
mm(3,2)= m(3)*m(2)

```

```

mm(3,3) = m(3)*m(3)
C *****DELTA CALCULATION *****
DO i=1,3
  DO j=1,3
    DELTA(i,j)=ZERO
  END DO
  DELTA(i,i)=ONE
END DO
C *****IDEN CALCULATION*****
DO i=1,9
  DO j=1,9
    IDEN(i,j)=ZERO
  END DO
  IDEN(i,i)=ONE
END DO
C *****FIBER STRAIN CALCULATION*****
DO i=1,3
  DO j=1,3
    ESF(i,j)=(1.5D0*ESM*(mm(i,j)-(1.5D0*DELTA(i,j))))
  END DO
END DO
DO i=1,3
  DO j=1,3
    IF (ESF(i,j).GT. ONE) THEN
      ESF(i,j)=ESF(i,j)
    ENDIF
  END DO
END DO
C *****CONNECTIVE TISSUE STRAIN*****
DO i=1,3
  DO j=1,3
    FTF(i,j)= ZERO
  END DO
END DO
C
FTF(1,1)=F(1,1)*F(1,1)+F(2,1)*F(2,1)+F(3,1)*F(3,1)
FTF(2,2)=F(1,2)*F(1,2)+F(2,2)*F(2,2)+F(3,2)*F(3,2)
FTF(3,3)=F(1,3)*F(1,3)+F(2,3)*F(2,3)+F(3,3)*F(3,3)
FTF(1,2)=F(1,1)*F(1,2)+F(2,1)*F(2,2)+F(3,1)*F(3,2)
FTF(2,1)=F(1,2)*F(1,1)+F(2,2)*F(2,1)+F(3,2)*F(3,1)
FTF(3,2)=F(1,3)*F(1,2)+F(2,3)*F(2,2)+F(3,3)*F(3,2)
FTF(2,3)=F(1,2)*F(1,3)+F(2,2)*F(2,3)+F(3,2)*F(3,3)
FTF(1,3)=F(1,1)*F(1,3)+F(2,1)*F(2,3)+F(3,1)*F(3,3)
FTF(3,1)=F(1,3)*F(1,1)+F(2,3)*F(2,1)+F(3,3)*F(3,1)
C
ESCT(1,1)=HALF*(FTF(1,1)-DELTA(1,1))
ESCT(2,2)=HALF*(FTF(2,2)-DELTA(2,2))
ESCT(3,3)=HALF*(FTF(3,3)-DELTA(3,3))
ESCT(1,2)=HALF*(FTF(1,2)-DELTA(1,2))
ESCT(2,1)=HALF*(FTF(2,1)-DELTA(2,1))
ESCT(3,2)=HALF*(FTF(3,2)-DELTA(3,2))
ESCT(2,3)=HALF*(FTF(2,3)-DELTA(2,3))
ESCT(1,3)=HALF*(FTF(1,3)-DELTA(1,3))
ESCT(3,1)=HALF*(FTF(3,1)-DELTA(3,1))
C *****NOMINAL STRAIN TIME DERIVATIVE*****
DESMODT=(ESM0-TEMP1)/DTIME
TEMP1=ESM0
C *****ACTIVE FUNCTION CALCULATION*****
  IF (TIME(2).LT.TD) THEN
    FACT=ZERO
  ELSE IF (TIME(2).GE.TD.AND.TIME(2).LT.TA) THEN
    FACT=1.0d0*(HALF*(ONE-COS(Pi*(TIME(2)-TD)/(TA-TD))))**q
  ELSE IF (time(2).gt.TA.AND.time(2).lt.0.05d0) then

```

```

                FACT=1.0d0
END IF
C *****ACTIVE ESM0*****
ESM0A=(ESM0+ONE)*(KK*(ONE-FACT)+ONE)-ONE
C *****FLEN*****
IF (ESM0A.LT.ES5) THEN
    FLEN=0.0D0
ELSE IF (ESM0A.GE.ES5.AND.ESM0A.LT.ES4) THEN
    FLEN=ABS(F5+(F4-F5)*(ESM0A-ES5)/(ES4-ES5))
ELSE IF (ESM0A.GE.ES4.AND.ESM0A.LT.ES3) THEN
    FLEN=ABS(F4+(ONE-F4)*(ESM0A-ES4)/(ES3-ES4))
ELSE IF (ESM0A.GE.ES3.AND.ESM0A.LT.ES2) THEN
    FLEN=ONE
ELSE IF (ESM0A.GE.ES2.AND.ESM0A.LT.ES1) THEN
    FLEN=ABS(ONE-(ESM0A-ES2)/(ES1-ES2))
ELSE
    FLEN=0.0d0
END IF
C *****FRAT*****
ESMR_ST=DESM0DT/ESR_MIN
IF (ESMR_ST.LT.ZERO) THEN
    FRAT=abs(1.8d0-0.8d0*(ONE+ESMR_ST)/(ONE-7.56d0*ESMR_ST/KKK))
ELSE
    FRAT=abs((ONE-ESMR_ST)/(ONE+ESMR_ST/KKK))
END IF
STMACT=(FACT*FLEN*FRAT)
C ***** PASSIVE STRESS CALCULATION*****
ABESM0=ABS(ESM0)
IF (ESM0A.LE.ZERO) THEN
    STMPAS=ZERO
else IF (ESM0A.GT.0.0D0.AND.ESM0A.LT.ESC) THEN
    STMPAS=(C1*(ESM0A)**C2)
ELSE if (ESM0A.GE.ESC) then
    STMPAS=(C3*ESM0A+C4)
END IF
C ***** NOMINAL STRESS IN MUSCLE*****
STM0=STMAX*(FACT*FLEN*FRAT)+STMPAS
C *****TRUE STRESS IN MUSCLE SCALAR*****
STM=(ONE+ESM0)*STM0
C *****FIBER STRESS TENSOR*****
DO i=1,3
    DO j=1,3
        STF(i,j)=STM*(mm(i,j))
    END DO
END DO
C *****DFGRD0 INCREMENT-DDFGRD*****
DO i=1,3
    DO j=1,3
        DDFGRD(i,j)=DFGRD1(i,j)-TD0(i,j)
    END DO
END DO
C
DO i=1,3
    DO j=1,3
        TD0(i,j)=DFGRD1(i,j)
    END DO
END DO
C *****mmmmm CALCULATION*****
mmmm(1,1)=m(1)*m(1)*m(1)*m(1)
mmmm(1,2)=m(1)*m(1)*m(2)*m(2)
mmmm(1,3)=m(1)*m(1)*m(3)*m(3)
mmmm(1,4)=m(1)*m(1)*m(1)*m(2)
mmmm(1,5)=m(1)*m(1)*m(2)*m(3)

```

mmmm (1, 6) =m (1) *m (1) *m (3) *m (1)
mmmm (1, 7) =m (1) *m (1) *m (2) *m (1)
mmmm (1, 8) =m (1) *m (1) *m (3) *m (2)
mmmm (1, 9) =m (1) *m (1) *m (1) *m (3)

C

mmmm (2, 1) =m (2) *m (2) *m (1) *m (1)
mmmm (2, 2) =m (2) *m (2) *m (2) *m (2)
mmmm (2, 3) =m (2) *m (2) *m (3) *m (3)
mmmm (2, 4) =m (2) *m (2) *m (1) *m (2)
mmmm (2, 5) =m (2) *m (2) *m (2) *m (3)
mmmm (2, 6) =m (2) *m (2) *m (3) *m (1)
mmmm (2, 7) =m (2) *m (2) *m (2) *m (1)
mmmm (2, 8) =m (2) *m (2) *m (3) *m (2)
mmmm (2, 9) =m (2) *m (2) *m (1) *m (3)

C

mmmm (3, 1) =m (3) *m (3) *m (1) *m (1)
mmmm (3, 2) =m (3) *m (3) *m (2) *m (2)
mmmm (3, 3) =m (3) *m (3) *m (3) *m (3)
mmmm (3, 4) =m (3) *m (3) *m (1) *m (2)
mmmm (3, 5) =m (3) *m (3) *m (2) *m (3)
mmmm (3, 6) =m (3) *m (3) *m (3) *m (1)
mmmm (3, 7) =m (3) *m (3) *m (2) *m (1)
mmmm (3, 8) =m (3) *m (3) *m (3) *m (2)
mmmm (3, 9) =m (3) *m (3) *m (1) *m (3)

C

mmmm (4, 1) =m (1) *m (2) *m (1) *m (1)
mmmm (4, 2) =m (1) *m (2) *m (2) *m (2)
mmmm (4, 3) =m (1) *m (2) *m (3) *m (3)
mmmm (4, 4) =m (1) *m (2) *m (1) *m (2)
mmmm (4, 5) =m (1) *m (2) *m (2) *m (3)
mmmm (4, 6) =m (1) *m (2) *m (3) *m (1)
mmmm (4, 7) =m (1) *m (2) *m (2) *m (1)
mmmm (4, 8) =m (1) *m (2) *m (3) *m (2)
mmmm (4, 9) =m (1) *m (2) *m (1) *m (3)

C

mmmm (5, 1) =m (2) *m (3) *m (1) *m (1)
mmmm (5, 2) =m (2) *m (3) *m (2) *m (2)
mmmm (5, 3) =m (2) *m (3) *m (3) *m (3)
mmmm (5, 4) =m (2) *m (3) *m (1) *m (2)
mmmm (5, 5) =m (2) *m (3) *m (2) *m (3)
mmmm (5, 6) =m (2) *m (3) *m (3) *m (1)
mmmm (5, 7) =m (2) *m (3) *m (2) *m (1)
mmmm (5, 8) =m (2) *m (3) *m (3) *m (2)
mmmm (5, 9) =m (2) *m (3) *m (1) *m (3)

C

mmmm (6, 1) =m (3) *m (1) *m (1) *m (1)
mmmm (6, 2) =m (3) *m (1) *m (2) *m (2)
mmmm (6, 3) =m (3) *m (1) *m (3) *m (3)
mmmm (6, 4) =m (3) *m (1) *m (1) *m (2)
mmmm (6, 5) =m (3) *m (1) *m (2) *m (3)
mmmm (6, 6) =m (3) *m (1) *m (3) *m (1)
mmmm (6, 7) =m (3) *m (1) *m (2) *m (1)
mmmm (6, 8) =m (3) *m (1) *m (3) *m (2)
mmmm (6, 9) =m (3) *m (1) *m (1) *m (3)

C

mmmm (7, 1) =m (2) *m (1) *m (1) *m (1)
mmmm (7, 2) =m (2) *m (1) *m (2) *m (2)
mmmm (7, 3) =m (2) *m (1) *m (3) *m (3)
mmmm (7, 4) =m (2) *m (1) *m (1) *m (2)
mmmm (7, 5) =m (2) *m (1) *m (2) *m (3)
mmmm (7, 6) =m (2) *m (1) *m (3) *m (1)
mmmm (7, 7) =m (2) *m (1) *m (2) *m (1)
mmmm (7, 8) =m (2) *m (1) *m (3) *m (2)

```

mmmm(7,9)=m(2)*m(1)*m(1)*m(3)

C

mmmm(8,1)=m(3)*m(2)*m(1)*m(1)
mmmm(8,2)=m(3)*m(2)*m(2)*m(2)
mmmm(8,3)=m(3)*m(2)*m(3)*m(3)
mmmm(8,4)=m(3)*m(2)*m(1)*m(2)
mmmm(8,5)=m(3)*m(2)*m(2)*m(3)
mmmm(8,6)=m(3)*m(2)*m(3)*m(1)
mmmm(8,7)=m(3)*m(2)*m(2)*m(1)
mmmm(8,8)=m(3)*m(2)*m(3)*m(2)
mmmm(8,9)=m(3)*m(2)*m(1)*m(3)

C

mmmm(9,1)=m(1)*m(3)*m(1)*m(1)
mmmm(9,2)=m(1)*m(3)*m(2)*m(2)
mmmm(9,3)=m(1)*m(3)*m(3)*m(3)
mmmm(9,4)=m(1)*m(3)*m(1)*m(2)
mmmm(9,5)=m(1)*m(3)*m(2)*m(3)
mmmm(9,6)=m(1)*m(3)*m(3)*m(1)
mmmm(9,7)=m(1)*m(3)*m(2)*m(1)
mmmm(9,8)=m(1)*m(3)*m(3)*m(2)
mmmm(9,9)=m(1)*m(3)*m(1)*m(3)

C
***** B calculation*****
B(1,1)=HALF*((DELTA(1,1)*m(1)+DELTA(1,1)*m(1))*m(1)+(DELTA(1,1)
1*m(1)+DELTA(1,1)*m(1))*m(1))-TWO*m(1)*m(1)*m(1)*m(1)
B(1,2)=HALF*((DELTA(1,2)*m(1)+DELTA(1,2)*m(1))*m(2)+(DELTA(1,2)
1*m(1)+DELTA(1,2)*m(1))*m(2))-TWO*m(1)*m(1)*m(2)*m(2)
B(1,3)=HALF*((DELTA(1,3)*m(1)+DELTA(1,3)*m(1))*m(3)+(DELTA(1,3)
1*m(1)+DELTA(1,3)*m(1))*m(3))-TWO*m(1)*m(1)*m(3)*m(3)
B(1,4)=HALF*((DELTA(1,1)*m(1)+DELTA(1,1)*m(1))*m(1)+(DELTA(1,2)
1*m(1)+DELTA(1,2)*m(1))*m(1))-TWO*m(1)*m(1)*m(1)*m(2)
B(1,5)=HALF*((DELTA(1,2)*m(1)+DELTA(1,2)*m(1))*m(2)+(DELTA(1,3)
1*m(1)+DELTA(1,3)*m(1))*m(2))-TWO*m(1)*m(1)*m(2)*m(3)
B(1,6)=HALF*((DELTA(1,3)*m(1)+DELTA(1,3)*m(1))*m(3)+(DELTA(1,1)
1*m(1)+DELTA(1,1)*m(1))*m(3))-TWO*m(1)*m(1)*m(3)*m(1)
B(1,7)=HALF*((DELTA(1,2)*m(1)+DELTA(1,2)*m(1))*m(2)+(DELTA(1,1)
1*m(1)+DELTA(1,1)*m(1))*m(2))-TWO*m(1)*m(1)*m(2)*m(1)
B(1,8)=HALF*((DELTA(1,3)*m(1)+DELTA(1,3)*m(1))*m(3)+(DELTA(1,2)
1*m(1)+DELTA(1,2)*m(1))*m(3))-TWO*m(1)*m(1)*m(3)*m(2)
B(1,9)=HALF*((DELTA(1,1)*m(1)+DELTA(1,1)*m(1))*m(1)+(DELTA(1,3)
1*m(1)+DELTA(1,3)*m(1))*m(1))-TWO*m(1)*m(1)*m(1)*m(3)

C

B(2,1)=HALF*((DELTA(2,1)*m(2)+DELTA(2,1)*m(2))*m(1)+(DELTA(2,1)
1*m(2)+DELTA(2,1)*m(2))*m(1))-TWO*m(2)*m(2)*m(1)*m(1)
B(2,2)=HALF*((DELTA(2,2)*m(2)+DELTA(2,2)*m(2))*m(2)+(DELTA(2,2)
1*m(2)+DELTA(2,2)*m(2))*m(2))-TWO*m(2)*m(2)*m(2)*m(2)
B(2,3)=HALF*((DELTA(2,3)*m(2)+DELTA(2,3)*m(2))*m(3)+(DELTA(2,3)
1*m(2)+DELTA(2,3)*m(2))*m(3))-TWO*m(2)*m(2)*m(3)*m(3)
B(2,4)=HALF*((DELTA(2,1)*m(2)+DELTA(2,1)*m(2))*m(2)+(DELTA(2,2)
1*m(2)+DELTA(2,2)*m(2))*m(1))-TWO*m(2)*m(2)*m(1)*m(2)
B(2,5)=HALF*((DELTA(2,2)*m(2)+DELTA(2,2)*m(2))*m(3)+(DELTA(2,3)
1*m(2)+DELTA(2,3)*m(2))*m(2))-TWO*m(2)*m(2)*m(2)*m(3)
B(2,6)=HALF*((DELTA(2,3)*m(2)+DELTA(2,3)*m(2))*m(1)+(DELTA(2,1)
1*m(2)+DELTA(2,1)*m(2))*m(3))-TWO*m(2)*m(2)*m(3)*m(1)
B(2,7)=HALF*((DELTA(2,2)*m(2)+DELTA(2,2)*m(2))*m(2)+(DELTA(2,1)
1*m(2)+DELTA(2,1)*m(2))*m(2))-TWO*m(2)*m(2)*m(2)*m(1)
B(2,8)=HALF*((DELTA(2,3)*m(2)+DELTA(2,3)*m(2))*m(3)+(DELTA(2,2)
1*m(2)+DELTA(2,2)*m(2))*m(3))-TWO*m(2)*m(2)*m(3)*m(2)
B(2,9)=HALF*((DELTA(2,1)*m(2)+DELTA(2,1)*m(2))*m(1)+(DELTA(2,3)
1*m(2)+DELTA(2,3)*m(2))*m(1))-TWO*m(2)*m(2)*m(1)*m(3)

C

B(3,1)=HALF*((DELTA(3,1)*m(3)+DELTA(3,1)*m(3))*m(1)+(DELTA(3,1)
1*m(3)+DELTA(3,1)*m(3))*m(1))-TWO*m(3)*m(3)*m(1)*m(1)
B(3,2)=HALF*((DELTA(3,2)*m(3)+DELTA(3,2)*m(3))*m(2)+(DELTA(3,2)

```



```

1 *m(3)+DELTA(3,2)*m(1)*m(3)-TWO*m(1)*m(3)*m(3)*m(2)
B(9,9)=HALF*((DELTA(1,1)*m(3)+DELTA(3,1)*m(1))*m(1)+(DELTA(1,3)
1 *m(3)+DELTA(3,3)*m(1))*m(1))-TWO*m(1)*m(3)*m(1)*m(3)
C *****dFLEN/dESM0 CALCULATION*****
IF (ESM0A.GE.ES5.AND.ESM0A.LT.ES4) THEN
    DFLENDES=(F4-F5)/(ES4-ES5)
ELSE IF (ESM0A.GE.ES4.AND.ESM0A.LT.ES3) THEN
    DFLENDES=(ONE-F4)/(ES3-ES4)
ELSE IF (ESM0A.GE.ES3.AND.ESM0A.LT.ES2) THEN
    DFLENDES=ZERO
ELSE
    DFLENDES=-ONE/(ES1-ES2)
END IF
C *****dFRAT/dESR*****
IF (ESMR_ST.LT.ZERO) THEN
    DFRATDES=-0.8D0*((ONE/ESR_MIN*(ONE-7.56D0*ESMR_ST/KKK)-
1 (-7.56D0/(KKK*ESR_MIN))* (ONE+ESMR_ST))/
2 (ONE-7.56D0*ESMR_ST/KKK)**TWO)
ELSE
    DFRATDES=(-(ONE+ESMR_ST/KKK)/ESR_MIN-
1 ((ONE-ESMR_ST)/(KKK*ESR_MIN)))/(ONE+ESMR_ST/KKK)**TWO
END IF
C *****dFPASS/dESM0*****
IF (ESM0A.LE.ZERO) THEN
    dFPASSdESM0=ZERO
ELSE IF (ESM0A.GT.ZERO.AND.ESM0A.LT.ESC) THEN
    dFPASSdESM0=C1*C2*(ESM0A)**(C2-ONE)
ELSE IF (ESM0A.GE.ESC) THEN
    dFPASSdESM0=C3
END IF
C *****G CALCULATION*****
G=(ONE+ESM0)*(STMAX*(fact*frat*dflenDES)+ dFPASSdESM0)
C *****CF-Jaumann Elasticity Tensor- CALCULATION*****
DO i=1,9
    DO j=1,9
        CEF(i,j)=((ONE+ESM0)*(STM0+G)*mmmm(i,j)+STM*B(i,j))
    END DO
END DO
C *****CONNECTIVE TISSUE 4TH-ORDER ELASTICITY TENSOR*****
C LE=C-IJKL
C LE1=c-ijkl
C SPK=2nd-Pila-Kirchhof
C KCT=Kirchhof Stress
C STCT=Cauchy stress
C CECT=Jaumann Elasticity tensor
DO i=1,9
    DO j=1,9
        LE(i,j)=ZERO
    END DO
END DO
LE(1,1)=LAME1+TWO*LAME2
LE(1,2)=LAME1
LE(1,3)=LAME1
LE(1,4)=ZERO
LE(1,5)=ZERO
LE(1,6)=ZERO
LE(1,7)=ZERO
LE(1,8)=ZERO
LE(1,9)=ZERO
C
LE(2,1)=LAME1
LE(2,2)=LAME1+TWO*LAME2
LE(2,3)=LAME1

```

```
LE (2, 4) =ZERO
LE (2, 5) =ZERO
LE (2, 6) =ZERO
LE (2, 7) =ZERO
LE (2, 8) =ZERO
LE (2, 9) =ZERO
```

C

```
LE (3, 1) =LAME1
LE (3, 2) =LAME1
LE (3, 3) =LAME1+TWO*LAME2
LE (3, 4) =ZERO
LE (3, 5) =ZERO
LE (3, 6) =ZERO
LE (3, 7) =ZERO
LE (3, 8) =ZERO
LE (3, 9) =ZERO
```

C

```
LE (4, 1) =ZERO
LE (4, 2) =ZERO
LE (4, 3) =ZERO
LE (4, 4) =TWO*LAME2
LE (4, 5) =ZERO
LE (4, 6) =ZERO
LE (4, 7) =ZERO
LE (4, 8) =ZERO
LE (4, 9) =ZERO
```

C

```
LE (5, 1) =ZERO
LE (5, 2) =ZERO
LE (5, 3) =ZERO
LE (5, 4) =ZERO
LE (5, 5) =TWO*LAME2
LE (5, 6) =ZERO
LE (5, 7) =ZERO
LE (5, 8) =ZERO
LE (5, 9) =ZERO
```

C

```
LE (6, 1) =ZERO
LE (6, 2) =ZERO
LE (6, 3) =ZERO
LE (6, 4) =ZERO
LE (6, 5) =ZERO
LE (6, 6) =TWO*LAME2
LE (6, 7) =ZERO
LE (6, 8) =ZERO
LE (6, 9) =ZERO
```

C

```
LE (7, 1) =ZERO
LE (7, 2) =ZERO
LE (7, 3) =ZERO
LE (7, 4) =ZERO
LE (7, 5) =ZERO
LE (7, 6) =ZERO
LE (7, 7) =TWO*LAME2
LE (7, 8) =ZERO
LE (7, 9) =ZERO
```

C

```
LE (8, 1) =ZERO
LE (8, 2) =ZERO
LE (8, 3) =ZERO
LE (8, 4) =ZERO
LE (8, 5) =ZERO
LE (8, 6) =ZERO
```

```

LE (8, 7)=ZERO
LE (8, 8)=TWO*LAME2
LE (8, 9)=ZERO
C
LE (9, 1)=ZERO
LE (9, 2)=ZERO
LE (9, 3)=ZERO
LE (9, 4)=ZERO
LE (9, 5)=ZERO
LE (9, 6)=ZERO
LE (9, 7)=ZERO
LE (9, 8)=ZERO
LE (9, 9)=TWO*LAME2
C *****CALCULATING DETERMINANT OF DFGRD1 GRADIENT*****
DET=DFGRD1 (1, 1) * (DFGRD1 (2, 2) *DFGRD1 (3, 3) -DFGRD1 (3, 2) *DFGRD1 (2, 3))
1 -DFGRD1 (1, 2) * (DFGRD1 (2, 1) *DFGRD1 (3, 3) -DFGRD1 (2, 3) *DFGRD1 (3, 1))
2 +DFGRD1 (1, 3) * (DFGRD1 (2, 1) *DFGRD1 (3, 2) -DFGRD1 (2, 2) *DFGRD1 (3, 1))
C
LE1 (1, 1)=F (1, 1) *F (1, 1) *F (1, 1) *F (1, 1) *LE (1, 1)
LE1 (1, 2)=F (1, 1) *F (1, 1) *F (2, 2) *F (2, 2) *LE (1, 2)
LE1 (1, 3)=F (1, 1) *F (1, 1) *F (3, 3) *F (3, 3) *LE (1, 3)
LE1 (1, 4)=ZERO
LE1 (1, 5)=ZERO
LE1 (1, 6)=ZERO
LE1 (1, 7)=ZERO
LE1 (1, 8)=ZERO
LE1 (1, 9)=ZERO
C
LE1 (2, 1)=F (2, 2) *F (2, 2) *F (1, 1) *F (1, 1) *LE (2, 1)
LE1 (2, 2)=F (2, 2) *F (2, 2) *F (2, 2) *F (2, 2) *LE (2, 2)
LE1 (2, 3)=F (2, 2) *F (2, 2) *F (3, 3) *F (3, 3) *LE (2, 3)
LE1 (2, 4)=ZERO
LE1 (2, 5)=ZERO
LE1 (2, 6)=ZERO
LE1 (2, 7)=ZERO
LE1 (2, 8)=ZERO
LE1 (2, 9)=ZERO
C
LE1 (3, 1)=F (3, 3) *F (3, 3) *F (1, 1) *F (1, 1) *LE (3, 1)
LE1 (3, 2)=F (3, 3) *F (3, 3) *F (2, 2) *F (2, 2) *LE (3, 2)
LE1 (3, 3)=F (3, 3) *F (3, 3) *F (3, 3) *F (3, 3) *LE (3, 3)
LE1 (3, 4)=ZERO
LE1 (3, 5)=ZERO
LE1 (3, 6)=ZERO
LE1 (3, 7)=ZERO
LE1 (3, 8)=ZERO
LE1 (3, 9)=ZERO
C
LE1 (4, 1)=ZERO
LE1 (4, 2)=ZERO
LE1 (4, 3)=ZERO
LE1 (4, 4)=F (1, 1) *F (2, 2) *F (1, 1) *F (2, 2) *LE (4, 4)
LE1 (4, 5)=ZERO
LE1 (4, 6)=ZERO
LE1 (4, 7)=ZERO
LE1 (4, 8)=ZERO
LE1 (4, 9)=ZERO
C
LE1 (5, 1)=ZERO
LE1 (5, 2)=ZERO
LE1 (5, 3)=ZERO
LE1 (5, 4)=ZERO
LE1 (5, 5)=F (2, 2) *F (3, 3) *F (2, 2) *F (3, 3) *LE (5, 5)

```

```

LE1 (5, 6)=ZERO
LE1 (5, 7)=ZERO
LE1 (5, 8)=ZERO
LE1 (5, 9)=ZERO
C
LE1 (6, 1)=ZERO
LE1 (6, 2)=ZERO
LE1 (6, 3)=ZERO
LE1 (6, 4)=ZERO
LE1 (6, 5)=ZERO
LE1 (6, 6)=F (3, 3) *F (1, 1) *F (3, 3) *F (1, 1) *LE (6, 6)
LE1 (6, 7)=ZERO
LE1 (6, 8)=ZERO
LE1 (6, 9)=ZERO
C
LE1 (7, 1)=ZERO
LE1 (7, 2)=ZERO
LE1 (7, 3)=ZERO
LE1 (7, 4)=ZERO
LE1 (7, 5)=ZERO
LE1 (7, 6)=ZERO
LE1 (7, 7)=F (2, 2) *F (1, 1) *F (2, 2) *F (1, 1) *LE (7, 7)
LE1 (7, 8)=ZERO
LE1 (7, 9)=ZERO
C
LE1 (8, 1)=ZERO
LE1 (8, 2)=ZERO
LE1 (8, 3)=ZERO
LE1 (8, 4)=ZERO
LE1 (8, 5)=ZERO
LE1 (8, 6)=ZERO
LE1 (8, 7)=ZERO
LE1 (8, 8)=F (3, 3) *F (2, 2) *F (3, 3) *F (2, 2) *LE (8, 8)
LE1 (8, 9)=ZERO
C
LE1 (9, 1)=ZERO
LE1 (9, 2)=ZERO
LE1 (9, 3)=ZERO
LE1 (9, 4)=ZERO
LE1 (9, 5)=ZERO
LE1 (9, 6)=ZERO
LE1 (9, 7)=ZERO
LE1 (9, 8)=ZERO
LE1 (9, 9)=F (1, 1) *F (3, 3) *F (1, 1) *F (3, 3) *LE (9, 9)
C
C *****SECOND PIOLA KICHHOF STRESS CONNECTIVE TISSUE CALCULATION-
SPK(i, j) *****
EKK=ESCT (1, 1)+ESCT (2, 2)+ESCT (3, 3)
C
SPK (1, 1)=LAME1 *EKK *DELTA (1, 1) +TWO *LAME2 *ESCT (1, 1)
SPK (1, 2)=LAME1 *EKK *DELTA (1, 2) +TWO *LAME2 *ESCT (1, 2)
SPK (1, 3)=LAME1 *EKK *DELTA (1, 3) +TWO *LAME2 *ESCT (1, 3)
SPK (2, 1)=LAME1 *EKK *DELTA (2, 1) +TWO *LAME2 *ESCT (2, 1)
SPK (2, 2)=LAME1 *EKK *DELTA (2, 2) +TWO *LAME2 *ESCT (2, 2)
SPK (2, 3)=LAME1 *EKK *DELTA (2, 3) +TWO *LAME2 *ESCT (2, 3)
SPK (3, 1)=LAME1 *EKK *DELTA (3, 1) +TWO *LAME2 *ESCT (3, 1)
SPK (3, 2)=LAME1 *EKK *DELTA (3, 2) +TWO *LAME2 *ESCT (3, 2)
SPK (3, 3)=LAME1 *EKK *DELTA (3, 3) +TWO *LAME2 *ESCT (3, 3)
C
FS (1, 1)=F (1, 1) *SPK (1, 1) +F (1, 2) *SPK (2, 1) +F (1, 3) *SPK (3, 1)
FS (1, 2)=F (1, 1) *SPK (1, 2) +F (1, 2) *SPK (2, 2) +F (1, 3) *SPK (3, 2)
FS (1, 3)=F (1, 1) *SPK (1, 3) +F (1, 2) *SPK (2, 3) +F (1, 3) *SPK (3, 3)
FS (2, 1)=F (2, 1) *SPK (1, 1) +F (2, 2) *SPK (2, 1) +F (2, 3) *SPK (3, 1)

```

```

FS (2,2)=F (2,1)*SPK (1,2)+F (2,2)*SPK (2,2)+F (2,3)*SPK (3,2)
FS (2,3)=F (2,1)*SPK (1,3)+F (2,2)*SPK (2,3)+F (2,3)*SPK (3,3)
FS (3,1)=F (3,1)*SPK (1,1)+F (3,2)*SPK (2,1)+F (3,3)*SPK (3,1)
FS (3,2)=F (3,1)*SPK (1,2)+F (3,2)*SPK (2,2)+F (3,3)*SPK (3,2)
FS (3,3)=F (3,1)*SPK (1,3)+F (3,2)*SPK (2,3)+F (3,3)*SPK (3,3)
C
FSFT (1,1)=FS (1,1)*FT (1,1)+FS (1,2)*FT (2,1)+FS (1,3)*FT (3,1)
FSFT (1,2)=FS (1,1)*FT (1,2)+FS (1,2)*FT (2,2)+FS (1,3)*FT (3,2)
FSFT (1,3)=FS (1,1)*FT (1,3)+FS (1,2)*FT (2,3)+FS (1,3)*FT (3,3)
FSFT (2,1)=FS (2,1)*FT (1,1)+FS (2,2)*FT (2,1)+FS (2,3)*FT (3,1)
FSFT (2,2)=FS (2,1)*FT (1,2)+FS (2,2)*FT (2,2)+FS (2,3)*FT (3,2)
FSFT (2,3)=FS (2,1)*FT (1,3)+FS (2,2)*FT (2,3)+FS (2,3)*FT (3,3)
FSFT (3,1)=FS (3,1)*FT (1,1)+FS (3,2)*FT (2,1)+FS (3,3)*FT (3,1)
FSFT (3,2)=FS (3,1)*FT (1,2)+FS (3,2)*FT (2,2)+FS (3,3)*FT (3,2)
FSFT (3,3)=FS (3,1)*FT (1,3)+FS (3,2)*FT (2,3)+FS (3,3)*FT (3,3)
C
TCT (1,1)=FSFT (1,1)
TCT (1,2)=FSFT (1,2)
TCT (1,3)=FSFT (1,3)
TCT (2,1)=FSFT (2,1)
TCT (2,2)=FSFT (2,2)
TCT (2,3)=FSFT (2,3)
TCT (3,1)=FSFT (3,1)
TCT (3,2)=FSFT (3,2)
TCT (3,3)=FSFT (3,3)
C
*****CONNECTIVE TISSUE CAUCHY STRESS TENSOR*****
STCT (1,1)=TCT (1,1)/DET
STCT (1,2)=TCT (1,2)/DET
STCT (1,3)=TCT (1,3)/DET
STCT (2,1)=TCT (2,1)/DET
STCT (2,2)=TCT (2,2)/DET
STCT (2,3)=TCT (2,3)/DET
STCT (3,1)=TCT (3,1)/DET
STCT (3,2)=TCT (3,2)/DET
STCT (3,3)=TCT (3,3)/DET
C
*****JAUMANN ELASTICITY TENSOR - CONNECTIVE TISSUE*****
CECT (1,1)=DET*LE1 (1,1)+DELTA (1,1)*KCT (1,1)+KCT (1,1)*DELTA (1,1)
CECT (1,2)=DET*LE1 (1,2)+DELTA (1,2)*KCT (1,2)+KCT (1,2)*DELTA (1,2)
CECT (1,3)=DET*LE1 (1,3)+DELTA (1,3)*KCT (1,3)+KCT (1,3)*DELTA (1,3)
CECT (1,4)=DET*LE1 (1,4)+DELTA (1,1)*KCT (1,2)+KCT (1,1)*DELTA (1,2)
CECT (1,5)=DET*LE1 (1,5)+DELTA (1,2)*KCT (1,3)+KCT (1,2)*DELTA (1,3)
CECT (1,6)=DET*LE1 (1,6)+DELTA (1,3)*KCT (1,1)+KCT (1,3)*DELTA (1,1)
CECT (1,7)=DET*LE1 (1,7)+DELTA (1,2)*KCT (1,1)+KCT (1,2)*DELTA (1,1)
CECT (1,8)=DET*LE1 (1,8)+DELTA (1,3)*KCT (1,2)+KCT (1,3)*DELTA (1,2)
CECT (1,9)=DET*LE1 (1,9)+DELTA (1,1)*KCT (1,3)+KCT (1,1)*DELTA (1,3)
C
CECT (2,1)=DET*LE1 (2,1)+DELTA (2,1)*KCT (2,1)+KCT (2,1)*DELTA (2,1)
CECT (2,2)=DET*LE1 (2,2)+DELTA (2,2)*KCT (2,2)+KCT (2,2)*DELTA (2,2)
CECT (2,3)=DET*LE1 (2,3)+DELTA (2,3)*KCT (2,3)+KCT (2,3)*DELTA (2,3)
CECT (2,4)=DET*LE1 (2,4)+DELTA (2,1)*KCT (2,2)+KCT (2,1)*DELTA (2,2)
CECT (2,5)=DET*LE1 (2,5)+DELTA (2,2)*KCT (2,3)+KCT (2,2)*DELTA (2,3)
CECT (2,6)=DET*LE1 (2,6)+DELTA (2,3)*KCT (2,1)+KCT (2,3)*DELTA (2,1)
CECT (2,7)=DET*LE1 (2,7)+DELTA (2,2)*KCT (2,1)+KCT (2,2)*DELTA (2,1)
CECT (2,8)=DET*LE1 (2,8)+DELTA (2,3)*KCT (2,2)+KCT (2,3)*DELTA (2,2)
CECT (2,9)=DET*LE1 (2,9)+DELTA (2,1)*KCT (2,3)+KCT (2,1)*DELTA (2,3)
C
CECT (3,1)=DET*LE1 (3,1)+DELTA (3,1)*KCT (3,1)+KCT (3,1)*DELTA (3,1)
CECT (3,2)=DET*LE1 (3,2)+DELTA (3,2)*KCT (3,2)+KCT (3,2)*DELTA (3,2)
CECT (3,3)=DET*LE1 (3,3)+DELTA (3,3)*KCT (3,3)+KCT (3,3)*DELTA (3,3)
CECT (3,4)=DET*LE1 (3,4)+DELTA (3,1)*KCT (3,2)+KCT (3,1)*DELTA (3,2)
CECT (3,5)=DET*LE1 (3,5)+DELTA (3,2)*KCT (3,3)+KCT (3,2)*DELTA (3,3)
CECT (3,6)=DET*LE1 (3,6)+DELTA (3,3)*KCT (3,1)+KCT (3,3)*DELTA (3,1)
CECT (3,7)=DET*LE1 (3,7)+DELTA (3,2)*KCT (3,1)+KCT (3,2)*DELTA (3,1)

```

CECT (3, 8) =DET*LE1 (3, 8)+DELTA (3, 3) *KCT (3, 2)+KCT (3, 3) *DELTA (3, 2)
 CECT (3, 9) =DET*LE1 (3, 9)+DELTA (3, 1) *KCT (3, 3)+KCT (3, 1) *DELTA (3, 3)

C

CECT (4, 1) =DET*LE1 (4, 1)+DELTA (1, 1) *KCT (2, 1)+KCT (1, 1) *DELTA (2, 1)
 CECT (4, 2) =DET*LE1 (4, 2)+DELTA (1, 2) *KCT (2, 2)+KCT (1, 2) *DELTA (2, 2)
 CECT (4, 3) =DET*LE1 (4, 3)+DELTA (1, 3) *KCT (2, 3)+KCT (1, 3) *DELTA (2, 3)
 CECT (4, 4) =DET*LE1 (4, 4)+DELTA (1, 1) *KCT (2, 2)+KCT (1, 1) *DELTA (2, 2)
 CECT (4, 5) =DET*LE1 (4, 5)+DELTA (1, 2) *KCT (2, 3)+KCT (1, 2) *DELTA (2, 3)
 CECT (4, 6) =DET*LE1 (4, 6)+DELTA (1, 3) *KCT (2, 1)+KCT (1, 3) *DELTA (2, 1)
 CECT (4, 7) =DET*LE1 (4, 7)+DELTA (1, 2) *KCT (2, 1)+KCT (1, 2) *DELTA (2, 1)
 CECT (4, 8) =DET*LE1 (4, 8)+DELTA (1, 3) *KCT (2, 2)+KCT (1, 3) *DELTA (2, 2)
 CECT (4, 9) =DET*LE1 (4, 9)+DELTA (1, 1) *KCT (2, 3)+KCT (1, 1) *DELTA (2, 3)

C

CECT (5, 1) =DET*LE1 (5, 1)+DELTA (2, 1) *KCT (3, 1)+KCT (2, 1) *DELTA (3, 1)
 CECT (5, 2) =DET*LE1 (5, 2)+DELTA (2, 2) *KCT (3, 2)+KCT (2, 2) *DELTA (3, 2)
 CECT (5, 3) =DET*LE1 (5, 3)+DELTA (2, 3) *KCT (3, 3)+KCT (2, 3) *DELTA (3, 3)
 CECT (5, 4) =DET*LE1 (5, 4)+DELTA (2, 1) *KCT (3, 2)+KCT (2, 1) *DELTA (3, 2)
 CECT (5, 5) =DET*LE1 (5, 5)+DELTA (2, 2) *KCT (3, 3)+KCT (2, 2) *DELTA (3, 3)
 CECT (5, 6) =DET*LE1 (5, 6)+DELTA (2, 3) *KCT (3, 1)+KCT (2, 3) *DELTA (3, 1)
 CECT (5, 7) =DET*LE1 (5, 7)+DELTA (2, 2) *KCT (3, 1)+KCT (2, 2) *DELTA (3, 1)
 CECT (5, 8) =DET*LE1 (5, 8)+DELTA (2, 3) *KCT (3, 2)+KCT (2, 3) *DELTA (3, 2)
 CECT (5, 9) =DET*LE1 (5, 9)+DELTA (2, 1) *KCT (3, 3)+KCT (2, 1) *DELTA (3, 3)

C

CECT (6, 1) =DET*LE1 (6, 1)+DELTA (3, 1) *KCT (1, 1)+KCT (3, 1) *DELTA (1, 1)
 CECT (6, 2) =DET*LE1 (6, 2)+DELTA (3, 2) *KCT (1, 2)+KCT (3, 2) *DELTA (1, 2)
 CECT (6, 3) =DET*LE1 (6, 3)+DELTA (3, 3) *KCT (1, 3)+KCT (3, 3) *DELTA (1, 3)
 CECT (6, 4) =DET*LE1 (6, 4)+DELTA (3, 1) *KCT (1, 2)+KCT (3, 1) *DELTA (1, 2)
 CECT (6, 5) =DET*LE1 (6, 5)+DELTA (3, 2) *KCT (1, 3)+KCT (3, 2) *DELTA (1, 3)
 CECT (6, 6) =DET*LE1 (6, 6)+DELTA (3, 3) *KCT (1, 1)+KCT (3, 3) *DELTA (1, 1)
 CECT (6, 7) =DET*LE1 (6, 7)+DELTA (3, 2) *KCT (1, 1)+KCT (3, 2) *DELTA (1, 1)
 CECT (6, 8) =DET*LE1 (6, 8)+DELTA (3, 3) *KCT (1, 2)+KCT (3, 3) *DELTA (1, 2)
 CECT (6, 9) =DET*LE1 (6, 9)+DELTA (3, 1) *KCT (1, 3)+KCT (3, 1) *DELTA (1, 3)

C

CECT (7, 1) =DET*LE1 (7, 1)+DELTA (2, 1) *KCT (1, 1)+KCT (2, 1) *DELTA (1, 1)
 CECT (7, 2) =DET*LE1 (7, 2)+DELTA (2, 2) *KCT (1, 2)+KCT (2, 2) *DELTA (1, 2)
 CECT (7, 3) =DET*LE1 (7, 3)+DELTA (2, 3) *KCT (1, 3)+KCT (2, 3) *DELTA (1, 3)
 CECT (7, 4) =DET*LE1 (7, 4)+DELTA (2, 1) *KCT (1, 2)+KCT (2, 1) *DELTA (1, 2)
 CECT (7, 5) =DET*LE1 (7, 5)+DELTA (2, 2) *KCT (1, 3)+KCT (2, 2) *DELTA (1, 3)
 CECT (7, 6) =DET*LE1 (7, 6)+DELTA (2, 3) *KCT (1, 1)+KCT (2, 3) *DELTA (1, 1)
 CECT (7, 7) =DET*LE1 (7, 7)+DELTA (2, 2) *KCT (1, 1)+KCT (2, 2) *DELTA (1, 1)
 CECT (7, 8) =DET*LE1 (7, 8)+DELTA (2, 3) *KCT (1, 2)+KCT (2, 3) *DELTA (1, 2)
 CECT (7, 9) =DET*LE1 (7, 9)+DELTA (2, 1) *KCT (1, 3)+KCT (2, 1) *DELTA (1, 3)

C

CECT (8, 1) =DET*LE1 (8, 1)+DELTA (3, 1) *KCT (2, 1)+KCT (3, 1) *DELTA (2, 1)
 CECT (8, 2) =DET*LE1 (8, 2)+DELTA (3, 2) *KCT (2, 2)+KCT (3, 2) *DELTA (2, 2)
 CECT (8, 3) =DET*LE1 (8, 3)+DELTA (3, 3) *KCT (2, 3)+KCT (3, 3) *DELTA (2, 3)
 CECT (8, 4) =DET*LE1 (8, 4)+DELTA (3, 1) *KCT (2, 2)+KCT (3, 1) *DELTA (2, 2)
 CECT (8, 5) =DET*LE1 (8, 5)+DELTA (3, 2) *KCT (2, 3)+KCT (3, 2) *DELTA (2, 3)
 CECT (8, 6) =DET*LE1 (8, 6)+DELTA (3, 3) *KCT (2, 1)+KCT (3, 3) *DELTA (2, 1)
 CECT (8, 7) =DET*LE1 (8, 7)+DELTA (3, 2) *KCT (2, 1)+KCT (3, 2) *DELTA (2, 1)
 CECT (8, 8) =DET*LE1 (8, 8)+DELTA (3, 3) *KCT (2, 2)+KCT (3, 3) *DELTA (2, 2)
 CECT (8, 9) =DET*LE1 (8, 9)+DELTA (3, 1) *KCT (2, 3)+KCT (3, 1) *DELTA (2, 3)

C

CECT (9, 1) =DET*LE1 (9, 1)+DELTA (1, 1) *KCT (3, 1)+KCT (1, 1) *DELTA (3, 1)
 CECT (9, 2) =DET*LE1 (9, 2)+DELTA (1, 2) *KCT (3, 2)+KCT (1, 2) *DELTA (3, 2)
 CECT (9, 3) =DET*LE1 (9, 3)+DELTA (1, 3) *KCT (3, 3)+KCT (1, 3) *DELTA (3, 3)
 CECT (9, 4) =DET*LE1 (9, 4)+DELTA (1, 1) *KCT (3, 2)+KCT (1, 1) *DELTA (3, 2)
 CECT (9, 5) =DET*LE1 (9, 5)+DELTA (1, 2) *KCT (3, 3)+KCT (1, 2) *DELTA (3, 3)
 CECT (9, 6) =DET*LE1 (9, 6)+DELTA (1, 3) *KCT (3, 1)+KCT (1, 3) *DELTA (3, 1)
 CECT (9, 7) =DET*LE1 (9, 7)+DELTA (1, 2) *KCT (3, 1)+KCT (1, 2) *DELTA (3, 1)
 CECT (9, 8) =DET*LE1 (9, 8)+DELTA (1, 3) *KCT (3, 2)+KCT (1, 3) *DELTA (3, 2)
 CECT (9, 9) =DET*LE1 (9, 9)+DELTA (1, 1) *KCT (3, 3)+KCT (1, 1) *DELTA (3, 3)

C

```

C *****MUSCLE STRESS*****
  STRESS(1)=STF(1,1)+STCT(1,1)
  STRESS(2)=STF(2,2)+STCT(2,2)
  STRESS(3)=STF(3,3)+STCT(3,3)
  STRESS(4)=STF(1,2)+STCT(1,2)
  STRESS(5)=STF(2,3)+STCT(2,3)
  STRESS(6)=STF(3,1)+STCT(3,1)
C *****CE CALCULATION*****
DO i=1,6
  DO j=1,6
    DDSDE(i,j)=CEF(i,j)+CECT(i,j)
  END DO
END DO
RETURN
END

```

Appendix C

Previous Versions of Chapters Three and Four

CHAPTER THREE: CONTINUUM CONSTITUTIVE MODELLING OF THE SKELETAL MUSCLE

In this chapter, a nonlinear, fiber-reinforced continuum constitutive model is employed to simulate the biomechanical behavior of the muscle. The model was first developed by Liang and colleagues (Liang *et al.*, 2006) based on van Leeuwen and Keir experimental and numerical works (Van Leeuwen and Kier 1997) to simulate muscle hydrostats. Later, Spyrou and Aravas (Spyrou and Aravas, 2011; Spyrou, 2009) further developed Liang's approach to model the muscle and tendon tissues. In this dissertation, we are using similar approach. At first, the constitutive equations are derived in Section 3.1 and then, the numerical formulation and the approach of discretizing the derived equations are presented in Section 3.2.

The notation used in this chapter and the following ones are described briefly. Boldface symbols represent vector and tensors. The Cartesian coordinate system with base vectors $e_i (i = 1, 2, 3)$ is used. The superscript T indicates the transpose, a superposed dot specifies material time derivative, the preface "det" implies the determinant, and the symbol ∇ is the Jaumann derivative index. The following products will be used in this work (assume that \mathbf{a} , \mathbf{b} , \mathbf{c} , and \mathbf{d} are vectors, \mathbf{A} and \mathbf{B} are second-order tensors, and \mathbf{C} and \mathbf{D} are fourth-order tensors):

$$(\mathbf{ab})_{ij} = a_i b_j, (\mathbf{abcd})_{ijkl} = a_i b_j c_k d_l, (\mathbf{a} \cdot \mathbf{A})_i = a_j A_{ji}, (\mathbf{A} \cdot \mathbf{a})_i = A_{ji} a_j, \mathbf{A} : \mathbf{B} = A_{ij} B_{ij}, (\mathbf{A} : \mathbf{C})_{ij} = A_{kl} C_{kl ij}, (\mathbf{C} : \mathbf{A})_{ij} = C_{kl ij} A_{kl}, \text{ and } (\mathbf{C} : \mathbf{D})_{ijkl} = C_{ijpq} D_{pqkl}.$$

3.1 Constitutive Model

3.1.1 Principal Structure of the Constitutive Model

The skeletal muscle is a composite material composed of fibers aligned in a matrix that is known as connective tissue. The passive and active forces are generated by the fibers along the fibers direction. A schematic view of the fiber orientation in the muscle in general, and in a finite element in particular is shown in Fig. 3.1.

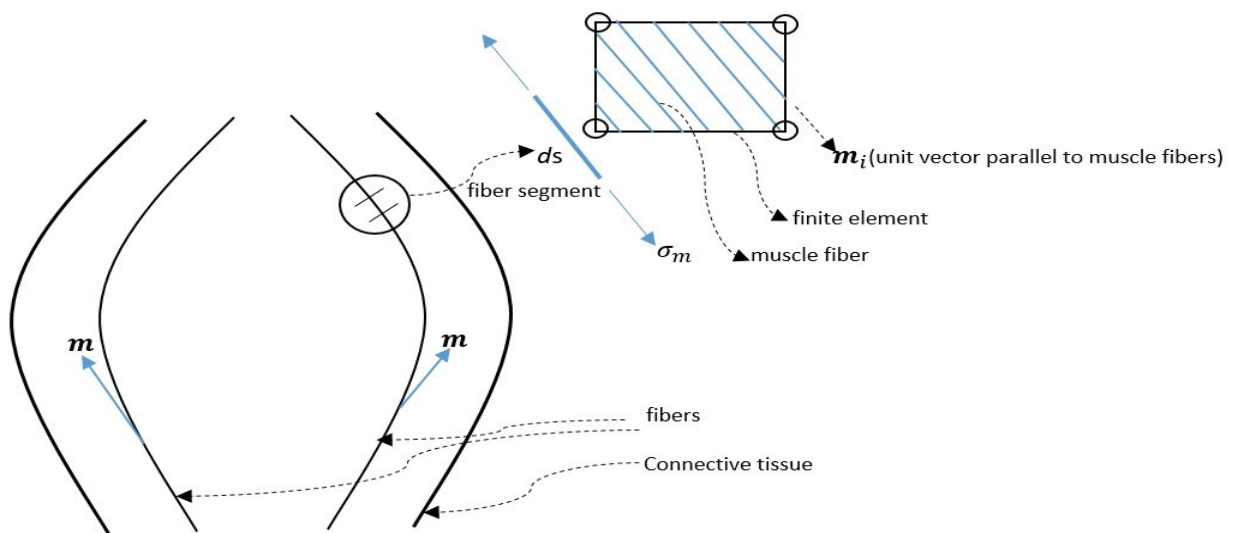


Figure C 3.1 Schematic view of a deformed muscle, fibers direction within the tissue, and an infinitesimal segment of the fiber ds . The orientation of the fibers within a continuum finite element is also depicted. σ_m represents the Cauchy stress in the fiber direction

Using the Spyrou approach, let the undeformed fibers direction at every material point to be defined by a unit vector, \mathbf{m}_0 . Then the deformed configuration of that material point at each time increment is derived as:

$$\mathbf{m} = \frac{1}{\mathbf{F} \cdot \mathbf{m}_0} |\mathbf{F} \cdot \mathbf{m}_0| \quad (3.1.1)$$

where \mathbf{F} is the deformation gradient tensor.

The Eulerian logarithmic approach is employed to define the strain tensor:

$$\boldsymbol{\varepsilon} = \ln \mathbf{V} \quad (3.1.2)$$

where $\mathbf{V} = \sqrt{\mathbf{F} \cdot \mathbf{F}^T}$. The stretch ratio determines the change in the length of each infinitesimal segment of the fiber in the \mathbf{m} direction.

$$\lambda_m = \frac{ds}{ds_0} = \sqrt{\mathbf{m}_0 \cdot \mathbf{F}^T \cdot \mathbf{F} \cdot \mathbf{m}_0} \quad (3.1.3)$$

where ds_0 is the fiber segment original length, and ds is its current length. The axial logarithmic strain in the fiber direction is:

$$\varepsilon_m = \ln \lambda_m \quad (3.1.4)$$

And the rate of change of ε_m is written as:

$$\dot{\varepsilon}_m = \frac{\dot{\lambda}_m}{\lambda_m} = \mathbf{m} \cdot \mathbf{D} \cdot \mathbf{m} = \mathbf{m} \mathbf{m} : \mathbf{D} \quad (3.1.5)$$

where \mathbf{D} is the deformation rate tensor which is the symmetric part of spatial velocity gradient tensor.

The logarithmic strain tensor of the fiber based on the concept of volume conservation and incompressibility of the material can be derived as:

$$\boldsymbol{\varepsilon}^f = \frac{3}{2} \varepsilon_m \left(\mathbf{m} \mathbf{m} - \frac{1}{3} \boldsymbol{\delta} \right) \quad (3.1.6)$$

where δ is the second order identity tensor.

It is assumed that the difference between the total strain and the fiber strain is associated with the connective tissue:

$$\boldsymbol{\varepsilon}^{\text{ct}} = \boldsymbol{\varepsilon} - \boldsymbol{\varepsilon}^{\text{f}} \quad (3.1.7)$$

The nominal strain of the fiber is determined as:

$$\varepsilon_0^{\text{m}} = \frac{ds - ds_0}{ds_0} = \lambda_{\text{m}} - 1 = \exp(\varepsilon_{\text{m}}) - 1 \text{ or } \varepsilon_{\text{m}} = \ln(1 + \varepsilon_0^{\text{m}}) \quad (3.1.8)$$

Likewise, nominal stress in the fiber is related to the fiber true stress as:

$$\sigma_0^{\text{m}} = \sigma^{\text{m}} \frac{A}{A_0} = \sigma^{\text{m}} \frac{ds_0}{ds} = \frac{\sigma^{\text{m}}}{\lambda_{\text{m}}} = \frac{\sigma^{\text{m}}}{1 + \varepsilon_0^{\text{m}}} \quad (3.1.9)$$

where A_0 and A are the fiber's initial and current cross sectional area.

Consequently, $\boldsymbol{\sigma}^{\text{f}}$ can be defined as:

$$\boldsymbol{\sigma}^{\text{f}} = \sigma^{\text{m}} \mathbf{m} \mathbf{m} \quad (3.1.10)$$

And finally, the total stress in the muscle is assumed to be the sum of stresses in the fibers and the connective tissue:

$$\boldsymbol{\sigma} = \boldsymbol{\sigma}^{\text{f}} + \boldsymbol{\sigma}^{\text{ct}} \quad (3.1.11)$$

3.1.2 Fiber Stress Calculation

The muscle fibers generate two types of the forces: active and passive. While the active force is a function of the activation level, fiber length, and velocity of contraction, the passive force is

just a function of the length of the fiber. In general, the nominal longitudinal stress in a muscle fiber is written as sum of the active nominal longitudinal stress, $\sigma_0^{m \text{ (act)}}$, and the passive one, $\sigma_0^{m \text{ (pas)}}$:

$$\sigma_0^m = \sigma_0^{m \text{ (act)}} + \sigma_0^{m \text{ (pas)}} \quad (3.1.12)$$

Following Liang's approach, $\sigma_0^{m \text{ (act)}}$ and $\sigma_0^{m \text{ (pas)}}$ are defined as:

$$\sigma_0^{m \text{ (act)}} = \sigma_{\max} f_a(t) \cdot f_l(\epsilon_0^m) \cdot f_v(\dot{\epsilon}_0^m) \text{ and } \sigma_0^{m \text{ (pas)}} = \sigma_0^{m \text{ (pas)}}(\epsilon_0^m) \quad (3.1.13)$$

where σ_{\max} is the maximum isometric stress at the optimal fiber length, f_a is the activation function that relates the pattern of the activation to time, f_l is the length function that shows the relation between the active stress and the fiber nominal longitudinal strain, ϵ_0^m , and finally, f_v is the velocity function that shows the effect of velocity of contraction or nominal longitudinal strain rate on the overall nominal longitudinal stress of the fiber. Therefore, the total nominal stress in the fiber is written as:

$$\sigma_0^m = \sigma_{\max} f_a(t) \cdot f_l(\epsilon_0^m) \cdot f_v(\dot{\epsilon}_0^m) + \sigma_0^{m \text{ (pas)}}(\epsilon_0^m) \quad (3.1.14)$$

3.1.3 Connective Tissue Stress Calculation

The connective tissue is assumed to behave as an isotropic linear hyperelastic material:

$$\boldsymbol{\sigma}^{\text{ct}} = \frac{1}{J} \mathcal{L}^e : \boldsymbol{\epsilon}^{\text{ct}} \quad (3.1.15)$$

In the above equation, $J = \det \mathbf{F}$ and \mathcal{L}^e is the elasticity tensor:

$$\mathcal{L}^e = 2\mu\mathbf{K} + 3k\mathbf{J}, \quad \mathbf{J} = \frac{1}{3}\boldsymbol{\delta}\boldsymbol{\delta}, \quad \mathbf{K} = \mathbf{I} - \mathbf{J} \quad (3.1.16)$$

Where μ and k are the shear and bulk modulus of the muscle connective tissue, respectively. \mathbf{J} and \mathbf{K} are the fourth-order deviatoric and spherical projection tensors. \mathbf{I} is the fourth-order identity tensor:

$$I_{ijkl} = \frac{1}{2}(\delta_{ik}\delta_{jl} + \delta_{il}\delta_{jk}) \quad (3.1.17)$$

3.1.4 Generalizing the Constitutive Equations to Pennate Structures

In case of pennate structure, there are more fiber bundles in different directions. The method of superposition is used to sum up all stresses in different directions. Therefore, the constitutive equations of fibers can be rewritten as:

$$\boldsymbol{\varepsilon}^f = \frac{3}{2}\sum_{i=1}^n \varepsilon_m^{(i)} \left(\mathbf{m}^{(i)}\mathbf{m}^{(i)} - \frac{1}{3}\boldsymbol{\delta} \right), \quad \mathbf{m}^{(i)} = \frac{1}{|\mathbf{F}\cdot\mathbf{m}^{(i)}|} \mathbf{F}\cdot\mathbf{m}^{(i)} \quad (3.1.18)$$

$$\lambda_m^{(i)} = \sqrt{\mathbf{m}_0^{(i)} \cdot \mathbf{F}^T \cdot \mathbf{F} \cdot \mathbf{m}_0^{(i)}}, \quad \varepsilon_0^{m(i)} = \lambda_m^{(i)} - 1, \quad \varepsilon_m^{(i)} = \ln \lambda_m^{(i)} \quad (3.1.19)$$

$$\boldsymbol{\sigma}^f = \sum_{i=1}^n \sigma^{m(i)} \mathbf{m}^{(i)}\mathbf{m}^{(i)}, \quad \sigma^{m(i)} = (1 + \varepsilon_0^{m(i)})\sigma_0^{m(i)} \quad (3.1.20)$$

$$\sigma_0^{m(i)} = \sigma_{\max}^{(i)} \left(f_a^{(i)}(t) f_l^{(i)}(\varepsilon_0^{m(i)}) f_v^{(i)}(\dot{\varepsilon}_0^{m(i)}) \right) + \sigma_{\text{pas}}^{m(i)} \quad (3.1.21)$$

3.2 Numerical Formulation and Discretization of the Constitutive Model

3.2.1 Deformable Body General Equilibrium Equation

To implement the constitutive equations derived in Section 3.1 into the FE solver, the Cauchy stress and material Jacobian tensors should be derived. Therefore, the equilibrium equation of a general deformable body (Fig. 3.2) is described as:

$$\frac{\partial \sigma_{ij}}{\partial x_i} + \rho b_i = 0 \quad (3.2.1)$$

Where σ_{ij} is a typical component of the Cauchy stress tensor, \mathbf{b} is body force per unit of mass, and ρ is the mass density.

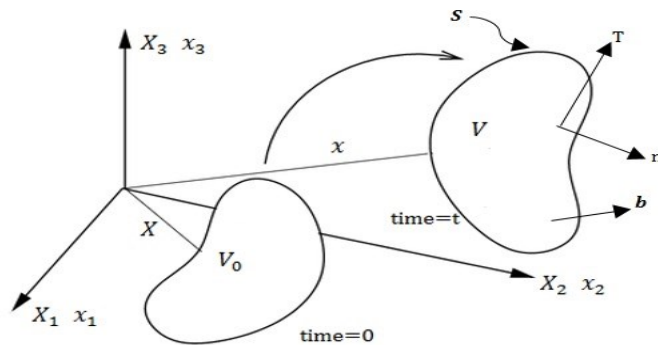


Figure C 3.2 Configuration of a continuum body in a Cartesian coordinate system and its motion.

As shown in Fig.3.2, the body volume changes from V_0 at $\text{time}=0$ to V at $\text{time}=t$. the volume is confined to a boundary surface, S , which is divided to two parts: S_u and S_σ . The displacement vector \mathbf{u} is known on S_u , and the traction forces per unit of area, \mathbf{T} , are known on S_σ :

$$\mathbf{u} = \hat{\mathbf{u}} \equiv \text{known on } S_u \text{ and } \mathbf{n} \cdot \boldsymbol{\sigma} = \mathbf{T} \equiv \text{known on } S_\sigma \quad (3.2.2)$$

To have a displacement field, $u(x)$, that satisfies the first part of Eq. 3.2.2, the Eq. 3.2.1 can be written as:

$$\int_V \left[\frac{\partial \sigma_{ij}(u)}{\partial x_j} + \rho b_i \right] v_i^* dV + \int_{S_\sigma} [T_i - n_j \sigma_{ij}(u)] v_i^* dS = 0 \quad (3.2.3)$$

Where v_i^* represents virtual velocity field that fulfills the condition $v_i^* = 0$ on S_u .

Eq. 3.2.3 can be replaced by the Eq. 3.2.4 using the Green theorem to find a displacement field that satisfies $\mathbf{u} = \hat{\mathbf{u}}$ on S_u . This is the first step in the FE formulation of the problem.

$$\mathbf{G}(u(x)) \equiv \int_V \boldsymbol{\sigma}(u(x)) : \mathbf{D}^* dV - \int_V \rho \mathbf{b} \cdot \mathbf{v}^* dV - \int_S \mathbf{T} \cdot \mathbf{v}^* dS = 0 \quad (3.2.4)$$

Where \mathbf{D}^* is given by

$$D_{ij}^* = \frac{1}{2} \left(\frac{\partial v_i^*}{\partial x_j} + \frac{\partial v_j^*}{\partial x_i} \right) \quad (3.2.5)$$

By considering $\boldsymbol{\sigma}$ as a symmetric tensor, Eq. 3.2.4 is written as:

$$G(u(x)) \equiv \int_V \boldsymbol{\sigma}(u(x)) : \mathbf{L}^* dV - \int_V \rho \mathbf{b} \cdot \mathbf{v}^* dV - \int_S \mathbf{T} \cdot \mathbf{v}^* dS = 0 \quad (3.2.6)$$

where

$$L_{ij}^* = \frac{\partial v_i^*}{\partial x_j} \quad (3.2.7)$$

3.2.2 Finite Element Implementation

To transform the previously mentioned equations to the finite element setting, the amount of displacement increment, $\Delta u(x)$, at the end of each time increment is calculated:

$$u_{n+1}(x) = u_n(x) + \Delta u(x) \quad (3.2.8)$$

By using finite element interpolation matrix, $N(x)$, the displacement increment vector is related to the nodal displacement at each element, Δu_e^N :

$$\{\Delta u(x)\} = [N(x)]\{\Delta u_e^N\} \quad (3.2.9)$$

Similarly, virtual velocity vector \mathbf{v}^* and velocity gradient $\mathbf{L}^* = \partial \mathbf{v}^* / \partial \mathbf{x}_{n+1}$ are written as:

$$\{v^*(x)\} = [N(x)]\{v_e^{*N}\} \quad (3.2.10)$$

$$\{L^*(x)\} = [B_L(x)]\{v_e^{*N}\} \quad (3.2.11)$$

Then, by substituting the above equations in Eq. 3.2.6, it is rewritten as:

$$G = [v^{*N}] \Lambda \left(\int_{V_{n+1}^e} [B_L]_{n+1}^T \{\sigma\}_{n+1} dV - \int_{V_{n+1}^e} [N]_{n+1}^T \rho \{b\}_{n+1} dV - \int_{S_{\sigma}^e|_{n+1}} [N]_{n+1}^T \{T\}_{n+1} dS \right) \quad (3.2.12)$$

where Λ is the “assembly operator”, and $[v^{*N}]$ is row of virtual nodal velocities.

Also, the applied load vector $\{F\}_{n+1}$ is described as:

$$\{F\}_{n+1} = \Lambda \left(\int_{V_{n+1}^e} [B_L]_{n+1}^T \{\sigma\}_{n+1} dV \right) \quad (3.2.13)$$

which is equal to:

$$\{F\}_{n+1} = \Lambda \left(\int_{V_{n+1}^e} [N]_{n+1}^T \rho \{b\}_{n+1} dV + \int_{S_{\sigma}^e|_{n+1}} [N]_{n+1}^T \{T\}_{n+1} dS \right) \quad (3.2.14)$$

Thus, the residual force vector $R(\Delta u^N)$ can be defined as:

$$\{R(\Delta u^N)\}_{n+1} \equiv \Lambda \left(\int_{V_{n+1}^e} [B_L]_{n+1}^T \{\sigma\}_{n+1} dV \right) - \{F\}_{n+1} = 0 \quad (3.2.15)$$

Hence, the corresponding Jacobian or stiffness matrix $[K]$ is derived from the following equations:

$$G = [v^{*N}] \{R\}_{n+1} = 0 \quad (3.2.16)$$

$$dG = [v^{*N}] \left[\frac{\partial \{R(\Delta u^N)\}_{n+1}}{\partial \{\Delta u^N\}} \right] d\{\Delta u^N\} = [v^{*N}] [K] d\{\Delta u^N\} \quad (3.2.17)$$

3.2.3 Calculation of the Jacobian

By applying the finite element discretization method to the continuum form of G and comparing results to Eq. 3.2.17, the Jacobian matrix $[K]$ can be calculated. The following equations explain the procedure:

$$G(\Delta \mathbf{u}) = \int_{\check{V}} \text{tr} \left(\boldsymbol{\sigma} \cdot \frac{\partial \mathbf{v}^*}{\partial \mathbf{x}} \right) dV - \int_{V_0} \rho_0 \mathbf{b} \cdot \mathbf{v}^* dV_0 - \int_{S_0^g} \mathbf{T}^0 \cdot \mathbf{v}^* dS_0 \quad (3.2.18)$$

Where ρ_0 and \mathbf{T}^0 are the initial density and the nominal traction vector, respectively. It should be mentioned that all parameters used from now on are measured at the end of the increment.

$$d\mathbf{x} = d\mathbf{x}_{n+1} = d(\mathbf{x}_n + \Delta \mathbf{u}) = d(\Delta \mathbf{u}) \quad (3.2.19)$$

The first part on the right side of Eq. 3.2.18 can be written as:

$$\int_{\check{V}} \text{tr} \left(\boldsymbol{\sigma} \cdot \frac{\partial \mathbf{v}^*}{\partial \mathbf{x}} \right) dV = \int_{V_0} \text{tr} \left(\boldsymbol{\sigma} \cdot \frac{\partial \mathbf{v}^*}{\partial \mathbf{X}} \cdot \frac{\partial \mathbf{X}}{\partial \mathbf{x}} \right) J dV_0 = \int_{V_0} \text{tr} \left(\boldsymbol{\sigma} \cdot \frac{\partial \mathbf{v}^*}{\partial \mathbf{X}} \cdot \mathbf{F}^{-1} \right) J dV_0 \quad (3.2.20)$$

Then Eq. 3.2.18 is rewritten as:

$$G(\Delta \mathbf{u}) = \int_{V_0} \text{tr} \left(\boldsymbol{\sigma} \cdot \frac{\partial \mathbf{v}^*}{\partial \mathbf{X}} \cdot \mathbf{F}^{-1} \right) J dV_0 - \int_{V_0} \rho_0 \mathbf{b} \cdot \mathbf{v}^* dV_0 - \int_{S_0^g} \mathbf{T}^0 \cdot \mathbf{v}^* dS_0 \quad (3.2.21)$$

Moreover, by assuming that the applied loads are independent of the body motion, follower loads ($\int_{V_0} \rho_0 \mathbf{b} \cdot \mathbf{v}^* dV_0$) are excluded from the previous equations, and hence, differential form of G becomes

$$dG = \int_{V_0} \text{tr} \left\{ \frac{\partial \mathbf{v}^*}{\partial \mathbf{X}} \cdot \left[d(\mathbf{F}^{-1}) \cdot \boldsymbol{\sigma} + \mathbf{F}^{-1} \cdot d\boldsymbol{\sigma} + \mathbf{F}^{-1} \cdot \boldsymbol{\sigma} \frac{dJ}{J} \right] \right\} J dV_0 \quad (3.2.22)$$

where

$$\frac{\partial \mathbf{v}^*}{\partial \mathbf{X}} = \frac{\partial \mathbf{v}^*}{\partial \mathbf{x}} \cdot \frac{\partial \mathbf{x}}{\partial \mathbf{X}} = \mathbf{L}^* \cdot \mathbf{F} \quad (3.2.23)$$

By substituting Eq. 3.2.23 into Eq. 3.2.22, it becomes

$$dG = \int_V \text{tr} \left\{ \mathbf{L}^* \cdot \left[\mathbf{F} \cdot d(\mathbf{F}^{-1}) \cdot \boldsymbol{\sigma} + d\boldsymbol{\sigma} + \frac{dJ}{J} \boldsymbol{\sigma} \right] \right\} dV \quad (3.2.24)$$

Next, each term inside the brackets is introduced:

$$\mathbf{F} = \frac{\partial \mathbf{x}}{\partial \mathbf{X}} \Rightarrow d\mathbf{F} = \frac{\partial(d\mathbf{x})}{\partial \mathbf{X}} \text{ or } d\mathbf{F} = \frac{\partial(d(\Delta \mathbf{u}))}{\partial \mathbf{X}} \quad (3.2.25)$$

also,

$$\mathbf{F} \cdot \mathbf{F}^{-1} = \boldsymbol{\delta} \Rightarrow d\mathbf{F} \cdot \mathbf{F}^{-1} + \mathbf{F} \cdot d\mathbf{F}^{-1} = 0 \Rightarrow \mathbf{F} \cdot d\mathbf{F}^{-1} = -d\mathbf{F} \cdot \mathbf{F}^{-1} \quad (3.2.26)$$

Combining Eq. 3.2.25 and 26 results in

$$\mathbf{F} \cdot d\mathbf{F}^{-1} = -\frac{\partial[d(\Delta \mathbf{u})]}{\partial \mathbf{X}} \cdot \frac{\partial \mathbf{X}}{\partial \mathbf{x}} = -\frac{\partial[d(\Delta \mathbf{u})]}{\partial \mathbf{x}} \Rightarrow \mathbf{F} \cdot d\mathbf{F}^{-1} = -d\mathbf{L} \quad (3.2.27)$$

where

$$d\mathbf{L} \equiv \frac{\partial[d(\Delta \mathbf{u})]}{\partial \mathbf{x}} \quad (3.2.28)$$

On the other hand, using the derivative $\frac{\partial J}{\partial F_{ki}}$ leads to

$$\begin{aligned} dJ &= J(F^{-1})_{ik} dF_{ki} = J(F^{-1} \cdot d\mathbf{F})_{ii} = J \text{tr}(F^{-1} \cdot d\mathbf{F}) = J \text{tr} \left(\frac{\partial \mathbf{X}}{\partial \mathbf{x}} \cdot \frac{\partial(d\Delta \mathbf{u})}{\partial \mathbf{X}} \right) \\ &= J \text{tr} \left(\frac{\partial(d\Delta \mathbf{u})}{\partial \mathbf{x}} \right) = J \text{tr}(d\mathbf{L}) \end{aligned} \quad (3.2.29)$$

or

$$\frac{dJ}{J} = dL_{kk} \quad (3.2.30)$$

Finally, to simplify the calculation of the variation of the stress tensor $\boldsymbol{\sigma}$ with respect to the displacement increment, $\Delta \mathbf{u}$, the following approach is applied

$$\overset{\nabla}{\boldsymbol{\sigma}} = \mathbf{C} : \mathbf{D} = \mathbf{C} : \mathbf{L} \quad (3.2.31)$$

Where $\overset{\nabla}{\boldsymbol{\sigma}}$ and \mathbf{C} are fourth-order tensors, $\mathbf{L} = \partial \mathbf{v} / \partial \mathbf{x}$, and $\mathbf{D} = (1/2)(\mathbf{L} + \mathbf{L}^T)$.

then

$$\dot{\boldsymbol{\sigma}} = \overset{\nabla}{\boldsymbol{\sigma}} - \boldsymbol{\sigma} \cdot \mathbf{W} + \mathbf{W} \cdot \boldsymbol{\sigma} = \mathbf{C} : \mathbf{L} - \frac{1}{2} \boldsymbol{\sigma} \cdot (\mathbf{L} - \mathbf{L}^T) + \frac{1}{2} (\mathbf{L} - \mathbf{L}^T) \cdot \boldsymbol{\sigma} \quad (3.2.32)$$

and differential stress is approximately

$$d\boldsymbol{\sigma} \cong \mathbf{C} : d\mathbf{L} - \frac{1}{2} \boldsymbol{\sigma} \cdot (d\mathbf{L} - d\mathbf{L}^T) + \frac{1}{2} (d\mathbf{L} - d\mathbf{L}^T) \cdot \boldsymbol{\sigma} \quad (3.2.33)$$

substituting Eqs. 3.2.27-3.2.30, and Eq. 3.2.33 into Eq. 3.2.24

$$dG = \int_V \mathbf{L}^* : \left[\mathbf{C} : d\mathbf{L} - \frac{1}{2} \boldsymbol{\sigma} \cdot (d\mathbf{L} + d\mathbf{L}^T) + \frac{1}{2} (d\mathbf{L} - d\mathbf{L}^T) \cdot \boldsymbol{\sigma} + dL_{kk} \boldsymbol{\sigma} \right] dV \quad (3.2.34)$$

The alternative form of Eq. 3.2.34 is

$$dG = \int_V \mathbf{L}^* : (\mathbf{C} + \boldsymbol{\Sigma} + \boldsymbol{\sigma} \boldsymbol{\delta}) : d\mathbf{L} dV \quad (3.2.35)$$

where

$$\Sigma_{ijkl} = \frac{1}{2}(\delta_{ik}\sigma_{jl} - \delta_{il}\sigma_{jk} - \sigma_{ik}\delta_{jl} + \sigma_{il}\delta_{jk}) \quad (3.2.36)$$

and using the following equations

$$\{L^*\} = [B_L]\{v_e^{*N}\} \text{ and } \{dL\} = [B_L]\{du_e^N\} \quad (3.2.37)$$

in Eq. 3.2.35 to find

$$dG = [v_e^N] \left(\Lambda \int_{V_e} [B_L]^T ([C] + [\Sigma] + \{\sigma\}\{\delta\}) [B_L] dV \right) d\{\Delta u^N\} \quad (3.2.38)$$

Therefore, comparing the above equation to Eq. 3.2.17, gives us the stiffness matrix

$$[K] = \Lambda [k^e] \quad (3.2.39)$$

where $[k^e]$ is the “element stiffness matrix”

$$[k^e] = \int_{V_e} [B_L]^T ([C] + [\Sigma] + \{\sigma\}\{\delta\}) [B_L] dV \quad (3.2.40)$$

3.2.4 The Linearization Moduli

The ultimate purpose of numerical implementation of the constitutive equations is to relate stress function and its derivatives to the strain and its derivatives

$$\overset{\nabla}{\boldsymbol{\sigma}} = \mathbf{C} : \mathbf{D} \quad \text{or} \quad \partial \boldsymbol{\sigma} = \mathbf{C} : \partial \boldsymbol{\varepsilon} \quad (3.2.41)$$

To calculate the Jacobian tensor which is the basis of equilibrium equations in the FE solvers, the so-called “linearization moduli” of the algorithm that handles the constitutive equations are required. These moduli are defined in terms of the fourth-order tensor \mathbf{C} .

In this section the approximate method of calculating \mathbf{C} is introduced. Back to the total stress of the muscle, $\boldsymbol{\sigma} = \boldsymbol{\sigma}^f + \boldsymbol{\sigma}^{ct}$, its derivative can be implied as:

$$\dot{\boldsymbol{\sigma}} = \dot{\boldsymbol{\sigma}}^f + \dot{\boldsymbol{\sigma}}^{ct} \quad (3.2.42)$$

Recalling the fiber part of the stress tensor, $\boldsymbol{\sigma}^f = \sigma^m \mathbf{m}\mathbf{m}$, its derivative is defined as

$$\dot{\boldsymbol{\sigma}}^f = \dot{\sigma}^m \mathbf{m}\mathbf{m} + \sigma^m (\dot{\mathbf{m}}\mathbf{m} + \mathbf{m}\dot{\mathbf{m}}) \quad (3.2.43)$$

where

$$\sigma^m = (1 + \varepsilon_0^m) \sigma_0^m = \exp(\varepsilon_m) \sigma_0^m \quad (3.2.44)$$

To obtain the derivative of the Cauchy stress $\dot{\sigma}^m$, $\dot{\varepsilon}^m$ and $\dot{\varepsilon}_0^m$ must be derived first:

$$\dot{\varepsilon}^m = \mathbf{m} \cdot \mathbf{D} \cdot \mathbf{m} = (\mathbf{m}\mathbf{m}) : \mathbf{D} \quad (3.2.45)$$

and

$$\varepsilon_0^m = \exp(\varepsilon_m) - 1 \Rightarrow \dot{\varepsilon}_0^m = \exp(\varepsilon_m) \dot{\varepsilon}_m \quad (3.2.46)$$

by substituting Eq.3.2.24 into Eq. 3.2.25

$$\dot{\varepsilon}_0^m = (1 + \varepsilon_0^m) (\mathbf{m}\mathbf{m}) : \mathbf{D} \quad (3.2.47)$$

The nominal stress in the fiber has the form of:

$$\sigma_{0|n+1}^m = f(\varepsilon_{0|n+1}^m, \frac{\varepsilon_{0|n+1}^m - \varepsilon_{0|n}^m}{\Delta t}, t_{n+1}) \quad (3.2.48)$$

Hence, $\dot{\sigma}^m$ becomes

$$\dot{\sigma}_0^m = \frac{\partial f}{\partial \varepsilon_0^m} \dot{\varepsilon}_0^m + \frac{1}{\Delta t} \frac{\partial f}{\partial \dot{\varepsilon}_0^m} \dot{\varepsilon}_0^m = \left(\frac{\partial f}{\partial \varepsilon_0^m} + \frac{1}{\Delta t} \frac{\partial f}{\partial \dot{\varepsilon}_0^m} \right) \dot{\varepsilon}_0^m \xrightarrow{(3.2.37)} \dot{\sigma}_0^m = \mathbf{G}(\mathbf{m}\mathbf{m}) : \mathbf{D} \quad (3.2.49)$$

where

$$\mathbf{G} = (1 + \varepsilon_0^m) \left(\frac{\partial f}{\partial \varepsilon_0^m} + \frac{1}{\Delta t} \frac{\partial f}{\partial \dot{\varepsilon}_0^m} \right) \quad (3.2.50)$$

therefore,

$$\begin{aligned} \dot{\sigma}^m &= \exp(\varepsilon_m) (\dot{\varepsilon}^m \sigma_0^m + \dot{\sigma}_0^m) \xrightarrow{(3.2.36), (3.2.39)} \dot{\sigma}^m \\ &= \exp(\varepsilon_m) [\sigma_0^m (\mathbf{m}\mathbf{m}) : \mathbf{D} + \mathbf{G}(\mathbf{m}\mathbf{m}) : \mathbf{D}] \\ &= (1 + \varepsilon_0^m) (\sigma_0^m + \mathbf{G})(\mathbf{m}\mathbf{m}) : \mathbf{D} \end{aligned} \quad (3.2.51)$$

The second part of Eq. 3.2.33, $(\overset{\nabla}{\mathbf{m}\mathbf{m}} + \overset{\nabla}{\mathbf{m}\mathbf{m}})$, is calculated using the following relations

$$\dot{\mathbf{m}} = (\mathbf{W} + \mathbf{D} \cdot \mathbf{m}\mathbf{m} - \mathbf{m}\mathbf{m} \cdot \mathbf{D}) \cdot \mathbf{m} \Rightarrow \overset{\nabla}{\mathbf{m}} = (\mathbf{D} \cdot \mathbf{m}\mathbf{m} - \mathbf{m}\mathbf{m} \cdot \mathbf{D}) \cdot \mathbf{m} \quad (3.2.52)$$

or

$$\overset{\nabla}{\mathbf{m}} = \mathbf{D} \cdot \mathbf{m} - \mathbf{m}(\mathbf{m}\mathbf{m}) : \mathbf{D} \quad (3.2.53)$$

so

$$\begin{aligned} \overset{\nabla}{\mathbf{m}\mathbf{m}} + \overset{\nabla}{\mathbf{m}\mathbf{m}} &= [\mathbf{D} \cdot \mathbf{m} - \mathbf{m}(\mathbf{m}\mathbf{m}) : \mathbf{D}] \mathbf{m} + \mathbf{m} [\mathbf{D} \cdot \mathbf{m} - \mathbf{m}(\mathbf{m}\mathbf{m}) : \mathbf{D}] \\ &= \mathbf{D} \cdot \mathbf{m}\mathbf{m} + \mathbf{m}\mathbf{D} \cdot \mathbf{m} - 2\mathbf{m}\mathbf{m}(\mathbf{m}\mathbf{m}) : \mathbf{D} \end{aligned} \quad (3.2.54)$$

which indicates that:

$$\overset{\nabla}{\mathbf{m}}\mathbf{m} + \mathbf{m}\overset{\nabla}{\mathbf{m}} = \mathbf{B} : \mathbf{D} \quad (3.2.55)$$

where

$$B_{ijkl} = \frac{1}{2} [(\delta_{ik}m_j + \delta_{jk}m_i)m_k + (\delta_{il}m_j + \delta_{jl}m_i)m_k] - 2m_im_jm_km_l \quad (3.2.56)$$

Substituting Eq. 3.2.41 and Eq.3.2.45 into Eq. 3.2.33 results in

$$\overset{\nabla}{\sigma}^f = (1 + \varepsilon_0^m)(\sigma_0^m + G)(\mathbf{m}\mathbf{m}) : \mathbf{D}\mathbf{m}\mathbf{m} + \sigma^m \mathbf{B} : \mathbf{D} \quad (3.2.57)$$

or

$$\overset{\nabla}{\sigma}^f = \mathbf{C}^f : \mathbf{D} \quad (3.2.58)$$

and finally,

$$\mathbf{C}^f = (1 + \varepsilon_0^m)(\sigma_0^m + G)\mathbf{m}\mathbf{m}\mathbf{m}\mathbf{m} + \sigma^m \mathbf{B} \quad (3.2.59)$$

Similar approach can be used to calculate $\overset{\nabla}{\sigma}^{ct}$ and \mathbf{C}^{ct} . By taking the derivative of Eq. 3.1.15, we find

$$\overset{\nabla}{\sigma}^{ct} = \frac{1}{j} \mathcal{L}^e : \overset{\nabla}{\boldsymbol{\varepsilon}}^{ct} - \frac{j}{j^2} \mathcal{L}^e : \boldsymbol{\varepsilon}^{ct} \cong \frac{1}{j} \mathcal{L}^e : \mathbf{D}^{ct} - \sigma^{ct} \boldsymbol{\delta} : \mathbf{D} \quad (3.2.60)$$

Where $j = jD_{kk}$ and $\overset{\nabla}{\boldsymbol{\varepsilon}} \cong \mathbf{D}$.

The fiber portion of \mathbf{D} is calculated by taking the derivative of Eq. 3.1.6

$$\mathbf{D}^f \cong \overset{\nabla}{\boldsymbol{\varepsilon}}^f = \frac{3}{2} \dot{\varepsilon}_m \left(\mathbf{m}\mathbf{m} - \frac{1}{3} \boldsymbol{\delta} \right) + \frac{3}{2} \varepsilon_m (\overset{\nabla}{\mathbf{m}}\mathbf{m} + \mathbf{m}\overset{\nabla}{\mathbf{m}}) \quad (3.2.61)$$

Substituting Eq. 3.2.35 through 3.2.45 into the above equation gives

$$\begin{aligned} \mathbf{D}^f &= \frac{3}{2} (\mathbf{m}\mathbf{m}) : \mathbf{D} \left(\mathbf{m}\mathbf{m} - \frac{1}{3} \boldsymbol{\delta} \right) + \frac{3}{2} \varepsilon_m \mathbf{B} : \mathbf{D} \Rightarrow \mathbf{D}^f \\ &= \frac{3}{2} \left[\left(\mathbf{m}\mathbf{m} - \frac{1}{3} \boldsymbol{\delta} \right) \mathbf{m}\mathbf{m} + \varepsilon_m \mathbf{B} \right] : \mathbf{D} \end{aligned} \quad (3.2.62)$$

Therefore,

$$\overset{\nabla}{\boldsymbol{\varepsilon}}^{\text{ct}} = \overset{\nabla}{\boldsymbol{\varepsilon}} - \overset{\nabla}{\boldsymbol{\varepsilon}}^f \Rightarrow \mathbf{D}^{\text{ct}} \cong \mathbf{D} - \mathbf{D}^f \quad (3.2.63)$$

which leads to

$$\mathbf{D}^{\text{ct}} = \left\{ \mathbf{I} - \frac{3}{2} \left[\left(\mathbf{m}\mathbf{m} - \frac{1}{3} \boldsymbol{\delta} \right) \mathbf{m}\mathbf{m} + \varepsilon_m \mathbf{B} \right] \right\} : \mathbf{D} \quad (3.2.64)$$

where \mathbf{I} is the fourth-order symmetric identity tensor

$$I_{ijkl} = \frac{1}{2} (\delta_{ik} \delta_{jl} + \delta_{il} \delta_{jk}) \quad (3.2.65)$$

Hence, $\overset{\nabla}{\boldsymbol{\sigma}}^{\text{ct}}$ and \mathbf{C}^{ct} are derived as

$$\overset{\nabla}{\boldsymbol{\sigma}}^{\text{ct}} = \mathbf{C}^{\text{ct}} : \mathbf{D} \quad (3.2.66)$$

and

$$\mathbf{C}^{\text{ct}} = \frac{1}{J} \mathcal{L}^e : \left\{ \mathbf{I} - \frac{3}{2} \left[\left(\mathbf{m}\mathbf{m} - \frac{1}{3} \boldsymbol{\delta} \right) \mathbf{m}\mathbf{m} + \varepsilon_m \mathbf{B} \right] \right\} - \overset{\nabla}{\boldsymbol{\sigma}}^{\text{ct}} \boldsymbol{\delta} \quad (3.2.67)$$

Consequently, the overall linearization moduli of the muscle are the summation of the fiber and connective tissue linearization moduli:

$$\overset{\nabla}{\boldsymbol{\sigma}} \cong \mathbf{C} : \mathbf{D} \quad \text{with} \quad \mathbf{C} = \mathbf{C}^f + \mathbf{C}^{\text{ct}} \quad (3.2.68)$$

CHAPTER FOUR: NUMERICAL IMPLEMENTATION, VERIFICATION AND VALIDATION OF THE MATERIAL MODEL

In this chapter, the implementation of the constitutive equations and their numerical formulation into the UMAT subroutine is presented. Subsequently, the UMAT is verified by conducting a simple test, and finally, the material model of the muscle is validated against existing experimental data and numerical simulation studies of the extension of a squid fish.

4.1. UMAT Implementation

To implement the material model explained in chapter three, a user defined subroutine, UMAT, is developed. The UMAT is written in FORTRAN language, and is compiled into ABAQUS/Standard solver. The derived Cauchy stress and Jacobian (Elasticity) tensors are calculated at each integrated point at the end of each iteration. Before the UMAT is inserted into the actual cervical spine model, it should be generally verified using simple examples that test the code. To achieve this aim, a single element is created to confirm the accuracy of the stress and Jacobian tensors' update at each increment. Moreover, the developed UMAT needs to be validated by comparing its predictions to the existing experimental data in the relevant literature. The ABAQUS Documentation User Subroutine Reference Manual (ABAQUS Documentation 2013) is used as the main reference for developing the UMAT that is explained in this chapter.

The UMAT is used to define material models that are not available in the ABAQUS material library. In the ABAQUS input file (.inp), under the material section, the “*User Material” command is used to call the UMAT for the set of elements that the UMAT is assigned to them.

The UMAT interface automatically transfers all the functions and parameters used in the code i.e., deformation gradient, stress, and time, at the beginning of each increment. The deformation gradient at the end of the increment (F_{n+1} at $\text{time}(2) = \text{time}(1) + \Delta\text{time}$) is also calculated by the UMAT. The user should calculate the values of other quantities at the end of each increment as listed here:

$$V_{n+1} = \sqrt{F_{n+1} \cdot F_{n+1}^T} = \sum_{i=1}^3 \lambda_i n_i n_i \quad (4.1)$$

$$\varepsilon_{n+1} = \ln V_{n+1} = \sum_{i=1}^3 \ln \lambda_i n_i n_i \quad (4.2)$$

$$\lambda_{m|n+1} = \sqrt{m_0 \cdot F_{n+1}^T \cdot F_{n+1} \cdot m_0} \quad (4.3)$$

$$\varepsilon_{0|n+1}^m = \lambda_{m|n+1} - 1 \text{ and } \varepsilon_{m|n+1} = \ln \lambda_{m|n+1} \quad (4.4)$$

$$m_{n+1} = \frac{1}{|F_{n+1} \cdot m_0|} F_{n+1} \cdot m_0 \quad (4.5)$$

$$\varepsilon_{|n+1}^f = \frac{3}{2} \varepsilon_{m|n+1} (m_{n+1} m_{n+1} - \frac{1}{3} \delta) \quad (4.6)$$

$$\varepsilon_{n+1}^{ct} = \varepsilon_{n+1} - \varepsilon_{n+1}^f \quad (4.7)$$

$$\dot{\varepsilon}_0^m = \frac{\varepsilon_{0|n+1}^m - \varepsilon_{0|n}^m}{\Delta t} \quad (4.8)$$

$$\sigma_{0|n+1}^m = \sigma_{\max} \left(f_a(t_{n+1}) f_l(\varepsilon_{0|n+1}^m) f_v(\dot{\varepsilon}_0^m) \right) + \sigma_{\text{pas}}^m(\varepsilon_{0|n+1}^m) \quad (4.9)$$

$$\sigma_{n+1}^m = (1 + \varepsilon_{0|n+1}^m) \sigma_{0|n+1}^m \quad (4.10)$$

$$\sigma_{n+1}^f = \sigma_{n+1}^m m_{n+1} m_{n+1} \quad (4.11)$$

$$\sigma_{n+1}^{ct} = \frac{1}{\det F_{n+1}} \mathcal{L}^e: \varepsilon_{n+1}^{ct} \quad (4.12)$$

$$\sigma_{n+1} = \sigma_{n+1}^f + \sigma_{n+1}^{ct} \quad (4.13)$$

The functions in Eq. 4.9 are summarized here:

The activation function, f_a , is given by:

$$f_a = \begin{cases} 0 & t \leq t_d \\ \left[0.5 \left(1 - \cos \left(\frac{\pi(t - t_d)}{t_a - t_d} \right) \right) \right]^q & t_d < t < t_a + t_d \\ 1 & t \geq t_a + t_d \end{cases} \quad (4.14)$$

t_d is delay time, t_a is the time between the beginning of the activation and full activation ($f_a=1$), and q is used to modify the activation function profile. Fig. 4.1 shows an activation function profile based on Eq. 4.14 where $t_d=20$ millisecond, $t_a=40$ millisecond, and the constant q is assumed to be 15. After full activation time, f_a remains constant.

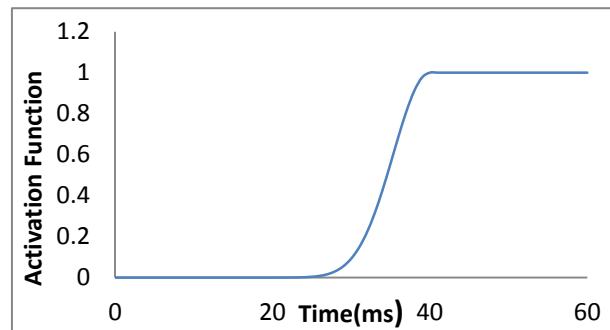


Figure C 4.1 Activation function vs. time for the tentacle muscle.

The length function, f_l is derived from the experimental works on the microstructures of the sarcomeres of tentacle muscle fibers.

$$f_l = \begin{cases} f_5 + (f_4 - f_5)(\varepsilon_0^m - \varepsilon_5)/(\varepsilon_4 - \varepsilon_5) & \varepsilon_5 \leq \varepsilon_0^m < \varepsilon_4 \\ f_4 + (1 - f_4)(\varepsilon_0^m - \varepsilon_4)/(\varepsilon_3 - \varepsilon_4) & \varepsilon_4 \leq \varepsilon_0^m < \varepsilon_3 \\ 1 & \varepsilon_3 \leq \varepsilon_0^m < \varepsilon_2 \\ 1 - (\varepsilon_0^m - \varepsilon_2)/(\varepsilon_1 - \varepsilon_2) & \varepsilon_2 \leq \varepsilon_0^m < \varepsilon_1 \end{cases} \quad (4.15)$$

The characteristics parameters, f_l and ε_i are calculated as follow

$$\varepsilon_1 = \frac{l_{myo} - (1/2)l_{bz}}{l_{0sarc}} \quad (4.16)$$

$$\varepsilon_2 = \frac{(1/2)l_{bz}}{l_{0sarc}} \quad (4.17)$$

$$\varepsilon_3 = -\frac{(1/2)l_{bz}}{l_{0sarc}} \quad (4.18)$$

$$\varepsilon_4 = \frac{l_{myo} - l_{act} - (1/2)l_{bz}}{l_{0sarc}} \quad (4.19)$$

$$\varepsilon_5 = -\frac{l_{min} - (1/2)l_{0sarc}}{l_{0sarc}} \quad (4.20)$$

$$f_4 = 1 - D_{act} \frac{l_{act} - l_{myo}}{l_{myo} - l_{bz}} \quad (4.21)$$

$$f_5 = 1 - D_{act} \frac{l_{act} + l_z - l_{min}}{l_{myo} - l_{bz}} - (D_{myo} + C_{myo}) \frac{l_{act} - l_{myo}}{l_{myo} - l_{bz}} \quad (4.22)$$

where l_{myo} is the length of myosin filament, l_{act} is the sum of the length of two opposing actin filaments in one sarcomere, l_{bz} is the length of the bare zone on the myosin, l_z is the width of

Z-disc, the initial length of the sarcomere, $l_{0sarc} = l_{act} + l_z + (1/2)l_{bz}$, D_{act} and D_{myo} are parameters to account for cross-bridge losses owing to actin overlap and interaction between myosin filament and the Z-disc. Lastly, C_{myo} is introduced to account for resistive forces as a result of the collision of the myosin filaments with the Z-disc of the sarcomere (Liang et. al., 2006). The length function is shown in Fig. 4.2.

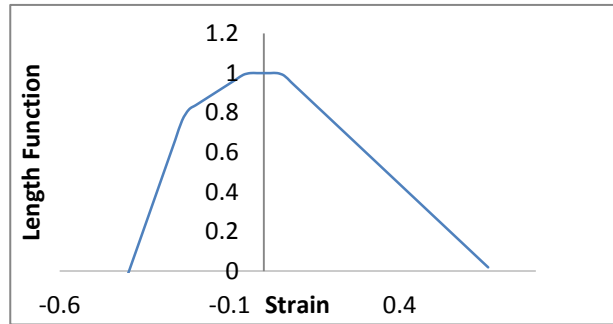


Figure C 4.2 Length function vs. strain for the tentacle muscle.

velocity function, f_v , is given as

$$f_v = \begin{cases} 1.8 - 1.8 \frac{1 + \dot{\epsilon}_m^*}{1 - 7.56\dot{\epsilon}_m^*/k} & \dot{\epsilon}_m^* < 0 \\ \frac{1 - \dot{\epsilon}_m^*}{1 + \dot{\epsilon}_m^*/k} & \dot{\epsilon}_m^* > 0 \end{cases} \quad (4.23)$$

where k is a constant, $\dot{\epsilon}_m^* = \dot{\epsilon}_m^0 / \dot{\epsilon}_{min}$, and $\dot{\epsilon}_{min}$ is a characteristic strain rate associated with the tentacle muscle. Fig. 4.3 describes a schematic velocity function against the strain rate of shortening (left side) or lengthening (right side) of the tentacle muscle.

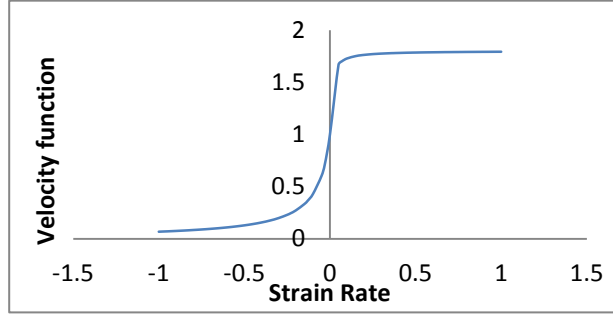


Figure C 4.3 Velocity function vs. strain rate for the tentacle muscle.

Finally, the passive function is formulated as

$$\sigma_{pas}^m = \begin{cases} 0 & \epsilon_0^m \leq 0 \\ c_1(\epsilon_0^m)^{c_2} & 0 < \epsilon_0^m < \epsilon_c \\ c_3\epsilon_0^m + c_4 & \epsilon_0^m \geq \epsilon_c \end{cases} \quad (4.24)$$

Where ϵ_c is called critical strain. c_i are summarized in Table. 4.1.

Fig. 4.4 shows a normalized passive function.

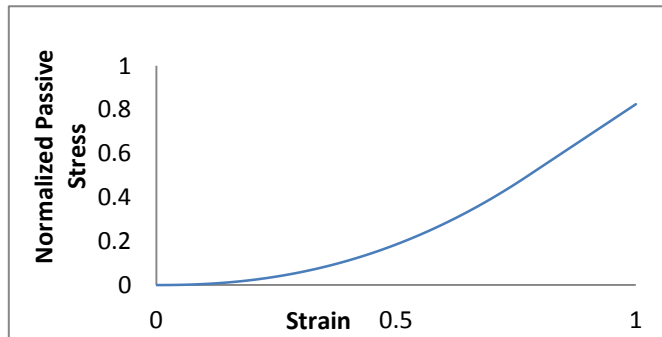


Figure C 4.4 Normalized Passive Stress function vs. strain for the tentacle muscle.

All the parameters, functions, and equations used in this chapter to simulate the tentacle extension are from van Leeuwen and Kier work (1997).

Table C 4.1 Constant muscle parameters used in this study, their units and values.

Parameter	Unit	Value	Parameter	Unit	Value
t_d	ms	0.0	ε_c	-	0.773
t_a	ms	40	ε_5	-	-0.4
ρ	Kg/m ³	1050	D_{act}	-	0.68
l_z	μm	0.06	D_{myo}	-	1.90
l_{bz}	μm	0.14	C_{myo}	-	0.44
c_1	kPa	887	q	-	15
c_3	kPa	1450	k	-	0.25
c_4	kPa	-625	c_2	-	2.26

Table C 4.2 Parameters vary linearly from the base to the end of the stalk.

Parameter	Unit	At stalk base	At stalk end
σ_{max}	kPa	161	70
$\dot{\varepsilon}_{min}$	s ⁻¹	-30	-55
l_{act}	μm	1.21	0.73
l_{myo}	μm	0.97	0.5

4.2. UMAT Verification

To verify the UMAT and observe the material model behavior, two tests are performed:

- 1) A 3D brick element is created to probe the accuracy of the numerical procedure and the developed FORTRAN code.
- 2) A FE model is constructed to simulate the extension of a squid fish tentacle. Experimental studies reported similarity between the tentacle and human musculature behaviour (van Leeuwen and Kier, 1997).

All analyses are performed using the dynamic implicit version of ABAQUS. Nonlinear Geometries Effects (NLGEOM) is considered in all tests. And also, quadratic brick elements are used in the models.

4.2.1. One Element Model Validation Test

In the first step, a mesh with only one element (1mm × 1mm × 1mm dimensions) is generated as shown in Fig. 4.5. The UMAT is assigned to the element. The backward face of the element is fixed, and the running time is 60 milliseconds. Fibers are located along the z-direction. to investigate the effect of the activation, no external load is applied.

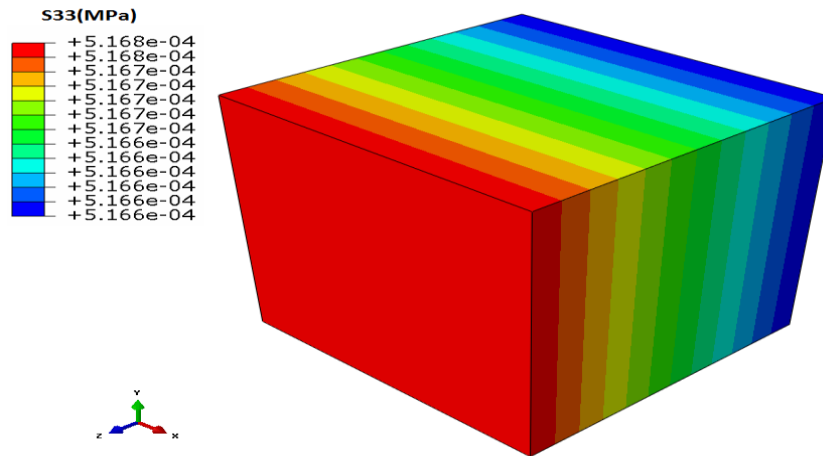


Figure C 4.5 Stress distribution (z-component) in a cube element subjected to activation signal to verify the UMAT behavior.

The stress-strain distribution in the element is shown in Fig. 4.6 agrees well with the well-known force-displacement curve of a skeletal muscle (Guyton and Hall 2011).

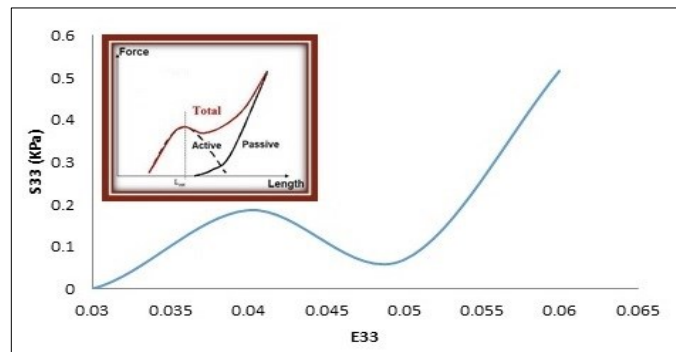


Figure C 4.6 Stress distribution in the muscle as function of strain in the fiber direction (z-axis).

4.2.2. Extension of a Squid Tentacle Validation Test

Due to the lack of experimental data about the human musculature microstructure and ethical concerns about *in-vivo* tests on human subjects, and also, due to the similarity between the extension of squid fish tentacle during the strike to catch a prey and the human muscle fiber's contraction mechanisms, the extension of the tentacle has been studied both experimentally and numerically in the relevant literature (Van Leeuwen and Kier, 1997; Liang *et al.*, 2006; Spyrou and Aravas, 2011). Fig. 4.7 presents a schematic view of a squid fish in general, and its tentacle structure in particular.

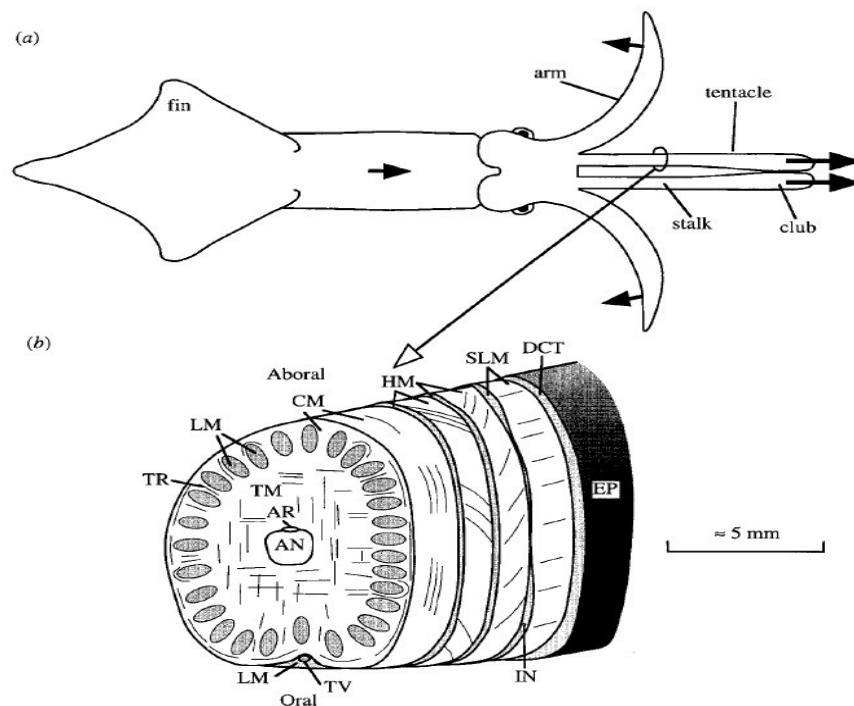


Figure C 4.7 (a) Diagram of a squid. **(b)** Diagram of the morphology of the tentacular stalk in squid with its muscle groups (Van Leeuwen and Kier, 1997).

Fig. 4.8(a) shows the FE configuration of the tentacle. The stalk of the tentacle is modeled as deformable body with the properties described in Section 4.1. The shear modulus and Poisson's

ratio of the connective tissue are 5 kPa and 0.499, respectively. The club is not involved in the elongation of the tentacle. Therefore, it is considered as undeformable passive, homogeneous and elastic material. Due to symmetry, only one quarter of the tentacle is modeled. The tentacle base remains fixed during the extension, while its tip is free to elongate. No other boundary condition is imposed to the model.

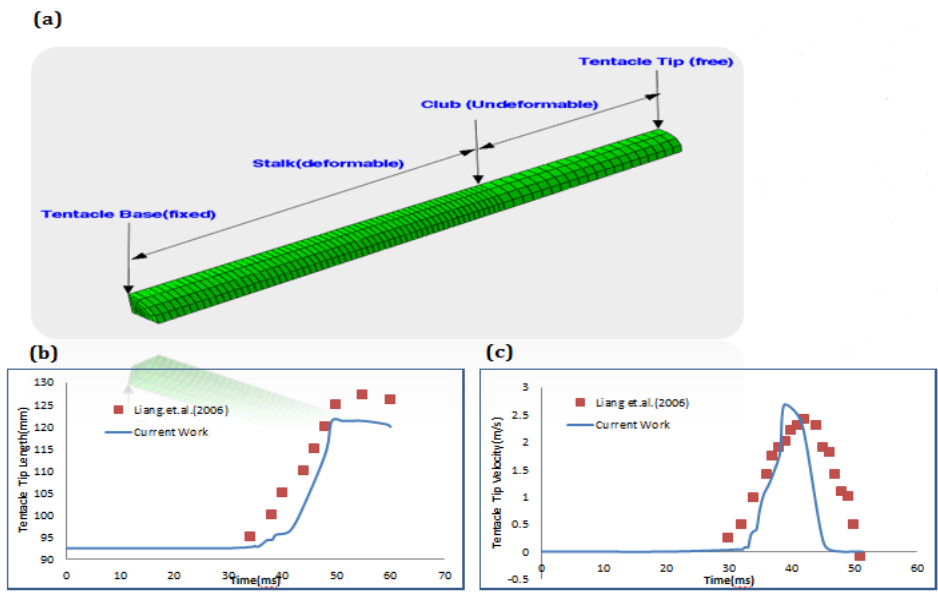


Figure C 4.8 Top figure shows the FE model of a squid fish tentacle. Bottom figures compare the prediction of the current model with the results reported by Liang *et al.*, (2006).

The simulation results show good agreement with the real behavior of the tentacle captured by cameras during the strike phase to catch the prey. Figs. 4.8b-4.8c show a comparison between the results of the simulations done in this study and data reported by Liang *et al.*,(2006). The evolution of the tentacle length during a strike (Fig. 4.8b), and the history of the velocity of the tentacle tip (Fig. 4.8c) have been compared. The results are in a good agreement both qualitatively and quantitatively with the previous studies.

Appendix D

UMAY based on Spyrou and Aravas (2011) Formulation

```
*****
**  UMAT FOR ABAQUS/STANDARD  **
*****
*USER SUBROUTINE
  SUBROUTINE UMAT (STRESS, STATEV, DDSDD, SSE, SPD, SCD,
1  RPL, DDSDDT, DRPLDE, DRPLDT,
2  STRAN, DSTRAN, TIME, DTIME, TEMP, DTEMP, PREDEF, DPRED, CMNAME,
3  NDI, NSHR, NTENS, NSTATV, PROPS, NPROPS, COORDS, DROT, PNEWDT,
4  CELENT, DFGRD0, DFGRD1, NOEL, NPT, LAYER, KSPT, KSTEP, KINC)
C
  INCLUDE 'ABA_PARAM.INC'
C
  CHARACTER*80 CMNAME
C
  IMPLICIT NONE
  DIMENSION STRESS (NTENS), STATEV (NSTATV),
1  DDSDD (NTENS, NTENS), DDSDDT (NTENS), DRPLDE (NTENS),
2  STRAN (NTENS), DSTRAN (NTENS), TIME (2), PREDEF (1), DPRED (1),
3  PROPS (NPROPS), COORDS (3), DROT (3, 3), DFGRD0 (3, 3), DFGRD1 (3, 3)
C
  PARAMETER ZERO=0.D0, ONE=1.D0, TWO=2.D0, THREE=3.D0, NINE=9.D0
  PARAMETER SIX=6.D0, FOUR=4.D0, HALF=ONE/TWO, Pi=3.14D0
C
  INTEGER i, j, NTENS, NSTATV, NPROPS
  REAL*8 STM, STM0, ESM0A, DESMODT, ESM, ESM0, LAMDA, LAMDA1, TEMP1, KK
  REAL*8 STMAX, FLEN, FRAT, FACT, STMPAS, DF, TD, TA, G, GG, KB, NU, E
  REAL*8 q, ES5, ES4, ES3, ES2, ES1, F5, F4, DENSITY, STL, LST, CDES
  REAL*8 L_myo, L_bz, L_0sarc, L_act, L_min, L_z, D_act, D_myo, C_myo
  REAL*8 ESMR_ST, ESMOR, ESR_MIN, KKK, ESC, C1, C2, C3, C4, DSTRESS
  REAL*8 DESMDT, DFLENDESM0, DFRATDESR, ESR, DSTMODT, TD0, CdL
  REAL*8 DSTMDT, DET, TEMPFLEN, TEMPFRAT, DFLENDES, BBAR, DLDLT
  REAL*8 F, FT, V, V1, PROPS, ES, M0, M0FT, FM0, M, MM, DELTA, ESF, ESCT
  REAL*8 DFGRD0, DFGRD1, DTIME, IDEN, TIME, STF, LE, FINV, DDFGRD
  REAL*8 DL, DLT, MMM, B, CF, MMDELL, MMDELMM, IDENMM, XX, XXX, LE_ESCT
  REAL*8 STCT, STD, CCT, C, DLLT, ST, DST, dFPASSdESM0, des, estemp
  REAL*8 STRESS, STATEV, DDSDD, DDSDDT, DRPLDE, STRAN, DSTRAN, DSTDES
  REAL*8 PREDEF, DPRED, COORDS, DROT, D, DSTFDT, DCT, DSTCTDES, DSTFDES
  REAL*8 STMACT, ABESM0
C
  DIMENSION F (3, 3), FT (3, 3), V1 (3, 3), V (3, 3), DSTRESS (6)
  DIMENSION ES (3, 3), m0 (3), m0FT (3), Fm0 (3), des (3, 3)
  DIMENSION m (3), mm (3, 3), DELTA (3, 3), ESF (3, 3), CDES (3, 3)
  DIMENSION ESCT (3, 3), STF (3, 3), TD0 (6, 6), estemp (3, 3)
  DIMENSION LE (6, 6), STCT (3, 3), ST (3, 3), LST (3, 3), dLLT (3, 3), CdL (3, 3)
  DIMENSION D (3, 3), B (6, 6), DSTFDT (6, 1), CF (6, 6), DF (3, 3), DCT (3, 3)
  DIMENSION DSTCTDES (3, 3), DSTFDES (3, 3), DSTDES (3, 3), IDEN (6, 6)
  DIMENSION LE_ESCT (3, 3), FINV (3, 3), DDFGRD (3, 3), dL (3, 3), dLT (3, 3)
  DIMENSION CCT (6, 6), mmmmm (6, 6), mmDEL (3, 3), mmDELmm (6, 6)
  DIMENSION XX (6, 6), XXX (6, 6), STD (6, 6), C (6, 6), STL (3, 3)
  DIMENSION dST (3, 3), IDENMM (6, 6), BBAR (6), DLDLT (3, 3)
C
  *****SPECIFIED MATERIAL PROPERTIES*****
  G=SHEAR MODULUS
  K=BULK MODULUS
  DFGRD0=deformation gradient tensor at the beginning of each increment
  DFGRD1=deformation gradient tensor at the end of each increment
  ES= muscle total strain array
C
```

```

C      m0= initial vector of fiber direction
C      m=fiber direction vector at each increment
C      mm= m*m(attention: it is vector product Not dot product of vectors)
C      ESM0= nominal strain(engineering strain)in m direction
C      DESMODT= time drivative of ESM0 in each increment
C      ESM= muscle true strain in m direction
C      DELTA= 3*3 Identity matrix
C      ESF= fiber strain matrix
C      ESCT= connective tissue strain matrix
C      ESM0A= active ESM0
C      STM0= nominal stress in m direction
C      STM= true stress in m direction
C      STF= true stress array of fiber
C      STCT= true stress tensor of connective tissue
C      ST= STF + STCT
C      *****CONSTANTS USED IN DIFF PARTS OF EQUATIONS*****
C      KK= a constant in used calculation of ESM0A
C      STMAX= max stress in the muscle tissue
C      FLEN= length function which shows how muscle force is related to its strain or
length variation
C      FRAT= strain rate function which shows dependance of muscle force on its strain
rate
C      FACT= activation function which shows dependance of muscle force on the
activation level
C      STMPAS= passive part of muscle stress
C      L_act= length of 2 opposing actin filaments in 1 sarcomere
C      L_min
C      L_z= width of Z-disc
C      D_act= parameter to account for cross-bridge loses owing to actin overlap
C      D_myo= parameter to account for interaction between filament and Z-disc
C      C_myo= parameter to account for resistive forces as a result of collision of
myosin with Z-disc
C      ESMR_ST= muscle strain rate
C      ESMOR= nominal muscle strain rate
C      ESR_MIN= minimum(unloaded)muscle strain rate
C      KKK= constant
C      ESC= critical strain above which the relationship is linear
C      C1,C2,C3,C4= constants
C      TD= Delay time
C      TA= full activation time
C      q= constant
C      L_myo= myosin filament length
C      L_bz= length of bare zone on myosin filament
C      ES5= (L_min - L_0sarc)/ L_0sarc
C      *****
E=PROPS(1)
NU=PROPS(2)
STMAX=PROPS(3)
ESR_MIN=PROPS(4)
L_act=PROPS(5)
L_myo=PROPS(6)
GG=E/(TWO*(ONE+NU))
LAME1=E*NU/((ONE+NU)*(ONE-TWO*NU))
LAME2=GG
L_z=0.06D-3
D_act=0.68D0
D_myo=1.90D0
C_myo=0.44D0
KKK=25D-2
KK=15.0D-2
ESC=0.773D0
C1=887.0D-3
C2=2.26D0

```

```

C3=-55.0d0
C4=-625.0d0
TD=0.0d0
TA=0.04d0
q=15.D0
L_bz=0.14D-3
L_0sarc= L_act + L_z + HALF * L_bz
ES5=-0.4D0
L_min=ES5*L_0sarc+L_0sarc
ES4= (L_myo - L_act - HALF*L_bz) / L_0sarc
ES3= - HALF*L_bz / L_0sarc
ES2= HALF*L_bz / L_0sarc
ES1= (L_myo - HALF*L_bz) / L_0sarc
F5= ONE - D_act*(L_act + L_z - L_min)/(L_myo - L_bz)
1 - (D_myo + C_myo)*(L_act + L_z - L_min)/(L_myo - L_bz)
F4= ONE - D_act*(L_act - L_myo)/(L_myo - L_bz)
C *****STRESS FORMULATION*****
DO i=1,3
  DO j=1,3
    F(i,j)=DFGRD0(i,j)
  END DO
END DO
C *****TRANSPOSE (DFGRD1) *****
DO i=1,3
  DO j=1,3
    FT(i,j)=F(j,i)
  END DO
END DO
C *****STRAIN CALCULATION*****
V1(1,1)=F(1,1)*FT(1,1)+F(1,2)*FT(2,1)+F(1,3)*FT(3,1)
V1(1,2)=F(1,1)*FT(1,2)+F(1,2)*FT(2,2)+F(1,3)*FT(3,2)
V1(1,3)=F(1,1)*FT(1,3)+F(1,2)*FT(2,3)+F(1,3)*FT(3,3)
C
V1(2,1)=F(2,1)*FT(1,1)+F(2,2)*FT(2,1)+F(2,3)*FT(3,1)
V1(2,2)=F(2,1)*FT(1,2)+F(2,2)*FT(2,2)+F(2,3)*FT(3,2)
V1(2,3)=F(2,1)*FT(1,3)+F(2,2)*FT(2,3)+F(2,3)*FT(3,3)
C
V1(3,1)=F(3,1)*FT(1,1)+F(3,2)*FT(2,1)+F(3,3)*FT(3,1)
V1(3,2)=F(3,1)*FT(1,2)+F(3,2)*FT(2,2)+F(3,3)*FT(3,2)
V1(3,3)=F(3,1)*FT(1,3)+F(3,2)*FT(2,3)+F(3,3)*FT(3,3)
c*****calculation eigenvalues and eigen vectors of V1****
! I(1,1)=1.0d0
! I(2,2)=1.0d0
! I(3,3)=1.0d0
! I(1,2)=0.0d0
! I(1,3)=0.0d0
! I(2,1)=0.0d0
! I(2,3)=0.0d0
! I(3,2)=0.0d0
! I(3,1)=0.0d0
! DO i=1,3
! DO j=1,3
!   BB(i,j) = 0.0D0
! END DO
! END DO
c
! p1 = V1(1,2)^2 + V1(1,3)^2 + V1(2,3)^2
! write(7,*) 'p1',p1
! if (p1 == 0.0D0)
c % A is diagonal.
!   eig1 = V1(1,1)
!   eig2 = V1(2,2)
!   eig3 = V1(3,3)

```

```

!       else
!       qq =(V1(1,1)+V1(2,2)+V1(3,3))/3.D0
!       p2 =(V1(1,1)-qq)^2.d0+(V1(2,2)-qq)^2.d0+(V1(3,3)-qq)^2.d0+2.d0*p1
!       p = sqrt(p2 / 6.d0)
!       write(7,*) 'p',p
!       DO i=1,3
!           DO j=1,3
!               BB(i,j) = (1.D0 / p) * (V1(i,j) - qq * I(i,j))      ! I is the identity
matrix
!           END DO
!       END DO
!       write(7,*) 'BB',BB
!       r =(BB(1,1)*(BB(2,2)*BB(3,3)-BB(3,2)*BB(2,3))
!       1  -BB(1,2)*(BB(2,1)*BB(3,3)-BB(2,3)*BB(3,1))
!       2  +BB(1,3)*(BB(2,1)*BB(3,2)-BB(2,2)*BB(3,1)))/ 2.D0
!       write(7,*) 'r',r
c % In exact arithmetic for a symmetric matrix -1 <= r <= 1
c % but computation error can leave it slightly outside this range.
!       if (r <= -1.D0)
!           phi = pi / 3.D0
!       elseif (r >= 1.D0)
!           phi = 0.D0
!       else
!           phi = acos(r) / 3.D0
!       end if
c
c % the eigenvalues satisfy eig3 <= eig2 <= eig1
!       eig1 = qq + 2.D0 * p * cos(phi)
!       eig3 = qq + 2.D0 * p * cos(phi + (2.D0*pi/3.D0))
!       eig2 = 3.D0 * qq - eig1 - eig3      ! since trace(A) = eig1 + eig2 + eig3
!       end if
!       write(7,*) 'eig1',eig1
!       write(7,*) 'eig2',eig2
!       write(7,*) 'eig3',eig3
c*****
!       DO i=1,3
!           DO j=1,3
!               V(i,j)=SQRT(abs(V1(i,j)))
!           END DO
!       END DO
c
!       DO i=1,3
!           DO j=1,3
!               ES(i,j)=ABS(LOG(V(i,j)))
!           END DO
!       END DO
c
!       DO i=1,3
!           DO j=1,3
!               EStemp(i,j)=zero
!           END DO
!       END DO
c
DES(1,1)=ES(1,1)- EStemp(1,1)
DES(2,2)=ES(2,2)- EStemp(2,2)
DES(3,3)=ES(3,3)- EStemp(3,3)
DES(1,2)=ES(1,2)- EStemp(1,2)
DES(1,3)=ES(1,3)- EStemp(1,3)
DES(2,3)=ES(2,3)- EStemp(2,3)
DES(3,2)=ES(3,2)- EStemp(3,2)
DES(3,1)=ES(3,1)- EStemp(3,1)
DES(2,1)=ES(2,1)- EStemp(2,1)
c

```

```

DO i=1,3
  DO j=1,3
    EStemp(i,j)=ES(i,j)
  END DO
END DO
C
m0(1)=ZERO
m0(2)=ZERO
m0(3)=ONE
C
DO i=1,3
  DO j=1,3
    m0FT(i)=m0(j)*FT(j,i)
  END DO
END DO
C
DO i=1,3
  DO j=1,3
    Fm0(i)=F(i,j)*m0(j)
  END DO
END DO
C
LAMDA1= m0FT(1)*Fm0(1)+ m0FT(2)*Fm0(2)+ m0FT(3)*Fm0(3)
C
*****NOMINAL STRAIN(ENGINEERING)*****
TEMP1=ZERO
ESM0=(LAMDA1-ONE)
C
*****TRUE STRAIN*****
ESM=(log(ABS(ESM0)))
C
*****FIBER DIRECTION*****
DO i=1,3
m(i)=1.d0/(SQRT(abs(Fm0(1)**2.d0+Fm0(2)**2.d0+Fm0(3)**2.d0)))
1*Fm0(i)
END DO
C
*****mm calculation*****
mm(1,1)= m(1)*m(1)
mm(1,2)= m(1)*m(2)
mm(1,3)= m(1)*m(3)
mm(2,1)= m(2)*m(1)
mm(2,2)= m(2)*m(2)
mm(2,3)= m(2)*m(3)
mm(3,1)= m(3)*m(1)
mm(3,2)= m(3)*m(2)
mm(3,3)= m(3)*m(3)
C
*****DELTA CALCULATION*****
DO i=1,3
  DO j=1,3
    DELTA(i,j)=ZERO
  END DO
  DELTA(i,i)=ONE
END DO
C
*****IDEN CALCULATION*****
DO i=1,6
  DO j=1,6
    IDEN(i,j)=ZERO
  END DO
  IDEN(i,i)=ONE
END DO
C
*****FIBER STRAIN CALCULATION*****
DO i=1,3
  DO j=1,3
    ESF(i,j)=ESM*(mm(i,j)-((ONE/THREE)*DELTA(i,j)))
  END DO
END DO

```

```

C *****CONNECTIVE TISSUE STRAIN*****
  ESCT(1,1)=ES(1,1) - ESF(1,1)
  ESCT(2,2)=ES(2,2) - ESF(2,2)
  ESCT(3,3)=ES(3,3) - ESF(3,3)
  ESCT(1,2)=ES(1,2) - ESF(1,2)
  ESCT(2,1)=ES(2,1) - ESF(2,1)
  ESCT(3,2)=ES(3,2) - ESF(3,2)
  ESCT(2,3)=ES(2,3) - ESF(2,3)
  ESCT(1,3)=ES(1,3) - ESF(1,3)
  ESCT(3,1)=ES(3,1) - ESF(3,1)
C *****NOMINAL STRAIN TIME DERIVATIVE*****
DESM0DT=ESM0/DTIME
TEMP1=ESM0
C *****ACTIVE FUNCTION CALCULATION*****
  IF (TIME(2).LT.TD) THEN
    FACT=ZERO
  ELSE IF (TIME(2).GE.TD.AND.TIME(2).LT.TA) THEN
    FACT=1.0d0*(HALF*(ONE-COS(Pi*(TIME(2)-TD)/(TA-TD))))**q
  ELSE IF (time(2).gt.TA.AND.time(2).lt.0.06d0) then
    FACT=ONE
  END IF
C *****ACTIVE ESM0*****
ESM0A=(ESM0+ONE)*(KK*(ONE-FACT)+ONE)-ONE
C *****FLEN*****
IF (ESM0A.LT.ES5) THEN
  FLEN=ZERO
ELSE IF (ESM0A.GE.ES5.AND.ESM0A.LT.ES4) THEN
  FLEN=ABS(F5+(F4-F5)*(ESM0A-ES5)/(ES4-ES5))
ELSE IF (ESM0A.GE.ES4.AND.ESM0A.LT.ES3) THEN
  FLEN=ABS(F4+(ONE-F4)*(ESM0A-ES4)/(ES3-ES4))
ELSE IF (ESM0A.GE.ES3.AND.ESM0A.LT.ES2) THEN
  FLEN=ONE
ELSE IF (ESM0A.GE.ES2.AND.ESM0A.LT.ES1) THEN
  FLEN=ABS(ONE-(ESM0A-ES2)/(ES1-ES2))
ELSE
  FLEN=ZERO
END IF
C *****FRAT*****
ESMR_ST=DESM0DT/ESR_MIN
IF (ESMR_ST.LT.ZERO) THEN
  FRAT=(1.8d0-0.8d0*(ONE+ESMR_ST)/(ONE-7.56d0*ESMR_ST/KKK))
ELSE
  FRAT=((ONE-ESMR_ST)/(ONE+ESMR_ST/KKK))
END IF
STMACT=(FACT*FLEN*FRAT)
C ***** PASSIVE STRESS CALCULATION*****
ABESM0=ABS(ESM0)
IF (ESM0A.LE.ZERO) THEN
  STMPAS=ZERO
else IF (ESM0A.GT.0.0D0.AND.ESM0A.LT.ESC) THEN
  STMPAS=abs(C1*(ESM0A)**C2)
  ELSE IF (ESM0A.GE.ESC) then
    STMPAS=abs(C3*ESM0A+C4)
  END IF
C ***** NOMINAL STRESS IN MUSCLE*****
STM0=STMAX*(FACT*FLEN*FRAT)+STMPAS
C *****TRUE STRESS IN MUSCLE SCALAR*****
STM=(ONE+ESM0)*STM0
C *****FIBER STRESS TENSOR*****
DO i=1,3
  DO j=1,3
    STF(i,j)=STM*(mm(i,j))
  END DO

```

```

END DO
C *****CONNECTIVE TISSUE 4TH-ORDER ELASTICITY TENSOR*****
LE (1, 1)=KB+FOUR/THREE*GG
LE (1, 2)=KB-TWO/THREE*GG
LE (1, 3)=KB-TWO/THREE*GG
LE (1, 4)=ZERO
LE (1, 5)=ZERO
LE (1, 6)=ZERO
C
LE (2, 1)=KB-TWO/THREE*GG
LE (2, 2)=KB+FOUR/THREE*GG
LE (2, 3)=KB-TWO/THREE*GG
LE (2, 4)=ZERO
LE (2, 5)=ZERO
LE (2, 6)=ZERO
C
LE (3, 1)=KB-TWO/THREE*GG
LE (3, 2)=KB-TWO/THREE*GG
LE (3, 3)=KB+FOUR/THREE*GG
LE (3, 4)=ZERO
LE (3, 5)=ZERO
LE (3, 6)=ZERO
C
LE (4, 1)=ZERO
LE (4, 2)=ZERO
LE (4, 3)=ZERO
LE (4, 4)=GG
LE (4, 5)=ZERO
LE (4, 6)=ZERO
C
LE (5, 1)=ZERO
LE (5, 2)=ZERO
LE (5, 3)=ZERO
LE (5, 4)=ZERO
LE (5, 5)=GG
LE (5, 6)=ZERO
C
LE (6, 1)=ZERO
LE (6, 2)=ZERO
LE (6, 3)=ZERO
LE (6, 4)=ZERO
LE (6, 5)=ZERO
LE (6, 6)=GG
C *****CALCULATING DFGRD1 GRADIENT*****
DET=DFGRD0 (1, 1) * (DFGRD1 (2, 2) *DFGRD1 (3, 3) -DFGRD1 (3, 2) *DFGRD1 (2, 3))
1 -DFGRD0 (1, 2) * (DFGRD1 (2, 1) *DFGRD1 (3, 3) -DFGRD1 (2, 3) *DFGRD1 (3, 1))
2 +DFGRD0 (1, 3) * (DFGRD1 (2, 1) *DFGRD1 (3, 2) -DFGRD1 (2, 2) *DFGRD1 (3, 1))
C *****DFGRD1 INVERSE CALCULATION -FINV-*****
DO i=1, 3
DO j=1, 3
FINV(i, j) = (ONE/DET) *FT (i, j)
END DO
END DO
C *****DFGRD0 INCREMENT-DDFGRD*****
DO i=1, 3
DO j=1, 3
DDFGRD (i, j) =DFGRD1 (i, j) -TD0 (i, j)
END DO
END DO
C
DO i=1, 3
DO j=1, 3
TD0 (i, j) =DFGRD1 (i, j)

```

```

      END DO
      END DO
C *****dL=DDFGRD.FINV*****
dL(1,1)=(ONE/DET)*(DDFGRD(1,1)*DFGRD0(1,1)+DDFGRD(1,2)*DFGRD0(2,1)
1 +DDFGRD(1,3)*DFGRD0(3,1))
dL(1,2)=(ONE/DET)*(DDFGRD(1,1)*DFGRD0(2,1)+DDFGRD(1,2)*DFGRD0(2,2)
1 +DDFGRD(1,3)*DFGRD0(3,2))
dL(1,3)=(ONE/DET)*(DDFGRD(1,1)*DFGRD0(3,1)+DDFGRD(1,2)*DFGRD0(2,3)
1 +DDFGRD(1,3)*DFGRD0(3,3))
C
dL(2,1)=(ONE/DET)*(DDFGRD(2,1)*DFGRD0(1,1)+DDFGRD(2,2)*DFGRD0(2,1)
1 +DDFGRD(2,3)*DFGRD0(3,1))
dL(2,2)=(ONE/DET)*(DDFGRD(2,1)*DFGRD0(2,1)+DDFGRD(2,2)*DFGRD0(2,2)
1 +DDFGRD(2,3)*DFGRD0(3,2))
dL(2,3)=(ONE/DET)*(DDFGRD(2,1)*DFGRD0(3,1)+DDFGRD(2,2)*DFGRD0(2,3)
1 +DDFGRD(2,3)*DFGRD0(3,3))
C
dL(3,1)=(ONE/DET)*(DDFGRD(3,1)*DFGRD0(1,1)+DDFGRD(3,2)*DFGRD0(2,1)
1 +DDFGRD(3,3)*DFGRD0(3,1))
dL(3,2)=(ONE/DET)*(DDFGRD(3,1)*DFGRD0(2,1)+DDFGRD(3,2)*DFGRD0(2,2)
1 +DDFGRD(3,3)*DFGRD0(3,2))
dL(3,3)=(ONE/DET)*(DDFGRD(3,1)*DFGRD0(3,1)+DDFGRD(3,2)*DFGRD0(2,3)
1 +DDFGRD(3,3)*DFGRD0(3,3))
C *****dL TRANSPOSE(dLT)*****
DO i=1,3
  DO j=1,3
    dLT(i,j)= dL(j,i)
  END DO
END DO
C *****dL-dLT =DLDLT CALCULATION*****
DO i=1,3
  DO j=1,3
    DLDLT(i,j)= dL(i,j)-dLT(i,j)
  END DO
END DO
C *****mnmnm CALCULATION*****
mnmnm(1,1)=m(1)*m(1)*m(1)*m(1)
mnmnm(1,2)=m(1)*m(1)*m(2)*m(2)
mnmnm(1,3)=m(1)*m(1)*m(3)*m(3)
mnmnm(1,4)=m(1)*m(1)*m(1)*m(2)
mnmnm(1,5)=m(1)*m(1)*m(2)*m(3)
mnmnm(1,6)=m(1)*m(1)*m(3)*m(1)
C
mnmnm(2,1)=m(2)*m(2)*m(1)*m(1)
mnmnm(2,2)=m(2)*m(2)*m(2)*m(2)
mnmnm(2,3)=m(2)*m(2)*m(3)*m(3)
mnmnm(2,4)=m(2)*m(2)*m(1)*m(2)
mnmnm(2,5)=m(2)*m(2)*m(2)*m(3)
mnmnm(2,6)=m(2)*m(2)*m(3)*m(1)
C
mnmnm(3,1)=m(3)*m(3)*m(1)*m(1)
mnmnm(3,2)=m(3)*m(3)*m(2)*m(2)
mnmnm(3,3)=m(3)*m(3)*m(3)*m(3)
mnmnm(3,4)=m(3)*m(3)*m(1)*m(2)
mnmnm(3,5)=m(3)*m(3)*m(2)*m(3)
mnmnm(3,6)=m(3)*m(3)*m(3)*m(1)
C
mnmnm(4,1)=m(1)*m(2)*m(1)*m(1)
mnmnm(4,2)=m(1)*m(2)*m(2)*m(2)
mnmnm(4,3)=m(1)*m(2)*m(3)*m(3)
mnmnm(4,4)=m(1)*m(2)*m(1)*m(2)
mnmnm(4,5)=m(1)*m(2)*m(2)*m(3)
mnmnm(4,6)=m(1)*m(2)*m(3)*m(1)

```

```

mmmm (5, 1) =m (2) *m (3) *m (1) *m (1)
mmmm (5, 2) =m (2) *m (3) *m (2) *m (2)
mmmm (5, 3) =m (2) *m (3) *m (3) *m (3)
mmmm (5, 4) =m (2) *m (3) *m (1) *m (2)
mmmm (5, 5) =m (2) *m (3) *m (2) *m (3)
mmmm (5, 6) =m (2) *m (3) *m (3) *m (1)
C
mmmm (6, 1) =m (3) *m (1) *m (1) *m (1)
mmmm (6, 2) =m (3) *m (1) *m (2) *m (2)
mmmm (6, 3) =m (3) *m (1) *m (3) *m (3)
mmmm (6, 4) =m (3) *m (1) *m (1) *m (2)
mmmm (6, 5) =m (3) *m (1) *m (2) *m (3)
mmmm (6, 6) =m (3) *m (1) *m (3) *m (1)
C
***** B calculation*****
B (1, 1) =HALF* ((DELTA (1, 1) *m (1) +DELTA (1, 1) *m (1) ) *m (1) + (DELTA (1, 1)
1 *m (1) +DELTA (1, 1) *m (1) ) *m (1) ) -TWO*m (1) *m (1) *m (1) *m (1)
C
B (1, 2) =HALF* ((DELTA (1, 2) *m (1) +DELTA (1, 2) *m (1) ) *m (2) + (DELTA (1, 2)
1 *m (1) +DELTA (1, 2) *m (1) ) *m (2) ) -TWO*m (1) *m (1) *m (2) *m (2)
C
B (1, 3) =HALF* ((DELTA (1, 3) *m (1) +DELTA (1, 3) *m (1) ) *m (3) + (DELTA (1, 3)
1 *m (1) +DELTA (1, 3) *m (1) ) *m (3) ) -TWO*m (1) *m (1) *m (3) *m (3)
C
B (1, 4) =HALF* ((DELTA (1, 1) *m (1) +DELTA (1, 1) *m (1) ) *m (2) + (DELTA (1, 2)
1 *m (1) +DELTA (1, 2) *m (1) ) *m (1) ) -TWO*m (1) *m (1) *m (1) *m (2)
C
B (1, 5) =HALF* ((DELTA (1, 2) *m (1) +DELTA (1, 2) *m (1) ) *m (3) + (DELTA (1, 3)
1 *m (1) +DELTA (1, 3) *m (1) ) *m (2) ) -TWO*m (1) *m (1) *m (2) *m (3)
C
B (1, 6) =HALF* ((DELTA (1, 3) *m (1) +DELTA (1, 3) *m (1) ) *m (1) + (DELTA (1, 1)
1 *m (1) +DELTA (1, 1) *m (1) ) *m (3) ) -TWO*m (1) *m (1) *m (3) *m (1)
C
B (2, 1) =HALF* ((DELTA (2, 1) *m (2) +DELTA (2, 1) *m (2) ) *m (1) + (DELTA (2, 1)
1 *m (2) +DELTA (2, 1) *m (2) ) *m (1) ) -TWO*m (2) *m (2) *m (1) *m (1)
C
B (2, 2) =HALF* ((DELTA (2, 2) *m (2) +DELTA (2, 2) *m (2) ) *m (2) + (DELTA (2, 2)
1 *m (2) +DELTA (2, 2) *m (2) ) *m (2) ) -TWO*m (2) *m (2) *m (2) *m (2)
C
B (2, 3) =HALF* ((DELTA (2, 3) *m (2) +DELTA (2, 3) *m (2) ) *m (3) + (DELTA (2, 3)
1 *m (2) +DELTA (2, 3) *m (2) ) *m (3) ) -TWO*m (2) *m (2) *m (3) *m (3)
C
B (2, 4) =HALF* ((DELTA (2, 1) *m (2) +DELTA (2, 1) *m (2) ) *m (2) + (DELTA (2, 2)
1 *m (2) +DELTA (2, 2) *m (2) ) *m (1) ) -TWO*m (2) *m (2) *m (1) *m (2)
C
B (2, 5) =HALF* ((DELTA (2, 2) *m (2) +DELTA (2, 2) *m (2) ) *m (3) + (DELTA (2, 3)
1 *m (2) +DELTA (2, 3) *m (2) ) *m (2) ) -TWO*m (2) *m (2) *m (2) *m (3)
C
B (2, 6) =HALF* ((DELTA (2, 3) *m (2) +DELTA (2, 3) *m (2) ) *m (1) + (DELTA (2, 1)
1 *m (2) +DELTA (2, 1) *m (2) ) *m (3) ) -TWO*m (2) *m (2) *m (3) *m (1)
C
B (3, 1) =HALF* ((DELTA (3, 1) *m (3) +DELTA (3, 1) *m (3) ) *m (1) + (DELTA (3, 1)
1 *m (3) +DELTA (3, 1) *m (3) ) *m (1) ) -TWO*m (3) *m (3) *m (1) *m (1)
C
B (3, 2) =HALF* ((DELTA (3, 2) *m (3) +DELTA (3, 2) *m (3) ) *m (2) + (DELTA (3, 2)
1 *m (3) +DELTA (3, 2) *m (3) ) *m (2) ) -TWO*m (3) *m (3) *m (2) *m (2)
C
B (3, 3) =HALF* ((DELTA (3, 3) *m (3) +DELTA (3, 3) *m (3) ) *m (3) + (DELTA (3, 3)
1 *m (3) +DELTA (3, 3) *m (3) ) *m (3) ) -TWO*m (3) *m (3) *m (3) *m (3)
C
B (3, 4) =HALF* ((DELTA (3, 1) *m (3) +DELTA (3, 1) *m (3) ) *m (2) + (DELTA (3, 2)
1 *m (3) +DELTA (3, 2) *m (3) ) *m (1) ) -TWO*m (3) *m (3) *m (1) *m (2)
C
B (3, 5) =HALF* ((DELTA (3, 2) *m (3) +DELTA (3, 2) *m (3) ) *m (3) + (DELTA (3, 3)

```

```

1 *m (3)+DELTA (3,3) *m (3) ) *m (2) ) -TWO*m (3) *m (3) *m (2) *m (3)
C
B (3,6)=HALF* ( (DELTA (3,3) *m (3) +DELTA (3,3) *m (3) ) *m (1) + (DELTA (3,1)
1 *m (3) +DELTA (3,1) *m (3) ) *m (3) ) -TWO*m (3) *m (3) *m (3) *m (1)
C
B (4,1)=HALF* ( (DELTA (1,1) *m (2) +DELTA (2,1) *m (1) ) *m (1) + (DELTA (1,1)
1 *m (2) +DELTA (2,1) *m (1) ) *m (1) ) -TWO*m (1) *m (2) *m (1) *m (1)
C
B (4,2)=HALF* ( (DELTA (1,2) *m (2) +DELTA (2,2) *m (1) ) *m (2) + (DELTA (1,2)
1 *m (2) +DELTA (2,2) *m (1) ) *m (2) ) -TWO*m (1) *m (2) *m (2) *m (2)
C
B (4,3)=HALF* ( (DELTA (1,3) *m (2) +DELTA (2,3) *m (1) ) *m (3) + (DELTA (1,3)
1 *m (2) +DELTA (2,3) *m (1) ) *m (3) ) -TWO*m (1) *m (2) *m (3) *m (3)
C
B (4,4)=HALF* ( (DELTA (1,1) *m (2) +DELTA (2,1) *m (1) ) *m (2) + (DELTA (1,2)
1 *m (2) +DELTA (2,2) *m (1) ) *m (1) ) -TWO*m (1) *m (2) *m (1) *m (2)
C
B (4,5)=HALF* ( (DELTA (1,2) *m (2) +DELTA (2,2) *m (1) ) *m (3) + (DELTA (1,3)
1 *m (2) +DELTA (2,3) *m (1) ) *m (2) ) -TWO*m (1) *m (2) *m (2) *m (3)
C
B (4,6)=HALF* ( (DELTA (1,3) *m (2) +DELTA (2,3) *m (1) ) *m (1) + (DELTA (1,1)
1 *m (2) +DELTA (2,1) *m (1) ) *m (3) ) -TWO*m (1) *m (2) *m (3) *m (1)
C
B (5,1)=HALF* ( (DELTA (2,1) *m (3) +DELTA (3,1) *m (2) ) *m (1) + (DELTA (2,1)
1 *m (3) +DELTA (3,1) *m (2) ) *m (1) ) -TWO*m (2) *m (3) *m (1) *m (1)
C
B (5,2)=HALF* ( (DELTA (2,2) *m (3) +DELTA (3,2) *m (2) ) *m (2) + (DELTA (2,2)
1 *m (3) +DELTA (3,2) *m (2) ) *m (2) ) -TWO*m (2) *m (3) *m (2) *m (2)
C
B (5,3)=HALF* ( (DELTA (2,3) *m (3) +DELTA (3,3) *m (2) ) *m (3) + (DELTA (2,3)
1 *m (3) +DELTA (3,3) *m (2) ) *m (3) ) -TWO*m (2) *m (3) *m (3) *m (3)
C
B (5,4)=HALF* ( (DELTA (2,1) *m (3) +DELTA (3,1) *m (2) ) *m (2) + (DELTA (2,2)
1 *m (3) +DELTA (3,2) *m (2) ) *m (1) ) -TWO*m (2) *m (3) *m (1) *m (2)
C
B (5,5)=HALF* ( (DELTA (2,2) *m (3) +DELTA (3,2) *m (2) ) *m (3) + (DELTA (2,3)
1 *m (3) +DELTA (3,3) *m (2) ) *m (2) ) -TWO*m (2) *m (3) *m (2) *m (3)
C
B (5,6)=HALF* ( (DELTA (2,3) *m (3) +DELTA (3,3) *m (2) ) *m (1) + (DELTA (2,1)
1 *m (3) +DELTA (3,1) *m (2) ) *m (3) ) -TWO*m (2) *m (3) *m (3) *m (1)
C
B (6,1)=HALF* ( (DELTA (3,1) *m (1) +DELTA (1,1) *m (3) ) *m (1) + (DELTA (3,1)
1 *m (1) +DELTA (1,1) *m (3) ) *m (1) ) -TWO*m (3) *m (1) *m (1) *m (1)
C
B (6,2)=HALF* ( (DELTA (3,2) *m (1) +DELTA (1,2) *m (3) ) *m (2) + (DELTA (3,2)
1 *m (1) +DELTA (1,2) *m (3) ) *m (2) ) -TWO*m (3) *m (1) *m (2) *m (2)
C
B (6,3)=HALF* ( (DELTA (3,3) *m (1) +DELTA (1,3) *m (3) ) *m (3) + (DELTA (3,3)
1 *m (1) +DELTA (1,3) *m (3) ) *m (3) ) -TWO*m (3) *m (1) *m (3) *m (3)
C
B (6,4)=HALF* ( (DELTA (3,1) *m (1) +DELTA (1,1) *m (3) ) *m (2) + (DELTA (3,2)
1 *m (1) +DELTA (1,2) *m (3) ) *m (1) ) -TWO*m (3) *m (1) *m (1) *m (2)
C
B (6,5)=HALF* ( (DELTA (3,2) *m (1) +DELTA (1,2) *m (3) ) *m (3) + (DELTA (3,3)
1 *m (1) +DELTA (1,3) *m (3) ) *m (2) ) -TWO*m (3) *m (1) *m (2) *m (3)
C
B (6,6)=HALF* ( (DELTA (3,3) *m (1) +DELTA (1,3) *m (3) ) *m (1) + (DELTA (3,1)
1 *m (1) +DELTA (1,1) *m (3) ) *m (3) ) -TWO*m (3) *m (1) *m (3) *m (1)
C
write (7,*) 'B',B
C
*****dFLEN/dESM0 CALCULATION*****
IF (ESM0A.GE.ES5.AND.ESM0A.LT.ES4) THEN
    DFLENDES=(F4-F5) / (ES4-ES5)
ELSE IF (ESM0A.GE.ES4.AND.ESM0A.LT.ES3) THEN

```

```

DFLENDES= (ONE-F4) / (ES3-ES4)
ELSE IF (ESM0A.GE.ES3.AND.ESM0A.LT.ES2) THEN
DFLENDES=ZERO
ELSE
DFLENDES=-ONE/ (ES1-ES2)
END IF
C *****dFRAT/dESR*****
IF (ESMR_ST.LT.ZERO) THEN
DFRATDES= -0.8D0 * ((ONE/ESR_MIN * (ONE-7.56D0 * ESMR_ST / KKK) -
1 (-7.56D0 / (KKK * ESR_MIN)) * (ONE + ESMR_ST)) /
2 (ONE - 7.56D0 * ESMR_ST / KKK) ** TWO)
ELSE
DFRATDES = (- (ONE + ESMR_ST / KKK) / ESR_MIN -
1 ((ONE - ESMR_ST) / (KKK * ESR_MIN))) / (ONE + ESMR_ST / KKK) ** TWO
END IF
C *****dFPASS/dESM0*****
IF (ESM0A.LE.ZERO) THEN
dFPASSdESM0=ZERO
ELSE IF (ESM0A.GT.ZERO.AND.ESM0A.LT.ESC) THEN
dFPASSdESM0=C1*C2*(ESM0A)**(C2-1.D0)
ELSE IF (ESM0A.GE.ESC) THEN
dFPASSdESM0=C3
END IF
C *****G CALCULATION*****
G=(ONE+ESM0)*(STM0*(fact*frat*dflenDES))
1 + dFPASSdESM0)
C *****CF CALCULATION*****
DO i=1,6
DO j=1,6
CF(i,j)=(ONE+ESM0)*(STM0+G)*mmmm(i,j)+STM*B(i,j)
END DO
END DO
C *****CCT CALCULATION*****
C *****mmDEL CALCULATION*****
DO i=1,3
DO j=1,3
mmDEL(i,j)=mm(i,j)-ONE/THREE*DELTA(i,j)
END DO
END DO
C *****mmDELmm CALCULATION*****
mmDELmm(1,1)=mmDEL(1,1)*mm(1,1)
mmDELmm(1,2)=mmDEL(1,1)*mm(2,2)
mmDELmm(1,3)=mmDEL(1,1)*mm(3,3)
mmDELmm(1,4)=mmDEL(1,1)*mm(1,2)
mmDELmm(1,5)=mmDEL(1,1)*mm(2,3)
mmDELmm(1,6)=mmDEL(1,1)*mm(3,1)
C
mmDELmm(2,1)=mmDEL(2,2)*mm(1,1)
mmDELmm(2,2)=mmDEL(2,2)*mm(2,2)
mmDELmm(2,3)=mmDEL(2,2)*mm(3,3)
mmDELmm(2,4)=mmDEL(2,2)*mm(1,2)
mmDELmm(2,5)=mmDEL(2,2)*mm(2,3)
mmDELmm(2,6)=mmDEL(2,2)*mm(3,1)
C
mmDELmm(3,1)=mmDEL(3,3)*mm(1,1)
mmDELmm(3,2)=mmDEL(3,3)*mm(2,2)
mmDELmm(3,3)=mmDEL(3,3)*mm(3,3)
mmDELmm(3,4)=mmDEL(3,3)*mm(1,2)
mmDELmm(3,5)=mmDEL(3,3)*mm(2,3)
mmDELmm(3,6)=mmDEL(3,3)*mm(3,1)
C
mmDELmm(4,1)=mmDEL(1,2)*mm(1,1)
mmDELmm(4,2)=mmDEL(1,2)*mm(2,2)

```

```

mmDELmm (4, 3) = mmDEL (1, 2) * mm (3, 3)
mmDELmm (4, 4) = mmDEL (1, 2) * mm (1, 2)
mmDELmm (4, 5) = mmDEL (1, 2) * mm (2, 3)
mmDELmm (4, 6) = mmDEL (1, 2) * mm (3, 1)
C
mmDELmm (5, 1) = mmDEL (2, 3) * mm (1, 1)
mmDELmm (5, 2) = mmDEL (2, 3) * mm (2, 2)
mmDELmm (5, 3) = mmDEL (2, 3) * mm (3, 3)
mmDELmm (5, 4) = mmDEL (2, 3) * mm (1, 2)
mmDELmm (5, 5) = mmDEL (2, 3) * mm (2, 3)
mmDELmm (5, 6) = mmDEL (2, 3) * mm (3, 1)
C
mmDELmm (6, 1) = mmDEL (3, 1) * mm (1, 1)
mmDELmm (6, 2) = mmDEL (3, 1) * mm (2, 2)
mmDELmm (6, 3) = mmDEL (3, 1) * mm (3, 3)
mmDELmm (6, 4) = mmDEL (3, 1) * mm (1, 2)
mmDELmm (6, 5) = mmDEL (3, 1) * mm (2, 3)
mmDELmm (6, 6) = mmDEL (3, 1) * mm (3, 1)
C
*****
DO i=1, 6
  DO j=1, 6
    IDENMM (i, j) = IDEN (i, j) - (3.0d0/2.0d0) * (mmDELmm (i, j) + ESM0*B (i, j))
  END DO
END DO
C
*****
XX (1, 1) = LE (1, 1) * IDENMM (1, 1) + LE (1, 2) * IDENMM (2, 1) + LE (1, 3)
1 * IDENMM (3, 1) + LE (1, 4) * IDENMM (4, 1) + LE (1, 5) * IDENMM (5, 1) + LE (1, 6)
2 * IDENMM (6, 1)
C
XX (1, 2) = LE (1, 1) * IDENMM (1, 2) + LE (1, 2) * IDENMM (2, 2) + LE (1, 3)
1 * IDENMM (3, 2) + LE (1, 4) * IDENMM (4, 2) + LE (1, 5) * IDENMM (5, 2) + LE (1, 6)
2 * IDENMM (6, 2)
C
XX (1, 3) = LE (1, 1) * IDENMM (1, 3) + LE (1, 2) * IDENMM (2, 3) + LE (1, 3)
1 * IDENMM (3, 3) + LE (1, 4) * IDENMM (4, 3) + LE (1, 5) * IDENMM (5, 3) + LE (1, 6)
2 * IDENMM (6, 3)
C
XX (1, 4) = LE (1, 1) * IDENMM (1, 4) + LE (1, 2) * IDENMM (2, 4) + LE (1, 3)
1 * IDENMM (3, 4) + LE (1, 4) * IDENMM (4, 4) + LE (1, 5) * IDENMM (5, 4) + LE (1, 6)
2 * IDENMM (6, 4)
C
XX (1, 5) = LE (1, 1) * IDENMM (1, 5) + LE (1, 2) * IDENMM (2, 5) + LE (1, 3)
1 * IDENMM (3, 5) + LE (1, 4) * IDENMM (4, 5) + LE (1, 5) * IDENMM (5, 5) + LE (1, 6)
2 * IDENMM (6, 5)
C
XX (1, 6) = LE (1, 1) * IDENMM (1, 6) + LE (1, 2) * IDENMM (2, 6) + LE (1, 3)
1 * IDENMM (3, 6) + LE (1, 4) * IDENMM (4, 6) + LE (1, 5) * IDENMM (5, 6) + LE (1, 6)
2 * IDENMM (6, 6)
C
*****
XX (2, 1) = LE (2, 1) * IDENMM (1, 1) + LE (2, 2) * IDENMM (2, 1) + LE (2, 3)
1 * IDENMM (3, 1) + LE (2, 4) * IDENMM (4, 1) + LE (2, 5) * IDENMM (5, 1) + LE (2, 6)
2 * IDENMM (6, 1)
C
XX (2, 2) = LE (2, 1) * IDENMM (1, 2) + LE (2, 2) * IDENMM (2, 2) + LE (2, 3)
1 * IDENMM (3, 2) + LE (2, 4) * IDENMM (4, 2) + LE (2, 5) * IDENMM (5, 2) + LE (2, 6)
2 * IDENMM (6, 2)
C
XX (2, 3) = LE (2, 1) * IDENMM (1, 3) + LE (2, 2) * IDENMM (2, 3) + LE (2, 3)
1 * IDENMM (3, 3) + LE (2, 4) * IDENMM (4, 3) + LE (2, 5) * IDENMM (5, 3) + LE (2, 6)
2 * IDENMM (6, 3)
C
XX (2, 4) = LE (2, 1) * IDENMM (1, 4) + LE (2, 2) * IDENMM (2, 4) + LE (2, 3)
1 * IDENMM (3, 4) + LE (2, 4) * IDENMM (4, 4) + LE (2, 5) * IDENMM (5, 4) + LE (2, 6)

```

$2 * IDENMM(6, 4)$
 C
 $XX(2, 5) = LE(2, 1) * IDENMM(1, 5) + LE(2, 2) * IDENMM(2, 5) + LE(2, 3)$
 $1 * IDENMM(3, 5) + LE(2, 4) * IDENMM(4, 5) + LE(2, 5) * IDENMM(5, 5) + LE(2, 6)$
 $2 * IDENMM(6, 5)$
 C
 $XX(2, 6) = LE(2, 1) * IDENMM(1, 6) + LE(2, 2) * IDENMM(2, 6) + LE(2, 3)$
 $1 * IDENMM(3, 6) + LE(2, 4) * IDENMM(4, 6) + LE(2, 5) * IDENMM(5, 6) + LE(2, 6)$
 $2 * IDENMM(6, 6)$
 C
 $XX(3, 1) = LE(3, 1) * IDENMM(1, 1) + LE(3, 2) * IDENMM(2, 1) + LE(3, 3)$
 $1 * IDENMM(3, 1) + LE(3, 4) * IDENMM(4, 1) + LE(3, 5) * IDENMM(5, 1) + LE(3, 6)$
 $2 * IDENMM(6, 1)$
 C
 $XX(3, 2) = LE(3, 1) * IDENMM(1, 2) + LE(3, 2) * IDENMM(2, 2) + LE(3, 3)$
 $1 * IDENMM(3, 2) + LE(3, 4) * IDENMM(4, 2) + LE(3, 5) * IDENMM(5, 2) + LE(3, 6)$
 $2 * IDENMM(6, 2)$
 C
 $XX(3, 3) = LE(3, 1) * IDENMM(1, 3) + LE(3, 2) * IDENMM(2, 3) + LE(3, 3)$
 $1 * IDENMM(3, 3) + LE(3, 4) * IDENMM(4, 3) + LE(3, 5) * IDENMM(5, 3) + LE(3, 6)$
 $2 * IDENMM(6, 3)$
 C
 $XX(3, 4) = LE(3, 1) * IDENMM(1, 4) + LE(3, 2) * IDENMM(2, 4) + LE(3, 3)$
 $1 * IDENMM(3, 4) + LE(3, 4) * IDENMM(4, 4) + LE(3, 5) * IDENMM(5, 4) + LE(3, 6)$
 $2 * IDENMM(6, 4)$
 C
 $XX(3, 5) = LE(3, 1) * IDENMM(1, 5) + LE(3, 2) * IDENMM(2, 5) + LE(3, 3)$
 $1 * IDENMM(3, 5) + LE(3, 4) * IDENMM(4, 5) + LE(3, 5) * IDENMM(5, 5) + LE(3, 6)$
 $2 * IDENMM(6, 5)$
 C
 $XX(3, 6) = LE(3, 1) * IDENMM(1, 6) + LE(3, 2) * IDENMM(2, 6) + LE(3, 3)$
 $1 * IDENMM(3, 6) + LE(3, 4) * IDENMM(4, 6) + LE(3, 5) * IDENMM(5, 6) + LE(3, 6)$
 $2 * IDENMM(6, 6)$
 C
 C
 $XX(4, 1) = LE(4, 1) * IDENMM(1, 1) + LE(4, 2) * IDENMM(2, 1) + LE(4, 3)$
 $1 * IDENMM(3, 1) + LE(4, 4) * IDENMM(4, 1) + LE(4, 5) * IDENMM(5, 1) + LE(4, 6)$
 $2 * IDENMM(6, 1)$
 C
 $XX(4, 2) = LE(4, 1) * IDENMM(1, 2) + LE(4, 2) * IDENMM(2, 2) + LE(4, 3)$
 $1 * IDENMM(3, 2) + LE(4, 4) * IDENMM(4, 2) + LE(4, 5) * IDENMM(5, 2) + LE(4, 6)$
 $2 * IDENMM(6, 2)$
 C
 $XX(4, 3) = LE(4, 1) * IDENMM(1, 3) + LE(4, 2) * IDENMM(2, 3) + LE(4, 3)$
 $1 * IDENMM(3, 3) + LE(4, 4) * IDENMM(4, 3) + LE(4, 5) * IDENMM(5, 3) + LE(4, 6)$
 $2 * IDENMM(6, 3)$
 C
 $XX(4, 4) = LE(4, 1) * IDENMM(1, 4) + LE(4, 2) * IDENMM(2, 4) + LE(4, 3)$
 $1 * IDENMM(3, 4) + LE(4, 4) * IDENMM(4, 4) + LE(4, 5) * IDENMM(5, 4) + LE(4, 6)$
 $2 * IDENMM(6, 4)$
 C
 $XX(4, 5) = LE(4, 1) * IDENMM(1, 5) + LE(4, 2) * IDENMM(2, 5) + LE(4, 3)$
 $1 * IDENMM(3, 5) + LE(4, 4) * IDENMM(4, 5) + LE(4, 5) * IDENMM(5, 5) + LE(4, 6)$
 $2 * IDENMM(6, 5)$
 C
 $XX(4, 6) = LE(4, 1) * IDENMM(1, 6) + LE(4, 2) * IDENMM(2, 6) + LE(4, 3)$
 $1 * IDENMM(3, 6) + LE(4, 4) * IDENMM(4, 6) + LE(4, 5) * IDENMM(5, 6) + LE(4, 6)$
 $2 * IDENMM(6, 6)$
 C
 $XX(5, 1) = LE(5, 1) * IDENMM(1, 1) + LE(5, 2) * IDENMM(2, 1) + LE(5, 3)$
 $1 * IDENMM(3, 1) + LE(5, 4) * IDENMM(4, 1) + LE(5, 5) * IDENMM(5, 1) + LE(5, 6)$
 $2 * IDENMM(6, 1)$
 $XX(5, 2) = LE(5, 1) * IDENMM(1, 2) + LE(5, 2) * IDENMM(2, 2) + LE(5, 3)$

```

1 *IDENMM(3,2)+LE(5,4)*IDENMM(4,2)+LE(5,5)*IDENMM(5,2)+LE(5,6)
2 *IDENMM(6,2)
C
XX(5,3)=LE(5,1)*IDENMM(1,3)+LE(5,2)*IDENMM(2,3)+LE(5,3)
1 *IDENMM(3,3)+LE(5,4)*IDENMM(4,3)+LE(5,5)*IDENMM(5,3)+LE(5,6)
2 *IDENMM(6,3)
C
XX(5,4)=LE(5,1)*IDENMM(1,4)+LE(5,2)*IDENMM(2,4)+LE(5,3)
1 *IDENMM(3,4)+LE(5,4)*IDENMM(4,4)+LE(5,5)*IDENMM(5,4)+LE(5,6)
2 *IDENMM(6,4)
C
XX(5,5)=LE(5,1)*IDENMM(1,5)+LE(5,2)*IDENMM(2,5)+LE(5,3)
1 *IDENMM(3,5)+LE(5,4)*IDENMM(4,5)+LE(5,5)*IDENMM(5,5)+LE(5,6)
2 *IDENMM(6,5)
C
XX(5,6)=LE(5,1)*IDENMM(1,6)+LE(5,2)*IDENMM(2,6)+LE(5,3)
1 *IDENMM(3,6)+LE(5,4)*IDENMM(4,6)+LE(5,5)*IDENMM(5,6)+LE(5,6)
2 *IDENMM(6,6)
C
XX(6,1)=LE(6,1)*IDENMM(1,1)+LE(6,2)*IDENMM(2,1)+LE(6,3)
1 *IDENMM(3,1)+LE(6,4)*IDENMM(4,1)+LE(6,5)*IDENMM(5,1)+LE(6,6)
2 *IDENMM(6,1)
C
XX(6,2)=LE(6,1)*IDENMM(1,2)+LE(6,2)*IDENMM(2,2)+LE(6,3)
1 *IDENMM(3,2)+LE(6,4)*IDENMM(4,2)+LE(6,5)*IDENMM(5,2)+LE(6,6)
2 *IDENMM(6,2)
C
XX(6,3)=LE(6,1)*IDENMM(1,3)+LE(6,2)*IDENMM(2,3)+LE(6,3)
1 *IDENMM(3,3)+LE(6,4)*IDENMM(4,3)+LE(6,5)*IDENMM(5,3)+LE(6,6)
2 *IDENMM(6,3)
C
XX(6,4)=LE(6,1)*IDENMM(1,4)+LE(6,2)*IDENMM(2,4)+LE(6,3)
1 *IDENMM(3,4)+LE(6,4)*IDENMM(4,4)+LE(6,5)*IDENMM(5,4)+LE(6,6)
2 *IDENMM(6,4)
C
XX(6,5)=LE(6,1)*IDENMM(1,5)+LE(6,2)*IDENMM(2,5)+LE(6,3)
1 *IDENMM(3,5)+LE(6,4)*IDENMM(4,5)+LE(6,5)*IDENMM(5,5)+LE(6,6)
2 *IDENMM(6,5)
C
XX(6,6)=LE(6,1)*IDENMM(1,6)+LE(6,2)*IDENMM(2,6)+LE(6,3)
1 *IDENMM(3,6)+LE(6,4)*IDENMM(4,6)+LE(6,5)*IDENMM(5,6)+LE(6,6)
2 *IDENMM(6,6)
C
*****
DO i=1,6
  DO j=1,6
    XXX(i,j)=XX(i,j)/DET
  END DO
END DO
C
*****
LE_ESCT(1,1)=LE(1,1)*ESCT(1,1)+LE(1,2)*ESCT(2,2)+LE(1,3)*ESCT(3,3)
1 +LE(1,4)*ESCT(1,2)+LE(1,5)*ESCT(2,3)+LE(1,6)*ESCT(3,1)
C
LE_ESCT(2,2)=LE(2,1)*ESCT(1,1)+LE(2,2)*ESCT(2,2)+LE(2,3)*ESCT(3,3)
1 +LE(2,4)*ESCT(1,2)+LE(2,5)*ESCT(2,3)+LE(2,6)*ESCT(3,1)
C
LE_ESCT(3,3)=LE(3,1)*ESCT(1,1)+LE(3,2)*ESCT(2,2)+LE(3,3)*ESCT(3,3)
1 +LE(3,4)*ESCT(1,2)+LE(3,5)*ESCT(2,3)+LE(3,6)*ESCT(3,1)
C
LE_ESCT(1,2)=LE(4,1)*ESCT(1,1)+LE(4,2)*ESCT(2,2)+LE(4,3)*ESCT(3,3)
1 +LE(4,4)*ESCT(1,2)+LE(4,5)*ESCT(2,3)+LE(4,6)*ESCT(3,1)
C
LE_ESCT(2,3)=LE(5,1)*ESCT(1,1)+LE(5,2)*ESCT(2,2)+LE(5,3)*ESCT(3,3)
1 +LE(5,4)*ESCT(1,2)+LE(5,5)*ESCT(2,3)+LE(5,6)*ESCT(3,1)

```

```

C      LE_ESCT(3,1)=LE(6,1)*ESCT(1,1)+LE(6,2)*ESCT(2,2)+LE(6,3)*ESCT(3,3)
1      +LE(6,4)*ESCT(1,2)+LE(6,5)*ESCT(2,3)+LE(6,6)*ESCT(3,1)
C
      LE_ESCT(2,1)=LE_ESCT(1,2)
      LE_ESCT(3,2)=LE_ESCT(2,3)
      LE_ESCT(1,3)=LE_ESCT(3,1)
C      ***** CONNECTIVE TISSUE STRESS TENSOR*****
      DO i=1,3
        DO j=1,3
          STCT(i,j)= ONE/DET * LE_ESCT(i,j)
        END DO
      END DO
C      ***** MUSCLE STRESS TENSOR*****
      STRESS(1)=STF(1,1)+STCT(1,1)
      STRESS(2)=STF(2,2)+STCT(2,2)
      STRESS(3)=STF(3,3)+STCT(3,3)
      STRESS(4)=STF(1,2)+STCT(1,2)
      STRESS(5)=STF(2,3)+STCT(2,3)
      STRESS(6)=STF(3,1)+STCT(3,1)
C      *****STD CONNECTIVE TISSUE STRESS AND DELTA PRODUCT      CALCULATION*****
      STD(1,1)=STCT(1,1)*DELTA(1,1)
      STD(1,2)=STCT(1,1)*DELTA(2,2)
      STD(1,3)=STCT(1,1)*DELTA(3,3)
      STD(1,4)=STCT(1,1)*DELTA(1,2)
      STD(1,5)=STCT(1,1)*DELTA(2,3)
      STD(1,6)=STCT(1,1)*DELTA(3,1)
C
      STD(2,1)=STCT(2,2)*DELTA(1,1)
      STD(2,2)=STCT(2,2)*DELTA(2,2)
      STD(2,3)=STCT(2,2)*DELTA(3,3)
      STD(2,4)=STCT(2,2)*DELTA(1,2)
      STD(2,5)=STCT(2,2)*DELTA(2,3)
      STD(2,6)=STCT(2,2)*DELTA(3,1)
C
      STD(3,1)=STCT(3,3)*DELTA(1,1)
      STD(3,2)=STCT(3,3)*DELTA(2,2)
      STD(3,3)=STCT(3,3)*DELTA(3,3)
      STD(3,4)=STCT(3,3)*DELTA(1,2)
      STD(3,5)=STCT(3,3)*DELTA(2,3)
      STD(3,6)=STCT(3,3)*DELTA(3,1)
C
      STD(4,1)=STCT(1,2)*DELTA(1,1)
      STD(4,2)=STCT(1,2)*DELTA(2,2)
      STD(4,3)=STCT(1,2)*DELTA(3,3)
      STD(4,4)=STCT(1,2)*DELTA(1,2)
      STD(4,5)=STCT(1,2)*DELTA(2,3)
      STD(4,6)=STCT(1,2)*DELTA(3,1)
C
      STD(5,1)=STCT(2,3)*DELTA(1,1)
      STD(5,2)=STCT(2,3)*DELTA(2,2)
      STD(5,3)=STCT(2,3)*DELTA(3,3)
      STD(5,4)=STCT(2,3)*DELTA(1,2)
      STD(5,5)=STCT(2,3)*DELTA(2,3)
      STD(5,6)=STCT(2,3)*DELTA(3,1)
C
      STD(6,1)=STCT(3,1)*DELTA(1,1)
      STD(6,2)=STCT(3,1)*DELTA(2,2)
      STD(6,3)=STCT(3,1)*DELTA(3,3)
      STD(6,4)=STCT(3,1)*DELTA(1,2)
      STD(6,5)=STCT(3,1)*DELTA(2,3)
      STD(6,6)=STCT(3,1)*DELTA(3,1)
C      *****CCT CALCULATION*****

```

```

DO i=1,6
  DO j=1,6
    CCT(i,j)=(XXX(i,j)-STD(i,j))
  END DO
END DO
C *****C CALCULATION*****
DO i=1,3
  DO j=1,3
    DDSDE(i,j)=CF(i,j)+ CCT(i,j)
  END DO
END DO
C *****C:dL=CdL CALCULATION*****
CDES(1,1)=C(1,1)*DES(1,1)+C(1,2)*DES(2,2)+C(1,3)*DES(3,3)
1 +C(1,4)*DES(1,2)+C(1,5)*DES(2,3)+C(1,6)*DES(3,1)
CDES(2,2)=C(2,1)*DES(1,1)+C(2,2)*DES(2,2)+C(2,3)*DES(3,3)
1 +C(2,4)*DES(1,2)+C(2,5)*DES(2,3)+C(2,6)*DES(3,1)
CDES(3,3)=C(3,1)*DES(1,1)+C(3,2)*DES(2,2)+C(3,3)*DES(3,3)
1 +C(3,4)*DES(1,2)+C(3,5)*DES(2,3)+C(3,6)*DES(3,1)
C
CDES(1,2)=C(4,1)*DES(1,1)+C(4,2)*DES(2,2)+C(4,3)*DES(3,3)
1 +C(4,4)*DES(1,2)+C(4,5)*DES(2,3)+C(4,6)*DES(3,1)
CDES(2,3)=C(5,1)*DES(1,1)+C(5,2)*DES(2,2)+C(5,3)*DES(3,3)
1 +C(5,4)*DES(1,2)+C(5,5)*DES(2,3)+C(5,6)*DES(3,1)
CDES(3,1)=C(6,1)*DES(1,1)+C(6,2)*DES(2,2)+C(6,3)*DES(3,3)
1 +C(6,4)*DES(1,2)+C(6,5)*DES(2,3)+C(6,6)*DES(3,1)
C
CDES(2,1)=CDES(1,2)
CDES(3,2)=CDES(2,3)
CDES(1,3)=CDES(3,1)
C *****DSTRESS CALCULATION*****
DSTRESS(1)=CDES(1,1)-(1.0d0/2.0d0)*(stress(1)*dldlt(1,1)+stress(4)
1*dldlt(2,1)+stress(6)*dldlt(3,1) -(dldlt(1,1)*stress(1)+dldlt(2,1)
2*stress(4)+dldlt(3,1)*stress(6))
C
DSTRESS(2)=CDES(2,2)-(1.d0/2.d0)*(stress(4)*dldlt(1,2)+stress(2)
1*dldlt(2,2)+stress(5)*dldlt(3,2) -(dldlt(1,2)*stress(4)+dldlt(2,2)
2*stress(2)+dldlt(3,2)*stress(5))
C
DSTRESS(3)=CDES(3,3)-(1.d0/2.d0)*(stress(6)*dldlt(1,3)+stress(5)
1*dldlt(2,3)+stress(3)*dldlt(3,3) -(dldlt(1,3)*stress(6)+dldlt(2,3)
2*stress(5)+dldlt(3,3)*stress(3))
C
DSTRESS(4)=CDES(1,2)-(1.d0/2.d0)*(stress(1)*dldlt(1,2)+stress(4)
1*dldlt(2,2)+stress(6)*dldlt(3,2) -(dldlt(1,2)*stress(1)+dldlt(1,2)
2*stress(4)+dldlt(3,2)*stress(6))
C
DSTRESS(5)=CDES(2,3)-(1.d0/2.d0)*(stress(4)*dldlt(1,3)+stress(2)
1*dldlt(2,3)+stress(5)*dldlt(3,3) -(dldlt(1,3)*stress(4)+dldlt(2,3)
2*stress(2)+dldlt(3,3)*stress(5))
C
DSTRESS(6)=CDES(3,1)-(1.d0/2.d0)*(stress(1)*dldlt(1,3)+stress(4)
1*dldlt(2,3)+stress(6)*dldlt(3,3) -(dldlt(1,3)*stress(1)+dldlt(2,3)
2*stress(4)+dldlt(3,3)*stress(6))
C *****STREE CALCULATION*****
STRESS(1)=STRESS(1)+DSTRESS(1)
STRESS(2)=STRESS(2)+DSTRESS(2)
STRESS(3)=STRESS(3)+DSTRESS(3)
STRESS(4)=STRESS(4)+DSTRESS(4)
STRESS(5)=STRESS(5)+DSTRESS(5)
STRESS(6)=STRESS(6)+DSTRESS(6)
C
RETURN
END

```